

REVIEW ARTICLE

Major results from the stellarator Wendelstein 7-AS

To cite this article: M Hirsch *et al* 2008 *Plasma Phys. Control. Fusion* **50** 053001

View the [article online](#) for updates and enhancements.

Related content

- [Physics of island divertors](#)
Y. Feng, F. Sardei, P. Grigull *et al.*
- [Experiments close to the beta-limit in W7-AS](#)
A Weller, J Geiger, A Werner *et al.*
- [ECRH at W7-A and W7-AS](#)
V. Erckmann, H.P. Laqua, H. Maaßberg *et al.*

Recent citations

- [First results of the multi-purpose real-time processing video camera system on the Wendelstein 7-X stellarator and implications for future devices](#)
S. Zoleznik *et al*
- [Role of isotope mass and evidence of fluctuating zonal flows during the L-H transition in the TJ-II stellarator](#)
U Losada *et al*
- [First steps towards modeling of ion-driven turbulence in Wendelstein 7-X](#)
F. Warmer *et al*

REVIEW ARTICLE**Major results from the stellarator Wendelstein 7-AS**

**M Hirsch, J Baldzuhn, C Beidler, R Brakel, R Burhenn, A Dinklage,
H Ehmler, M Endler, V Erckmann, Y Feng, J Geiger, L Giannone,
G Grieger, P Grigull, H-J Hartfuß, D Hartmann, R Jaenicke, R König,
H P Laqua, H Maaßberg, K McCormick, F Sardei, E Speth, U Stroth,
F Wagner, A Weller, A Werner, H Wobig, S Zoleznik for the W7-AS Team¹**

Max-Planck-Institut für Plasmaphysik, EURATOM Association, Teilinstitut Greifswald,
D-17491 Greifswald, Germany

Received 22 May 2006 , in final form 21 December 2007

Published 10 March 2008

Online at stacks.iop.org/PPCF/50/053001

Abstract

Wendelstein 7-AS was the first modular stellarator device to test some basic elements of stellarator optimization: a reduced Shafranov shift and improved stability properties resulted in β -values up to 3.4% (at 0.9 T). This operational limit was determined by power balance and impurity radiation without noticeable degradation of stability or a violent collapse. The partial reduction of neoclassical transport could be verified in agreement with calculations indicating the feasibility of the concept of drift optimization. A full neoclassical optimization, in particular a minimization of the bootstrap current was beyond the scope of this project. A variety of non-ohmic heating and current drive scenarios by ICRH, NBI and in particular, ECRH were tested and compared

¹ The W7-AS Team: V I Afanasiev (guest), M Anton, R Balbin, J Baldzuhn, M Ballico, N Basse, S Bäumel, C D Beidler, Th Bindemann, J Bleuel, R Brakel, B Branas, M Bruchhausen, R Büchse, R Burhenn, H P Callaghan (guest), G Cattanei, J-H Chatenet (guest), J Das, A Dinklage, A Dodhy, D Dorst, K S Dyabilin (guest), S Egorov (guest), H Ehmler, A Elsner, M Endler, K Engelhardt, V Erckmann, T Estrada, Y Feng, S Fiedler, M Fink, C Fuchs, F Gadelmeier, F Gandini (guest), U Gasparino, A Geier, J Geiger, T Geist, S Geißler, L Giannone, C Görner, G Grieger, P Grigull, O Grulke, H Hacker, M Haese, E Harmeyer, H J Hartfuß, D Hartmann, O Heinrich, G Herre, F Herrnegger, D Hildebrandt, M Hirsch, J V Hofmann, E Holzhauer, R Horn, K Hübner, K Ida (guest), Y Igkitkhanov, S-I Itoh (guest), K Itoh (guest), A B Izvozchikov, H Jäckel, R Jaenicke, J Junker, M Kaiser, F Karger, W Kasparek, M Kick, A Kislyakov (guest), J Kisslinger, Th Klinger, S Klose, J Knauer, C Kocsis (guest), R König, R Komen, K Kondo (guest), Ch Konrad, J P T Koponen, H Kroiss, M Krychowiak, S Kubo (guest), G Kuehner, A Kus, I Lakicevic, H P Laqua, H Laqua, A Lazaros, L Ledl, E De la Luna, L V Lubyako (guest), T Luce (guest), J Lyon (guest), H Maaßberg, C Mahn, W Mandl, N B Marushchenko, K McCormick, G Michel, G Müller, G A Müller, D Naujoks, U Neuner, H Niedermeyer, J-M Noterdaeme (guest), C Nührenberg, W Ohlendorf, W Ott, M Otte, E Pasch, F P Penningsfeld, W Pernreiter, M Peters (guest), U Pfeiffer, V Plyusnin (guest), F Rau, N Ramasubramanian (guest), S Reimbold, H Renner, M Richter-Glötzl, H Ringler, M Rome, A Rudy, N Ruhs, N Rust, J Saffert, E Sallander, J Sallander, J Sanchez (guest), J Sapper, F Sardei, S Sattler, F Schneider, U Schneider, M Schubert, V Y Sergeev (guest), A G Shalashov (guest), G Siller, E Simmet, E Speth, U Stroth, E V Suvorov (guest), W Svendsen, A C Y Teo, A Teubel, G Theimer, H Thomsen, V M Timokhin (guest), M Tutter, E Unger, H Verbeek, Ph Verplancke, F Volpe, F Wagner, H Walter, A Weller, Ch Wendland, U Wenzel, A Werner, F Wesner, B Wolle, H Wobig, E Würsching, H Yamada (guest), M Zarnstorff (guest), P Zeiler, M Zerbini (guest), X Zhang (guest), D Zimmerman, M Zippe, S Zoepfel, S Zoleznik.

successfully with their theoretical predictions. Besides, new heating schemes of overdense plasmas were developed such as RF mode conversion heating—Ordinary mode, Extraordinary mode, Bernstein-wave (OXB) heating—or 2nd harmonic O-mode (O2) heating. The energy confinement was about a factor of 2 above ISS95 without degradation near operational boundaries. A number of improved confinement regimes such as core electron-root confinement with central $T_e \leq 7$ keV and regimes with strongly sheared radial electric field at the plasma edge resulting in $T_i \leq 1.7$ keV were obtained. As the first non-tokamak device, W7-AS achieved the H-mode and moreover developed a high density H-mode regime (HDH) with strongly reduced impurity confinement that allowed quasi-steady-state operation ($\tau \approx 65 \cdot \tau_E$) at densities $\bar{n}_e \approx 4 \times 10^{20} \text{ m}^{-3}$ (at 2.5 T). The first island divertor was tested successfully and operated with stable partial detachment in agreement with numerical simulations. With these results W7-AS laid the physics background for operation of an optimized low-shear steady-state stellarator.

(Some figures in this article are in colour only in the electronic version)

Contents

1. Introduction	3
1.1. The Wendelstein stellarator line	4
1.2. The principles of stellarator optimization towards W7-AS	7
1.3. Concept and aims of the Wendelstein 7-AS project	8
2. The W7-AS experiment	9
2.1. Coil systems	9
2.2. Vacuum magnetic field configurations	10
2.3. Equilibrium properties	13
2.4. Stability properties	14
2.5. Wall conditioning, limiters and divertor	15
2.6. Heating systems	15
2.7. Diagnostic equipment and diagnostic development	17
3. Neoclassics and kinetic theory	21
3.1. Elements of drift optimization in W7-AS	22
3.2. Neoclassical transport coefficients	24
3.3. Ambipolar radial electric field	27
3.4. Transport analysis	30
3.5. Impurity transport	31
3.6. Bootstrap and inductive currents	32
4. Heating and current drive	36
4.1. Electron cyclotron resonance heating and current drive	37
4.2. Neutral beam heating	52
4.3. Ion cyclotron resonance heating	58
5. Energy confinement	61
5.1. Global energy confinement scaling	62
5.2. Impact of rational surfaces and magnetic shear on electron energy transport	65
5.3. Local heat transport	69
5.4. Observations on turbulence and turbulent transport	80

6.	Particle and impurity behaviour	85
6.1.	Particle confinement	85
6.2.	Impurity confinement	91
6.3.	Density limit	100
6.4.	Summary	104
7.	H-mode regimes	105
7.1.	The quiescent H-mode	106
7.2.	The H-mode transition	109
7.3.	ELMs	113
7.4.	operational conditions	115
7.5.	Achievement of the HDH mode	118
7.6.	Properties of the HDH mode	118
7.7.	Transition from quiescent H-mode to HDH	123
7.8.	Discussion on H-mode physics in W7-AS	125
7.9.	Conclusion on H-modes in W7-AS	127
8.	Plasma edge and divertor physics	128
8.1.	Introduction	128
8.2.	The island divertor concept	129
8.3.	The W7-AS island divertor	130
8.4.	Experimental results	131
8.5.	Modelling and theoretical assessment	141
8.6.	Conclusion	151
9.	MHD stability	153
9.1.	Introductory remarks	153
9.2.	Pressure driven modes	153
9.3.	Current induced MHD-effects	155
9.4.	Fast ion driven Alfvén instabilities	160
9.5.	Discussion	167
10.	High- β operation	168
10.1.	Introductory remarks	168
10.2.	Formation and optimization of high- β discharges	168
10.3.	Confinement and operational limits	170
10.4.	Equilibrium studies	172
10.5.	MHD stability—low mode number	177
10.6.	MHD stability—high mode number	178
10.7.	Discussion	180
11.	Summary and conclusions	181
11.1.	Main results	182
11.2.	W7-AS relevance for W7-X	184
11.3.	Prospects for the Helias reactor	187
11.4.	Concluding remarks	188
	Acknowledgments	188
	References	189

1. Introduction

Toroidal magnetic confinement requires twisted magnetic field lines. In a stellarator configuration as proposed by Lyman Spitzer Jr 1951 ([Spitzer 1958](#)) the necessary poloidal magnetic field component is generated by currents flowing in external coils whereas in a

tokamak the poloidal magnetic field is generated by a net toroidal current flowing in the plasma. Stellarators share most of the relevant technology with tokamaks. Their conceptual advantage is a steady-state capability without the need for current drive and a lack of current driven instabilities. A drawback is that stellarators are not compatible with axisymmetry which provides the possibility of additional loss channels for collisionless particles. In addition, both the three-dimensional magnetic field structure and the edge plasma shape must be sufficiently accurate to ensure acceptable load distributions to the first wall. On the other hand, the three dimensionality of the stellarator fields, together with the concept of non-planar modular field coils, offer the possibility of tailoring the magnetic geometry by using the third (geometrical) degree of freedom for optimization. The Wendelstein line at IPP Garching pursues this concept of stellarator optimization—the ‘advanced stellarator’ Wendelstein 7-AS was the first one to test some of its basic elements.

1.1. The Wendelstein stellarator line

The Wendelstein stellarator activities at IPP Garching started after the Geneva conference in 1958 where the stellarator concept was published. An overview over the Wendelstein devices preceding W7-AS is given in [Grieger et al \(1985\)](#). In Princeton the first results with the rather large Model-C-Stellarator had not at all satisfied the expectations ([Grove et al 1961](#)) as its magnetic configuration resulted in Bohm-diffusion which was far from what was needed for reactor conditions. These negative results led IPP to start a series of basic proof-of-principle investigations with plasmas as close as possible to thermodynamic equilibrium. W1-A ($l = 3$ helical windings, $R = 0.35$ m, $a = 0.02$ m, $B = 1$ T, Cs-plasmas) ([DeAngelo et al 1963](#)) and W1-B ($l = 2$ helical windings, other parameters identical with W1-A) ([Eckhart et al 1965](#), [Berkl et al 1966](#)) were race-track stellarator configurations similar in shape to the Model-C-Stellarator but much smaller in size. Mainly because of their transitions between straight and curved sections, their confinement properties turned out to be extremely vulnerable to even small magnetic error fields. Therefore the next step, W2-A, had a circular magnetic axis and five-fold toroidal symmetry ($m = 5$, $l = 2$ helical windings, $R = 0.5$ m, $a = 0.05$ m, $B < 0.6$ T). Ba-plasmas were produced on the magnetic axis by contact ionization. It was shown that for thermal plasmas classical confinement of Pfirsch–Schlüter type ([Pfirsch and Schläuter 1962](#)) could be reached under stationary conditions provided that (1) the coil system was properly designed and built accurately enough, and (2) the twist of the magnetic field lines, obtained as the rotational transform $\tau = d\chi/d\psi$ where χ and ψ are the poloidal and toroidal fluxes, respectively, was large enough for providing equilibrium everywhere over the plasma cross-section, and (3) the magnetic shear, $d\tau/dr$, was close to zero ([Berkl et al 1968](#)). These results led to the selection of low-shear properties for all the following Wendelstein devices.

Since W2-A could be operated under steady-state conditions as the contact ionization was on a small tantalum ball heated by a CO₂ laser beam, the effect of magnetic field structure on confinement could be studied by varying τ during the discharge. Figure 1 shows that particle confinement got dramatically low at low-order resonant values of τ such as 1/3, 1/2, etc. At higher order resonances their importance decreased. For the regions between the resonances the confinement reaches the quoted classical values of the Pfirsch–Schlüter transport regime ([Grieger et al 1971](#)). It was suspected that magnetic islands—caused by error fields—in combination with convective cells were the primary reason for the collapse of confinement at rational τ -values ([Grieger et al 1971](#)). In a modified version this τ -dependence of plasma confinement is a basic characteristic of all later Wendelstein stellarators when operated at low shear ([Grieger et al \(1985\)](#) and section 5.1 of this review).

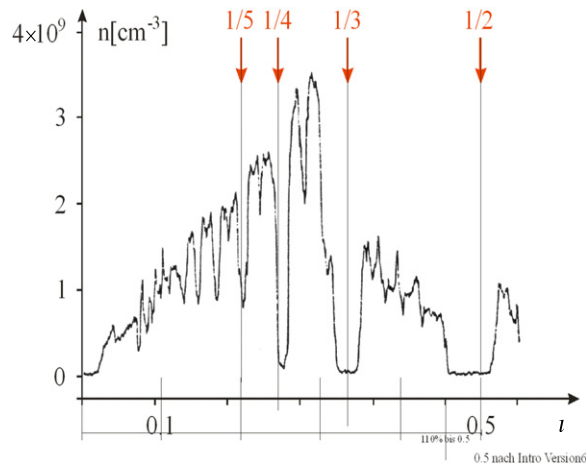


Figure 1. Resonances in plasma loss rate. For fixed input flux the density of a Ba-plasma is plotted as a function of t . Minima in the density, i.e. maxima in loss rates occur if t is close to a rational value. Some major resonances are indicated in red. The about 10% discrepancy between the plotted calculated t -scale and the observed position of the resonances is thought to be due to errors in the mechanical positioning of the helical field windings.

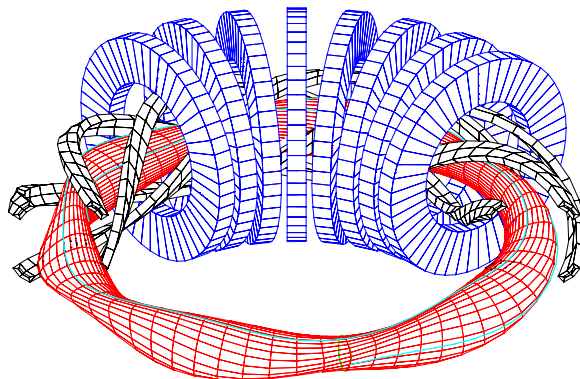


Figure 2. Scheme of Wendelstein 7-A, a classical $l = 2$ stellarator with five toroidal field periods.

W2-B was built with the same dimensions as W2-A but operated with hydrogen and equipped with a stray-field free ohmic heating (OH) transformer ($I \leq 3$ kA) and a higher magnetic field, $B < 1.25$ T (Hacker *et al* 1975). Energy confinement turned out to be compatible with that of equivalent tokamaks.

W7-A, a classical medium-size stellarator ($R = 2$ m, $a = 0.1$ m, $l = 2$ helical windings, five-fold toroidal symmetry, $B < 3.4$ T, figure 2), contributed with fusion relevant data. Based on the experience from the former experiments great care was taken to keep the shear of the vacuum field close to zero within the plasma region and to fabricate the helical windings with the highest possible accuracy to minimize field errors. A large number of toroidal field coils was used to minimize the toroidal ripple in order to get clear results on neoclassical losses by particles trapped in the helical ripples. W7-A was equipped with a large air-core OH transformer for tokamak-like plasma start-up and heating with

typically a few ten kiloamperes plasma current ([Grieger et al 1986](#)). Later on neutral beam injection heating (NBI) and electron cyclotron resonance heating (ECRH) were added. During 10 years (1976 to 1985) the experiments in W7-A accumulated a large number of results (for summaries see [Grieger et al \(1985, 1986\)](#)); three of them are highlighted here as they were of great importance for general stellarator research and strongly influenced the program of W7-AS.

For the conditions available on W7-A with ohmic heating ($n_e \leq 6 \times 10^{19} \text{ m}^{-3}$, $T_e \leq 900 \text{ eV}$, $T_i \leq 220 \text{ eV}$) disruptive instabilities and the preceding $m = 2$ resistive tearing modes could be avoided by a sufficiently large external component of the rotational transforms, $t > 0.14$ ([Blaumoser et al 1976](#), [Cannici et al 1978b](#)). These effects have been substantiated and explained ([W7A-Team \(1980\)](#), for corresponding investigations in W7-AS see section 9.3). As a consequence W7-A was able to explore the density limit in a regime without current disruption where the maximum sustainable density was determined by the power balance with impurity radiation as the main loss channel only. When approaching this operational boundary the confinement degraded with increasing density but without a violent collapse ([Cannici et al 1978a](#)).

Second, in 1980, plasma operation without net toroidal current could be realized with NBI heating demonstrating that stellarators without net toroidal current are able to confine a plasma with parameters comparable to those in tokamaks ([Team W7-A and NI Group 1980](#), [W7A-Team and NI Group 1982](#)). Central ion temperatures of $T_i \approx 1 \text{ keV}$ at line averaged densities of $\bar{n}_e = 10^{20} \text{ m}^{-3}$ could be achieved despite a rather unfavourable heating geometry which only allowed nearly perpendicular injection. The surprisingly high plasma parameters could only be understood in the framework of neoclassical theory by the build-up of a negative radial electric field by lost orbit ions and the resulting poloidal plasma rotation. This radial electric field leads to a significant reduction of neoclassical ion heat conductivity and, simultaneously, to an improvement of the heating efficiency due to a reduction of the orbit losses of hot ions. The build-up of the ambipolar radial electric field is a main element for understanding improved stellarator confinement regimes (see sections 3.3 and 6.3 for corresponding investigations at W7-AS).

A third important step was the application of the first high-power gyrotrons which became available in 1983 when electron cyclotron resonance heating experiments on W7-A started successfully with a 28 GHz gyrotron (200 kW, 40 ms pulse length, [Barkley et al \(1988\)](#)). This was the start-up of an exceedingly successful phase of ECRH technology and application which has now resulted in the industrial availability of megawatt-scale cw gyrotrons at 140 GHz for steady-state operation (see section 4.1 for corresponding investigations at W7-AS).

Together with the low-shear Wendelstein line at IPP other types of helical devices were investigated elsewhere. All of them, including W7-A, were based on winding laws for the coils without a preceding three-dimensional (3D) optimization of the confining magnetic field. In contrast to the Wendelstein stellarator line, heliotron configurations ([Uo et al \(1971\)](#), examples Heliotron-E ([Wakatani 1996](#)), CHS ([Okamura et al 1999](#)) and LHD ([Motojima et al 2003](#))) and Torsatron configurations ([Gourdon et al \(1968\)](#), example ATF) start from helical windings for which the return path is left away. They are characterized by medium to high shear. A modular coil system and from that a fully 3D optimization are difficult to realize. Another helical concept is the Heliac, which was expected to have very good stability properties, examples are TJ-II ([Alejaldre et al 2002](#)) and H-1 ([Shats et al 1994](#)). Their coil concept consists of a circular centre coil producing a part of the poloidal field components and a set of (planar) toroidal field coils which are displaced helically around this centre coil. A synopsis of the different stellarator concepts is given in [Carreras et al \(1988\)](#).

1.2. The principles of stellarator optimization towards W7-AS

For a classical stellarator there remain severe physics problems in the extrapolation to reactor grade plasmas. First, high-energy, low-collisionality particles trapped in the 3D structure of the B -field are subject to a large ∇B -drift. The resulting neoclassical transport degrades the confinement strongly with temperature and would thus not allow for reactor conditions. Second, the equilibrium pressure limit resulting from the Shafranov shift of the flux surfaces relative to each other is too low for economic reactor operation. Therefore it became evident that the classical stellarator concept had to be improved for the confinement of low-collisionality plasmas, the confinement of energetic particles and for higher equilibrium and stability limits.

A corresponding programme launched at IPP Garching in 1978 followed the strategy of the former Wendelstein devices to develop a stellarator with low shear using modular coils that enable a fully 3D (drift) optimization. Plasma currents, such as secondary pressure driven currents like the Pfirsch–Schlüter and the bootstrap current, should be minimized to avoid sources of free energy and associated instabilities and to maintain the optimized magnetic configuration independent of pressure. The concept of drift optimization was based on the ideas of Palumbo (1968), who showed that in toroidal equilibria the guiding-centre drift normal to magnetic surfaces is zero—and consequently all neoclassical fluxes—if $|B|$ is constant along orthogonals to the magnetic field lines on magnetic surfaces. In such cases the geodesic curvature, κ_g , of the field lines on the magnetic surface vanishes, i.e. the field lines are geodesics (Pfirsch and Wobig 1965). The geodesic curvature also governs the ratio of parallel to perpendicular pressure driven currents j_{\parallel}/j_{\perp} (Pfirsch–Schlüter currents parallel to B to diamagnetic currents perpendicular to B) which gives rise to the Shafranov-shift. Reducing the geodesic curvature therefore increases the obtainable high- β equilibrium limit and simultaneously reduces neoclassical transport at least in the collisional and the plateau regime. Palumbo called these equilibria isodynamic (Palumbo 1971).

An ideal isodynamic system is incompatible with toroidal connectivity which requires curvature (Wobig 1993). As an approach Schlüter and Dommaschk (1981) modelled vacuum magnetic fields using the quantity $Q = \int dl/B$ as a measure where the integration in Q is performed along a field line over one field period. A minimum variation of Q , $S = \langle Q^2 \rangle - \langle Q \rangle^2$, where the brackets indicate averages on a magnetic surface, is a figure of merit for the drift optimization of passing particles.

A significant reduction of j_{\parallel}/j_{\perp} over all the plasma cross-section can be achieved only if the detrimental effect of the toroidal curvature is overcome with the help of $l = 1$ helical components of the magnetic field. However, the $l = 1$ components increase the local curvature and, unavoidably, also the population of trapped particles. Thus the danger exists that in configurations with reduced j_{\parallel}/j_{\perp} and optimized drift orbits of *passing* particles enhanced *trapped* particle losses occur in the low-collisionality regime. This danger can be mitigated by an appropriate choice of the toroidal variation of $|B|$ in order to localize particles in a region of small curvature of the field line where drift velocities are small. These predictions were verified with 3D MHD codes (Bauer *et al.* 1978, Chodura and Schröder 1981) and Monte-Carlo simulations of transport (Brossmann *et al.* 1982); results are summarized in Chodura *et al.* (1981).

The realization of such distinct 3D advanced stellarator configurations is based on the concept of modular field coils or Wobig–Rehker coils (Wobig and Rehker 1972) illustrated in figure 3. The idea resulted from the fact that any toroidal vacuum field in a domain which is tangential to the boundary surface of this domain can be produced by a current sheath on this surface. Discretizing this sheath into current lines and application of analytical winding laws yield a set of poloidally closed coils (Harmeyer *et al.* 1985, Merkel 1987). Such a system of

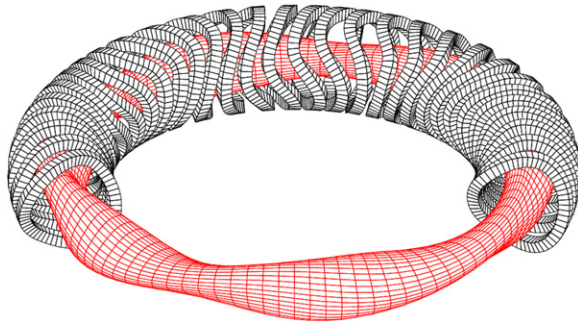


Figure 3. Scheme of a classical $l = 2$ stellarator with five toroidal field periods (similar to figure 2) but with a modular coil system.

modular coils also reduces the forces between helical windings and the toroidal field system of a classical stellarator to manageable levels. Since in a system of modular coils the rotational transform τ is fixed, additional toroidal field (TF) coils must be superimposed if experimental flexibility, e.g. a variation of τ , is desired.

1.3. Concept and aims of the Wendelstein 7-AS project

A benchmark experiment was considered necessary to test the optimization concept, the feasibility of modular coil manufacturing and the confinement of such a system. The idea was to design a ‘partially optimized’ advanced stellarator under the constraints set by the existing dimensions of W7-A to use a part of its already existing equipment, e.g. mechanical structures, OH transformer as well as vertical and toroidal field coils. The aims defined for this W7-AS project—where ‘AS’ stands for advanced stellarator—were ([Broermann et al 1982](#), [W7AS-Team 1981](#)):

- to investigate plasma behaviour in a partially optimized magnetic field configuration for which theory predicts improved plasma equilibrium and smaller neoclassical transport losses compared with classical $l = 2$ configurations;
- to investigate a plasma without ohmic heating to avoid current driven instabilities;
- to develop and employ methods of plasma generation and heating without OH current and use them for high- β and high power studies;
- to make use of a modular set of poloidally closed coils instead of the conventional helix / toroidal field coil system;
- to use these modular coils for an increase of the plasma minor radius for a better separation between plasma core and boundary.

For the concept realization, studies of vacuum field configurations were made with the aim of reducing pressure driven currents j_{\parallel}/j_{\perp} by minimizing the variation of Q . A low plasma aspect ratio ($A \approx 10$) was favoured against a further drift optimization. This aspect ratio and the limited inner bore of the reused W7-A toroidal field coils ruled out configurations with helix-like magnetic axis resembling an emerging $l = 1$ helical component of the magnetic field. Therefore the main element for a reduction of the ratio j_{\parallel}/j_{\perp} became a reduced average *toroidal* curvature as achieved by an average elongation as in an elongated tokamak (details in sections 2.2 and 2.3). The magnetic fields which could be realized did not allow to test the possibilities of properly selected stellarator fields to minimize also the bootstrap current (see [Wobig \(1999\)](#)). Due to the dominant toroidal magnetic field components the bootstrap

Table 1. Characteristics of the W7-AS experiment. Maximum plasma parameters achieved are listed in section 11.

Coils system	Modular coils
Toroidal symmetry	$m = 5$
Major radius R_0	2 m
Plasma radius	Up to 0.18 m
Toroidal field B_ϕ	Up to 2.6 T
External rotational transform (low shear)	0.3–0.6
Magnetic well $\Delta V'/V'$	–0.015 to +0.01

current in W7-AS is similar to that of an equivalent elongated tokamak (details in section 3.6). The existence of a magnetic well was taken into account as a side condition to ensure MHD stability in a magnetic field configuration with low global magnetic shear (see section 2.4). The toroidal field period of W7-AS is $m = 5$. First tests of the island divertor were added as an aim later, after this divertor concept had been developed for the needs of the fully optimized stellarator W7-X. The test of a modular coil system was considered as a technical issue of strategic importance for a stellarator reactor.

A summary of this optimization work was presented at the IAEA Conference in Baltimore in 1982 together with the concept of the W7-AS device (Brossmann *et al* 1982). The proposal on Wendelstein 7-AS was submitted in 1981 and after a phase of preparatory studies the contracts on modular coils, the main components of the experiment, were signed in 1982. After a construction phase of 6 years the magnetic surfaces could be measured in summer 1988. First plasma was produced by ECRH in October 1988; the experiment was shut down in summer 2002. A brief summary of the W7-AS results is given in Wagner *et al* (2005).

2. The W7-AS experiment

This section describes the W7-AS device—coil system (section 2.1), vacuum vessel and first wall (section 2.5)—and its periphery, the available heating systems (section 2.6) and diagnostic equipment (section 2.7). Together with the vacuum magnetic field configurations (section 2.2), the degree of optimization with respect to equilibrium (section 2.3) and stability (section 2.4) is discussed.

The realization of W7-AS as an upgrade of W7-A introduced geometrical constraints. Essentially, the small torus vessel with the helical windings of W7-A was replaced by a larger, 3D-shaped vacuum vessel surrounded by the *modular* field (MF) coils. Ten of the *toroidal* field (TF) coils of W7-A were modified (enlarged inner bore) to fit around the MF coils. Thus the W7-AS stellarator became a medium-size experiment with a major radius of about 2 m and a rather small average plasma radius of $a \leq 18$ cm, resulting in aspect ratios larger than 11. For more data see table 1; plasma parameters achieved for different scenarios are given in section 5.1 and summarized in section 11.

2.1. Coil systems

The coil system of W7-AS was the first example in which a desired magnetic configuration is the starting point in the coil geometry design. For computational efficiency the optimized configuration was represented by a series of Dommaschk potentials (Dommaschk 1978) from which the magnetic fields, the flux surfaces, etc could be computed numerically. The geometry of the coils was derived from surface currents which had been calculated on a given torus defined

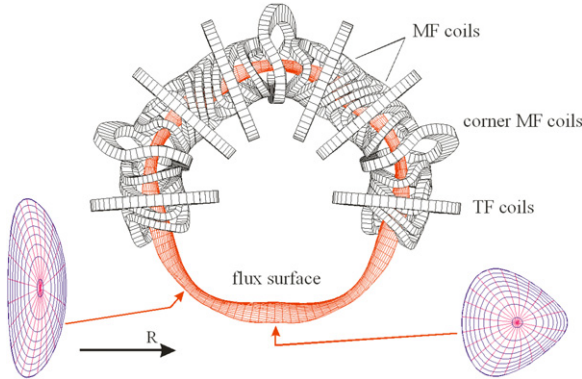


Figure 4. Top view of an outside flux surface together with part of the magnetic field coils.

by analytic functions with variable major radius, aspect ratio and rotating elliptic cross-section ([Dommaschk 1981](#)). The discretization of the surface current pattern led to a modular field coil system with nine different modular coils per field period. At the corners one coil was enlarged to provide access for almost tangential neutral beam injection. Additional side conditions not yet included in the configuration optimization were a maximization of available space for the vacuum vessel, a minimization of the curvature radii of the coils to facilitate coil construction and a minimization of the magnetic field variation close to the magnetic axis. Details on design and engineering aspects can be found in [Sapper and Renner \(1990\)](#) and [Mathis and Sapper \(1990\)](#).

The resulting plasma geometry together with a part of the modular field and toroidal field coils is shown in figure 4. The 45 non-planar MF coils are arranged in five toroidal periods and provide both toroidal and poloidal field components sufficient to generate closed magnetic flux surfaces with $\tau \approx 0.4$ and negligible shear. Additional coils are needed only to enable experimental flexibility. The planar TF coils allow variation of the toroidal field component and thus τ . All *poloidal* field coils were remnants from W7-A. The OH transformer was either used to compensate toroidal currents to zero (standard case) or to induce toroidal currents ($-35\text{ kA} < I_{\text{OH}} < +35\text{ kA}$, heating negligible as $P_{\text{OH}} < 10\text{ kW}$) in order to generate magnetic shear and to study current driven instabilities (see section 9.3). The advantage of a ‘net current-free’ mode of operation is that τ at the plasma edge is determined by the vacuum magnetic field alone. Thus the dependence of plasma confinement on τ under low magnetic shear conditions can be better controlled (see section 5.2). The vertical field coils ($0\text{ mT} < B_z < 40\text{ mT}$) were used to control the horizontal plasma position and to compensate the Shafranov shift. In a later phase a set of two control coils per field period resonant to the fivefold toroidal field symmetry was installed inside the vessel. They increased the flexibility of the edge magnetic structure as required for divertor- and high- β studies (see section 10.2).

Altogether, on W7-AS more than 56 000 magnetic field pulses have been performed (about 35 000 at full magnetic field of 2.5 T) demonstrating the feasibility of the modular field coil concept. Twice the coil support system has been improved to reduce deformations of the MF coils.

2.2. Vacuum magnetic field configurations

The magnetic field structure of W7-AS is indicated in figure 4 by the 3D shape of an outside flux surface. The magnetic axis is pentagon-shaped and nearly planar, the plasma cross-section

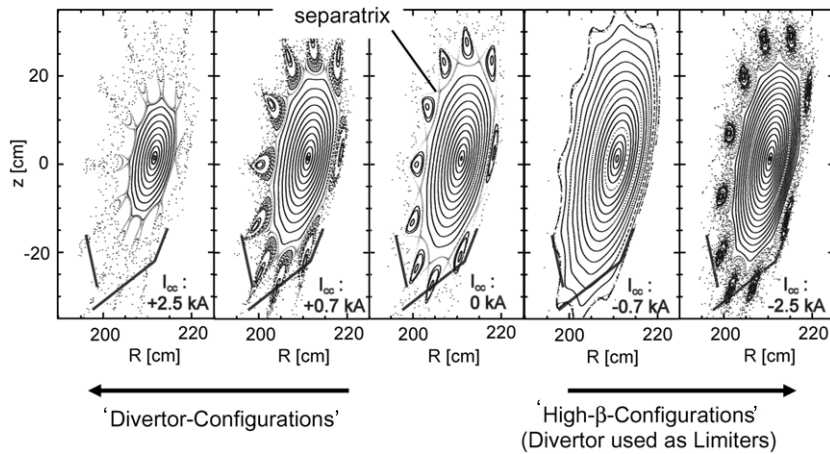


Figure 5. Field line tracing calculations at a poloidal plane $\varphi = 27^\circ$ showing the effect of control coils on the vacuum configuration. At the chosen $t/2$ without control coils ($I_{cc} = 0$) the plasma boundary is determined by the inner separatrix of the 5/10 natural island chain (middle). Currents in the modular coils I_m are negative for the case shown corresponding $B_\varphi = -2.5$ T. Negative values of the ratio I_{cc}/I_m (left) increase the edge islands. Slightly positive I_{cc}/I_m (middle right) reduce the island size, thus increasing the plasma volume. The divertor acts as a limiter in this case. Strongly positive I_{cc}/I_m (right) lead to overcompensated islands in the vacuum configuration, i.e. the natural islands occur again but with their poloidal phase shifted by π . The latter configurations were used for optimum high- β discharges (section 11).

varies from almost elliptical at the corners to more triangular in between (insets in figure 4). For the standard magnetic field configuration (MF coils used only) the rotational transform t is just below 0.4 and the average magnetic shear is almost zero. By means of the TF coils t can be varied $0.3 < t < 0.6$ depending on the average toroidal field strength. At high t the shear becomes progressively positive but remains small ($\Delta t/t \leq 0.04$ over the minor radius). At low t the vacuum shear is slightly negative (i.e. tokamak-like, t decreasing with radius), however, a vertical field reverses this situation. In the standard configuration the vacuum field is characterized by a magnetic well to ensure MHD stability despite the absence of shear (see section 2.3). The well vanishes if the magnetic axis is shifted inward by a vertical field. Additionally, the corner coils can be charged separately to provide a toroidal mirror field to influence the number and location of trapped particles. Vacuum shear and well are also influenced by the mirror field. In particular, the depth of the vacuum well is reduced for increased corner coil currents (Geiger *et al* 1994).

At low t closed smooth flux surfaces exist up to $r = 20$ cm, thus the plasma is typically limiter bounded. Edge islands resonant to $t = n/m$, where $n = 5$ is fixed by the number of field periods, are an intrinsic property of the chosen basis configuration resulting from the optimization procedure (Chodura *et al* 1981) and therefore called ‘natural’ islands (Rau *et al* 1982). With increasing t the size of these magnetic islands increases and for $t > 0.49$ the last closed flux surface is defined by the inner separatrix of the next relevant island chain (Jaenicke *et al* 1993) (see section 8). This resonant $n = 5$ perturbation can be increased or compensated by the control coils, resulting in a variable island divertor structure as shown in figure 5.

In stellarators, the shape and the quality of the realized vacuum magnetic flux surfaces as well as the value of the rotational transform t can be validated by means of an electron beam technique (Jaenicke *et al* 1993). Flux surface measurements performed at W7-AS in 1988

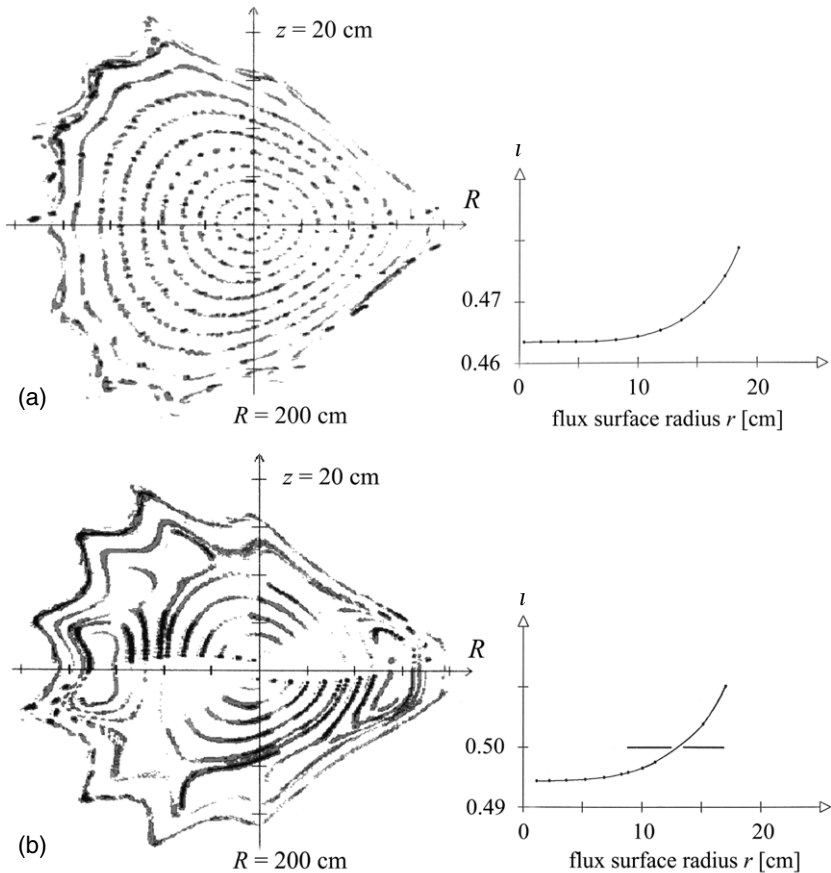


Figure 6. (a) Almost unperturbed flux surface for $t < 1/2$. Close to the boundary a chain of small secondary islands can be followed almost completely around the poloidal circumference. Black dots correspond to low transit numbers, grey dots to high transit numbers with an arbitrary scale. The measurement demonstrates that island widths down to 0.5 cm can be detected. (b) Magnetic field configuration with $t = 1/2$ at $r \approx 13$ cm. Due to the twofold resonance $t = 1/2 = 5/10$ within each of the two $m = 2$ islands five superimposed natural islands can just be discerned.

right before the beginning of the experiments demonstrated that the vacuum field properties of W7-AS were in close agreement with the calculated design values showing that good quality flux surfaces can be produced by means of modular field coils. Figure 6(a) gives an example for a case with a chain of small secondary islands close to the boundary. Additional field perturbations due to imperfections during coil fabrication and adjustment errors during coil assembly may break the fivefold toroidal symmetry. As an example figure 6(b) shows a flux surface measurement around $t = 1/2$ where 2 symmetry breaking islands ($t = 1/2$) are seen superimposed on the 10 internal natural islands ($t = 5/10$). Due to low shear the width of the $m = 2$ islands is relatively large. A perturbation of plasma confinement can be avoided by an appropriate value of t at the plasma edge (Jaenicke *et al.* 1993) and by the finite shear arising from internal currents (see section 5.2).

W7-AS was the first experiment where after shutdown the measurement of the flux surfaces was repeated for selected magnetic field configurations particularly sensitive to changes in rotational transform or island size (Otte and Jaenicke 2007). No significant changes were

found compared with the initial measurements made in 1988 indicating that the shape of the MF coils was essentially unchanged until shutdown although local deformations of the coils of up to 4 mm were measured during magnetic field pulses. For the standard configuration (no TF coils used) the effect of coil deformations at different magnetic field strengths was also studied by the electron beam technique. With magnetic field strength up to 2.4 T a *decrease* of $\Delta t/t \approx 2\%$ was measured which results from the tendency of the non-planar MF coils to flatten with increasing forces (Otte and Jaenicke 2007).

2.3. Equilibrium properties

Confining plasmas in an inhomogeneous magnetic field unavoidably leads to plasma pressure driven current densities modifying the externally supplied field. The strategy of the Wendelstein stellarators is to minimize the pressure driven currents such that the optimized properties of the equilibrium magnetic field configuration become almost independent of β (Grieger *et al* 1992). Neglecting net-toroidal currents the basic change of the magnetic configuration results from the Pfirsch–Schlüter (PS) equilibrium currents j_{\parallel} which on the 3D flux surface balance the diamagnetic current j_{\perp} such that $\nabla \cdot j_{\parallel} = -\nabla \cdot j_{\perp} = 2 \cdot j_{\perp} \cdot \nabla \ln(|B|)$. In an axisymmetric approximation with large aspect ratio (Pfirsch and Schlüter 1962) one obtains $j_{\parallel}/j_{\perp} \approx 2/t \cdot \cos \vartheta$, where ϑ is the poloidal angle. The dipole character of j_{\parallel} creates a vertical field which displaces the flux surfaces against each other and leads to the Shafranov-shift Δ . For classical stellarators with average circular cross-section and in the large aspect ratio approximation one derives $\Delta = (R/2) \cdot (1/t^2) \cdot \beta_0$ (e.g. Miyamoto (1980)). With $\Delta = a/2$ the nested flux surfaces approach each other resulting in an operational β_0 limit at $\beta_{0,\text{eq}} = t^2 \cdot (a/R)$ (Miyamoto 1980, Pustovitov 1994), which is considered too low to allow for an economic conventional stellarator reactor (Chodura *et al* 1981).

A reduction of j_{\parallel}/j_{\perp} can be achieved by avoiding a large variation of $|B|$ on flux surfaces. The W7-AS configuration with almost planar magnetic axis is close to a classical stellarator, thus the leading contribution to the poloidal variation of B on a flux surface arises from toroidal curvature. In this case one may use the model of a toroidally averaged stellarator (see Miyamoto (1980)) with an on-average elliptical cross-section defined by the equivalent cross-sectional area with $r^2 = a \cdot b$ and elongation $\kappa = b/a$, where b, a are the vertical and horizontal axes of the ellipse. As in an elongated tokamak, the average ellipticity reduces the poloidal variation of $|B|$ ($\propto 1/R$ in this model) by $1/\sqrt{\kappa}$, resulting in a decrease of the PS current density to $j_{\parallel} \approx j_{\perp} \cdot 2/(t \cdot \sqrt{\kappa}) \cos \theta$ which can be considered as a reduction of the effective average toroidal curvature by the same factor.

With an analysis following (Miyamoto 1980) the Shafranov-shift can be shown to be reduced to $\Delta = (R/2) \cdot \beta_0 / (t^2 \cdot f(\kappa))$ with $f(\kappa) = (1/2)(\kappa + 1/\kappa)\sqrt{\kappa} \approx \kappa$ for $1 \leq \kappa \leq 4$ (Geiger *et al* 2004b), resulting in an increase of the equilibrium β -limit to $\beta_{0,\text{eq}} = t^2 \cdot (a/R) \cdot f(\kappa)$. For the W7-AS standard configuration the effective elongation κ can be deduced from the (reduced) poloidal variation of $|B|$ which yields $\kappa \approx 2$ nearly independent of radius. The elongation is retrieved by analogy with an elongated tokamak from the radial behaviour of the normalized Fourier coefficient $b_{m=1,n=0}$ ($= B_{1,0}/B_{0,0}$) in Boozer coordinates. For the elongated tokamak the behaviour in our notation would be $r/(R\sqrt{\kappa})$. The value for κ varies between 1.7 and 2.5 depending on the configuration given by t, B_z and the magnetic mirror ratio (Dinklage *et al* 2007a). For the fully optimized W7-X one retrieves a factor of about 6 for the standard configuration. The reduction of the PS currents has been verified experimentally using flux loops outside of the plasma (Renner *et al* 1992) and from the reduced Shafranov shift as obtained by soft x-ray tomography (Jaenicke *et al* 1995, Weller *et al* 1997b). For an example, see section 10.4, figure 107.

For detailed equilibrium calculations in particular for the free boundary problem advanced stellarator equilibrium codes were applied. Most calculations used the NEMEC/VMEC-code ([Hirshman et al 1986a](#), [Callaghan et al 1997](#), [Yamada et al 1994](#)). Besides, fast experiment analysis was based on a restricted database of equilibria with the possibility of interpolation calculated with the KW-code ([Kisslinger and Wobig 1985](#)). This approach of fast equilibrium data provision was extended to the application of Function Parametrization, which is widely used at tokamak experiments, to show its usability for experiment evaluation at stellarators ([Callaghan et al 1997, 1998, 1999, 2000a,b](#)). A limited number of configurations was investigated with the codes PIES ([Zarnstorff et al 2004, 2005](#), [Reiman et al 2006, 2007](#)) and HINT/HINT2 ([Geiger and Hayashi 2002](#), [Geiger and Suzuki 2006](#)) which, as the KW-code, do not rely on the existence of nested flux surfaces (for examples of results see section 10, figure 106).

The PS currents result in the Shafranov shift of the axis with respect to the outer flux surface centre. Moreover, under free-boundary conditions the plasma column also shifts to larger major radii R . Directly connected to the Shafranov shift is the generation of a pressure induced magnetic well which usually becomes larger than the intrinsic vacuum one already at very moderate β -values. This is of particular importance for configurations which in vacuum have only a marginal magnetic well or even a magnetic hill. For W7-AS these are configurations shifted inward by a finite vertical field B_z or mirror configurations where B is enhanced in the elliptical plane ([Geiger et al 1994, 1995, 1996](#), [Rau et al 1994](#)). Furthermore, the PS currents also modify the t -profile. In general, an increase in β increases the central t -value but lowers t at the boundary ([Renner et al 1992](#)). As a consequence, with increasing β W7-AS develops a sheared t -profile, which may result in the appearance of low-order rational surfaces and hence may impact equilibrium and stability properties.

Additional changes of the magnetic equilibrium result from toroidal net-current densities which modify the t -profile ([Geiger et al 2003](#), [Geiger et al 2004a](#)). In a large aspect ratio approximation one obtains

$$\Delta t(r) = \frac{\mu_0 R}{B_\varphi r^2} \cdot \frac{I_{\text{pl}}^{\text{W7AS}}(r)}{2\pi},$$

where the sign of the plasma current has been defined positive if it increases t . This change in t is associated with two effects: first, the Shafranov shift and hence the corresponding β -limit is affected by the dependence of j_{\parallel}/j_{\perp} on t (section 10.4). Secondly, the change in the poloidal field components gives rise to a hoop force. The combination of both effects leads to characteristic changes in the shape of the flux surfaces ([Geiger and W7-AS Team 1993](#), [Callaghan et al 1997](#)), in particular if the current induced t is a significant fraction of the vacuum rotational transform. This has been demonstrated in W7-AS by x-ray tomography data ([Callaghan et al 1997](#), [Görner et al 1997](#)).

2.4. Stability properties

The basic ideal stability properties of the W7-AS magnetic configurations can be assessed by using the interchange stability criterion applied to currentless low-shear stellarators ([Nührenberg and Zille 1987](#)). Due to the omission of the stabilizing shear term this simplifies to $p'V'' - \langle j_{\parallel}^2 \rangle - \langle j_{\perp}^2 \rangle > 0$. Here $\langle \dots \rangle$ is a flux surface average defined in ([Nührenberg and Zille 1987](#)). The current densities are the destabilizing forces whereas $p'V''$ stabilizes if a magnetic well is present ($V'' < 0$). Therefore, in the design of W7-AS a vacuum magnetic well was considered to be mandatory to make up for the missing shear stabilization to achieve stability at low β . The simplified interchange criterion shows that reducing j_{\parallel}/j_{\perp}

should also pay off in an enhanced stability at low β . With increasing β the situation is more complex as ideal stability then depends on the subtle interplay between the different pressure induced effects: the deepening of the well, the increase of shear and the increase in the destabilizing potential of the current densities. If shear is present in the configuration, the interchange stability criterion given above corresponds basically to that of resistive modes (Nührenberg and Zille 1987).

The importance of a vacuum magnetic well for low-shear stellarators at low β is not entirely clear. With increasing β the plasma, self-generates a well due to the Shafranov-shift which at high- β becomes the dominant part and the vacuum well is negligible. Aiming at high- β , the vacuum well is thought to be necessary only for the plasma start-up. However, in W7-AS a marginal vacuum magnetic well or hill did not prevent the achievement of stable high- β states (for details see section 10). Also in other devices configurations with a marginal vacuum magnetic well/hill result in good experimental performance (Watanabe 2005). At W7-AS a detailed investigation of such strongly inward shifted configurations was not possible since full diagnostic accessibility and necessary experimental conditions were not compatible. In W7-X where the Shafranov-shift is strongly reduced and a self-stabilization is expected at higher β -values a magnetic well is considered to be necessary as a safety margin.

2.5. Wall conditioning, limiters and divertor

The stainless-steel walls of the vacuum vessel (Sapper and Renner 1990, Mathis and Sapper 1990) were routinely conditioned by baking at 150 °C (after openings), by glow discharges in He (during operation) and, since 1990, by boronization. The plasma was first bounded by two (top and bottom) movable limiters made of TiC-coated graphite (Grigull *et al* 1992), then by the same limiters, but the TiC-coated graphite replaced by bulk-boronized graphite (Grigull *et al* 1992). Since 1994 ten inboard limiters made of pure graphite were used (Grigull *et al* 1996, Sardei *et al* 1997). Thus the coverage of the plasma surface by carbon was increased stepwise. From the bulk-boronized limiters a permanent boronization of the wall due to sputtering of boron was expected, but the effect was too local and too low in order to significantly reduce the oxygen content and to replace glow discharges or boronization. The enlarged coverage of the plasma vessel by carbon led, however, to gradually improved density control and reduced impurity radiation from the core. Further fundamental improvements were achieved at the end of 2000 by replacing the inboard limiters by ten island divertor modules (Kisslinger *et al* 1995, Grigull *et al* 2001b) (section 8). This enabled quasi-stationary discharges at very high densities and, in this context, access to a new operational regime, the high density H-mode (HDH, see sections 7.5–7.7).

2.6. Heating systems

W7-AS was equipped with powerful non-ohmic heating systems from the very beginning (figure 7). The OH transformer was not suited to ignite or heat the plasma because the loop voltage was restricted to about 1 V, resulting in typical heating of $P_{\text{OH}} < 10 \text{ kW}$.

Electron cyclotron resonance heating (ECRH) had started on W7-A already in 1983 (Erckmann *et al* 1986a). At W7-AS first five 70 GHz gyrotrons, $4 \times 0.2 \text{ MW}$ for 3 s and $1 \times 0.2 \text{ MW}$ for 0.1 s (remnant from W7-A), were installed, usable at 1.25 and 2.5 T. The transmission line and the very flexible launching system are described in Erckmann *et al* (1990). 140 GHz gyrotrons with twice the cut-off density, i.e. $1.2 \times 10^{20} \text{ m}^{-3}$ at 2.5 T, became available 1991 (Erckmann *et al* 1991a) and replaced step by step some of the 70 GHz units. In the final stage, ECRH power up to 2.6 MW for about 1 s was available with one 70 GHz/500 kW and four 140 GHz gyrotrons. Heating, power modulation and current drive

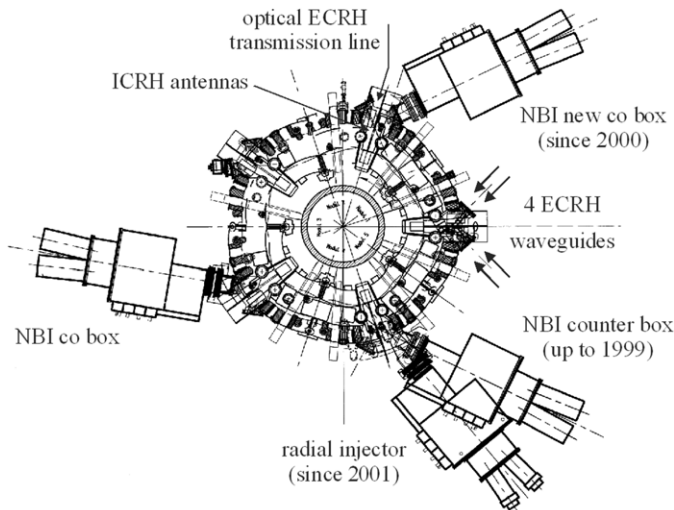


Figure 7. Position of the different heating systems of W7-AS. Co-injection is defined as parallel to a plasma current increasing the external rotational transform. In the last phase unidirectional co- or counter-NBI was possible only depending on the direction of the toroidal field.

experiments with this system are described in section 4.1. In parallel ECRH was developed technically and theoretically (for a review see [Erckmann and Gasparino \(1994\)](#)). Advanced heating methods were demonstrated by converting electron cyclotron waves via the OXB-mode conversion process into electrostatic electron Bernstein waves where no upper density limit, like the cut-off density, exists ([Laqua et al 1997, 2003a](#)) (details in section 4.1.7).

The 3 MW neutral beam injection (NBI) heating system ([Feist et al 1984](#)) consisted of two almost tangential beamlines with at first (in 1988) two sources and (since 1996) four sources each. The deposited heating power varied for the different sources resulting in up to 2.8 MW absorbed total power for up to 3 s allowing balanced injection. At low toroidal field and high density the heating efficiency of the counter sources decreased as fast ions were born preferentially at large plasma radii, resulting in prompt orbit losses ([Penningsfeld et al 1996, Jaenike et al 2000](#)). In 1998 the counter NBI box was turned resulting in uni-directional co-injection (figure 7). A nearly perpendicular oriented radial injector was installed (figure 7) at the place of the former counter box to create hot lost-orbit ions and to influence radial electric fields. For results on the heating and current drive physics of NBI see section 4.2. Neutral beam injection needs a target plasma (low density, but sufficiently high electron temperature). A reliable method for start-up is ECRH which is, however, restricted to the resonant magnetic fields of 1.25 and 2.5 T. Under good torus conditions (low wall recycling) application of non-resonant rf (10 kW at 900 MHz) was successfully used to create a target plasma at arbitrary toroidal fields (see e.g. [Ballico et al \(1991\)](#)). Plasma start-up by neutral beams alone had also been achieved but the breakdown being delayed by about 150 ms (see section 4.2.6, [Ott and Speth \(2002\), Jaenike et al \(2002a\)](#)).

Ion cyclotron resonance heating (ICRH) was developed from the very beginning using up to two generators with a nominal power of 2 MW and a frequency band of 34–110 MHz. Only after several modifications of the antenna system could plasma heating be demonstrated successfully in 1996 ([Cattanei et al 1996](#)). For further proof-of-principle tests in small 3D devices a conventional double strap antenna was installed in 1998. Several heating scenarios could be tested such as second harmonic hydrogen heating, hydrogen minority heating, hydrogen in

deuterium mode-conversion heating and magnetic beach heating (for details see section 4.3 and [Hartmann et al \(1998\)](#)). The ICRH program stopped in 2000 when the installation of the divertor modules required the removal of the ICRH antennas.

2.7. Diagnostic equipment and diagnostic development

At W7-AS, all contemporary standard diagnostic techniques were applied, using for diagnostic purposes permanently 90 to 100 ports out of 142 installed. An early survey was given in [Weller et al \(1997b\)](#). Diagnostic development at W7-AS led to first realizations of new types of diagnostics as well as first measurements of certain plasma parameters not accessible so far. Some developments were closely connected to the ECR heating scenario of W7-AS like electron Bernstein wave emission, EBE and the heat wave generation and tracking techniques. The need to improve understanding of the role of turbulence in transport stimulated fluctuation diagnostics. Diagnostics for the characterization of the island divertor are summarized in [McCormick et al \(1999a\)](#) and section 8.3. A stellarator specific difficulty is the mapping of diagnostic coordinates to the 3D magnetic field structure which was performed with an interpolation software between a database of equilibria calculated with the KW-code ([Kisslinger and Wobig 1985](#)). In the late phase of W7-AS integrated data analysis techniques have been applied combining previously separated diagnostic descriptions into a single model linked via Bayesian probability theory—a method which can result in an increase in accuracy and robustness ([Svensson et al 2004](#)).

2.7.1. Magnetics. A set of magnetic loops was installed to determine diamagnetic energy density, plasma current, the loop voltage and B-field fluctuations. In detail two *diamagnetic loops* with and without compensation in different poloidal planes were installed ([Laqua and Schneider 2000](#)). Six *saddle coils* in up- down-symmetry within one field period for plasma current characterization ([Gardner 1990](#)), two *flux loops* to determine the loop voltage in induced and driven current scenarios, four segmented Rogowski-coils to access the toroidal current density distribution ([Anton et al 1999a, 1999b](#)), plus 34 *Mirnov coils* for field fluctuation measurements and MHD measurements were available ([Anton et al 1997, Zegenhagen 2005, Zegenhagen et al 2006b, 2006a](#)). The use of magnetic information for profile recovery was tried by [Callaghan et al \(2000b\)](#) with an artificial magnetic diagnostic setup.

2.7.2. Langmuir probes. Sets of Langmuir probes were installed: multi-tip *fast reciprocating probes*, a *movable poloidal probe array* covering the inboard side SOL as well as *target-integrated probe arrays* providing important data on SOL structure, transport and target load ([Grigull et al 2002](#)). In the standard modes of operation the current–voltage characteristic was swept at a few kilohertz to obtain I_{sat} , T_e , n_e , and ϕ_{fl} , with sweeps up to 250 kHz I_{sat} and ϕ_{fl} were measured also at higher time resolution. For fluctuation analysis, a fast sweep technique at several megahertz was applied to single tips ([Balbin et al 1992, Giannone et al 1994, Pfeiffer et al 1998, Schubert et al 2002](#)) as well as to an array of 28 graphite probe tips arranged in poloidal and radial directions with time resolution of about 1 μs . Fluctuation correlation (section 5.4.1) could be measured along flux tubes over distances of a few metres ([Endler et al 1995b, Bleuel et al 2002](#)).

2.7.3. Thomson scattering.

Incoherent scattering. Two systems were installed to measure the main plasma parameters, electron density and temperature, a 20 channel single-shot system with a ruby laser was

later upgraded with a CCD high-resolution edge capability for edge and divertor studies ([Knauer et al 2003](#)). As a second system a periodic (17 ms) multi-channel system with Nd:YAG laser was installed in the last campaigns, covering with 3-channel polychromators and Si avalanche detectors the ranges 60–7000 eV, and 5×10^{18} – $5 \times 10^{20} \text{ m}^{-3}$, respectively, with radial resolution of about 2 cm ([Fischer et al 2002, 2003](#)).

Coherent Thomson scattering. Collective scattering experiments have been conducted using the gyrotron oscillators installed for electron heating purposes at W7-AS off resonance, aiming to characterize the plasma ion component ([Suvorov et al 1997, 1995a, 1995b, 1998](#)). Collective scattering diagnostics in the infrared ([Saffman et al 2001](#)) and at millimetre wavelengths ([Konrad 1995](#)) with simultaneous observation at four different angles are carried out in the framework of density fluctuation measurements (section 5.4).

2.7.4. Spectroscopy. A number of spectroscopic systems covered the wavelength range from about 1 to 1000 nm with the main objectives of determining impurity concentration and impurity transport purely passive as well as active in pellet injection and laser ablation experiments and to determine Z_{eff} ([Morita and Baldzuhn 1994](#)). In detail, a calibrated 0.3 m *multi-channel VUV grazing incidence SPRED spectrometer* for time resolved (4 ms) impurity survey with three different gratings to cover 10–170 nm, a *Czerny–Turner system* covering 200–800 nm ([Baldzuhn et al 1998a, 1998b](#)), two 0.3 m *VUV monochromators at normal incidence*, covering 15–250 nm, a 2.2 m *VUV/soft x-ray grazing incidence* multi channel spectrometer for 1–250 nm ([Unger 1992, 1995](#)), and a *Bragg system* with KAP-, PbSt- and Si- crystals for the soft x-ray region 0.1–2 nm. While the systems listed operate mainly at fixed sightlines, a 3-axis *scanning mirror system* based on a 1 m Czerny–Turner spectrometer with six gratings for 185–1500 nm allowed for time and space resolved measurements of impurity influxes, local densities, electric and magnetic fields, ion temperatures, ion drift velocities and continuum radiation ([Hofmann 1991, Fussmann et al 1990, Hofmann et al 1994](#)). A *Fabry–Perot spectrometer* with a hexagonal fibre arrangement was used to measure plasma rotation velocities ([Yoshinuma et al 2004](#)). The radial electric field and the ion temperature were measured from Doppler-shift and Doppler broadening of impurity lines either intrinsic as C (CIII) or B (BIV) ([Baldzuhn et al 1997b](#)) or after He-injection by gas puff. Excitation is either by electron impact or by active charge exchange resonance spectroscopy (CXRS) from interaction with a diagnostic H-beam ([Baldzuhn et al \(1995, 1997b, 1998b\)](#), see section 3.3) or a Li-beam ([Ehmller et al 2003a](#)). Active experiments to study ablation physics, impurity transport and cold pulse propagation were conducted with single pulse *laser blow-off systems* ([Ledl 1995, Burhenn et al 1999](#)), with impurity pellet injection ([Ledl 1999a, 1999b, Ledl et al 2004](#), section 6.2.1) and/or with a *repetitive excimer laser ablation system* injecting Li atoms ([Bruchhausen 2002](#)) which allowed also for density fluctuation measurements in the plasma edge ([Bruchhausen et al \(2002, 2004\)](#), section 5.4). *Pellet injection and supersonic gas jet* experiments were conducted to perform particle feeding and transport studies. Single pellet and pellet series could be produced at velocities of about 100–1000 m s⁻¹ and pellet sizes of up to 1 mm diameter ([Baldzuhn et al 2004, Baldzuhn and Sandmann 1993, Baldzuhn et al 2003a, 2003c](#)). Instruments used for island divertor spectroscopy, in particular the *He-beam spectrometer*, are summarized, in [König et al \(2003\)](#).

H_{α} . At start-up 12 fixed mounted detectors were installed consisting of photodiodes and filters to measure the H and D neutral fluxes at the plasma edge, with time resolution of a

few 10 kHz. In addition five fast channels (2 MHz) allowed for ELM observation. For more detailed divertor experiments and ELM and MARFE characterization and turbulence imaging a fast CCD camera system was installed ([Thomsen et al 2002b, 2004](#)).

Thermography. Two IR-cameras operating in the wavelength region from 3 to 5 μm were used to measure the surface temperature of the lower target tiles in module 1 and the upper tiles of module 2 with a frame rate of 315 Hz and 50 Hz, respectively, and with spatial resolution of 2 mm and 4 mm ([Hildebrandt et al 2003a](#)). A comparison of the measured heat fluxes with calorimetric and probe results is given in [Gadelmeier et al \(2004\)](#).

X-ray diagnostics. The set of x-ray diagnostics consisted of the *flexible x-ray camera system* comprising two cameras, with 36 radial channels each in an up- down-symmetrical arrangement, with detectors of microseconds time resolution ([Weller et al 1999b, 1990, Lazaros and Weller 1990](#)), the *electron temperature monitor system*, with two cameras, with 12 radial channels each, dedicated to determine the electron temperature profile applying the highpass-filter-method ([Weller et al 1999b, 1990](#)), and the *x-ray pulse height analysis system*, operating with Si(Li) detectors within an energy range 0.5–10 keV. From the slope of the spectrum of the continuum Bremsstrahlung, T_e can be gained, from superimposed lines impurity species can be identified. In addition to these basic systems, a *multi x-ray camera system (MiniSoX)*, dedicated to tomographic investigations of equilibrium and stability as well as MHD mode analysis was developed. It consisted of ten cameras with 32 channels each, able to verify the reduced Shafranov-shift of the optimized stellarator and to identify Alfvén-eigenmodes ([Navarro et al 1991, Görner et al 1997, 1998b, 1998a](#)).

Bolometry. The bolometer system was built up of three cameras, one with ten, the other two in a symmetric up–down arrangement like the soft x-ray cameras with 30 sightlines each using Au absorbers in a bridge configuration ([Giannone et al 2002b](#)). Typical parameters are time resolution 2 ms at a power resolution of 5 kW. Tomographic reconstruction of the emission profiles ([Giannone et al 1997](#)) were of particular importance at the density limit and in the HDH regime ([Giannone et al 2002a, 2003](#)).

2.7.5. Beam aided spectroscopy.

Li-beam. A 48 keV Li beam was used to determine via beam emission spectroscopy in the low- and mid-electron density ranges the electron density with high radial (1 cm) and temporal (0.2 ms) resolutions ([McCormick et al 1997, Ehmler 2001, Fiedler 1999, Brandenburg et al 1997](#)), as well as electron density fluctuations from correlations along the beam ([Zoletnik \(1998\), Zoletnik et al \(2005b\)](#), section 5.4). The beam was also successfully used for CXRS investigations ([Ehmler et al 2003a](#)).

H-beam. H or D injection using a diagnostic neutral beam with 34 keV at about 3 A neutral particle current was available allowing for space resolved CXRS and CX-NPA measurements. The diagnostic beam used an RF operated ion source and had a beam divergence of about 1°.

2.7.6. Microwave diagnostics. Microwave diagnostics summarize interferometry, polarimetry, reflectometry and ECE, here additionally electron-Bernstein wave emission (EBE). Overviews are given in [Hartfuß et al \(1997a\), Hartfuß \(1998\)](#).

Interferometry. A *Mach-Zehnder type FIR interferometer* with threee vertical sightlines used an HCN laser with about 40 mW of CW output power together with pyroelectric detectors. Local information could be gained with a *ten channel microwave interferometer* (Geist *et al* 1997) which could be operated at electron densities of up to about $7 \times 10^{19} \text{ m}^{-3}$ with high temporal resolution ($1 \mu\text{s}$). After tomographic reconstruction (Koponen and Dumbrajs 1997) radial resolution of the order 1 cm was possible allowing for gas oscillation and density pulse experiments.

Polarimetry. A novel type of sub-millimetre range (600 GHz) polarimeter was developed, based on linear bi-refringence (Cotton–Mouton-effect) of the magnetized plasma. Due to its field topology, W7-AS formed an ideal test bed for this kind of instrument suggested as robust density diagnostic for ITER (Fuchs and Hartfuß 1998, 1999, Bindemann *et al* 2002a, 2002b).

Reflectometry. The introduction of reflectometry in the late eighties initiated the development of various instruments at W7-AS starting with mono- and bistatic antenna *FM-CW systems* for density- and first density fluctuation estimations (Sanchez *et al* 1989, Navarro 1989). Later *heterodyne and AM-modulation* techniques were applied with increasing sophistication (Estrada 1992, Estrada *et al* 1993b, Hartfuß *et al* 1994b, Hirsch *et al* 1995b, 1996a, Zhuravlev *et al* 1997). The phenomenon of phase runaway and the understanding of its origin (Brañas *et al* 1999, Holzhauer *et al* 1998) finally led to the development of *Doppler-reflectometry* allowing for the simultaneous tracking of the poloidal propagation velocity of density turbulence and the monitoring of their amplitude (Hirsch *et al* 2001a, 2001b) with a time resolution of about $10 \mu\text{s}$ (Hirsch and Holzhauer (2004), examples in section 7.2).

ECE. The absolutely calibrated radiometers developed were adapted to the *B*-field defined by the ECRH heating scenario, 1.25 and 2.5 T. A novel type of *multi channel wideband heterodyne radiometer* was introduced (Hartfuß and Tutter 1985, Hartfuß 1987), allowing for the simultaneous measurement of the electron temperature at a number of radial positions with high spatial (1.5 cm) and temporal resolution ($10 \mu\text{s}$), well suited for profile evolution measurements and heat wave propagation studies (sections 4.1.3 and 5.3.3). An extreme broadband system with high flexibility of radial resolution has been realized (Fuchs and Hartfuß 2001a, 2001b). The high time response and the low noise of heterodyne radiometers allow for temperature fluctuation measurements, if adequate *correlation radiometer techniques* are applied to suppress the natural wave noise of ECE radiation (Sattler and Hartfuß 1993). The existence of small (0.5%) electron temperature fluctuations in the bulk of a fusion plasma could be demonstrated for the first time (Sattler *et al* 1994b) and their dependence on various plasma parameters was investigated (Hartfuß *et al* (1996), Häse *et al* (1999, 1997b), Hartfuß and Häse (1997), section 5.4.2). Various decorrelation techniques developed have been compared at W7-AS (Watts *et al* 2004). Different ECE observation techniques allowed also for electron energy distribution measurements (Pernreiter *et al* 1997, Haese *et al* 1998). 2D characterization of temperature fluctuation became possible with imaging radiometer arrays (Bäumel *et al* 1999, 2003b).

EBE. In high density plasmas where ECE is cut off the possibility to measure the mode converted electron Bernstein mode emission from the plasma opens new possibilities for temperature diagnostics with similar properties as ECE. The method was demonstrated for the first time in proof-of-principle experiments and demonstrated its

ability for space resolved measurements in heat wave experiments ([Laqua et al 1997, 1998](#), [Volpe et al 2002, 2003a, 2003b](#)).

Stray radiation. At high power ECRH a significant amount of non-absorbed stray radiation can exist, able to endanger windows and diagnostic systems. Detectors have been developed to quantify the amount, also confirming model calculations ([Gandini et al 2001a, 2001b](#), [Laqua et al 2001](#)).

2.7.7. Particle diagnostics.

Charge exchange neutral particle analysis (CXNPA). Active charge exchange diagnostic was installed allowing for ion temperature profile and ion energy distribution measurements ([Kick et al 1999](#)). The system was equipped with four vertically traversable neutral particle analyzers with 22 energy channels for each H and D operating at crossed E and B . Later the analyzers were modified to have 24 channels for both isotopes in an E parallel B analyzer configuration ([Chernyshev 2003](#), [Kick et al 1999](#)).

LENA. A low energy neutral particle time-of-flight analyzer (LENA) was installed for measurements of the energy distribution of the CX-flux in the range 20–100 eV.

Neutron diagnostics. Calibrated neutron counters (^3He - and BF_3 -proportional counter) were used to assess the total neutron flux, the central ion temperature (during $\text{H} \rightarrow \text{D}$ detection), the slowing down distribution and fast ion losses during $\text{D} \rightarrow \text{D}$ injection. In addition, a neutron activation system was installed to determine the fast and thermal neutron fluence and neutron transport ([Weller 1985, 1986](#), [Rust et al 1997](#), [Wolle et al 1999](#)).

Ion loss detector. A detection system for ions leaving the plasma has been developed and installed. The lost ions in a certain range of gyroradius and pitch angle pass a collimator and hit a scintillator array causing light which is detected via lenses and fibre bundles with a CCD camera system ([Werner et al 2000, 2001](#)).

3. Neoclassics and kinetic theory

Neoclassical theory is the only 1st-principle tool available for transport predictions in stellarators. This theory predicts that in the long-mean-free-path ($lmfp$) regime ripple-trapped particles dominate the radial transport ([Galeev et al 1979](#), [Kovrizhnykh 1984](#)) with their ∇B -drifts leading to unfavourable temperature scalings of the energy fluxes (at the worst $Q \propto T^{9/2}$ in the $1/\nu$ -regime). Although at low temperatures (e.g. in the plasma periphery) neoclassical transport becomes small and one must invoke ‘anomalous’ transport to explain W7-AS results the experimental particle and energy balances agree well with the neoclassical expectations in high-temperature discharges. As for the parallel transport, in common with most tokamak experiments, both the bootstrap current and the electric conductivity were well described by neoclassical theory in W7-AS, although both exhibit stellarator-specific features which are not to be observed in axisymmetric devices.

Section 3.1 describes the elements of drift optimization realized in the partial optimization concept of W7-AS. In section 3.2 the tools used to calculate the neoclassical transport coefficients, the bootstrap current coefficients and the parallel electric conductivity are given. In helical systems the ambipolar radial electric field plays a decisive role for transport as

highlighted in section 3.3. The transport analysis at W7-AS and the comparison with the neoclassical expectations are given in section 3.4. Neoclassical impurity transport and the accumulation problem are discussed in section 3.5 and finally section 3.6 yields the estimation of the bootstrap current and of the inductive current.

3.1. Elements of drift optimization in W7-AS

The prescription to minimize neoclassical losses by drift-optimization is the reduction of the radial particle drift away from the flux surfaces which can be achieved by a minimization of the geodesic curvature κ_g or by localizing trapped particles in regions of small geodesic curvature. Drift-optimization strategies that can be applied are (i) an increased average toroidal elongation, (ii) the concept of linked mirrors and (iii) the σ -model. Note that the concept of quasi-symmetries was introduced after construction of W7-AS had begun. Therefore it could not have an impact on the design strategy of the device.

The *averaged elongation* contributes the main improvement with respect to neoclassical transport in W7-AS. In Fourier representation the vacuum magnetic field in Boozer coordinates can be written as $B/B_0 = \sum_{m \geq 0, n} b_{mn}(r) \cdot \cos(m\vartheta - nN_p\varphi)$, where $\vartheta(\varphi)$ is the poloidal (toroidal) angle, $N_p = 5$ the number of field periods and the coefficients $b_{mn}(r)$ are functions of the effective radius r . W7-AS had a rather complex Fourier spectrum without a dominant multipolarity which would result from the helical coil system of an ideal classical $m = l$ stellarator configuration where $B/B_0 = 1 + b_{10} \cos(\vartheta) + \varepsilon_h \cos(l\vartheta - N_p\varphi)$ with $\varepsilon_h = b_{11}$ being the helical component. In a classical stellarator radial particle drifts depend on the ('nearly poloidal') variation of $|B|$ in the direction of the helical B -minimum. This variation scales with the toroidal curvature term b_{10} which due to the average elongation of W7-AS is significantly less than r/R_0 over the entire plasma cross-section (see section 2.3). The benefit of this elongation for the neoclassical transport in W7-AS is clearly verified both in the Pfirsch–Schlüter and in the plateau regime. This reduction effect on drift surfaces was verified by Monte-Carlo simulations of transport (Brossmann *et al.* 1982) and references therein) showing that the drift orbits of passing particles in a classical stellarator deviate from the magnetic surfaces by twice the distance of those in W7-AS. Thus the drift surfaces of passing particles are optimized nearly by the same factor as the Pfirsch–Schlueter currents (see section 2.3).

In the *linked-mirror concept* the trapped particles are kept away from toroidal positions of high curvature and thus virtually see a straight stellarator. Ideally, in W7-AS straight parts of the plasma column with fairly small poloidal variation of B (and thus reduced radial ∇B -drifts) are linked together by short parts with a strong (local) toroidal curvature, high elongation and the full poloidal B variation but also stronger B . Contour lines of $|B|$ within one field period are shown in figure 8. It can be seen that in W7-AS the linked mirror concept can be clearly violated: for the low- t standard configuration (figure 8(a), $I_5 = I_m$, $I_v = 0$) ripple-trapped particles are located around the elliptical plain $\varphi = 36^\circ$ with the strongest toroidal curvature, but also around the $\varphi = 18^\circ$ plane where a highly localized B -minimum significantly deepens at outer r . These minima of B are fairly localized and dominated by the $m = 1$, $n = -1$ helical component which is an intrinsic feature of the modular coil system of W7-AS, and, consequently, becomes more pronounced with increasing t (see the high- t standard configuration $t = 1/2$, $I_5 = I_m$ close to the separatrix in figure 8(c)). For the standard configuration, confinement can be partially improved by increasing B in the elliptical plain by means of the current I_5 in the large special coils (figure 8(b)).

For comparison figure 8(d) shows the standard configuration of W7-X which has a fairly large helical $m = 1$, $n = 1$ component that dominates in the straight part of the plasma column

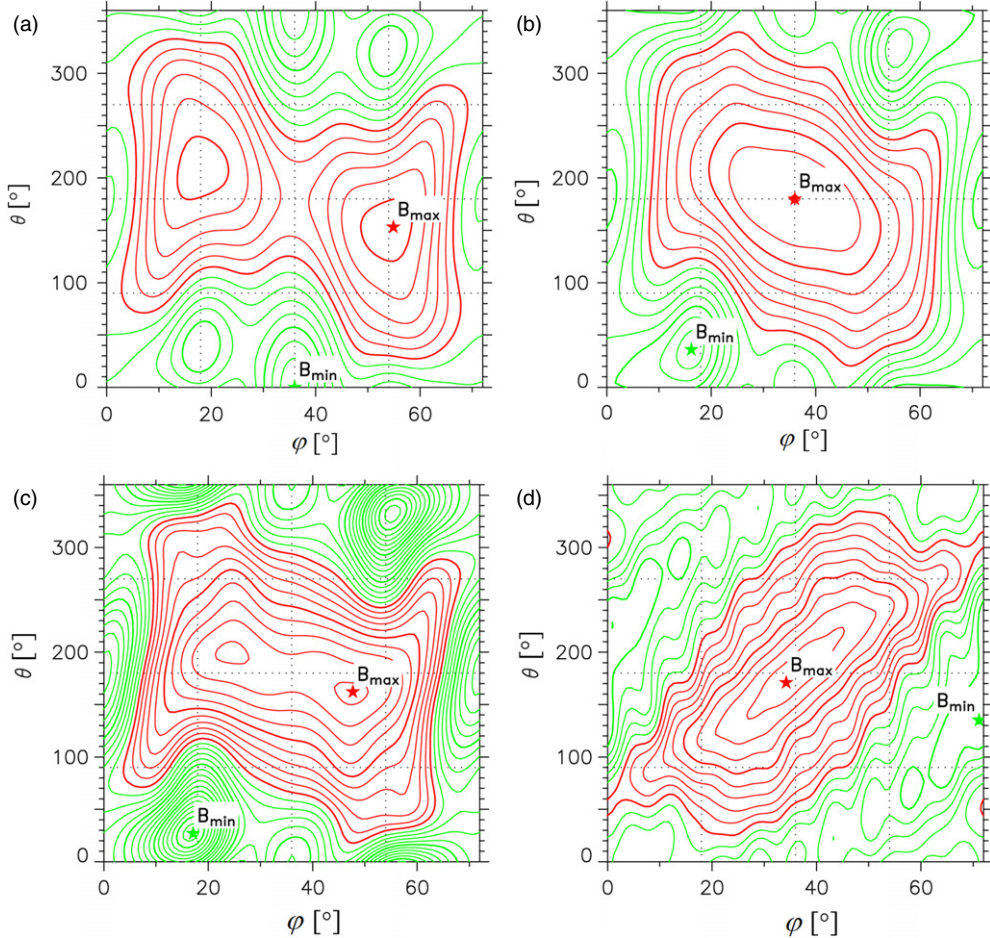


Figure 8. (Upper row) B_{mod} contours at half plasma radius $r/a \cong 0.5$; $\theta = 0$ assigns the equatorial plane at the outboard side. (Left) $t = 0.35$, standard configuration $I_5 = I_m$ (w7as-sc3). (Right) Same conditions but in the ‘partially optimized configuration’ with $I_5 = 1.2 \cdot I_m$ (w7as-1.2). (Lower row) B_{mod} contours close to the separatrix. (Left) High t configuration with $t \cong 0.51$, $I_5 = I_m$ (w7-as5) at $r = 14.7$ cm. (Right) The W7-X standard configuration (w7x-sc1) at $r = 50$ cm for comparison. All examples without vertical magnetic field. The increment of the contour levels is 1% in all cases.

resulting in a helically structured minimum of B . The local maximum of B on the inner side of the bean-shaped plane ensures that no trapped particles exist in this region of strong (local) toroidal curvature; no other localized B minima degrade the confinement. As a consequence the minimum of B is fairly constant on the flux surfaces. This is very similar to the criterium of σ -optimization (Mynick *et al* 1982, Shaing and Hokin 1983) which utilizes the fact that the bounce-averaged drift of deeply trapped particles in the l_{mfp} regime can be minimized if they are localized in regions which have only a small field variation $\nabla B/B$ along the direction of the trapping (poloidal or helical) B -minimum.

In summary, neoclassical confinement in W7-AS is only partially optimized. The highly localized minima of B counteract the benefit of the elongation in the l_{mfp} -regime and strongly deteriorate the confinement properties, in particular at the outer radii of high t -configurations.

This drawback is mitigated by the higher collisionalities at the plasma periphery. The establishment of a ‘proper’ E_r may be considered as an additional element of neoclassical transport reduction as the $E \times B$ -drift reduces neoclassical transport coefficients in stellarators, in particular by suppressing $1/v$ transport. However, E_r is not an external control parameter but determined from the ambipolarity of the fluxes themselves. Finally in W7-AS no attempt has been made to minimize the bootstrap current (see section 3.6).

3.2. Neoclassical transport coefficients

Following the standard approach, a solution of the first-order drift-kinetic equation (designated f_1) is sought by linearization with respect to a local Maxwellian, f_M , where the derivatives $\partial f_M / \partial r$ and $\partial f_M / \partial v$ are the leading terms driving the neoclassical transport; $\partial f_1 / \partial r$ and $\partial f_1 / \partial v$ are disregarded. Density, temperatures and the electric potential are assumed to be constant on flux surfaces, 1st-order variations within the flux surfaces are disregarded. Furthermore, the collision operator is approximated by the pitch-angle scattering term in the simplified Lorentz form without momentum conservation. This approximation is well justified in the $l mfp$ -regime of stellarators where the friction between passing and ripple-trapped particles represents a significant momentum sink strongly damping toroidal rotation and reducing the impact of parallel particle and heat flows on transport. For approaches to correct for momentum conservation see Solano *et al* (1998), Sugama and Nishimura (2002) in particular for the estimation of the bootstrap- and the NBI driven currents see Solano *et al* (1998).

With this approach, the linearized drift kinetic equation is reduced to a 3D-phase space with the two (magnetic) angles on a flux surface, ϑ and φ , and the pitch $p = v_{\parallel}/v$; i.e. r and v are only parameters. The corresponding moments of f_1 , the mono-energetic transport coefficients, are defined by integrals over ϑ , φ and p and depend only on r (implicitly on the $b_{mn}(r)$ Fourier spectrum), on the radial electric field (which appears in the form $E_r/v B$) and on the collisionality (in the form v/v). Here, the $E \times B$ -drift is treated in the incompressible form, $(B \times \nabla \phi)/B_0^2$, where $\phi(r)$ is the electric potential and B_0 a flux-surface averaged magnetic field see the appendix in Maaßberg *et al* (2000b). For large $E_r/v B_0$, e.g. for impurities and ions, this ordering may be violated: the compressible $E \times B$ -flow cannot be compensated by parallel flows leading to 1st-order density (and potential) variation on flux surfaces and affecting the transport properties.

Three mono-energetic transport coefficients that must be determined are the particle transport coefficient, Γ_{11}^* , the bootstrap current coefficient, Γ_{31}^* (the Ware pinch coefficient is given by the Onsager symmetry $\Gamma_{31}^* = -\Gamma_{13}^*$) and the parallel electric conductivity coefficient, Γ_{33}^* . Finally the v -convolution with appropriate moments yields the complete 3×3 transport matrix independently for each particle species. Analytic theory fails for calculating the mono-energetic transport coefficients for complex B configurations like W7-AS. Two numerical approaches are available, however, a Monte Carlo technique (Boozer and Kuo-Petric 1981) and a direct solution, the drift-kinetic equation solver, DKES (Hirshman *et al* 1986b, van Rij and Hirshman 1989). With Monte-Carlo techniques, the estimation of the bootstrap current coefficient requires extreme statistical accuracy and even a δf -technique shows no advantage for stellarator configurations (Schmidt 2002, Isaev *et al* 2006). In the DKES approach, however, no principle problems appear in estimating the Γ_{31}^* . This is the main reason that DKES was used to generate the database of mono-energetic transport coefficients for the main W7-AS configurations.

In DKES, the f_1 distribution function is Fourier expanded with respect to ϑ and φ and Legendre expanded with respect to p . For very low collisionalities f_1 is highly localized in the 3D phase space (e.g. in the trapped particle domain which dominates the transport in

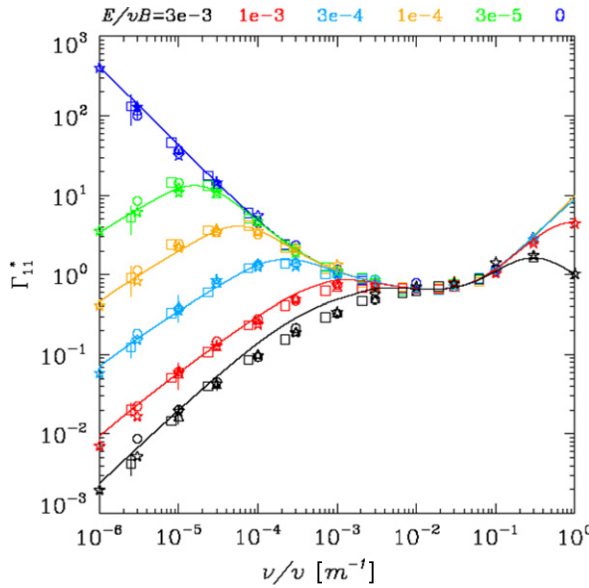


Figure 9. Mono-energetic diffusion coefficient, Γ_{11}^* (normalized to the plateau value of the equivalent tokamak with circular cross-section, i.e. $\kappa = 1$), versus the mono-energetic collisionality, written as the inverse mean-free-path, ν/ν , for the low- τ W7-AS standard configuration (w7as-sc3) at $r/a = 0.5$. Numerical results from DKES (Hirshman *et al* (1986b), triangles), and the Monte Carlo codes of (Beidler *et al* (1987), squares), (Tribaldos (2001), circles) and (Schmidt (2002), stars) are compared. The normalized radial electric field was assumed to have values of $E_r/vB = 0, 3 \times 10^{-5}, 10^{-4}, 3 \times 10^{-4}, 10^{-3}, 3 \times 10^{-3}$ with Γ_{11}^* being successively reduced at each increment.

the $1/\nu$ -regime for $E_r = 0$) leading to a fairly poor representation in the Fourier–Legendre expansion. Up to 800 Fourier modes and up to 180 Legendre polynomials are used. An optimized selection of Fourier modes is obtained from mode coupling in the $B \cdot \nabla B \partial f_1 / \partial p$ term, i.e. the dominant b_{mn} determine the f_1 Fourier spectrum. Although the system of linear equations is solved with a high degree of vectorization, DKES computations are very CPU-time expensive in particular in the $lmfp$ where the convergence properties defined by the residuals (van Rij and Hirshman 1989) become increasingly poor with decreasing ν/ν .

Figure 9 shows the benchmarking of the mono-energetic transport coefficient calculated by DKES with results of different Monte-Carlo approaches, including full- f schemes (Beidler *et al* 1987, Tribaldos 2001) following the method of Boozer and Kuo-Petravic (1981), and the δf -technique (Schmidt 2002). The solid lines represent theory-based fits to the numerical data (Beidler *et al* 1994). This benchmarking of quite different codes for the main stellarator configurations (W7-AS, LHD, W7-X, TJ-II, HSX, NCSX and QPS) is a result of an international collaboration on neoclassical transport (Beidler *et al* 2003b). Figure 9 shows the effect of the $E \times B$ -drift on Γ_{11}^* , in particular the suppression of the unfavourable $1/\nu$ -scaling of this transport coefficient.

As a figure of merit for the achieved optimization the effective helical ripple ε_{eff} can be used. For the most unfavourable $1/\nu$ -regime it compares the numerically calculated mono-energetic transport coefficient (see section 3.2) with those of an ideal classical configuration (with only one helical mode) where the transport coefficients can be estimated analytically (Beidler and Hitchon 1994). Figure 10 shows the ε_{eff} -profiles for the three W7-AS configurations described in figure 8. The W7-AS standard configuration (red dots) at $t = 1/3$

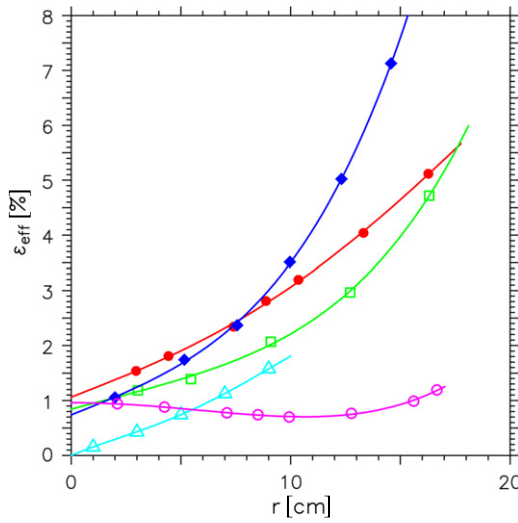


Figure 10. Effective helical ripple ε_{eff} versus radius for the W7-AS standard configuration $t \approx 0.35$, $I_5 = I_m$ (red dots, compare figure 8(a)), a drift-optimized mirror configuration $t \approx 0.35$, $I_5 = 1.2 \cdot I_m$ (green squares, compare figure 8(b)) and with $t \approx 0.51$, $I_5 = I_m$ (blue diamonds, compare figure 8(c)). For reference ε_{eff} for the W7-X ‘standard’ configuration (pink circles, figure 8(d)) and for the W7-A configuration with $t \approx 0.51$ (light blue triangles) are included. For W7-X the radius is compressed by a factor of 3. For W7-A, using the axis-expansion, $\varepsilon_{\text{eff}} = 4.4\%$ at $r = 18$ cm is obtained for this (extrapolated) configuration. W7-A is not an ideal classical stellarator: although the $l = 2$ helical winding directly yields the b_{21} mode, a significant b_{11} term appears due to the coupling of the b_{21} and the b_{10} modes (curvature effect), and ε_{eff} corresponds mainly to the b_{11} mode.

with the trapped particles mainly in the elliptical plane with strong toroidal curvature, is significantly ‘drift-amplified’ (despite the innermost radii). Partial improvement in the the $lmfp$ is achieved by increasing B in the larger coils of the elliptical plane $I_5 = 1.2 I_m$ (green squares). For the high t -configuration (blue dots) $\varepsilon_{\text{eff}}(r)$ reflects the disadvantageous deepening of B_{\min} at outer radii shown in figure 8. For reference, W7-A and W7-X are shown. Both have a fairly small ε_{eff} .

The three mono-energetic transport coefficients are computed for each W7-AS configuration on a 3D-grid consisting of r , v/v and E_r/vB . The coefficients required for the energy convolution are obtained with 3D-interpolation on that grid (Hirshman *et al.* 1986b). For an axisymmetric configuration, the thermal neoclassical transport matrix was benchmarked with the Hinton-Hazeltine model (Hinton and Hazeltine 1976); good agreement was obtained. Alternatively to the interpolation, a fit algorithm for the mono-energetic particle transport coefficient is implemented (Beidler *et al.* 1994) which is based on the different transport regimes of a classical stellarator configuration. With this energy convolution of the three mono-energetic transport coefficients for each species α , the neoclassical thermodynamic fluxes (particle flux density $\Gamma_\alpha^{\text{nc}}$, energy flux density Q_α^{nc} and the parallel current density $j_{\parallel}^{\text{nc}}$) are linked by the neoclassical transport matrix $D_{ij}^\alpha(r, n_\alpha, T_\alpha, E_r)$ to the thermodynamic forces (i.e. the gradients n'_α and T'_α and electric fields E_r and E_\parallel)

$$\begin{Bmatrix} \Gamma_\alpha^{\text{nc}} \\ Q_\alpha^{\text{nc}} \\ j_{\parallel\alpha}^{\text{nc}} \end{Bmatrix} = D_{ij}^\alpha \cdot \begin{Bmatrix} n'_\alpha/n_\alpha - q_\alpha \cdot E_r/T_\alpha \\ T'_\alpha/T_\alpha \\ E_\parallel \end{Bmatrix}. \quad (3.1)$$

In the DKES database, only W7-AS vacuum configurations are included and the effects of toroidal current densities are disregarded: the influence of the Shafranov shift (although reduced) on the b_{mn} -Fourier spectrum is not negligible; however, in high- β discharges neoclassical transport is of minor importance due to the low temperatures. For the high- T_i discharges, where neoclassical transport becomes dominant in the core, volume averaged $\beta \leq 1\%$ is reached. For the low- t standard configuration the effective helical ripple ε_{eff} (see figure 10), increases by only about 20% for $\beta \leq 0.9\%$; the effect on the bootstrap current coefficient is even smaller. Toroidal current densities (bootstrap, inductive, ECCD and NBCD) affect the t -profile and, consequently, also the confinement in the plateau and the Pfirsch–Schlüter regime. In the $lmfp$ -regime the radial transport depends much less on t , and equivalent to tokamaks, the bootstrap current scales roughly with $1/t$.

3.3. Ambipolar radial electric field

In the traditional neoclassical approach the local radial electric field, E_r , is calculated from the roots of the ambipolarity condition of the local (diffusive) particle flux densities defined by

$$\Gamma_\alpha^{\text{nc}} = -n_\alpha \cdot \left[D_{11}^\alpha \left(\frac{n'_\alpha}{n_\alpha} - \frac{q_\alpha E_r}{T_\alpha} \right) + D_{12}^\alpha \frac{T'_\alpha}{T_\alpha} \right] \quad (3.2)$$

with $\alpha = e, i, I$ (for electrons, ions and impurities, respectively) and $q_\alpha = z_\alpha e$ is the particle charge. In the bulk part of the plasma, impurity fluxes are considered as negligible, $\Gamma_I \approx 0$ assuming stationary conditions and no impurity sources. Impurities are taken into account both by an effective charge Z_{eff} when calculating the collision frequency and by using a reduced ion density such that $Z_i n_i < n_e$ when calculating the ion fluxes. Then the radial electric field is determined by the roots of

$$Z_i \Gamma_i(E_r) = \Gamma_e(E_r) \quad (3.3)$$

if additional non-ambipolar particle fluxes can be neglected. In the $lmfp$ regime of stellarators the neoclassical transport coefficients D_{jk}^α depend on E_r , such that multiple roots of the ambipolarity condition (equation (3.3)) can be obtained (Mynick and Hitchon 1983, Shaing *et al.* 1984); their number is always odd, the most positive one is called the electron-root, the most negative the ion-root.

For highly peaked T_e and fairly flat T_i profiles with $T_e(r) \gg T_i(r)$ as realized in the central part of low-density ECRH heated discharges the neoclassical electron flux exceeds the ion flux even for $E_r = 0$. Ambipolarity is sustained by a single ‘electron-root’ solution of equation (3.3) with strongly positive E_r which reduces the high Γ_e . Figure 11 shows electron and ion particle fluxes calculated for the core region ($r = 5\text{ cm}$) of an example discharge. Corresponding radial profiles are given in figure 12. In the plasma centre the measured E_r is strongly positive (figure 12(c)) with values $E_r \approx +400\text{ V cm}^{-1}$ as expected from neoclassical calculations (figure 11(left)). This feature is experimentally generally found in low-density ECRH discharges of helical devices where the energy balance is dominated by the electrons and the ions are energetically decoupled resulting in $T_e(r) \gg T_i(r)$ (for overviews see (Yokoyama *et al.* 2006, 2007, Wagner *et al.* 2006)). For W7-AS the transition to the electron-root is supported by the presence of the toroidal Fourier modes b_{0n} which lead to a non-vanishing effective helical ripple on the axis; the D_{jk}^e there can be significantly reduced by finite E_r (Yokoyama *et al.* 2006).

If T_e is close to T_i and $T'_i \neq 0$ —e.g. in the plasma interior of discharges at higher densities—an ion-root is expected in the inner region typically with flat or even hollow density profiles and moderate values of $|E_r|$ that strongly reduce the D_{jk}^i of the $1/v$ regime (compare figure 9). At outer radii, where stronger gradients T'_i and n' exist, the ion fluxes increase and are directed

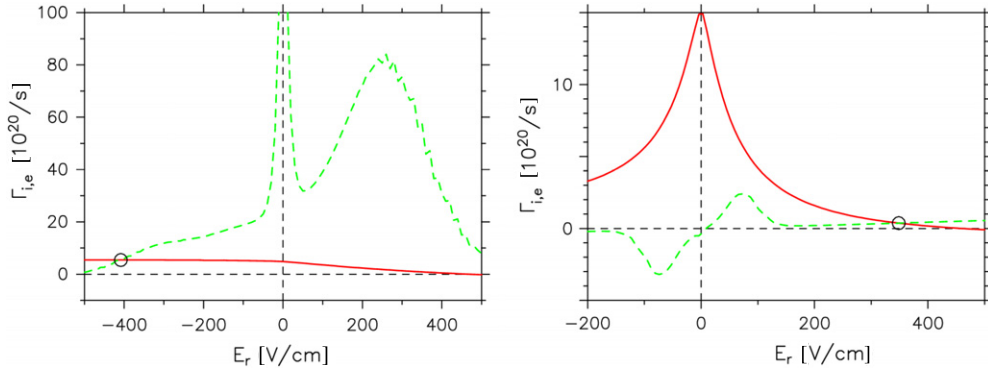


Figure 11. Neoclassical electron (solid line) and ion (dashed line) particle fluxes versus E_r calculated with DKES for the $t \cong 1/3$ standard configuration. The ambipolar E_r are indicated by circles. (Left) e-root, #36908, $r = 5\text{ cm}$, for profiles and parameters of this discharge see figure 12. (Right) #34313, in the gradient region ($r = 13\text{ cm}$), see figure 13.

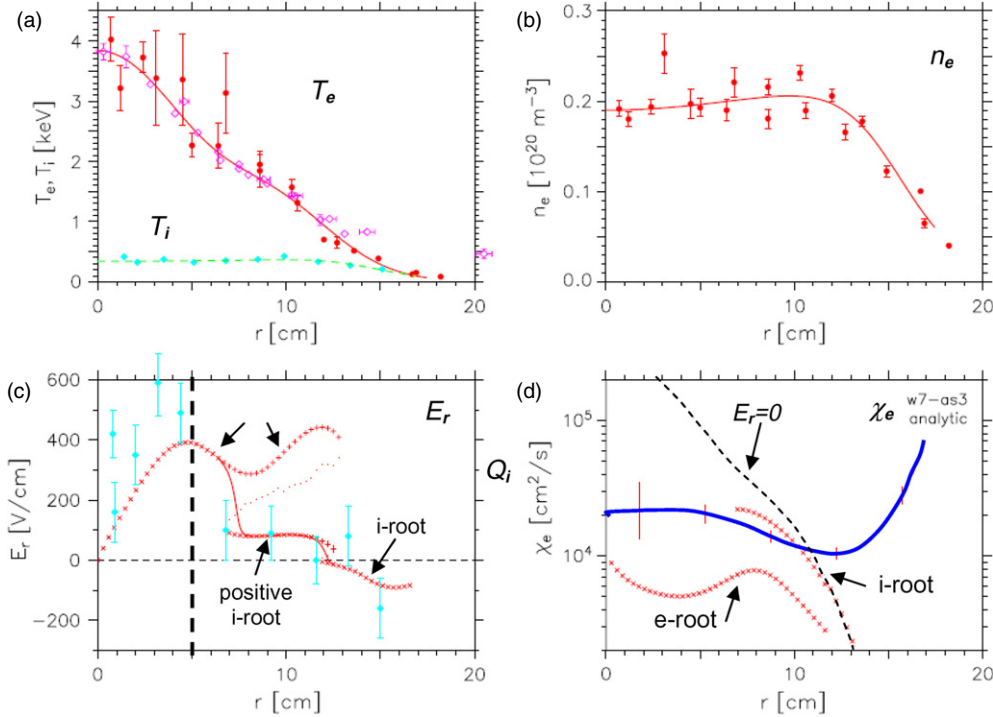


Figure 12. (Top) Profiles (T_e , T_i , n_e) for a discharge with electron-root conditions (#36908) in the plasma centre, $r < 7\text{ cm}$. (Bottom, left) E_r measured by CXRS and obtained with DKES from the ambipolarity condition of thermal fluxes. At medium radii an electron-root and a slightly positive ion-root are predicted. The dashed line indicates the radius for which the calculated fluxes are plotted in figure 11. At the plasma edge a moderate ion-root is the only predicted solution. The continuous line is obtained from thermodynamic considerations. (Bottom, right) χ_e from power balance (blue line) compared with DKES results taking the electron-root, the ion-root and $E_r = 0$. Adapted from (Baldzuhn *et al.* 1998b).

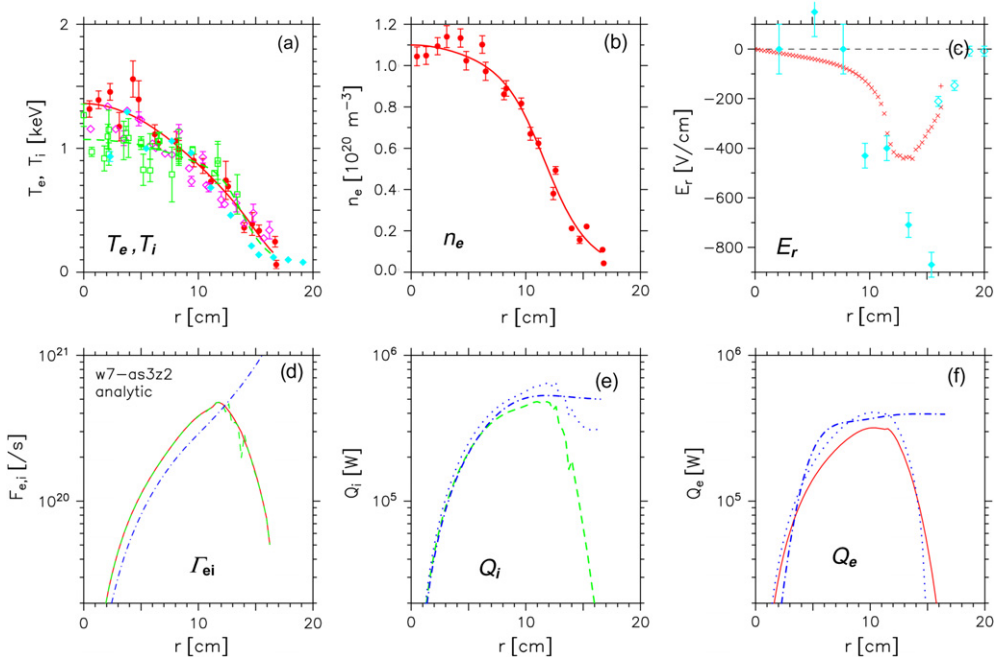


Figure 13. (Top) Profiles (T_e , T_i , n_e , E_r) for the discharge (#34609, ‘optimum confinement’ (OC), (see section 5.3.2) with ion-root conditions $T_i \approx T_e$, $T'_i \neq 0$ for all radii at $P_{NBI} = 1.35$ MW, $P_{ECRH} = 0.35$ MW, $n(0) = 1.1 \times 10^{20} \text{ m}^{-3}$. The E_r obtained with DKES from the ambipolarity condition of thermal fluxes are compared with measured E_r at the upper right (see figure 11). (Bottom line) The dark-blue dash-dotted line shows particle and heat fluxes from the particle balance and power balance analysis, respectively. Neoclassical expectations are given by red solid lines (electrons) and green dashed lines (ions). The neoclassical transport coefficients decrease in the outer radial region due to their temperature dependence. In this region, the experimentally found transport is anomalously high. From Kick *et al* (1999).

outward. As a consequence in all W7-AS discharges an ion-root with (often strongly) negative E_r is realized in this gradient region. Figure 11(right) shows an example of calculated electron and ion particle fluxes for $r = 13$ cm of such a discharge. Corresponding profiles are given in figure 13.

The situation becomes more complex if *multiple roots* of the ambipolarity condition exist. This is the case, e.g. if only the electron-root is realized in the innermost region and only the ion-root at outer radii. At intermediate radii, both roots are stable and exist together with a third unstable root (for example see figure 12(c)). A non-local description must be used to determine how the transition between both stable roots develops corresponding to a poloidal rotation shear layer. In a thermodynamic approach (minimization of the generalized heat production rate (Shaing 1984)), the *position* of this shear layer is determined by the constraint, that the dissipation of the energy of the poloidal plasma rotation is minimized. A simple criterion also can be found by variation of the energy principle with respect to the shear layer position under the assumption of a very small poloidal shear viscosity corresponding to a very narrow width of the transition region (Maaßberg *et al* 1993b). The position of the poloidal rotation shear layer is determined by

$$P_t(r) = \int (Z_i \Gamma_i^{nc} - \Gamma_e^{nc}) dE_r = 0; \quad (3.4)$$

the ion-root is realized for $P_t(r) > 0$, the electron-root for $P_t(r) < 0$. The *width* of the shear layer depends on the radial viscosity which is not a local quantity. The poloidal friction (mainly of the ions) drives additional radial fluxes allowing for the local deviation of the thermal ambipolarity condition. In principle, high-order expansions of the distribution function might resolve this problem (Hastings *et al* 1985, Hastings 1985) leading to a neoclassically estimated diffusion equation for E_r and a corresponding E_r -diffusion coefficient (Maaßberg *et al* 1993b). In a heuristic approach used for W7-AS (Maaßberg and Dylabin 1993), this coefficient (depending on T_i and E_r itself) is adjusted to a shear layer width of about 1–2 cm.

Measured and calculated E_r are compared for typical electron-root and ion-root conditions in figures 12 and 13, respectively. At W7-AS, E_r was measured spectroscopically from the Doppler shift of impurity lines (species: He, C⁶⁺, B³⁺) excited either by electron impact (passive spectroscopy) or by active charge exchange recombination (CXRS) from interaction with a diagnostic H-beam (Hofmann *et al* (1994), Baldzuhn *et al* (1997b, 1998b), figures 12 and 13) or a Li-beam (Ehmler *et al* 2003a). From the impurity line broadening $T_1(r)$ was obtained and the impurity ion pressure gradient and the diamagnetic drift $v_{i,\text{dia}} = \nabla p_i / (e \cdot n \cdot B)$ were derived. The $E \times B$ drift motion was obtained by subtracting the diamagnetic drift term from the measured rotation velocity. For the main ions (H, D) the diamagnetic drift velocity and the $E \times B$ -velocity were typically of the same magnitude, but pointing in opposite directions (Baldzuhn *et al* 1998b). Toroidal rotation is strongly damped by friction of passing particles with the ripple-trapped ones (Hofmann *et al* 1994). Except for unbalanced NBI the poloidal rotation velocity was much larger than the toroidal one and dominated the force balance equation. Measurements of $E_r(r)$ in general showed results that were consistent with the solutions of the ambipolarity condition for the neoclassical purely *thermal diffusive particle fluxes*. Dedicated experiments investigating additional *heating driven fluxes* of electrons (ECRH) and ions (first-orbit losses driven by NBI) are described together with ECRH heating physics in section 4.1 and with NBI heating in section 4.2, respectively.

3.4. Transport analysis

Transport analysis is based on measured profiles of $n_e(r)$, $T_e(r)$ and $T_i(r)$. All particle and energy sources/sinks are calculated using fits to experimental data. The balance equations for particles, electron and ion energy are integrated yielding the experimental particle flux density $\Gamma^{\text{ex}}(r)$, and the electron and ion energy flux densities, $Q_e^{\text{ex}}(r)$ and $Q_i^{\text{ex}}(r)$, respectively.

$$\begin{aligned}\Gamma^{\text{ex}}(r) &= \frac{1}{V'} \int_0^r S_p(r) dr, \\ Q_e^{\text{ex}}(r) &= \frac{1}{V'} \int_0^r [S_h^e - P_{ei} - P_{\text{rad}} - \Gamma^{\text{ex}} \cdot E_r] V' dr - T_e \cdot \Gamma, \\ Q_i^{\text{ex}}(r) &= \frac{1}{V'} \int_0^r [S_h^i + P_{ei} - P_{\text{CX}} + \Gamma^{\text{ex}} \cdot E_r] V' dr - T_i \cdot \Gamma.\end{aligned}\quad (3.5)$$

Here, the approximation $V' \propto r$ is well justified. In figures 12 and 13 examples of these experimental particle and energy flux densities are compared with their neoclassical predictions that have been calculated from the fits to the measured density and temperature profiles and by including the calculated ambipolar E_r .

The particle sources $S_p(r)$ from recycling and the gas valve used for feedback density control were calculated by the DEGAS code (Heifetz *et al* 1982, Sardei *et al* 1991) in the early phase of W7-AS and by the EIRENE code (Reiter 1992, Fiedler *et al* 1996,

[Heinrich et al 1997](#)) later on. Absolutely calibrated H_α measurements at the dominant recycling zones allowed for the estimation of the neutral gas profile as well as the ion CX losses. A sufficient H_α documentation of the major part of the vessel was lacking, such that $S_p(r)$ could be estimated only for limiter discharges. For NBI discharges, the contribution to $S_p(r)$ as well as to the electron and ion heating, $S_h^e(r)$ and $S_h^i(r)$, is estimated by the FAFNER code ([Penningsfeld et al 1996](#)). The ECRH power deposition profile is calculated by ray-tracing ([Gasparino et al 1990](#)). Since the ECRH power deposition is highly localized (at least at standard operation with 2nd harmonic X-mode), also a simple approximation by a Gaussian can be used. Finally, the radiative losses $P_{\text{rad}}(r)$ are modelled assuming corona equilibrium and scaled to the total power measured by bolometry. This approach turned out to be sufficient since the transport analysis was performed only for discharges with a fairly low radiation level being far from radiative collapse.

At high densities (typically exceeding $n_e \cong 8 \times 10^{19} \text{ m}^{-3}$) collisional power transfer between electron and ions, $P_{ei} \propto n_e^2 (T_e - T_i)/T_e^{3/2}$ becomes large and $(T_e - T_i)$ becomes too small with respect to the accuracy of the experimental data to perform separate power balances. In these cases a combined power balance analysis for electrons and ions must be performed (for examples see [Baldzuhn et al \(2000\)](#), [Stroth et al \(1998\)](#)).

Only in special cases is direct comparison of diffusion coefficients appropriate instead of comparing fluxes. For example, in the $1/\nu$ -regime the neoclassical energy diffusivity D_{22}^e coefficient (related to ∇T_e) dominates the off-diagonal coefficient as $D_{22}^e/D_{21}^e = 4.4$ ([Maaßberg et al 1999](#)). Thus for a small *ion-root* E_r (i.e. at conditions close to the $1/\nu$ -regime) and a fairly flat density profile, the direct comparison of D_{22}^e with the experimental $\chi_e = -Q_e/(n_e \nabla T_e)$ may be reasonable in which off-diagonal contributions are neglected. For ECRH discharges in some cases, an experimental $\chi_e(r)$ is estimated by integrating the electron energy balance with the purely diffusive ansatz for $Q_e = -n_e \chi_e \nabla T_e$ and by fitting the obtained $T_e(r)$ to the experimental data ([Maaßberg et al 1993b](#)). For example see figure 12(d).

In general for high temperatures the experimentally obtained fluxes in the plasma core agree well with their neoclassical expectations (see figures 12 and 13). For electron-root discharges (see figure 12) the pronounced ∇T_e develop around the region of positive E_r , i.e. at $r/a < 0.3$ correspond to a strongly reduced electron energy diffusivity χ_e obtained from power balance analysis. This low χ_e in the central part can only be explained if the strongly positive E_r resulting from electron-root conditions is taken into account (figure 12(d)). For lower temperatures in the core and generally for the low temperatures at the plasma edge (and thus reduced neoclassical transport) anomalous i.e. presumably turbulence driven contributions prevail (see figures 12 and 13). The observation that throughout almost all discharge conditions, the measured E_r agree well with the neoclassical calculations implies that these additional anomalous particle fluxes—which in the gradient region exceed the neoclassical ones by about an order of magnitude (figure 13, lower row, figure 12(c))—are to a high degree ambipolar. However, for the standard analysis E_r is estimated from the ambipolarity condition of the purely diffusive neoclassical fluxes. Experimental evidence of additional *anomalous convective particle fluxes* (e.g. driven by the heating) that may affect the ambipolar E_r will be discussed in section 5.3.

3.5. Impurity transport

Assuming $T_I = T_i$ and $n_I \ll n_i$, i.e. $n = n_e \cong Z_i n_i$, the flux densities of the impurity species Γ_I are described in the tracer model where the ambipolar E_r is still determined by the background plasma from $\Gamma_e \cong Z_i \Gamma_i$. For the standard ion-root $T_i \approx T_e$ the radial electric field

then is approximately given by $\Gamma_i(E_r) = 0$ such that from equation (3.2)

$$Z_i \frac{e E_r}{T_i} \cong \frac{n'}{n} + \delta_{12}^i \cdot \frac{T'_i}{T_i} \quad (3.6)$$

and the impurity fluxes in equation (3.2) become

$$\Gamma_I = -n_I D_{11}^I \left[\frac{n'_I}{n_I} - \frac{Z_I n'_i}{Z_i n_i} + \left(\delta_{12}^I - \frac{Z_I}{Z_i} \delta_{12}^i \right) \frac{T'_i}{T_i} \right], \quad (3.7)$$

where the $\delta_{12}^\alpha = D_{12}^\alpha / D_{11}^\alpha$. For stationary conditions, $\Gamma_I = 0$ the impurity density profile is estimated from

$$\frac{n'_I}{n_I} = \frac{Z_I}{Z_i} \left[\frac{n'}{n} + \delta_{12}^i \frac{T'_i}{T_i} \right] - \delta_{12}^I \frac{T'_i}{T_i}. \quad (3.8)$$

For pure transport regimes, i.e. if the energy convolution can be performed only within one regime (Maaßberg *et al.* 1999), the δ_{12}^α can be obtained analytically as $\delta_{12}^\alpha = 3/2$ in the plateau regime, 3.37 in the $1/\nu$ -regime, 1.36 in the $\sqrt{\nu}$ -regime and 0.75 in the (stellarator) ν -regime, respectively.

In a tokamak in the (deep) banana regime, the off-diagonal coefficient changes sign and becomes $\delta_{12}^\alpha = -0.173$ with very important consequences: for large Z_I , a peaked $n(r)$ and a flat $T_i(r)$ profile lead to a highly peaked impurity density, $n_I \propto n^{Z_I/Z_i}$, whereas for a flat $n(r)$ and a peaked $T_i(r)$ profile no accumulation is obtained provided the condition $n'/n - 0.173 \cdot (T'_i/T_i) > 0$ is fulfilled (note that all gradients are typically negative). In stellarators $\delta_{12}^\alpha > 0$ is always valid such that this ‘temperature screening’ effect cannot be obtained. Instead with a typically flat $n(r)$ and slightly peaked $T_i(r)$ profile, impurity accumulation with a peaked $n_I(r)$ profile

$$n_I \propto T_i^{((Z_I/Z_i)\delta_{12}^i - \delta_{12}^I)} \quad (3.9)$$

is predicted. It is a consequence of the negative E_r which leads to the strong inward impurity pinch (weighted with Z_I/Z_i) which must be balanced by very steep gradients ∇n_I . This scenario is the most dangerous at higher densities, i.e. in typical NBI discharges. Only in low-density ECRH discharges can the *positive* ion-root $Z_I E_r / T_i \cong -D_{12}^e / D_{11}^i \cdot T'_e / T_e$ prevent impurity accumulation. However, from a stellarator reactor perspective the conditions for the *positive* ion-root ($T_e \gg T_i$) are not of relevance. Impurity transport analyses comparing expected and observed fluxes are discussed in section 6.2

3.6. Bootstrap and inductive currents

The *bootstrap current* j_b resulting from the parallel momentum transfer from barely trapped to passing particles increases t in tokamaks and thus reduces the requirements for current drive needed for advanced operation. In contrast, helically trapped particles in stellarators result in a j_b component which lowers t . This bootstrap current inversion has been proven experimentally in the ATF stellarator (Murakami *et al.* 1991). It allows minimization of the total bootstrap current density following the strategy of the Wendelstein line to minimize pressure induced effects on the optimized configuration. However, precisely $j_b = 0$ can be achieved only locally as j_b depends on collisionality and radial electric field.

DKES code calculations of the mono-energetic bootstrap current coefficient Γ_{31}^* in W7-AS are shown in figure 14. The bootstrap current is tokamak-like due to the dominant toroidal Fourier components; the helical b_{mn} -Fourier modes are too small to drive Γ_{31}^* negative. The values of Γ_{31}^* are reduced by elongation as is the case also in an equivalently elongated tokamak (figure 14, dotted line). In stellarators the bootstrap current coefficients also depend

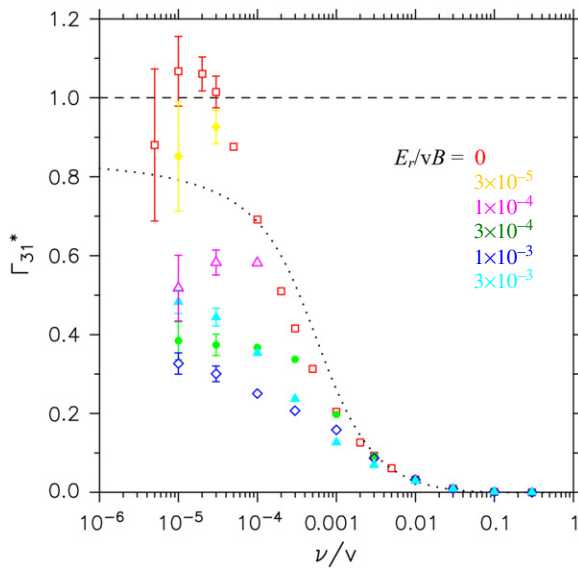


Figure 14. The mono-energetic bootstrap current coefficient Γ_{31}^* (normalized to the collisionless asymptote of the equivalent tokamak with circular cross-section, i.e. $\kappa = 1$ (Boozer and Gardner (1990); compare figure 8) versus the mono-energetic collisionality ν/ν at the low- t standard configuration (w7as-sc3) at $r/a = 0.5$. The normalized radial electric field was assumed to have values of $E_r/vB = 0$, (red open squares), 3×10^{-5} , 10^{-4} , 3×10^{-4} , 10^{-3} , 3×10^{-3} with Γ_{31}^* being successively reduced at each increment. The dotted line corresponds to a tokamak with equivalent elongation (independent of E_r !).

on the radial electric field (Ogawa *et al* 1992). In figure 14 the collisionless asymptote for intermediate E_r is about 0.4, not much less than the value for an equivalently elongated tokamak (dotted line) which is 0.8. For W7-X, however, the collisionless asymptote becomes as low as $\Gamma_{31}^* \approx 0.04$, showing the success of this optimization criterium. The predicted minimization of j_b for W7-X has been verified with two independent numerical techniques (Maaßberg *et al* 1993c). The relative effect of E_r on Γ_{31}^* is roughly comparable for W7-AS and W7-X. In contrast, for quasi-axisymmetric configurations such as NCSX the Γ_{31}^* depend only weakly on E_r , showing the analogy to a tokamak (Beidler *et al* 2003a).

A self-consistent calculation taking into account the effect of finite $\beta(r)$ and toroidal current density in the calculations of Γ_{31}^* was not conducted. The influence of a small Shafranov shift on the toroidal mirror terms—which determine toroidal length and the radial width of most of the banana orbits—is moderate. The toroidal current density changes t and thus the radial excursions of the barely trapped and passing orbits in the $lmfp$ regime influencing Γ_{31}^* . However, due to the typically net-current-free operation of W7-AS this variation of $t(r)$ is small at outer radii where the bootstrap current density plays the major role. This was verified by comparison with self-consistently modelled axisymmetric bootstrap current coefficients (Maaßberg and Beidler 2004). DKES calculations of Γ_{31}^* with a fixed b_{mn} -Fourier spectrum at very low collisionalities confirm this axisymmetric t dependence.

The total bootstrap current density for the species $\alpha = e, i$ is driven by the density and temperature gradients as well as by the radial electric field E_r such that from equation (3.1)

$$j_b^\alpha = D_{31}^\alpha \cdot \left[\frac{n'_\alpha}{n_\alpha} - q_\alpha \frac{E_r}{T_\alpha} + \frac{D_{32}^\alpha}{D_{31}^\alpha} \frac{T'_\alpha}{T_\alpha} \right]. \quad (3.10)$$

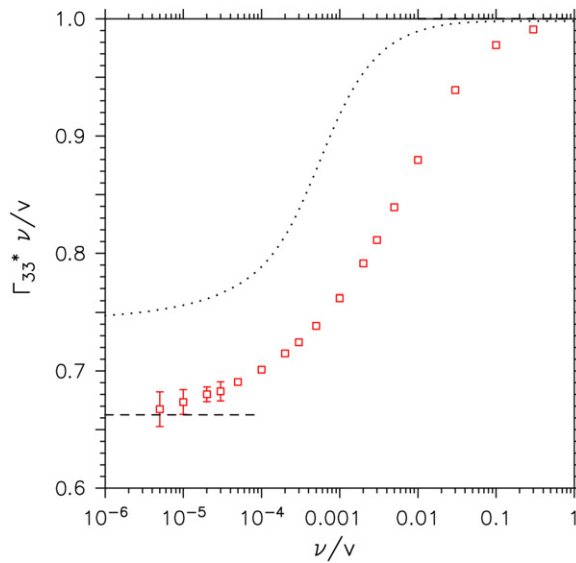


Figure 15. DKES results: the mono-energetic electric conductivity coefficient $\Gamma_{33}^* \cdot \nu/v$ (normalized to the collisional Spitzer value) versus the mono-energetic collisionality ν/v for the low- t standard configuration (w7as-sc3) at $r/a = 0.5$. The dotted line shows $\Gamma_{33}^* \cdot \nu/v$ for the equivalent tokamak.

For a typical *ion-root* scenario, where $T_e \approx T_i$ and negligible ion particle flux $\Gamma_i(E_r) = 0$ this yields with equation (3.6)

$$j_b^i \approx D_{31}^i \cdot \left[\frac{D_{32}^i}{D_{31}^i} - \delta_{12}^i \right] \cdot \frac{T'_i}{T_i} \quad \text{and} \quad j_b^e \approx D_{31}^e \cdot \left[\left(1 + \frac{T_i}{T_e} \right) \frac{n'}{n} + \delta_{12}^i \frac{T'_i}{T_e} + \frac{D_{32}^e}{D_{31}^e} \frac{T'_e}{T_e} \right]. \quad (3.11)$$

Thus for the bootstrap current coefficients $D_{31}^i \approx D_{31}^e$ and $D_{32}^i \approx D_{32}^e$ holds for these conditions, in contrast to the coefficients for particle and energy transport. Then the ambipolar E_r reduces the ion bootstrap contribution j_b^i but increases j_b^e . Consequently, for the total bootstrap current density $j_b(E_r \neq 0) \approx j_b^i + j_b^e$ only a weak dependence on E_r is obtained.

For a typical *electron-root* scenario profiles of T_i and n_e are very flat in the plasma centre and the ambipolar E_r can roughly be estimated by negligible electron fluxes $\Gamma_e = 0$. In such cases, the bootstrap current is carried predominantly by the electrons and one has

$$j_b \approx j_b^e \approx D_{31}^e \left[\frac{D_{32}^e}{D_{31}^e} - \delta_{12}^e \right] \cdot \frac{T'_e}{T_e}. \quad (3.12)$$

The electrons are in the $\sqrt{\nu}$ -regime where with the assumption of pure regimes $\delta_{12}^e = 1.36$ (see section 3.5). In the collisionless asymptote the bootstrap current coefficients become $D_{31}^e \propto nT/t$ and $D_{32}^e = D_{31}^e$. With these approximations one estimates $j_b = -0.36 \cdot D_{31}^e \cdot (T'_e/T_e)$. This approach is confirmed by the numerical calculation of j_b with the interpolation in the DKES database in the energy convolution (Maaßberg *et al* 2005).

The *parallel electric conductivity* is independent of E_r for those values under consideration. Figure 15 shows the mono-energetic conductivity coefficient $\Gamma_{33}^* \cdot \nu/v$ normalized to the collisional Spitzer value. This quantity directly reflects the impact of the trapped particles. The dashed line at low collisionalities indicates the passing particle fraction,

f_p , defined by

$$f_p = \frac{3}{4} \frac{\langle B^2 \rangle}{B_{\max}^2} \cdot \int_0^1 \frac{\lambda d\lambda}{\langle \sqrt{1 - \lambda} b \rangle}, \quad (3.13)$$

where B_{\max} is the absolute maximum of B on the flux surface, $b = B/B_{\max}$, $\langle \rangle$ denotes the flux surface average and λ is an integration variable. In the limit of $v \rightarrow 0$, only passing particles contribute to the inductive current. At finite v/v current diffusion due to friction of passing particles with the trapped ones increases $\Gamma_{33}^* \cdot v/v$. The bounce time of the barely trapped particles, i.e. those being reflected close to B_{\max} is fairly large, leading to the slow convergence of $\Gamma_{33}^* \cdot v/v$ to f_p at very-low collisionalities. The mono-energetic electric conductivity for the equivalent elongated tokamak configuration is given for comparison. The deviation at higher collisionalities reflects that the bounce-times of particles trapped in the local minima in W7-AS is much shorter than those of tokamak banana orbits. For W7-X, the deviation is increased due to the stronger toroidal mirror term b_{01} (leading to $f_p \approx 0.5$ for the standard configuration). Consequently, tokamak formulae for the parallel electric conductivity are not suited for calculating inductive current densities in W7-AS.

Due to the absence of a strong ohmic current small non-inductive plasma currents (bootstrap and heating-driven currents) can be investigated with a precision difficult to achieve in a tokamak. The different internal current contributions cannot be measured directly but are derived from current balance analysis under stationary conditions where the net plasma-current measured by the Rogowski coil is compensated to $I_p = 0$ by means of the Ohmic transformer such that

$$I_b + I_{OH} + I_{ECCD} + I_{NBCD} = 0,$$

where I_b is the bootstrap current, I_{OH} the inductive current by feedback control and I_{ECCD} , I_{NBCD} are EC and NBI driven currents, respectively (see sections 4.1 and 4.2). The result from current balance analysis is compared with the calculated total plasma current integrated from the radial profiles of the different current densities as calculated from the measured profiles $n_e(r)$ and $T_e(r)$. Stationarity is necessary as without feedback control of the plasma current I_p , the profiles $n_e(r)$ and $T_e(r)$ can be significantly affected by the transient rotational transform such that the profiles themselves remain transient (see section 5.2). Furthermore, current diffusion must be taken into account. In particular in low-density ECRH discharges with high T_e the L/R -time may become comparable to the discharge time such that steady-state conditions cannot be obtained without current feedback control.

Purely ECRH heated discharges with perpendicular launch avoid heating-driven currents such that the current balance analysis directly reveals the I_b . For the discharges used in figure 16 the bootstrap current is dominated by the electron pressure gradient, because $T_i \leq 0.2 \cdot T_e$ (see discussion related to equation (3.12)), the ion bootstrap current is almost negligible. Thus only the calculated electron component is displayed in the figure. Tokamak-like ('co') bootstrap currents up to 8 kA are observed in agreement with DKES calculations (Erckmann *et al* 1992d). Radial profiles of $j_b(r)$ and $j_{OH}(r)$ are discussed in Wendland *et al* (1999), the bootstrap current profile is significantly affected by the radial electric field. The agreement between calculated and measured bootstrap current is confirmed in perturbative current balance experiments by modulated ECCD, where the deposited power is kept constant while switching between co- and counter-current drive, which allows the separation of I_{ECCD} and I_b (section 4.1, Erckmann *et al* (1994), see also an example of calculated radial profiles of the current densities there).

For high performance 'optimum confinement' discharges (see section 5.3 and Kreter *et al* (2002)) I_b and I_{NBCD} of about 20 kA each are calculated in agreement with

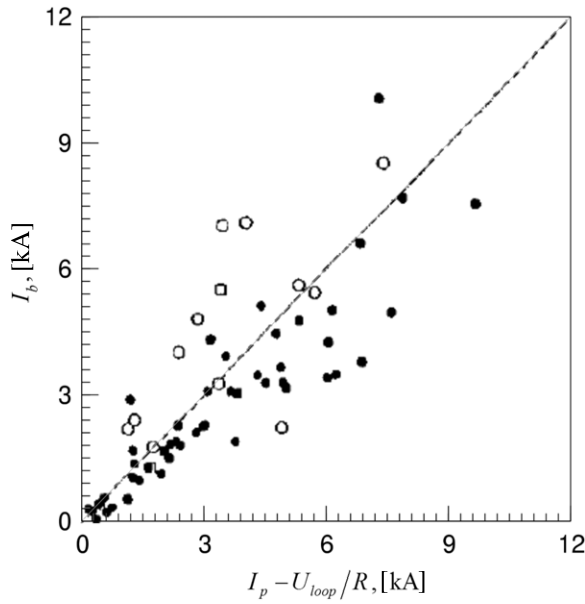


Figure 16. Calculated bootstrap current I_b from the DKES code as a function of the experimental quantity $I_p - U_{loop}/R$ for ECRH heated discharges ($2 \times 10^{19} \text{ m}^{-3} \leq n_e \leq 6 \times 10^{19} \text{ m}^{-3}$, $0.2 \text{ MW} \leq P_{\text{ECRH}} \leq 0.7 \text{ MW}$, $0.4 \text{ keV} \leq P_{\text{ECRH}} \leq 3.5 \text{ keV}$, at $B = 1.25 \text{ T}$ (open symbols) and $B = 2.5 \text{ T}$ (closed symbols)). The figure includes a large database with discharges at free running current as well as net-current-free discharges, where I_b is balanced by the OH-transformer (Gasparino 1990). Uncertainties exist in the Z_{eff} -profiles and in the unknown contributions from supra-thermal electrons in discharges with low density and high heating power.

current balance analysis (Marushchenko *et al.* 2002). The effect of the ion-root $E_r < 0$ on $j_b(r)$ is not significant (besides very strong $|E_r|$) as it increases electron and simultaneously decreases the ion contribution. The ohmic current and the NBCD current density profile are both fairly flat and partly cancel each other. High density, high- β discharges heated by unbalanced NBI with very short slowing down times are in the collisional regime even in the plasma centre $T_i \approx T_e \approx 0.25 \text{ keV}$ resulting in fairly small I_b and I_{NBCD} of about 1–2 kA (Marushchenko *et al.* 2002). A sensitivity study of the current balance analysis for high- β discharges was performed in Geiger *et al.* (2003).

4. Heating and current drive

Heating systems for stellarators must support plasma start-up, ensure configuration and current control during heating, and, ideally, also provide tools for the control of particle and impurities. Compatibility with steady-state operation is required in the next step W7-X stellarator. As none of the commonly used heating methods such as ohmic heating (OH), radio frequency (rf-) heating, and neutral beam injection heating (NBI) satisfies all requirements, a properly chosen ‘heating mix’ is important to address the various scientific goals. W7-AS was thus equipped with an OH-transformer, electron cyclotron resonance heating (ECRH), ion cyclotron resonance heating (ICRH), and NBI. The low shear vacuum configuration of the Wendelstein stellarators is very sensitive to internal plasma currents resulting from plasma equilibrium, finite pressure and heating specific asymmetries in the particle distribution

function (Erckmann *et al.* 1992d). Thus methods are required to control the net current and, ultimately, the internal current distribution (Gasparino *et al.* 1990). The OH-transformer at W7-AS turned out to be a valuable tool for configuration control (e.g. edge rotational transform) with small inductive currents, rather than for plasma start-up and bulk heating as in tokamaks. Configuration control by electron cyclotron current drive (ECCD) and current drive by NBI was thus an important topic at W7-AS and is expected to be a key technique for steady-state operation in W7-X (Michel *et al.* 2001), where no OH-transformer is foreseen. Selected heating specific investigations and the related theory are presented in this section for ECRH in section 4.1, for NBI in 4.2, and for ICRH in section 4.3.

ECRH was available in the initial state with 70 GHz at 1 MW heating power and was upgraded into a two-frequency system operating at 70/140 GHz with 0.5/2.3 MW, respectively. ECRH application is restricted to a discrete set of resonant magnetic fields and the cut-off condition sets a limit in the accessible plasma density for standard scenarios. Electron Bernstein wave (EBW) heating removes the density restriction; the excitation process, however, sets a lower density limit. ECRH investigations aimed at improving the understanding of wave-particle interaction in complex 3D stellarator fields. The important quantities like localized heating and power deposition, wave propagation and current drive were derived from dedicated experiments and related theory.

NBI is complementary to ECRH, as it does not depend on the magnetic field and inherently provides particle fuelling. The absence of a density limit qualifies NBI particularly for high- β investigations and high density scenarios. Two injector boxes with 1.5 MW each were arranged for balanced injection to minimize NBI-driven net currents. In the final state of the W7-AS one box was rearranged and NBI was operated with unidirectional injection.

ICRH was available with a source power of 2 MW. Two generators could be operated in a wide frequency range between 32 and 110 MHz. Several antenna types were applied to investigate optimized wave coupling in the complex 3D configuration of W7-AS.

4.1. Electron cyclotron resonance heating and current drive

4.1.1. Introduction. Net current free plasma start-up and heating with ECRH was achieved for the first time at W7-A in 1983 (Wilhelm *et al.* 1984a, Erckmann *et al.* 1983, 1984a) with 28 GHz at 200 kW output power for 40 ms pulses. All previous W7-A investigations were performed with ohmic plasma start-up as the only available method. Due to the low frequency, operation had to be restricted to a magnetic field of 1 T and a plasma density below the cut-off density of $n_{e,\text{crit}} \approx 1 \times 10^{19} \text{ m}^{-3}$ for the 1st harmonic O-mode (O1). Thus IPP initiated the industrial development of gyrotrons operating at 70 GHz, which corresponds to $B_{\text{res}} = 2.5 \text{ T}$ and $n_{e,\text{crit}} = 6.2 \times 10^{19} \text{ m}^{-3}$ (O1). This frequency allowed also to operate at 1.25 T with $n_{e,\text{crit}} = 3.1 \times 10^{19} \text{ m}^{-3}$ for 2nd harmonic X-mode (X2) operation. First plasma experiments with 70 GHz started already in 1984 at W7-A with a 200 kW, 100 ms source. W7-AS saw the power-upgrade to 1 MW microwave power generated by five gyrotrons with 200 kW each for 3 s pulses. Large progress in the transmission technology was made with respect to pure mode irradiation with well-defined polarization and narrow collimated beams (Erckmann *et al.* 1984a, 1985, 1986b), which was a necessary prerequisite for detailed investigations of microwave propagation and absorption. Pioneering experiments on ‘stimulated heat wave propagation’ were proposed and executed for the first time in 1984 at W7-A (Erckmann *et al.* 1984b). Corresponding experiments at W7-AS with both sophisticated diagnostics and improved theoretical interpretation are reviewed in section 4.1.3 (Hartfuß *et al.* 1986, Gasparino *et al.* 1998a, Erckmann *et al.* 1994). Stimulated heat wave propagation analysis became a powerful perturbation method for

heat transport studies in almost all ECRH-equipped fusion devices (see section 5.3.3 and Luce *et al* (1992), Peters *et al* (1994), Cox *et al* (1993), Ryter *et al* (2001)). As port access was better at W7-AS as compared with W7-A, the first in-vessel launcher with steerable launching mirrors for on/off-axis heating and current-drive developed by the IPF-Stuttgart group (Erckmann *et al* 1987, 1990) became available for day one operation of W7-AS in October 1988. This key technology allowed detailed investigations of phase-space wave-particle interaction physics (ECCD, ECRH) in a wide range from perpendicular to oblique launch ($<40^\circ$) at on- and off-axis deposition, selected results are reviewed in section 4.1.6, respectively. A sophisticated theoretical modelling as described in section 4.1.2 is required to arrive at a quantitative interpretation of the results.

The 70 GHz system was step by step replaced by a 140 GHz system, resulting in a final installation of four gyrotrons at 140 GHz with a total power of 2.3 MW and one gyrotron at 70 GHz with 0.5 MW for a pulse length of 1–3 s (Erckmann *et al* 2002). The latter was maintained to keep the option of 1.25 T operation open. The 140 GHz gyrotrons were developed for W7-AS by IAP Nizhny Novgorod and Kurchatov Institute Moscow in 1993, marking a milestone in the ECRH technology (Erckmann *et al* 1993a, 1993b). A quasi-optical transmission line was developed by IPF Stuttgart (Henle *et al* 1990). Pilot experiments using a 140 GHz prototype developed by Forschungszentrum Karlsruhe in 1991 confirmed the physics predictions for wave coupling and propagation in the extended density range up to $n_{e,\text{crit}} = 1.25 \times 10^{20} \text{ m}^{-3}$ (Erckmann *et al* 1991a, 1992c). The enhanced ECRH-power led to the discovery of new confinement regimes such as H-mode (Erckmann *et al* 1992a, 1993d), see section 7.1, and the electron-root confinement (section 5.3). Experiments with combined heating of ECRH and NBI focused on density control and investigation of the particle confinement; some results are reviewed in section 4.1.4. A significant stray radiation background has to be accepted in the vacuum vessel in the presence of strong ECRH, which is of particular importance for continuously operating devices. The toroidal distribution of stray radiation in the periphery between the plasma and the vacuum vessel was therefore investigated in view of W7-X and results are discussed in section 4.1.5. The experiments in the last period of the W7-AS lifetime focused on the β -limit and island-divertor studies. Both require high-density operation beyond the X2 density cut-off. Electron Bernstein waves (EBW) can propagate in plasmas without any upper density limit, the excitation of EBWs, however, is difficult. A promising scenario is the ordinary–extraordinary-Bernstein (OXB) mode conversion process (Preinhaelter and Kopecky 1973, Mjølhus 1984), which was demonstrated at W7-AS for the first time (Laqua *et al* 1997). Instead of an upper density limit, as for the standard ECRH-scenarios, the O-mode cut-off density sets a lower density limit for this scenario ($n_{e,\text{crit}} = 2.5 \times 10^{20} \text{ m}^{-3}$ for the O2-mode at 140 GHz). Results on EBW-heating and current drive are reviewed in section 4.1.7.

4.1.2. Kinetics for ECRH and ECCD modelling. The EC power deposition and current drive profiles are calculated in linear theory by a ray-tracing code which calculates rays and the k -vectors in a 3D Hamiltonian formulation from the ‘cold’ dispersion function (Gasparino *et al* 1990). Absorption and emission coefficients (for simulating ECE) are used in the weakly relativistic approach following (Bornatici *et al* 1983). The EC current drive is obtained from the adjoint approach (Taguchi 1989) both in the collisional and in the collisionless limit (Romé *et al* 1998) (a generalization to arbitrary collision frequencies is missing, so far). For the Fokker–Planck simulations, also the flux-surface averaged quasi-linear diffusion coefficient $D_{\perp\perp}(r, v_{\parallel}, v_{\perp})$ can be calculated.

To calculate the electron distribution function for the highly peaked central deposition with very high power densities a time-dependent 2D bounce-averaged Fokker–Planck code

was developed (Marushchenko *et al.* 1997). The variation of B on the flux surfaces within the highly focussed EC-wave beam is small allowing for a simplified mapping of the electron–wave interaction. The ECRH power source is described by the quasi-linear operator with $D_{\perp\perp}(r, v_{\parallel}, v_{\perp})$ either from the ray-tracing calculations or from analytical modelling (relativistic resonance condition, $\omega - k_{\parallel} v_{\parallel} - l\omega_c/\gamma$ with l being the harmonic number and γ the relativistic factor), where the finite EC beam width leads to spectral broadening with respect to k_{\parallel} . For the power sink (in addition to the small collisional ion heating), a stellarator-specific loss-cone model (Romé *et al.* 1997) is used. The model describes the convective radial energy flux of the ripple-trapped suprathermal electrons generated by the ECRH. This simulation of radial transport by a power sink in a 2D model is well justified even if the thermal energy transport corresponds to the neoclassical one in the $lmfp$ -regime. Since steep gradients at the loss-cone boundary (high power flux in velocity space) appear at high heating power levels, a complete nonlinear treatment of the collision term turned out to be mandatory. This code is well suited to analyse the ECCD efficiency even at high power levels (where the linear approach fails). An example of results is shown in figure 24.

Monte Carlo simulations are a complementary approach. Whereas the Fokker–Planck modelling is accurate in velocity space, but strongly simplified in real space, a Monte Carlo modelling is vice-versa. Since the phase-space volume of electrons interacting with the EC-waves is extremely small, a direct Monte Carlo technique fails. A Green’s function technique was developed (Murakami *et al.* 1996, 1998) to treat ECRH in the form of quasi-linear diffusion. A straight-forward convolution yields the radial electron particle and power fluxes driven by the ECRH. This Monte-Carlo technique is applied both for the radial broadening of the EC power deposition profile (Murakami *et al.* 1998, 2000) and for the suprathermal particle fluxes under electron root’ conditions (Maaßberg *et al.* 2000b).

4.1.3. X2- and O1-mode start-up, absorption and heating. In the first ECRH experiments at W7-A the 28 GHz, 200 kW, microwaves were launched from an open ended waveguide perpendicular to the magnetic axis. The waveguide mode TE₀₂ contained 50% O- and 50% X-mode polarization, i.e. the X-mode fraction is absorbed only after multiple reflections from the torus walls (dirty coupling). A significant improvement of the plasma parameters was measured with a well collimated and linearly polarized rf-beam at comparable power (Erckmann *et al.* 1985): as a result of the well localized power deposition the central electron temperature measured by Thomson scattering increased from 0.6 keV to 1.2 keV at a density of $0.5 \times 10^{19} \text{ m}^{-3}$ and showed the importance of pure mode irradiation.

Plasma start-up from the neutral gas was demonstrated by the pioneering experiments at the stellarators Heliotron-E (Uo *et al.* 1985), W7-A (Wilhelm *et al.* 1984a, 1984b) and JIPPT-2 (Okhubo *et al.* 1981). ECRH then became a standard method for net current-free plasma generation in stellarators. Linear theory does not explain the somewhat surprising experimental result of X2-plasma start-up from the neutral gas. Experimental and theoretical investigations contributed in clarifying the phenomenon (e.g. Carter *et al.* (1987), Cappa and Castejon (2004), Nagasaki *et al.* (2005)), although the underlying physics is not yet fully understood.

The typical range of plasma parameters obtained with ECRH is seen from standard scenario experiments with strong X2-mode heating from the low field side in the equatorial plane. Radial profiles of T_e and n_e for discharges with different densities at constant heating power of 1.2 MW are shown in figure 17 (Maaßberg *et al.* 2000b). The central electron temperatures range from 5.7 keV at $1.7 \times 10^{19} \text{ m}^{-3}$ to 3 keV at $7.5 \times 10^{19} \text{ m}^{-3}$. It is worth noting that the ions are energetically decoupled from the electrons under these conditions and the energy balance is dominated by the electrons. A pronounced steepening of the T_e gradients is seen in the plasma

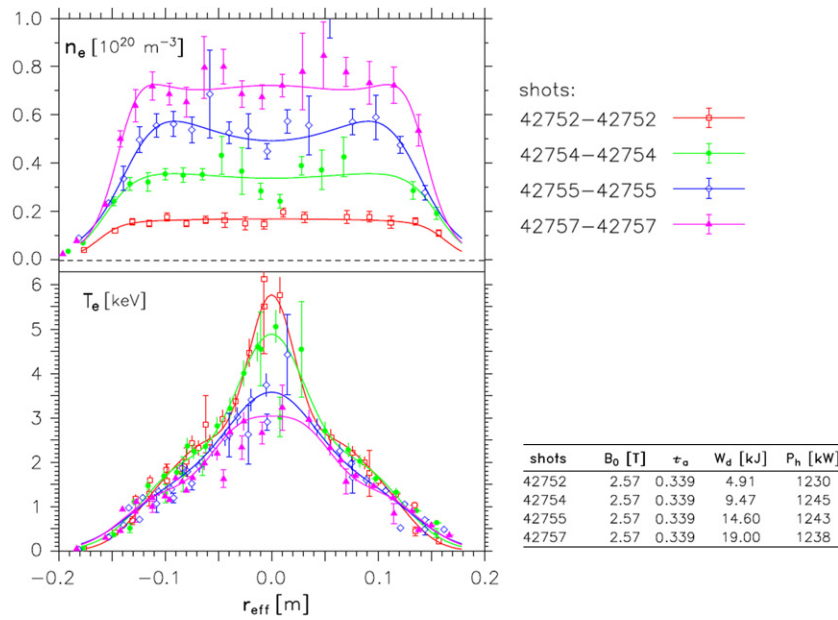


Figure 17. Radial profiles of the electron temperature and density at constant ECRH-power of 1.2 MW. The highest temperature is related to the lowest density and vice versa. $t_a = 0.34$, $B = 2.5$ T.

centre at densities below $4 \times 10^{19} \text{ m}^{-3}$. This enhanced core confinement is related to electron root conditions with strong positive central radial electric fields (see section 5.3).

Off-axis heating in W7-A could only be realized by tuning the magnetic field and thus the resonance layer (Erckmann *et al* 1986a). The improved launcher at W7-AS with in-vessel steerable launching mirrors (Erckmann *et al* 1990) allowed to steer each microwave beam to arbitrary poloidal (on/off-axis heating) and toroidal (on/off-axis current drive) launch angles. An example of profiles obtained with on- and off-axis heating is shown in figure 18 together with the ray tracing calculations in the 3D stellarator geometry. Whereas the T_e profile changes from peaked (on-axis deposition) to hollow (off-axis deposition), the n_e profile changes from slightly hollow (on-axis) to flat (off-axis), giving evidence for reduced particle confinement with strong on-axis heating (see section 4.1.4).

Stimulated heat wave propagation became a powerful method to determine the power deposition profile. Here a localized periodic perturbation of the electron temperature is stimulated by ECRH power modulation. This perturbation propagates away from the deposition region in the plasma thus driving a heat wave. From the local measurement of phase and amplitude of this heat wave, both the heat transport coefficient of the plasma and the power deposition profile in principle can be determined locally (Hartfuß *et al* 1986, Gasparino *et al* 1998a, Erckmann *et al* 1994). First experiments on heatpulse propagation induced by switching ECRH were performed at the Spherator FM-1 (Ejima *et al* 1974). The improved technique with periodically modulated ECRH allows to track a heat wave and was applied for the first time at W7-A (Erckmann *et al* 1984a, Griege *et al* 1986). For sufficiently high modulation frequency, the characteristic radial decay-length of the perturbed electron temperature amplitude becomes comparable to or smaller than the power deposition profile. Thus with this method an upper limit for the width of the power deposition profile

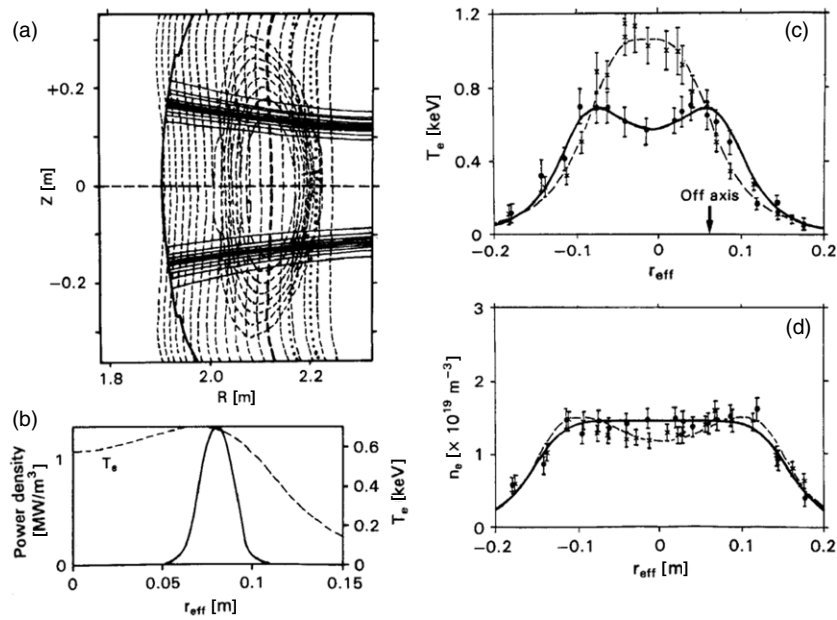


Figure 18. Ray tracing calculations for off-axis heating with two rf-beams at W7-AS and related profiles of the electron temperature T_e and density n_e . W7-AS flux-surfaces are shown together with contours of $|B| = \text{const.}$ almost vertical dashed lines with the resonance layer on axis) and the microwave rays (a), the off-axis power deposition profile is shown in (b). The T_e (c) and n_e -profiles (d) for off-axis heating (solid line) are compared with on-axis heating (dashed line).

can be obtained directly (Erckmann *et al* 1995a). This was proven in experiments, where rf-beams with different beam widths (full width at half maximum, FWHM of 4 and 6 cm) were used by modifying the launching optics. The deposition profile width at the resonance layer as determined by ray-tracing calculations for the different beam width agreed well with the experimental deposition width obtained from the modulation technique in the high frequency limit (Erckmann *et al* 1994). An example for a 6 cm off-axis power deposition in the vertical direction is given in figure 19. The electron temperature profile is flat within the power deposition region and also plotted for reference. The calculated FWHM of the power deposition profile from ray tracing is about 3 cm, which is slightly smaller than the measured one indicating some diffusive decay of the temperature wave amplitude. For X2-heating scenarios in stellarators with large ripple (e.g. L-2 and TJ-II) suprathermal trapped electrons can be generated by ECRH leading to a broadening of the ‘effective’ deposition profile as derived from ECE-temperatures in power modulation experiments. Even higher modulation frequencies are favourable to investigate this effect, the temperature modulation, however, then becomes smaller and is below the sensitivity limit of the ECE diagnostic system. In general discharges with higher density are characterized by a broader deposition profile, which is consistent with the defocusing of the rf-beams while approaching the cut-off density. The on-axis deposition profile as well as the profile of the electron heat diffusivity, as seen from figure 20, was derived from an experiment (Romé *et al* 1997), where the ECRH-power was modulated with an amplitude of 10–30% and the frequency was scanned from 0.05 to 5 kHz. The analysis requires a proper modelling of the transport effects in the transient energy balance (see section 5.3). The heat transport was described by a purely diffusive model. No evidence for a significant convective contribution was found. Calculated deposition profiles

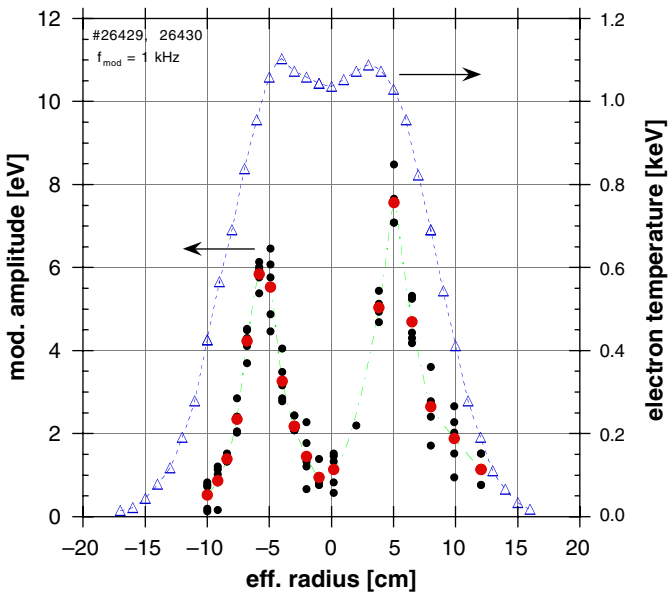


Figure 19. Electron temperature modulation amplitude (dots) measured by ECE diagnostics as a function of the effective minor radius for 0.2 MW off-axis ECRH at $r_{\text{eff}} = 6$ cm. The modulation frequency is 1 kHz, the modulation amplitude is 20%. The measured electron temperature profile is also plotted (triangles).

obtained from a 3D Hamiltonian ray-tracing code based on the assumption of a Maxwellian electron distribution function (single pass absorption) are usually peaked for both O- and X-mode. From the heat transport analysis of modulation experiments one obtains similarly peaked absorption profiles, but additionally a much broader contribution is present as seen in figure 20. Width and relative integral contribution with respect to the ‘thermal’ peaked part depend on the particular heating scenario, collisionality regime and magnetic configuration. The measured broadening of the deposition profile is attributed to the fast transport via the drift orbits of trapped electrons in the long mean free path regime (Romé *et al.* 1997). Taking the broader component of the power deposition profile into account, the input power is recovered by the heat transport analysis within the errors.

4.1.4. ECRH effects on particle confinement: ‘pump out’ and combined heating. As a common observation in many stellarators and tokamaks a drop of the line averaged density was measured during ECRH (e.g. Gilgenbach *et al.* (1980), Alikaev *et al.* (1984), Ringler *et al.* (1987), Pietrzyk *et al.* (1993)), which became known under the abbreviation ‘pump out’ or ‘density clamping’. The observation of this phenomenon is more difficult in stellarators as a reference plasma such as the Ohmic state in tokamaks is generally not available and an experimental comparison must be based on combined heating scenarios. Figure 21 shows that a purely NBI heated discharge with the density increasing in time can be ‘pumped’ and the density control can be recovered by adding ECRH at sufficiently high power (Erckmann *et al.* 1993a, 1993b, 1995a). As also the impurity confinement is affected (see section 6.2), ECRH may provide an option for density and/or impurity control in future devices. In general two explanations are possible, namely either ECRH acts on the particle confinement or it modifies the particle sources. For the latter a screening of the plasma from

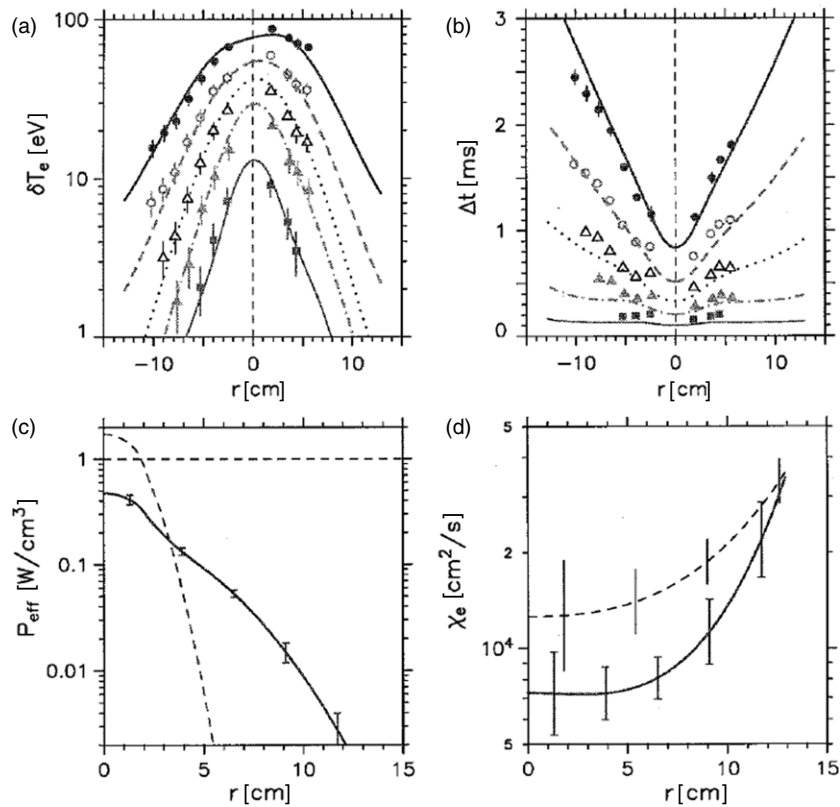


Figure 20. The temperature modulation amplitudes, δT_e (a) and the time delays, Δt (b) versus radius from ECRH power modulation experiments at $B_0 = 2.5$ T (O1-mode, 70 GHz) with on-axis deposition. The radial dependence is plotted for different modulation frequencies, $f_{\text{mod}} = 92$ (closed circles), 200 (open circles), 400 (open triangles), 800 (full triangles) and 2000 Hz (squares). The power deposition profile (c, solid line) is compared with the ‘ray-tracing profile’ shape (c, dashed line). The ‘effective’ heat conductivity, $\chi_e(r)$ (d, solid line) is compared with the $\chi_e(r)$ -profile derived from the stationary power balance analysis with the power deposition profile from ray tracing (d, dashed line).

neutral particle influx from external sources (gas feed) or recycling fluxes by ionization may be considered. Both effects are difficult to distinguish because of the generally poor knowledge of the neutral gas sources or, more precisely, the radial neutral gas profiles. A detailed discussion of particle transport in some selected cases is presented in section 6.1, where discharges with ECRH only, NBI only and combined heating are compared. A discussion of the impurity confinement in such experiments is presented in section 6.2.

The interpretation of experiments with ECRH becomes particularly difficult in the case where the single pass absorption is incomplete and multiple reflections from the torus walls must be taken into account. This power fraction is expected to be absorbed mainly at the plasma edge and may contribute to additional ionization and, consequently, lead to a significant screening of neutrals. A situation of comparable complexity is given if ECRH is applied at densities close to or above the cut-off density, because the power deposition is then not well defined and both effects, particle confinement degradation and screening cannot be separated clearly.

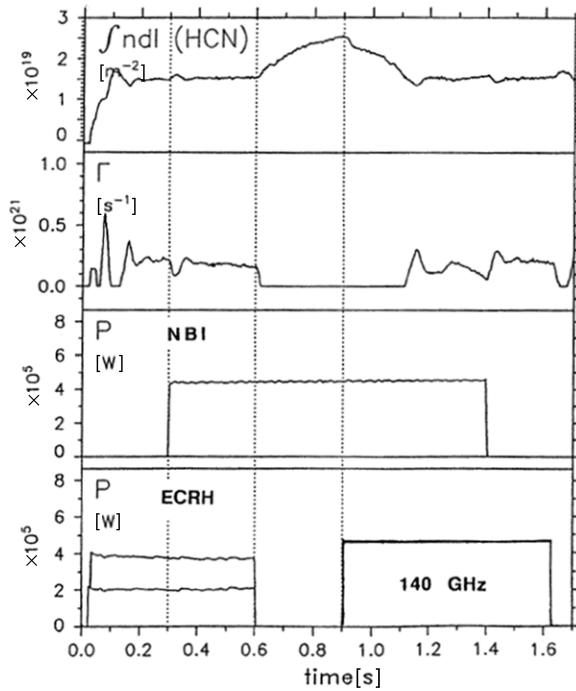


Figure 21. Time development of the line integrated plasma density $\int n_e dl$, the external gas flux Γ and the time sequence of the heating pulses P of NBI and ECRH (Eckmann and Gasparino 1994).

4.1.5. Stray radiation. In the presence of strong EC heating a significant microwave radiation background may rise due to mechanisms such as polarization mismatch of the launched mode, incomplete absorption (e.g. O2-mode heating) or uncontrolled density cut-off conditions. Besides direct irradiation by the non-absorbed beams a rather isotropic background level builds up also. First studies on beam deflection by plasma density fluctuations were performed using a pick-up waveguide array at the inner torus wall opposite to the ECRH-launchers. ECR-stray radiation was observed at poloidal positions even for optimized irradiation, where standard ray tracing methods failed to explain the results. A qualitative explanation was achieved by introducing density fluctuations in the ray-tracing calculations (Tutter *et al.* 1991), which become particularly important near the cut-off density. Temporal behaviour and distribution of the background radiation around the torus was investigated with a number of calibrated multi-mode wide angle ‘sniffer’ antennas (Gandini *et al.* 2001a). In the case of 1MW X2 heating at sufficiently large n_e and T_e where single pass absorption clearly exceeds 90% power fluxes were below 1 kW/m^2 even near the ECRH launching plane. On the torus side opposite to the ERCH launching plane the power flux is about an order of magnitude less. Maximum power load is observed if the single-pass absorption is reduced, e.g. during the plasma build-up phase, under O2 or OXB heating conditions or if X2 cut-off density is reached. In the latter case the stray radiation starts to rise already if the density becomes 80% of the X2 critical density since beam refraction already reduces the single-pass absorption (Gandini *et al.* 2001b, Laqua *et al.* 2001). For extrapolation to future devices two complementary codes were developed and benchmarked with the measurements: a 3D multi-reflection ray tracing code (Gandini *et al.* 2001a) and a multi-cell code assuming coupled oversized resonators homogeneously filled with isotropic radiation (Laqua *et al.* 2001). The

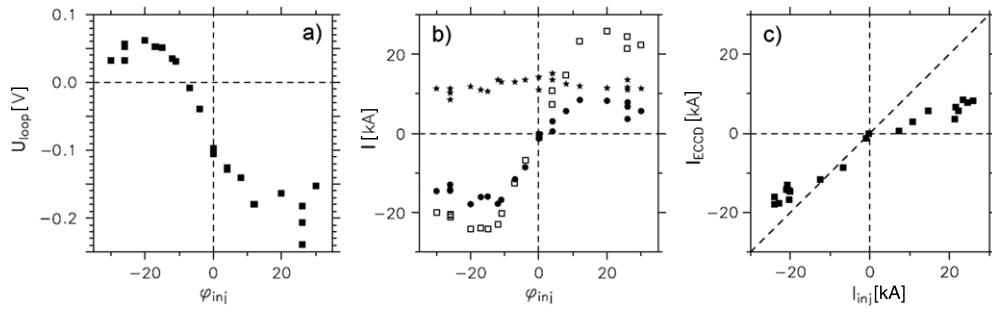


Figure 22. ECCD launch angle scan with 1.2 MW ECRH X-mode in net current free discharges at $n_e = 2.5 \times 10^{19} \text{ m}^{-3}$ in ‘standard’ configuration. (a) Loop voltage versus toroidal injection angle. (b) Linear prediction (open squares) and data of the EC-driven current derived from current balance (closed circles) together with the bootstrap current (stars). (c) EC-driven current from current balance versus the linear prediction (Erckmann *et al.* 2001).

effective average absorption at the walls can be determined from the measured toroidal distribution of the radiation in the vessel without plasma. In W7-AS the effective wall absorption was 30%, resulting also from the large number of portholes. The extrapolation to W7-X (Hartfuß *et al.* 2003) yields power fluxes as high as several 10 kW/m^2 to 150 kW/m^2 near the launching plane for 10 MW ECRH with O2.

4.1.6. ECCD and wave-particle interaction in phase space. Scanning the EC-wave-beam launch angle away from perpendicular incidence in the 3D stellarator magnetic field configuration introduces a rich field of physics (Maaßberg *et al.* 2005) such as Doppler-shifted absorption and current drive in presence of complex interaction with trapped and passing particles. Furthermore, the localized EC-driven currents introduce local shear, which has an impact on the confinement (see Erckmann *et al.* (1996)).

Basic experiments with the aim of separating the different effects were performed at W7-AS (Erckmann *et al.* 1990, Gasparino 1990, Gasparino *et al.* 1990) with up to 0.8 MW rf-power (four rf-beams) at 70 GHz at both the O1 mode ($B_{res} = 2.5 \text{ T}$) and the X2 mode ($B_{res} = 1.25 \text{ T}$), respectively. An experimental scan of the toroidal launch angle (resonance on axis) in O1-mode from the co- to the counter-current drive direction and the comparison with ray tracing calculations using the measured profiles of n_e and T_e is discussed in detail in Erckmann *et al.* (1991b). Here co- (counter-) CD denotes the current direction, which increases (decreases) the rotational transform, respectively. Co-CD thus corresponds to ECCD in the direction of the bootstrap current. A direct measurement of the current inversion while changing from Doppler blue- to red-shifted absorption was performed by launching a microwave beam at a fixed angle in a poloidal plane with almost vanishing magnetic field gradient and tuning the magnetic field shot by shot through the resonance (Erckmann *et al.* 1991b). The edge value of the rotational transform t_a was kept constant during the experiments using the OH-transformer. The measured quantity in all cases is the loop voltage required to compensate the EC-driven current. The characteristic signatures such as the launch angle for maximum CD as well as the linear dependence with power and the current direction inversion with Doppler shifted absorption are in good agreement with calculations.

A launch angle scan with 1.2 MW power in X2-mode from the low field side is shown in (figure 22) (Erckmann *et al.* 2001). The loop voltage required for inductive current

compensation is shown in figure 22(a) as a function of the launch angle φ_{ini} ($\varphi_{\text{ini}} = 0^\circ$ corresponds to perpendicular injection, i.e. $I_{\text{ECCD}} = 0$). For $\varphi_{\text{ini}} = 0^\circ$ a negative loop voltage is required to compensate the bootstrap current only, for $\varphi_{\text{ini}} = -10^\circ$ the EC-driven current compensates the bootstrap current and the loop voltage becomes zero. A linear superposition of I_{ECCD} , I_b and I_{OH} is assumed for a quantitative comparison. The bootstrap current I_b is calculated by the DKES code taking into account the ambipolar E_r ; the inductive current I_{OH} is calculated assuming neoclassical resistivity (effective charge ranges from $Z_{\text{eff}} = 3\text{--}6$ for the different discharges). The calculations are performed for each discharge using the measured profiles of n_e and T_e . The EC driven current $I_{\text{ECCD}} = -I_b - I_{\text{OH}}$ as derived from the current balance and the bootstrap current are plotted in figure 22(b) together with the data obtained from linear theoretical modelling of ECCD (Gasparino 1990). In figure 22(c) I_{ECCD} is plotted versus the EC-driven current calculated from linear theory with trapped particle effects included (Gasparino 1990, Romé *et al.* 1998, Gasparino *et al.* 1998b). The discrepancy is found to be larger for co-CD as compared with ctr-CD, and decreases with increasing density (Erckmann *et al.* 2001). The measured asymmetry of the current drive efficiency is not yet understood; it should be noted, however, that the radial profile of t and thus the local confinement changes significantly while scanning from co- to counter-current drive. Good agreement is found in the density range from $(0.6\text{--}0.8) \times 10^{20} \text{ m}^{-3}$, giving a hint that the simplifying assumptions (e.g. Maxwellian distribution function) of the quasi-linear theory are best met in the high density regime.

ECCD- and bootstrap current modulation techniques were applied at W7-AS for the first time (Erckmann *et al.* 1993c, 1994) to discriminate the local position of an on-axis driven EC-current and the bootstrap current by either modulating ECCD or the bootstrap current, respectively. Discharge conditions were chosen, with comparatively low temperatures and a characteristic skin-time of about 20 ms which is small compared with the inverse modulation frequency (10 Hz). According to theory, the EC-driven current is localized around the EC-resonance layer and the bootstrap current is localized in the pressure gradient region. The loop voltage response to the bootstrap or EC-driven current modulation was analysed and was found to be in excellent agreement with the time dependent solution of the voltage diffusion equation for both current components assuming radial current density distributions from the ray tracing (ECCD) and DKES code (bootstrap current). The modulation technique provides a very high resolution of about $\pm 20 \text{ A}$ in the detection of the EC-driven current. A linear relationship between the perturbed EC driven AC-current and the driving perturbed power was observed, which supports the validity of linear theory in the low-power regime, where the simplifying assumptions hold.

In general trapped particle populations reduce the ECCD efficiency, the related physics was investigated by operating W7-AS in different magnetic mirror configurations (Erckmann *et al.* 1995a), representative results are shown in figure 23: for case 1 the magnetic mirror maximum was placed in the ECRH launching plane at $\varphi_{\text{tor}} = 36^\circ$. Mainly passing particles are directly heated; the impact on the driven current results mainly from friction with the background trapped particles. For case 2 the minimum of the magnetic mirror was placed in the ECRH plane and wave absorption is dominated by trapped and barely passing particles. As shown in figures 24(a) and (b) at perpendicular launch with no ECCD, the loop voltage is non-zero for both cases and represents the voltage for bootstrap current compensation. In case 1 the maximum loop voltage and thus the maximum driven current is much larger ($\pm 13 \text{ A kW}^{-1}$ in figures 23(a) and (c)), as compared with case 2 where the EC-driven current is only about 0.8 A kW^{-1} (figures 23(b) and (d), note the different scales). In the latter case a large fraction of ECCD power is absorbed directly by trapped particles, which do not contribute to current drive. The ECCD efficiency even changes sign in case 2, which is a consequence of the ECRH

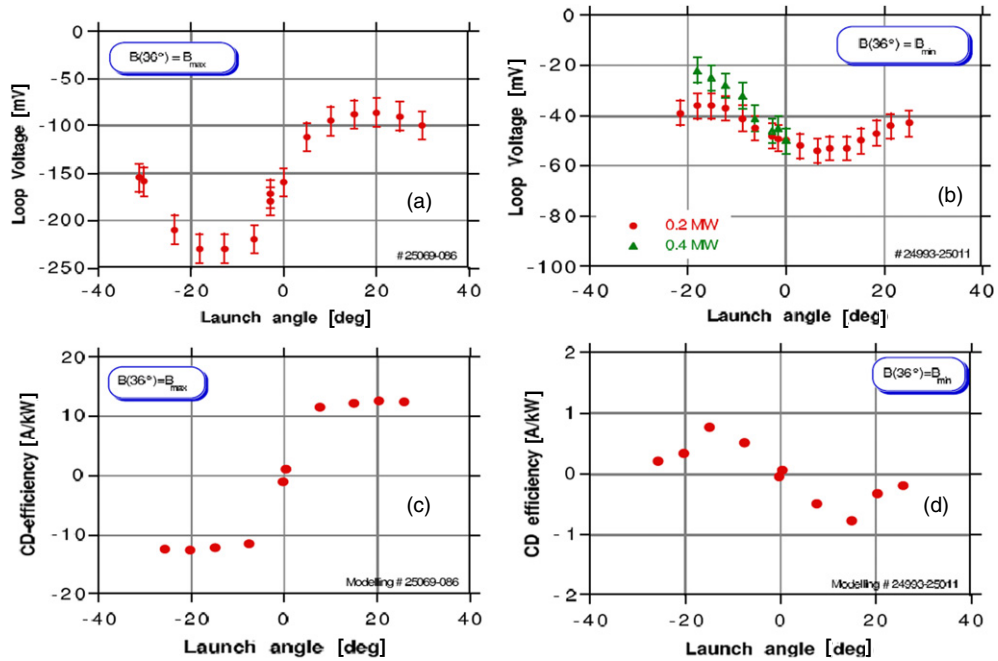


Figure 23. Effect of trapped particles on ECCD. (Top) Measured loop voltage versus launch angle with plasma net current $I_p = 0$ for magnetic field configurations with the maximum (a) and the minimum (b) of B located in the EC-launching plane. The ECCD power is 0.4 (triangles) and 0.2 MW (dots). (Bottom) CD-efficiency calculated from linear theoretical modelling for both cases (c), (d).

induced trapping of otherwise barely passing particles. The experimental results are well represented by the theoretical modelling as shown in figure 23.

Wave-particle interaction with either bulk or tail electrons can be investigated by comparing microwave launch from either the high field side (HFS) or the low field side (LFS). Basic features of the deformation of the electron distribution function are seen from figure 24 for wave coupling (X2-mode) from LFS (a) and HFS (b), respectively. In the HFS-launch scenario the power is preferably coupled to the less collisional suprathermal electrons. (This scenario is therefore sometimes considered as an ‘advanced’ scenario.) In W7-AS the current drive efficiency is, however, expected to be less than for LFS launch because some power is lost by momentum transfer to the trapped particles and even some current is driven into the reverse direction. This was confirmed by launching two independent 140 GHz beams with up to 0.4 MW power each from both the HFS and the LFS (Romé *et al* 2003) with an almost optimum launch angle of $\pm 19^\circ$. The total heating power is kept constant while switching one beam in the ctr direction stepwise from 0 to 200 kW and 400 kW and the other one in the co-direction from 400 kW down to 200 kW and 0 kW, respectively, as seen in figure 25. The bulk temperature and the integrated line density are comparable in both scenarios ($n_e = 3 \times 10^{19} \text{ m}^{-3}$, $T_e = 2 \text{ keV}$). Net current free operation was achieved with inductive compensation of both I_{ECCD} and I_b . In figure 25 the U_{loop} response for HFS and LFS ECCD is compared for two successive discharges. The experimental results confirm the theoretical expectations showing a slightly lower ECCD efficiency in the HFS case as compared with the LFS case with $I_{\text{cd}}^{\text{HFS}}/I_{\text{cd}}^{\text{LFS}} \simeq \Delta U_{\text{loop}}^{\text{HFS}}/\Delta U_{\text{loop}}^{\text{LFS}} \simeq 0.8$.

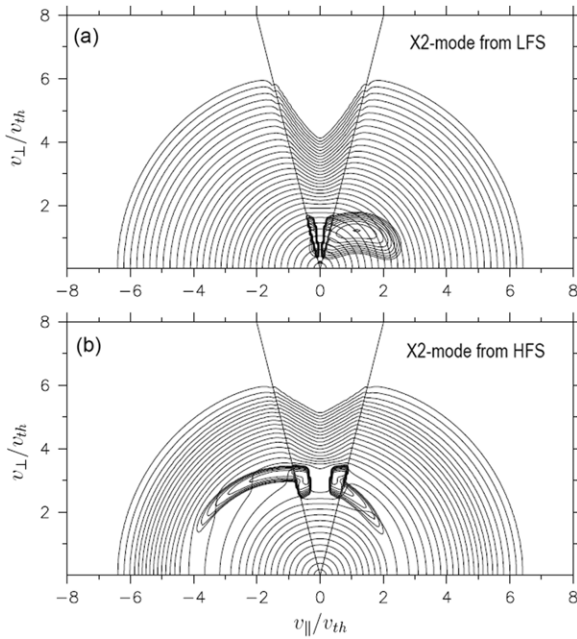


Figure 24. Contours of the electron distribution function, $f_e(v_{\parallel}, v_{\perp})$, together with the quasi-linear diffusion coefficient, $D_{\perp\perp}(v_{\parallel}, v_{\perp})$, as a function of the parallel and perpendicular velocities, v_{\parallel}, v_{\perp} (normalized to the thermal velocity, v_{th}) for a non-symmetric k_{\parallel} -spectrum of the microwave beam. The absorbed power density is 10 W cm^{-3} . The straight lines indicate the loss-cone (trapped electrons). (a) low field side launch with X2-mode; (b) high field side launch with X2-mode, $N_{\parallel}^{\text{hfs}} = N_{\parallel}^{\text{lfs}}$ (Romé *et al.* 2003).

4.1.7. Mode conversion heating and current drive via the OXB process. The standard ECRH scenarios have intrinsic density limitations by the cut-off condition. Higher densities are accessible with electron Bernstein wave (EBW) heating, which can be excited via the OXB mode conversion process (Laqua 2007). Its essential part is the conversion of an O-wave at oblique launch from the low field side into an X-wave at the O-wave cut-off layer (Preinhaelter and Kopecky 1973). The conversion requires an optimum launch angle of the O-wave with a corresponding parallel refractive index $N_{z,\text{opt}}^2 = Y \cdot (Y + 1)$ with $Y = \omega_c/\omega$, where ω is the wave frequency and ω_c is the electron cyclotron frequency. At this optimum launch angle the perpendicular refractive indices N_x of the O- and the X-wave along a wave trajectory in a density gradient are connected without passing a region of evanescence ($N_x^2 < 0$), as shown in figure 26. For non-optimal launch an evanescent region always exists near the cut-off surface, whose geometrical size depends on the density scale length $L = (\nabla n/n)^{-1}$. A considerable fraction of the energy flux can be transmitted through this region, if L becomes small (Mjølhus 1984), which is fulfilled in general for W7-AS density profiles. After the O-X-conversion the X-wave propagates back to the upper hybrid resonance (UHR) layer where the refractive index of the X-wave and the EBW are connected as shown in figure 26 and the X-wave converts into EBWs. The EBWs propagate towards the plasma centre where they are absorbed near the electron cyclotron resonance or, in the non-resonant case, by collisional damping.

Efficient OXB-heating with 70 GHz 1st harmonic EBWs was demonstrated for the first time in 1997 at W7-AS with both resonant and non-resonant fields (Laqua *et al.* 1997). Besides

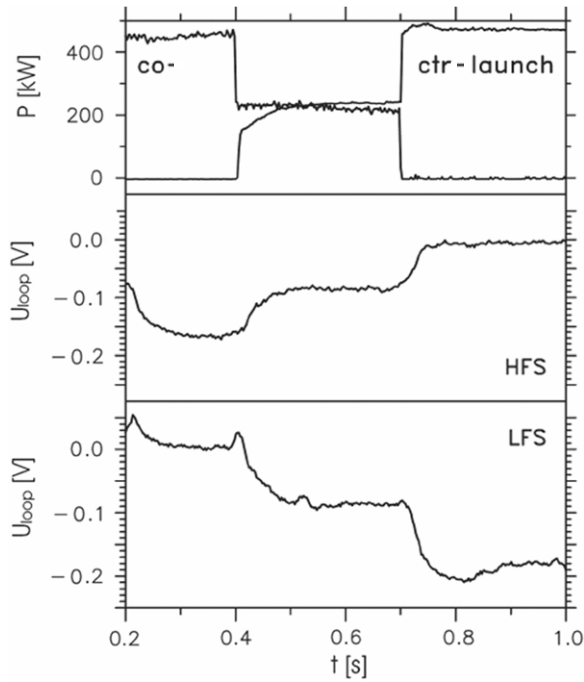


Figure 25. From top to bottom: time evolution of the power P of the two microwave beams in co- and counter-direction (the same for both HFS and LFS), and time evolution of the loop voltage, U_{loop} , for HFS (#49713) and LFS (#49714) launch, respectively. The time windows of pure co- (200–400 ms) and counter-launch (700–1000 ms) are indicated in the upper plot.

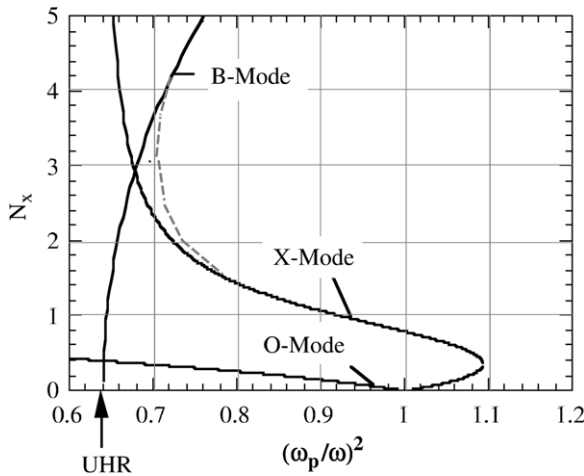


Figure 26. O-X-B conversion process at optimum launch angle showing the trajectory of the refractive index N_x of a wave travelling in a density gradient. The density gradient increases with increasing $(\omega_p/\omega)^2$ i.e. towards the right (Laqua *et al* 1997).

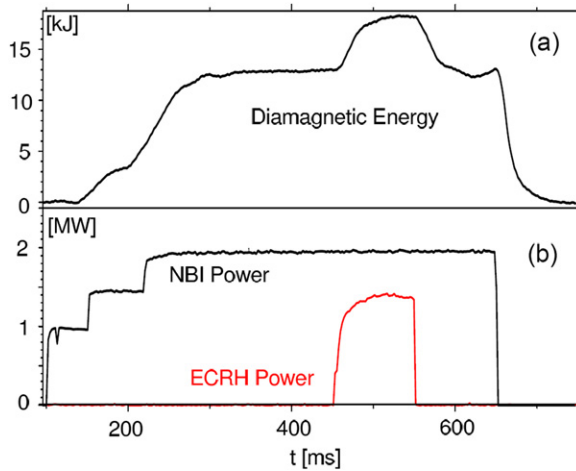


Figure 27. Total stored plasma energy (a) and heating power (b) as a function of time during electron Bernstein wave heating (140 GHz) at a density of $3.5 \times 10^{20} \text{ m}^{-3}$ and a magnetic field of 2.12 T (Erckmann *et al.* 2003).

the characteristic angular dependence of the O-X conversion also the parametric instability, which is typical for X-B conversion, could be verified experimentally.

An exploration of higher harmonic—and thus high density—OXB heating with 140 GHz EBWs became possible in a later state, where W7-AS was equipped with a divertor and the corresponding O-mode cut-off density of $2.4 \times 10^{20} \text{ m}^{-3}$ was achieved experimentally. At $B \leq 2.5 \text{ T}$ central rf-heating with 140 GHz EBWs requires an interaction with the 2nd or higher cyclotron harmonics and experiments were performed up to the 4th harmonic. An example with 2nd harmonic heating is shown in figure 27. Three 140 GHz beams with a total power of 1.5 MW were launched into an NBI sustained (up to 4 MW) high-density plasma (as much as $3.5 \times 10^{20} \text{ m}^{-3}$) (Erckmann *et al.* 2003). Central power deposition was achieved by tuning the magnetic field to 2.12 T. The central plasma temperature rises from about 270 eV to 310 eV during the EBW-heating and the temperature profile broadens. The plasma energy content increases during EBW-heating by about 40% and the EBW heating efficiency being comparable with NBI-heating. Since the plasma is optically thick for higher harmonic EBW, also third and fourth harmonic heating could be successfully demonstrated with 140 GHz at 1.5 T and 1.1 T, respectively (Laqua 2007).

EBW-current drive (EBW-CD) is expected to have a high efficiency, because the parallel refractive index of EBWs can become of the order 1 (Litvak *et al.* 1994) and first experiments were performed at W7-AS (Laqua *et al.* 1997). Since the CD efficiency scales with T_e/n_e experiments were performed at a reasonable low density of $1.05 \times 10^{20} \text{ m}^{-3}$ which requires 70 GHz first harmonic EBW-heating. An ECRH beam with 0.45 MW power was launched to a net-current free NBI (0.5–1 MW) sustained target plasma. The on-axis magnetic field was adjusted to 2.15 T for central power deposition. The large $N_z \approx 1$ component of the EBWs requires a stronger reduction of the resonant magnetic field than standard ECCD with electromagnetic waves. Net current free discharges with inductive compensation of the total plasma current are compared with discharges with zero loop voltage, where the plasma current can be measured directly as seen from figure 28. The plasma current rises to about 1.2 kA during the EBW application. CD-values derived from both methods agree well given the (large) experimental uncertainties while measuring the small plasma currents in the range of 0.1–1 kA

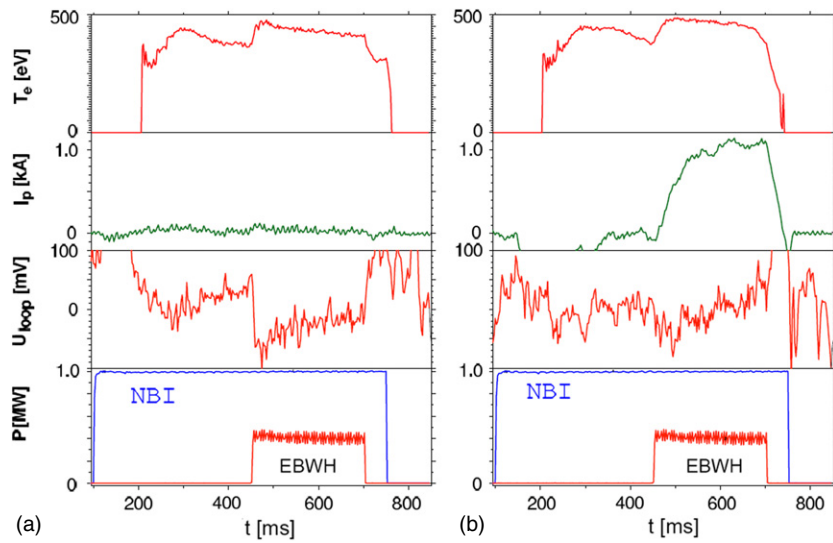


Figure 28. EBW-current drive at a plasma density of $1.1 \times 10^{20} \text{ m}^{-3}$. A net-current free discharge with inductive compensation of the EBCD current (a) is compared with a discharge with free running plasma current (b). The electron temperature T_e from SX-emission, the plasma net current I_p , the loop voltage U_{loop} and both the NBI and EBW-heating power are displayed as a function of time. Note that the plasma breakdown is delayed with respect to NBI switch-on in both cases and the I_p as well as U_{loop} cannot be interpreted on the basis of a well-defined plasma equilibrium in this phase.

in high-density plasmas. Additional experiments with co- and ctr-EBW-CD were investigated and a dimensionless CD-efficiency could be estimated for both the co- and counter-EBCD case (Laqua *et al* 2003a). The highest CD efficiency was measured in the case of co-EBCD, where a current of $1.8 (+1, -0.5)$ kA was derived from the experimental data with 0.45 MW input power.

The distortion of the electron distribution function and the resulting current for typical experimental parameters ($T_e \approx 0.7 \text{ keV}$, $n_e \approx 1.0 \times 10^{20} \text{ m}^{-3}$, $P \approx 0.45 \text{ MW}$ and $Z_{\text{eff}} \approx 1.5$) was obtained from Fokker-Planck calculations; an example is shown in figure 29. The calculated EBW-driven current is 2.5 kA, which is in fair agreement with the experimental data within the error bars. Due to the large parallel refractive index and the associated strong Doppler shift, the EC interaction takes place at more than twice v_{th} and the quasi-linear diffusion is located far away from the trapped electron loss cone. The perpendicular refractive index is about 40, which means that the wavelength is of the order of the gyroradius. In that case the quasi-linear diffusion operator splits into many maxima. The collisionality $\nu^* \approx 0.1$ and only tail electrons are in the long mean free path regime. The fraction of trapped electrons is about 0.2, but they do not participate directly in the wave interaction and the main mechanism for current drive is through the anisotropy of the distribution function as in standard ECCD theory.

4.1.8. Conclusions on ECRH/ECCD. A powerful ECRH and CD system is important for stellarator start-up, heating, density- and configuration control and is well suited for future steady-state operation of W7-X. Therefore strong effort was undertaken to improve the physics understanding of the wave-particle interaction in the complex magnetic configurations of W7-AS. The deposition profile as well as the wave propagation physics for different heating scenarios was studied in quantitative detail. The wave propagation and absorption is in general

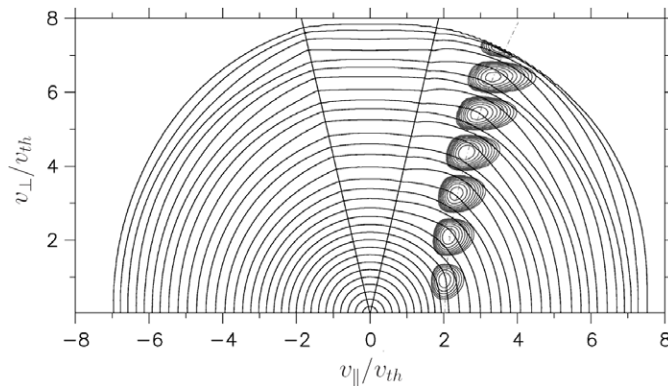


Figure 29. Contours of the electron distribution function, $f_e(v_{\parallel}/v_{th}, v_{\perp})$, together with the contours of $v^2 D_{pp}(v_{\parallel}, v_{\perp})$, as a function of the parallel and perpendicular velocities, v_{\parallel} , v_{\perp} (normalized to the thermal velocity, v_{th}) for EBW's (OXB scenario, low field side launch). The high collisionality inhibits the perturbation resulting from the loss-cone as well as the perturbation resulting from EBWCD ([Erckmann et al. 2003](#)).

well described by 3D ray tracing calculations. The deposition profiles are affected by the wave interaction with trapped particles in the long mean free path regime. The measured deposition profiles consist of a very narrow peaked component, which contains the main power fraction (70–100%) and is consistent with the ray-tracing results representing absorption by the thermal bulk of the electron distribution function. A second component contains up to 30% of the total power and is much broader and depends on the number and distribution of trapped particles. The direct and indirect (friction of passing particles with background trapped electrons) interaction of trapped particles with EC-waves also affects the current drive efficiency as measured in experiments with different magnetic mirror configurations and verified by CD-theory. The EC-wave interaction with different electron populations in velocity space was investigated by launching EC-waves from either HFS or LFS and a good theoretical understanding for the different wave-coupling and dissipation phenomena was developed. Sophisticated methods like heat wave excitation and perturbative current drive helped to improve the understanding of complex phase-space physics. An improved core confinement mode, the electron root confinement was discovered: the rapid loss of trapped particles generates strong positive electric fields in the plasma centre, which in turn improves the central bulk electron confinement, leading to electron temperatures of up to 6.8 keV.

Mode conversion heating and current drive via the O-X-B process were investigated experimentally. This heating scheme extends the ECRH application towards high densities beyond the cut-off density of the O-mode with no upper limit. Efficient OXB heating was demonstrated for the first time up to the fourth harmonic resonance at W7-AS. First EBW current drive experiments in over-dense plasmas were performed and good agreement with Fokker-Planck modelling is obtained.

As a consequence of the favourable W7-AS experience, an ambitious 10 MW, 140 GHz ECRH system operating in cw-mode ([Erckmann et al. 2007](#)) is under construction for W7-X.

4.2. Neutral beam heating

4.2.1. Introduction. NBI was designed as a ‘day one’ heating system for W7-AS, which is complementary to ECRH, as it does not depend on the magnetic field and inherently provides

particle fuelling during heating. The absence of a density limit like the cut-off density for ECRH qualifies NBI particularly as the heating method for high- β investigations. The 3 MW neutral beam heating system for W7-AS consisted of two injector boxes, which were equipped with four arc discharge sources each, operating up to 50 kV/25 A (hydrogen) or 55 kV/23 A (deuterium). The ratio of E_0 , $E_0/2$, $E_0/3$ species was 0.42 : 0.34 : 0.24 for a full neutral particle energy of $E_0 = 45$ keV (Speth 1989). The NBI-boxes were replicas of the ASDEX-system because the basic parameters were well matched to the W7-AS requirements. NBI took full advantage of the operational experience obtained at ASDEX (Feist *et al* 1984) and particular attention was given to develop a ‘clean’ NBI-system with a low impurity level of the beams (Ott *et al* 1983). Basic physics studies and first design considerations were already performed in a very early state of the W7-AS conceptual design (Lister 1985, Lister *et al* 1983). Near perpendicular injection in the elliptical plane would have led to a rather short plasma-beam interaction length, comparable to that of W7-A and high orbit losses would have to be accepted (section 4.2.2). Therefore the W7-AS coil configuration was designed with large corner-coils, which allowed the implementation of special ports for tangential NBI (see figures 4 and 7). Depending on the mounting position of the sources in the NBI-boxes a significantly increased absorption path length ranging from 2.5 m (inner sources) to 0.7 m (outer sources) was achieved. Accordingly, the deposited heating power varies for the different sources from 250 to 350 kW power per source. Plasma experiments started in 1988 with 1.5 MW injected power, where each NBI-box was equipped with 2 out of 4 possible sources and both boxes were arranged for balanced injection (Ott *et al* 1990, Penningsfeld *et al* 1991). The experiments aimed at balanced injection to minimize NBI-driven net-currents and the toroidal momentum transfer to the plasma (Hofmann *et al* 1994). In 1996 the NBI-power was upgraded to full capability with four sources per beam-line and the extraction voltage has been raised from 45 to 50 kV for hydrogen by regapping the extraction grids (Ott *et al* 1996, Penningsfeld *et al* 1996).

The experiments in the last phase of W7-AS operation aimed at investigating the β -limits under optimum confinement conditions with the highest heating power available (see section 10.2). Therefore in 2000 the system was modified for unidirectional (i.e. co- or counter only) injection of both NBI-boxes with a full installed power. This modification allowed an optimization of the heating efficiency, which is higher with co-NBI as compared with counter-NBI as discussed in section 4.2.3. Changing from full co- to full counter injection in this phase was performed by magnetic field reversal. Toroidal currents driven by unbalanced NBI were compensated by the inductive current drive to control the edge rotational transform. In the following sub-sections we review NBI-specific physics experiments such as kinetics for NBI and NBCD (section 4.2.2), NBI-power deposition (section 4.2.3), NBI driven radial electric field (section 4.2.4), fast particle physics (section 4.2.5), plasma start-up (section 4.2.6) and neutral beam current drive (section 4.2.7). Experiments with major contribution of NBI such as optimum confinement are presented in section 5.3; high- β physics is described in section 10, fast particle driven MHD and the direct measurement of the related fast ion losses are summarized in section 9.4.

4.2.2. Kinetics for NBI and NBCD. For calculation of the birth profile, the dominant losses channels, and finally global heating efficiency and heating profile, the 3D Monte-Carlo code FAFNER was developed (Lister 1985, Penningsfeld *et al* 1996). Starting from the field configuration, the measured T_e and n_e profiles and the beam parameters, FAFNER simulates the generation of the neutrals in the NBI boxes up to the ionization within the plasma, and the succeeding slowing-down of the fast ion population. The fast ion orbits are followed until thermalization or their escape from the plasma. This conventional approach is fairly CPU-time

expensive for long slowing-down times, i.e. at high temperatures. In an ‘advanced’ δf -Monte-Carlo technique (Schmidt and Werner 2003, Schmidt *et al* 2004), the simulation time can be much shorter than the slowing-down time without loss of accuracy (optimized technique for W7-X). In FAFNER, the equations of motion are formulated on a real space-grid of the magnetic field vector (i.e. not in magnetic coordinates) which requires an additional definition of the radial electric field and its gradient on the grid. With a simplified 1D distribution of neutrals, CX losses of fast ions can be included in the simulations. The birth profile of the fast ions represents the particle source, and the electron and the ion heating power density is obtained from the corresponding collision process (flux-surface averaged). In addition, the ion slowing-down contribution to the NB driven current can be calculated. The code saw several upgrades to treat different phenomena properly (Teubel and Penningsfeld 1992, 1994). The impact of first orbit losses on the radial electric field is calculated in Baldzuhn *et al* (2003b, appendix).

Neglecting the radial diffusion and the orbit losses, which are typically very small for the tangential NBI at W7-AS, a linear flux-surface averaged Fokker–Planck modelling can also be used. By taking simply the birth profile for the fast ion source, however, the difference of the deposition profiles for co- and counter-injection vanishes. The linear Fokker–Planck approach was used for estimating the fast ion distribution function. The electron Ohkawa current contribution was calculated in an adjoint approach both in the collisional (Hirshman 1980) and in the collisionless (Nakajima and Okamoto 1990) limit. Especially at low Z_{eff} , the friction with the trapped particles turned out to be important for the NBCD efficiency (Marushchenko *et al* 2002). Note that co-injection is defined such that the associated beam driven current increases the rotational transform. Due to the left-handed rotational transform of W7-AS this iota-increasing current is directed opposite to the beam direction, i.e. co-NBI is geometrically oriented opposite to a co-current of an equivalent tokamak case.

The fast ion distribution represents a source of free energy which can drive (kinetic) ion cyclotron instabilities. A kinetic stability analysis is performed in Shalashov *et al* (2003) for all NBI scenarios at W7-AS: perpendicular diagnostic NBI, tangential heating beams and oblique NBI (RADI). In addition, the full non-relativistic dielectric tensor for arbitrary distribution function is calculated.

4.2.3. Neutral beam-power deposition. The heating efficiency is determined by three major contributions, the shine-through losses, the charge exchange losses and the orbit losses. The main parameter that determines the shine-through is the line-integrated density $\int n_e \, dl$ along the beam path. Charge exchange losses depend on the penetration of the neutral gas into the plasma. Orbit losses resulting from the large gyroradii, in particular for smaller B -field strength and from the presence of inward shifted limiters, may strongly reduce NBI heating efficiency. Two mechanisms must be taken into account: besides prompt fast ion losses after a few poloidal rotations the pitch angle of ions may be changed during slowing down such that they are scattered into bad orbits and are lost on a the slowing-down time scale. However, for the W7-AS FAFNER code simulations showed that due to the nearly tangential injection ($(|v_{\parallel}|/v) < 0.75$) the heating ions are well confined (Kick *et al* 1996). Also for ions in the thermal bulk losses are negligible especially with the strong E_r observed in the gradient region of W7-AS. A similar result was obtained for ATF (Fowler *et al* 1991). In contrast, in W7-A the nearly perpendicular injection ($(|v_{\parallel}|/v) < 0.1$) leads to strong first orbit losses with *trapped* particles unless a negative or a positive radial electric field E_r develops such that the $E \times B$ drift results in a detrapping of the fast particles (Cattanei *et al* 1982, Penningsfeld *et al* 1985). The role of E_r in trapped particle confinement for W7-A and Heliotron-E is summarized in Hanatani and Penningsfeld (1992).

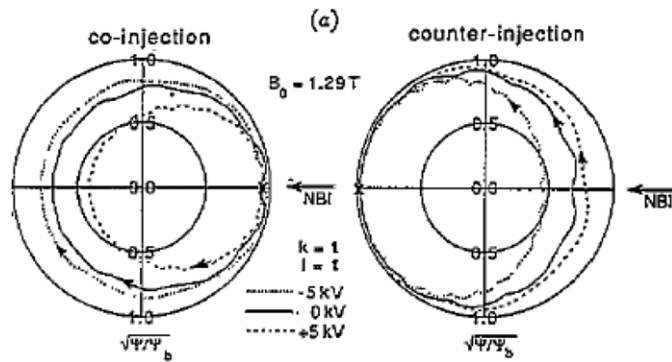


Figure 30. Projection of collisionless fast ion drift orbits onto a poloidal plane for typical initial kinetic ion energy $E_0/2 = 22.5$ keV, and counter-injection ($v_{\parallel}/v = -0.85$) and co-injection (i.e. $v_{\parallel}/v = +0.85$). Particles born outside the plotted drift orbits are due to prompt losses. Positive values of the potential increase the loss area for co-injection. The influence of the potential profile shape is less important than the overall potential strength V_0 (Teubel and Penningsfeld 1994).

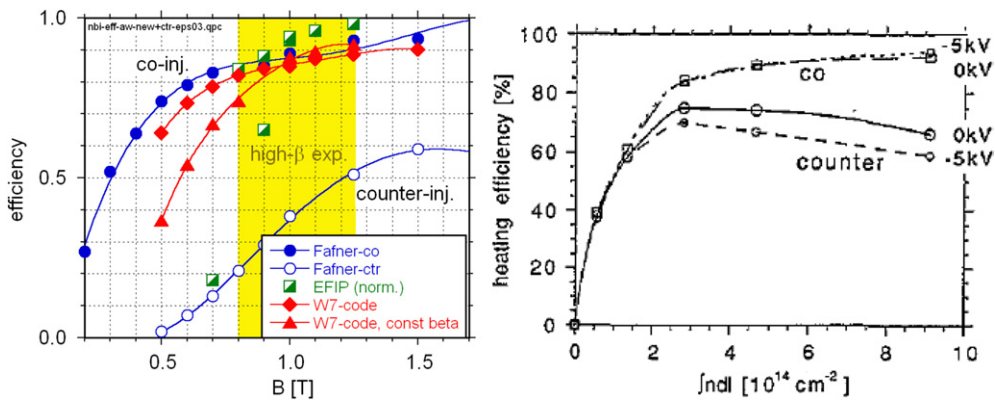


Figure 31. Calculated global heating efficiency for the co- and counter-sources. (Left) As a function of toroidal magnetic field. (Right) Dependence on the line-integrated density. For example a W7-AS shot series #13556 is taken assuming electric potential $V_0 = -5$ kV and 0 keV. Measured profiles show maximum $n_e(0) = 2.44 \times 10^{20} \text{ m}^{-3}$ and $T_e(0) = T_i(0) = 331 \text{ eV}$, $Z_{\text{eff}} = 1$, $B = 2.56 \text{ T}$ (Teubel and Penningsfeld 1994).

An example for drift-orbit calculations in W7-AS is shown in figure 30, details are given in Teubel and Penningsfeld (1994). Due to the nearly tangential injection all fast ions start as passing particles. For counter-injection statistically more drift orbits of the passing particles are shifted outward with respect to the flux surfaces than inward. Thus orbit losses play a stronger role for counter than for co-injection. Figure 30 also shows that even a relatively strong assumed electric potential of 5 kV does not change the orbit topology of fast passing particles significantly.

An example for the calculated global heating efficiency is shown in figure 31. For low densities shine-through losses dominate. Additionally, charge exchange losses are enhanced by the penetration of the neutral gas into the plasma. The efficiencies for co- and counter-injection are thus approximately equal at low densities. For high densities the orbit losses are the leading term as the fast ions are born preferentially at outer plasma radii (Penningsfeld *et al.* 1996).

Prompt orbit losses are small and almost independent (4–8%) from the density for co-injection. A substantial improvement by a finite E_r is therefore not possible. For counter injection the losses are larger because of the outward shift of the passing orbits with respect to the flux surfaces. It became obvious from these results that for high- β experiments, which inherently operate at high density rather than at high temperature, co-NBI would allow to make optimum use of the installed heating power. The different effective heating efficiencies were demonstrated experimentally (Ott *et al.* 1996, Jaenische *et al.* 2000). NBI was therefore rearranged (both injectors in co-direction) in the later phase of the W7-AS operation and balanced injection was given up in favour of higher heating efficiency.

The radial heating profile was determined by on-off modulation techniques of the NBI-power and measuring the radial propagation of the induced heat wave by ECE (Ott *et al.* 1998). This standard method, which proved to be a powerful tool with ECRH, becomes more complicated in the case of NBI, because the time scale for electron-heating is influenced by the slowing down time of injected particles, which varies radially. Taking this effect into account in the analysis restricts the experiment to low frequencies in the range 50–200 Hz. Good agreement between measured and calculated power deposition profiles was found, if only one beam was applied and modulated (Ott *et al.* 1999). A discrepancy between measured and calculated profiles was found in the plasma centre for heating scenarios with one stationary beam and a second one modulated (Rust *et al.* 2001), as well as for combined heating with 0.4 MW stationary ECRH and one modulated beam. Strong MHD activity was detected in the latter cases during the beam-on phase, which may explain the discrepancy (Rust *et al.* 2003).

4.2.4. NBI driven radial electric field. Physics studies to test the influence of a lost-orbit driven E_r on the gross-confinement and confinement transitions were performed with perpendicular injection using a separate nearly perpendicular oriented 0.5 MW NBI-system ('RADlal injector'). It was installed with slightly counter-orientated injection making use of the strong orbit losses of this direction (Rust *et al.* 2002, Baldzuhn *et al.* 2002, 2003b). The detailed results are described in Baldzuhn *et al.* (2003b). Total changes of up to -200 V cm^{-1} are obtained in the gradient region, with a temporal evolution dE_r/dt in good agreement with calculations. However, in most discharges E_r saturates soon such that the total effect remains small. A 10% increase of W_{dia} could be attributed to an induced confinement improvement, the additional heating effect of the RADlal injector could be neglected.

4.2.5. Slowing down and confinement of fast ions. NBI provides an experimental source to investigate the slowing-down processes as well as the confinement of fast ions in stellarators, which is of interest to extrapolate to the fast alpha particle in a stellarator reactor. Detailed studies with D-injection following the rise/decay times of fast particle fusion reactions after turn-on/turn-off of NBI were performed measuring the neutron rates with absolutely calibrated neutron counters for a large number of discharges with different plasma parameters and NBI power (Rust *et al.* 1995, 1997, 2000). The key point is the experimental determination of the fast ions density after the first orbit losses. As a major result, the relaxation process of injected ions was found to be in accordance with classical slowing down in W7-AS, at least for the period of one energy-relaxation time. The fast ions are confined in W7-AS at least over one energy relaxation time as long as MHD activity is absent. Fast particle driven MHD and the direct measurement of the related fast ion losses are summarized in section 9.4.

4.2.6. Plasma start-up with NBI alone. Plasma start-up and generation of a target-plasma for NBI was routinely performed by resonant rf-absorption using ECRH which restricts the

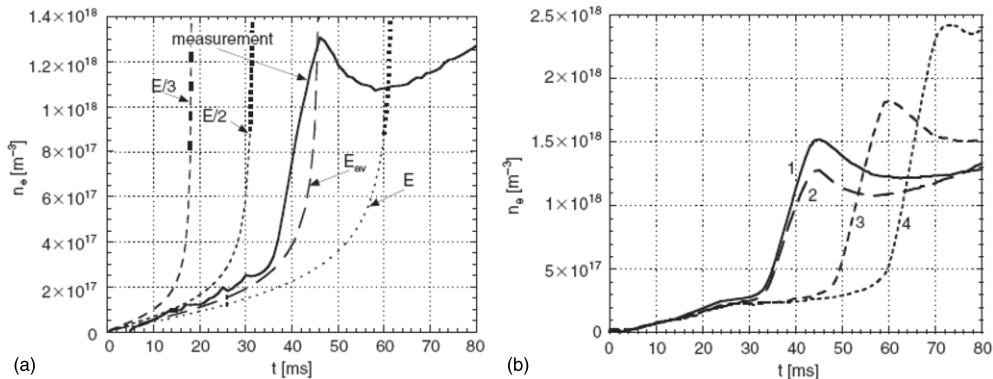


Figure 32. Time development of the density rise during plasma start-up with NBI. The turn-on time of the beams is at $t = 0$. (a) Comparison of the measurement (solid line) with theory for single species beams with energy E , $E/2$ and $E/3$ ($E = 32.5$ keV) and average energy E_{av} . (b) Sequence of pulses after wall cleaning pulse 1–4. The breakdown delay is shortest immediately after wall treatment (pulse no 1) (Ott and Speth 2002).

experiments to discrete magnetic fields. Non-resonant start-up assist was applied with a low power lower-hybrid system (10 kW) at 900 MHz, which allowed plasma generation at different magnetic field (Ballico *et al.* 1991). Even at such low power, the electron temperature in the generated plasma is sufficiently high that the plasma can serve as a target for neutral beam injection. The idea of plasma start-up with NBI alone at arbitrary magnetic field dates back to 1958 (Gibson *et al.* 1958). It took about 40 years until plasma start-up by beams alone was realized successfully in LHD (Watanabe *et al.* 2003). The key to building up the plasma is the achievement of an electron temperature, which is sufficiently high (3–5 eV) for ionization of the residual gas. The only source for energy transfer from the beams to the electrons is friction with fast ions, whereas electron cooling is mainly due to collisions with neutrals. An analytical model was developed to simulate the start-up conditions and successful experiments were performed following these theoretical guidelines (Jaenickke *et al.* 2002a). The neutral gas density must be kept as low as possible, until T_e starts rising above 3–5 eV. As soon as the electrons start participating in ionization, neutral gas can be added and the plasma density starts building up further. A careful control of the gas inventory and sophisticated wall treatment turned out to be necessary. As seen from figure 32(a), the model describes the measured time delay and density growth rate quite well. A strong influence of the wall conditions (cleaning discharges) on the breakdown delay was found as seen from figure 32(b). An electron heating power $<10^{-3} P_{NBI}$ (where $P_{NBI} = 1.6$ MW) is necessary to achieve start-up. This may explain why in the non-resonant start-up scenario the combination of a small rf-power below 10 kW is sufficient to assist plasma build-up with a beam power of only 400 kW under less favourable pressure and wall conditions.

4.2.7. Neutral beam current drive (NBCD). NBCD was derived from current balance analysis in net-current-free discharges. Based on measured profiles of n_e , T_e and T_i , the expected NBCD was calculated and compared with the bootstrap and the inductive current contributions estimated from DKES calculations. The ion current contribution was obtained from a Fokker–Planck code which assumes slowing-down on the flux surfaces. The electron Ohkawa contribution (due to momentum transfer from fast ions to electrons) was estimated in the collisional limit (Hirshman 1980) as well as in the collisionless limit

(Nakajima and Okamoto 1992). The effect of momentum transfer was also analysed in Solano *et al* (1998). In particular, at high collisionalities NBCD is very sensitive to Z_{eff} (for $Z_{\text{eff}} < 2$).

Low and high collisionalities have been analysed in detail. At low collisionalities and high temperatures with $B = 2.5 \text{ T}$, $n_e \approx 7 \times 10^{19} \text{ m}^{-3}$ and $T_e = 1.3 \text{ keV}$ the slowing-down time becomes approximately 10 ms (Marushchenko *et al* 2002). The collisionless approach for the electron Ohkawa current turned out to be reasonable and in fairly good agreement with the results derived from current balance. The radial profiles of the ohmic and the NBCD current are both fairly flat and partly cancel each other. At high collisionalities at very low temperatures in high- β discharges at low magnetic field, the collisional approach was applied, and again good agreement of the NBCD with the current balance was found (Geiger *et al* 2003) within the uncertainty of the Z_{eff} -profile.

4.2.8. Conclusion on NBI. A strong feature of NBI is the well established theoretical basis with respect to coupled power and its spatial distribution. A key element for the achievement of the high- β plasma regime with NBI at lower values of the magnetic field was the decision to give up balanced injection in favour of higher heating efficiency. An interesting new element in NBI physics is the non-resonant plasma start-up by NBI, a tool that may become particularly important for the next generation of stellarators.

4.3. Ion cyclotron resonance heating

4.3.1. ICRH system. An ion cyclotron resonance heating (ICRH) was installed from the very beginning applying up to two radio frequency generators with a nominal power of 2 MW and a frequency band of 34–110 MHz were used. They were connected via 50Ω transmission lines and a double stub-tuner network to the rf-antennas. Over the operation time of W7-AS three different rf-antennas were being operated. They were located either on the high- or on the low-field side of the plasma in the elliptical shaped cross-section where the magnetic field profile resembles that of a tokamak with a major radius of approximately 5 m.

The first antenna was of the conventional double strap type and located on the low field side and was successfully used to produce target plasmas for NBI discharges, thus relaxing the constraint of fixed field operation under ECRH (Ballico *et al* (1991), see section 4.2.3). Its shape was not adopted to the 3D plasma contour (Wesner *et al* 1988) so as not to limit the plasma aperture for any magnetic field configuration. This led to low coupling to the bulk plasma and increased the influence of the antenna electrical near field thus, no clear indications of plasma heating were observed.

The second antenna installed on the high field side was based on a novel ‘broad antenna’ concept. It was designed to reduce the parallel electric field, a probable culprit of generating an impurity influx into the plasma (Cattanei *et al* 1992). This antenna consisted of an assembly of 58 straight poloidal conductors that were fed in parallel at the top and the bottom in such a manner as to generate an almost sinusoidal toroidal variation of the poloidal rf-current. Thus the parallel electric rf-field in the vicinity of the antenna was reduced compared with a double strap antenna. This antenna unambiguously showed plasma heating with ICRH using the hydrogen minority absorption scenario. Also second harmonic hydrogen heating was shown in combination with NBI discharges. The heating efficiency was between 50% and 80%. However, the coupling of the antenna was poor; typically only half of the rf-power was radiated into the plasma (Cattanei *et al* 1996).

The third antenna was again of the double strap type, located on the high field side, but closely fitted to the 3D plasma shape. The heating efficiency was comparable to that of the broad

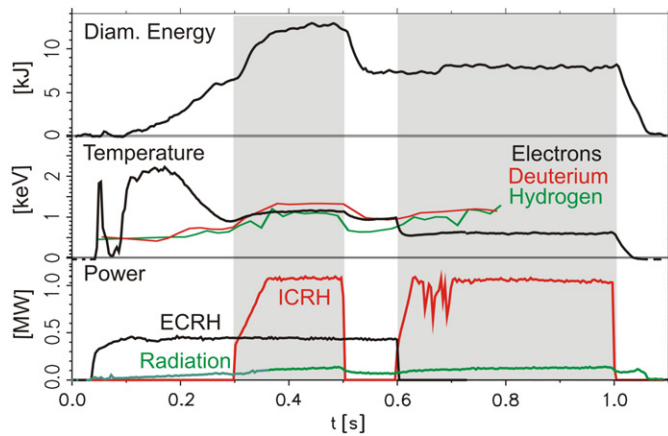


Figure 33. Discharge with ICRH in the hydrogen minority scenario.

antenna; the voltage standoff sufficiently high to apply as much as 1 MW of rf-power for several hundred milliseconds. Plasma heating and sustainment with ICRH as the only heating applied were possible for second harmonic hydrogen heating, hydrogen minority heating, hydrogen in deuterium mode-conversion heating and magnetic beach heating (Hartmann *et al.* 1998).

4.3.2. 2nd harmonic hydrogen heating. In second harmonic hydrogen heating the fast wave of frequency, ω , is absorbed near the resonance where $\omega = 2 \cdot \omega_H = 2eB/m_H$. The single pass absorption of the wave is approximately proportional to the plasma β .

Successful second harmonic heating was possible at $B = 1.25$ T and $B = 2.5$ T. The heating efficiency was derived from the increase in diamagnetic energy versus P_{ICRH} and use of the energy confinement scaling of W7-AS where P_{ICRH} is the total rf-power that is radiated from the antenna. The highest heating efficiencies of about 70% were obtained if the hydrogen resonance was located in the centre of the plasma and at high plasma β , as achieved with NBI target plasmas. The estimated single pass absorption in this case was about 25%. Reduced single pass absorption leads to stronger increases in the density during the ICRH phase, increased H_α radiation and increased signals of rf-pickup probes at the opposite toroidal location.

4.3.3. Hydrogen minority in deuterium heating. This is the heating scenario when both the hydrogen resonance and the two ion hybrid resonance are inside of the plasma. If the hydrogen resonance is located in the centre of the plasma, this requires the hydrogen concentration to be less than about 10% due to the large aspect ratio of W7-AS. In W7-AS such small hydrogen concentrations require preceding boronization of the torus walls with B_2D_6 since NBI is usually operated with H, and the graphite and the stainless steel walls constitute a large reservoir of hydrogen in the form of water.

A typical example (figure 33) demonstrates that ICRH was able to heat an ECRH target plasma and also to sustain the plasma on its own. The heating efficiency was as high as about 85% at rf-powers below 500 kW. At higher rf-powers the efficiency dropped. At these power levels also the hydrogen tail temperature did not increase any further due to increased fast hydrogen loss as measured with the fast particle loss detector. The highest hydrogen energies observed were about 50 keV. High heating efficiency was only obtained if the hydrogen

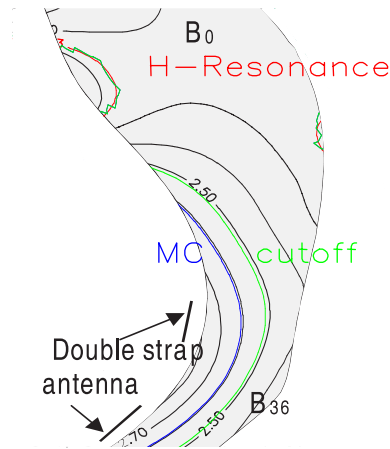


Figure 34. Horizontal cross-section of one half-module of W7-AS with $|B|$ contours in the magnetic mirror configuration where the $B = 2.5$ T ECRH resonance resides in the elliptical plane (bottom).

concentration was below 10%. Near steady-state conditions with rf-powers of 700 kW and discharges of up to 1 s could be obtained under these conditions.

4.3.4. Mode conversion heating. If the hydrogen concentration is increased further the distance between the fundamental resonance of hydrogen and the two-ion hybrid resonance becomes larger than the plasma radius. By lowering the generator frequency it is then possible to move the hydrogen resonance to the low field side outside of the plasma and have the two ion hybrid resonance in the plasma. This scenario is called mode conversion heating. The lowest frequency accessible to the rf-generators, 34 MHz, was used where at $B = 2.5$ T the hydrogen resonance is 8 cm outside the plasma in the horizontal midplane in front of the antenna and the two-ion hybrid resonance is located inside the plasma for hydrogen concentrations between 20% and 40%. The two-ion hybrid resonance is directly accessible from the high field side whereas from the low field side an associated cut-off requires wave tunnelling. Close to the two-ion hybrid resonance the fast wave can convert to an ion Bernstein wave which is then rapidly absorbed by electrons.

For hydrogen concentrations in the expected range plasma heating with heating efficiencies of about 80% was observed. From ICRH power modulation the power deposition profile was derived. The peak in the power deposition approximately agreed with the location of the hybrid resonance. The lossed particle analyzer detected some lost ions during the ICRH pulses but there was no significant change in the hydrogen flux measured with the CX analyzer.

4.3.5. Magnetic beach heating. In W7-AS the possibility to independently feed different sets of field coils allows the realization of a magnetic field configuration in which the field decreases toroidally away from the antenna in the elliptically shaped plane (high mirror configuration). In this heating scenario the two-ion hybrid resonance is inside the plasma while the hydrogen cyclotron resonance is outside the plasma in the antenna region, but enters the plasma at some toroidal location away from the antenna (figure 34). Since the group velocity perpendicular to the mode conversion layer approaches zero the fast wave can propagate toroidally towards decreasing magnetic field. Approaching the hydrogen resonance, it is converted into a slow wave (shear Alfvén wave). The slow wave finally is strongly damped on hydrogen via

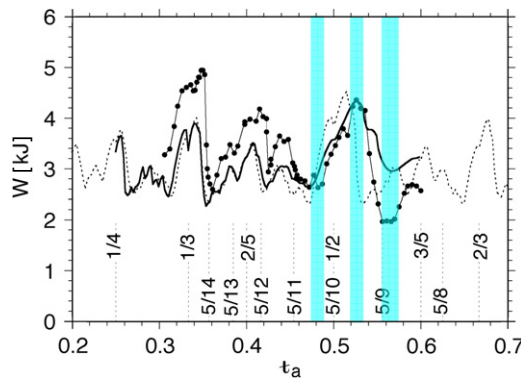


Figure 35. Variation of the plasma energy (symbols) with the boundary value of the rotational transform t_a in net current free discharges with $P_{\text{ECRH}} \leqslant 350 \text{ kW}$, $\bar{n}_e \cong 2.3 \times 10^{19} \text{ m}^{-3}$. The island divertor targets were not yet installed at the time of these experiments and the full available aperture of the vertically movable top/bottom rail limiters was used. Continuous and dashed lines show the calculated electron kinetic energy content obtained from the empirical transport model (see section 5.2) with the small shear in the vacuum field taken into account (full line) or not (dashed line). Vertical bars mark the operational range of the quiescent H-mode (see section 7.2).

cyclotron damping. In this scenario two different absorption mechanisms exist: absorption by electrons during mode conversion heating and absorption by hydrogen near the magnetic beach. The partition depends on the location of the hydrogen resonance and the hydrogen concentration. This mechanism could also explain the high hydrogen tail temperature observed during minority heating where the hydrogen concentration was too large to allow for significant wave tunnelling through the evanescent zone between the two-ion hybrid resonance and the associated cut-off before reaching the hydrogen resonance.

In this heating scenario it was possible to both heat ECRH target plasmas and sustain plasma by ICRH alone. In both cases high energetic hydrogen with energies up to 40 keV was observed, however, only if the hydrogen resonance was inside of the plasma. In the ICRH stand-alone plasma the hydrogen and electron temperature are approximately equal and both exceed the deuterium temperature. In addition the temperature ratio between the electron temperature and the hydrogen (bulk) temperature decreased with increasing magnetic mirror ratio.

The ICRH program stopped in 2000 when the installation of the divertor required the removal of the ICRH antennas.

5. Energy confinement

A characteristic feature of low-shear stellarators is the sensitive dependence of transport on the magnetic configuration for moderate plasma β and density. Figure 35 shows an extensive experimental scan of the edge rotational transform t_a (Jaenickke *et al* 1993) which nearly covers the complete range accessible in W7-AS, for early experiments see (Renner *et al* 1989, Ringler *et al* 1990). The example reveals the sensitivity of electron confinement to t_a in net current free discharges ($I_p = 0$) with low to moderate magnetic shear and low to moderate plasma densities $\bar{n}_e \leqslant 4 \times 10^{19} \text{ m}^{-3}$. Narrow ranges of maximum confinement exist close to the major rational values $t_a = 1/3$, $1/2$, and to a smaller extent $t_a = 2/5$. The optima are well separated by regions of degraded confinement where the plasma energy is smaller by a factor of up to 2. This dependence of electron energy transport on t and its gradient ∇t was

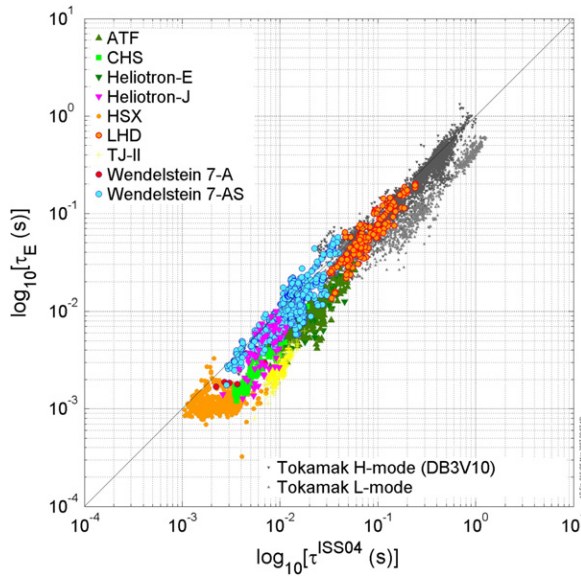


Figure 36. Scaling of experimental confinement times versus the ISS04. The coloured data indicate contributions to the International Stellarator Confinement Data Base. In grey data from the tokamak H-mode and L-mode scaling are shown for comparison versus the ISS04 prediction (Dinklage *et al* 2007a, 2007b).

already observed at the predecessors experiment W2-A (see section 1, figure 1) and W7-A (Grieger *et al* 1986, Wobig *et al* 1987).

This section first summarizes *global* energy confinement scalings performed in the t_a -ranges that allow for good confinement properties (section 5.1). In section 5.2 the impact of the magnetic configuration is discussed in detail concentrating on electron energy transport. Section 5.3 compares the results on *local* heat transport obtained from power balance analyses and perturbative methods with neoclassical expectations. Characteristics of turbulence and observations on turbulent transport are summarized in section 5.4. Earlier reviews comparing stellarator transport—with emphasis on W7-AS—with those of tokamaks have been given in Wagner and Stroth (1993), Stroth *et al* (1996a) and (Stroth 1998); early reports on W7-AS transport are Renner *et al* (1990), Kühner *et al* (1994).

5.1. Global energy confinement scaling

Helical systems cover a large magnetic configuration space which affects the 3D-specific neoclassical and possibly also the anomalous heat transport. Therefore, confinement time scaling laws for helical systems should be considered as a global reference only and predictions based on these intermachine, multi-configuration scaling have to be considered with caution (Yamada *et al* 2005, Dinklage *et al* 2007b, Yokoyama *et al* 2006). A comparison with tokamak scaling laws is possible only by replacement of the plasma current by magnetic field characteristics, in particular the rotational transform (Stroth *et al* 1996c).

The most prominent empirical scaling laws for stellarators are the ISS95/04 scalings (Stroth *et al* 1996c, Yamada *et al* 2005) where the latter, ISS04, shown in figure 36, is close to the parameter dependences of ISS95:

$$\tau_E^{\text{ISS04}} = (0.134 \text{ s}) \cdot a^{2.28} R^{0.64} P^{-0.61} n_e^{0.54} B^{0.84} t_{2/3}^{0.41}. \quad (5.1)$$

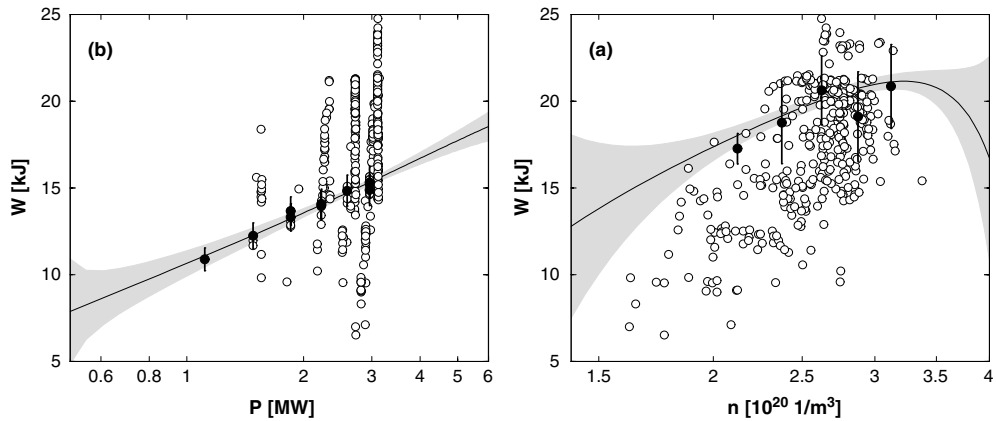


Figure 37. Energy content of W7-AS high- β data as functions of density (right) and absorbed power (left). The solid symbols indicate an experimental density scan ($P_{\text{heat}} = 3.1 \text{ MW}$, $B = 1.18 \text{ T}$, $a = 0.152 \text{ m}$) and a power scan ($\bar{n}_e = 2.4 \times 10^{20} \text{ m}^3$, $B = 0.95 \text{ T}$, $a = 0.154 \text{ m}$). Solid lines show the corresponding predictions of the ‘collisional high-beta model’ (Preuss et al. 2007) with the respective uncertainty (shaded area). The open circles show the set of all experimental data as they are employed for the predictive model irrespective of additional variations in \bar{n}_e , B , P_{heat} and a .

The global confinement time τ_E^{ISS04} is derived with a nonlinear regression of a power law in the volume preserving minor radius a in effective coordinates, major radius R (both in m), absorbed heating power P (in MW), line averaged mean electron density \bar{n}_e (in 10^{19} m^{-3}), the toroidal field B (in T) and $t_{2/3}$, the rotational transform at $r = 2/3 \cdot a$.

ISS04 is close to ideal gyro-Bohm scaling laws—in contrast to the Bohm-like one in tokamak L-mode confinement—and consistent with ion plateau scalings (Lackner and Gottardi 1990) as it applies to the tokamak H-mode. Gyro-Bohm scaling is in agreement with the assumption of transport being determined by processes which scale with local quantities only rather than with machine size.

Theory based scalings appear as an option for the extrapolation to reactor relevant scenarios. Moreover, for local transport it is possible to identify both anomalous and neoclassical first-principle mechanisms. The idea comprises a comparative test of confinement data against different theory based scaling power laws (Connor and Taylor 1977, Kadomtsev 1975, Preuss et al. 1999). This technique identified the so-called collisional low- β model as the most likely transport model for W7-AS low- β data (Dose et al. 1998b) and collisional high- β model as the most probable transport model for W7-AS high- β data (Preuss et al. 2007). Figure 37 shows the validation of high-beta theory scaling predictions with power and density scans.

From neoclassical transport, scalings for different collisionality regimes of ion and electron transport can be derived: for dominant ion heat transport the resulting ion plateau scaling (Lackner-Gottardi) is close to ISS04. With dominant electron heat transport (low density, ECRH heated electron-root discharges) the neoclassical scaling obtained from DKES calculations is supported by experimental density and power scans (Dinklage et al. 2007b).

5.1.1. Dependence of global W7AS confinement on scaling parameters.

Geometry. The major radius is fixed at $R \approx 2.0 \text{ m}$. The effective minor radius could be varied between $a = 0.12$ and 0.18 m . The sum of exponents of a and R indicates that τ_E

scales with volume. However, as already suggested by ISS95, the exponent of a is somewhat larger than two, while that of R is somewhat smaller than 1.

Magnetic field. Similarly to the scaling of geometric quantities, the scaling of τ_E with magnetic field strength corresponds to ion plateau scaling (Lackner and Gottardi 1990) predicting $\tau_E \propto B^{0.8}$ within the variability of technical regression approaches.

Rotational transform. The dominant fine structure in the t_a -dependence on the energy confinement time has already been described. Dedicated experiments at distinct optimum values ($t_a \approx 1/3, 1/2$) suggest an improvement of global confinement at higher values of the rotational transform (Brakel *et al* 1993). Using data collected in the t ranges with good confinement and minimizing the effect of the edge topology by an inward shifted limiter, $\tau_E \propto t_{2/3}^{0.4}$ is found (Yamada *et al* 2004), confirming ISS95. An unconstrained regression to the present data set of the international stellarator confinement database yields, however, a vanishing t -dependence (Dinklage *et al* 2007a); also the new LHD scaling does not show a significant dependence on t (Yamazaki *et al* 2003). It has to be noted that the statistical uncertainty of t -dependence is the largest amongst the different variables.

Power. Both in stellarators and in tokamaks the degradation of confinement time with heating power ($\tau_E \propto P^{-0.5}$) is a robust scaling feature of the energy confinement time τ_E . Examples for W7-AS are given in Ringler *et al* (1990), Stroth (1998). A significant dependence on the heating scheme was not found (Dinklage *et al* 2007a). Marginal dependences on the heating scheme were related to correlation effects in the data sets. Figure 37 shows the experimental results of a power scan.

Density. Stellarators show a distinct density dependence on τ_E up to the limit of $(1.5\text{--}2.0) \times 10^{20} \text{ m}^{-3}$. Unlike in tokamaks, this general density scaling appears to hold in larger devices as well, as results from LHD suggest (Yamada *et al* 2001). Figure 37(right), shows experimental results from a density scan. Indications for density saturation were, however, reported in Stroth (1998), Stroth *et al* (1995b) as well as in Dose *et al* (1998a), where a power-law ansatz was employed for taking saturation effects into account. These findings were obtained for discharges which suffered from impurity radiation at higher densities. The n_e -saturation disappeared at higher power, higher vessel carbon coverage and specifically in divertor operation. With divertor the plasma transited into the HDH regime where no density saturation was observed until detachment is achieved (Dinklage *et al* 2007a).

Isotopic mass. A distinct isotopic effect could not be revealed in global scalings in all accessible collisionality and β -ranges, neither with $T_e \gg T_i$ nor with $T_e \approx T_i$. However, some indications for a weak dependence were reported from dedicated studies performed with boronized walls (Stroth *et al* 1995b). From those investigations a dependence like $\tau_E \propto M^{0.2\pm0.15}$ was derived. This result could not be confirmed from global scaling studies in a broad database. Also no distinct dependence of the H-mode threshold on the isotopic mass could be obtained (Wagner *et al* 2005). This is different for the bifurcation to the HDH regime which was found to exhibit a different density threshold behaviour in deuterium discharges to that of hydrogen plasmas (see section 7.6, McCormick *et al* (2002)). In summary the isotopic mass dependence is different from tokamaks which exhibit a strong isotopic dependence in many confinement regimes. We note that for reversed shear conditions in advanced scenarios

Table 2. A survey of typical confinement parameters close to operational boundaries (not necessarily at the maximum value achieved) with some discharge for example.

Scenario	#	B (T)	a (m)	t_a	\bar{n}_e 10^{19} m^{-3}	T_e (keV)	T_i (keV)	W_{thermal} (kJ)	P_{abs} (MW)	τ_E (ms)	$n \cdot \tau_E \cdot T_i$ $10^{21} \text{ eV s m}^{-3}$
Max. fusion product	45791	2.5	0.186	0.345	11	0.7	$T_i \approx T_e$	20	0.33	60	4.6
Max. τ_E											
Max. T_e	49688	2.5	0.162	0.34	2	6.8	$T_i \leq T_e$	6.5	2	3.3	0.4
Max. T_i	31464	2.5	0.165	0.345	4.5	1.8	1.7	16	1.3	12	1.0
Detached divertor discharge	51321	2.5	0.12	0.56	35	0.40	$T_i \approx T_e$	16	1.3	12	1.7
Long attached discharge	54858	2.5	0.14	0.51 (5/10)	22	0.50	$T_i \approx T_e$	29	1.4	21	2.3
Maximum \bar{n}_e	53101	2.5	0.12	0.56	40	0.31	$T_i \approx T_e$	16	2.3	7.3	0.9
High β 1.25 T $\langle \beta \rangle = 2.4\%$	51385	1.25	0.151	0.51	24	0.36	$T_i \approx T_e$	21	3.1	6.8	0.6
High β 0.9 T $\langle \beta \rangle = 3.4\%$	56403	0.9	0.154	0.50	25	0.21	$T_i \approx T_e$	12.7	2.8	4.5	0.2

also tokamak confinement was reported to show a vanishing dependence on the isotopic mass ([Scott et al 1996](#), [Wagner et al 2005](#)).

Improved confinement regimes. In the so-called optimum confinement regime OC (see section 5.3) where the highest values of τ_E , T_i and $n \cdot \tau_E \cdot T_i$ are obtained, τ_E is enhanced with respect to the W7-AS subset of ISS95 data by up to a factor of 2 and by up to a factor of 2.5 with respect to the ISS95 scaling itself. W7-AS was the first non-tokamak to operate in the H-mode (see section 7). If a quiescent H-mode is reached, τ_E increases by up to a factor of 1.65. In the ELMMy H-mode the energy confinement time exceeds that in the preceding L-mode by up to a factor $\tau_H/\tau_L \cong 1.3\text{--}1.5$. In the HDH regime, the confinement is superior by a factor of 1.5–2 with respect to normal confinement (NC) (section 7.5). For examples see ([Wagner et al \(2005\)](#), figure 15).

Operational limits. Comparison of confinement data at operational limits (maximum T_e , T_i , n_e , β , τ_E , at detachment and for the best steady-state discharge) with the international stellarator scaling, the W7AS scaling, the Lackner–Gottardi scaling and the tokamak ELMMy H-mode scaling (IPB98(y,2)) demonstrates no striking degradation of confinement at those limits ([Wagner et al 2005](#)). An exception is the high density case for obvious reasons because enhanced edge radiation reduces the effective plasma radius. Rephrased to dimensionless parameters, the scalings are between Bohm and gyro-Bohm scaling but closer to gyro-Bohm. A survey of confinement parameters close to operational boundaries is given in table 2.

5.2. Impact of rational surfaces and magnetic shear on electron energy transport

Extensive efforts have been made at W7-AS to get more insight into the sensitive dependence of anomalous electron energy transport on rotational transform t and magnetic shear ∇t . The low-shear design of Wendelstein stellarators is ideally suited to probe separately both the t - and ∇t -dependence in discharges with small and large net plasma current I_p , resulting from the superposition of bootstrap current I_b , transformer driven inductive current I_{OH} and, optionally, ECRH and NBI driven currents.

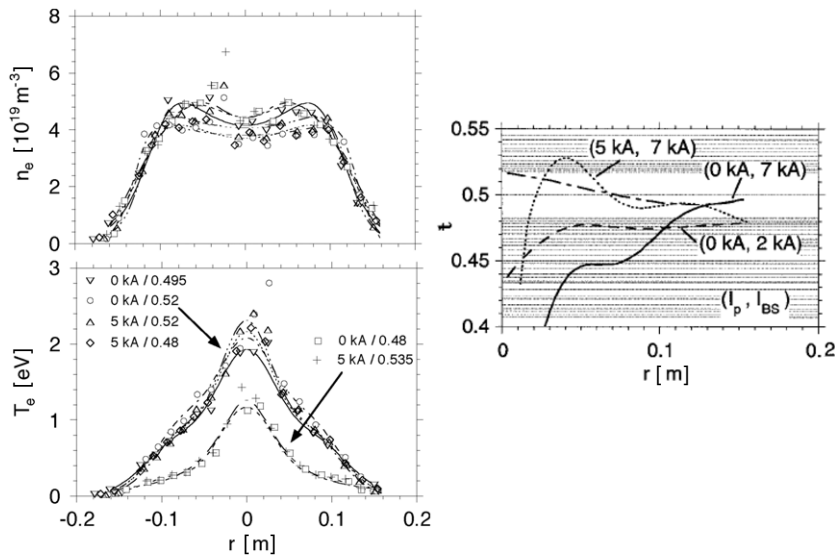


Figure 38. (Left) n_e - and T_e -profiles at degraded and optimum confinement using discharges from the scans in figure 39, for example (Brakel *et al* 1997). (Right) Calculated ι -profiles for the same discharges. Plasma current and bootstrap current are indicated in brackets. The rational values m/n , $m \leq 30$ are given as horizontal lines for reference.

For these studies electrons were selectively heated by ECRH ($P_{\text{ECRH}} \leq 450 \text{ kW}$) at plasma densities $n_e \leq 4 \times 10^{19} \text{ m}^{-3}$, where collisional energy transfer to the ions is small. As in tokamaks, electron energy transport at the plasma edge appears to be anomalously enhanced as compared with the neoclassical prediction. The current was inductively controlled to $I_p \leq 30 \text{ kA}$ where Ohmic heating may be neglected. The plasma pressure $\beta_0 < 1\%$ is sufficiently low that Pfirsch–Schlüter currents have only a small influence on the ι -profile (Renner *et al* 1992).

The extensive experimental scan in figure 35 nearly covers the complete range of rotational transform accessible in W7-AS. The additional overall decrease of the plasma energy observed towards high values of $\iota_a > 0.4$ is attributed to a topological effect, i.e. to the reduction of the effective plasma radius by the appearance of the large natural $5/m$ islands at the boundary with $m = 9, 10$ and 11 (see section 2, figure 5 and Kocsis *et al* (1995)). The global confinement variations with the edge rotational transform ι_a correlate with changes in the local electron energy transport as it is apparent from the measured T_e -profiles in figure 38. In contrast, the density profiles appear to be very robust. The latter is attributed to feedback control of the line-integrated density that causes enhanced particle losses to be replaced by enhanced gas puffing. Dedicated particle transport studies, however, show that the particle diffusivity at degraded and optimized confinement differs by a factor of 2 (Heinrich *et al* 1997). Furthermore, transient changes of the density profile are observed in experiments where the rotational transform is shifted dynamically across the critical values, e.g. by ramping or modulating the plasma current (Brakel *et al* 1997, Heinrich *et al* 1997, Zoretnik *et al* 2002). The transition is smooth, no H-mode like bifurcation can be observed.

This strong configuration dependence is, however, smeared out if sufficient positive or negative shear is introduced by the pressure driven bootstrap current or by running inductive or EC driven currents (Ringler *et al* 1990, Erckmann *et al* 1995b, 1996). Figure 39 shows the result of the variation of both ι_a and I_p with ι_a in the vicinity of $\iota_a \approx 0.5$ (Brakel *et al* 1997)

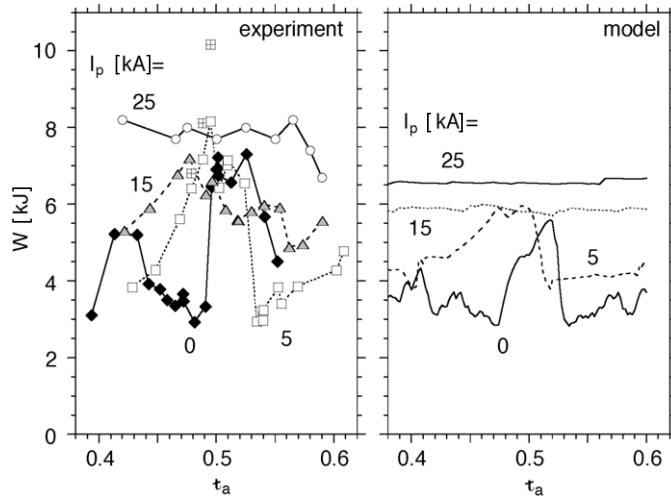


Figure 39. (Left) Measured W_{dia} and calculated electron kinetic energy content (right) from the empirical model versus t_a for various net plasma currents I_p . ($P_{\text{ECRH}} = 450 \text{ kW}$, $\bar{n}_e = 4 \times 10^{19} \text{ m}^{-3}$). For details see Brakel *et al* (1997), Brakel and W7-AS Team (2002).

and reduced limiter aperture to weaken the effect of natural boundary islands. By increasing the magnetic shear via the plasma current, the strong dependence of confinement on t_a ($I_p = 0$) is smoothed ($I_p = 5$ and 15 kA) and finally lost ($I_p = 25$ kA). The OH-power (<10 kW) in any case can be neglected as compared with ECRH power. Remarkably, with high currents the confinement levels at the maximum for any t_a indicating a beneficial role of magnetic shear applied by the plasma current. The sign of shear has no influence (Erckmann *et al* 1996).

Local power balance analysis (figure 40) shows that with increasing shear the electron heat conductivity χ_e^{PB} is strongly reduced in the gradient region $r \geq 5 \text{ cm}$ (by a factor of up to 5 in figure 40). In parallel, neoclassical transport displayed by χ_{neo} becomes larger throughout the volume since in the prevailing $1/\nu$ -regime the neoclassical heat conductivity increases with $T_e^{7/2}$. Both effects—reduction of anomalous transport and rising neoclassical transport—result in an increasingly large central region where most a large amount of the electron heat transport is carried by neoclassical fluxes. Towards the boundary, i.e. $r > 10 \text{ cm}$, transport remains anomalously high even with high shear. Consistent results are obtained at lower density, $n_e = 2 \times 10^{19} \text{ m}^{-3}$ (Erckmann *et al* 1996).

A simple empirical model (Brakel *et al* 1998), refined in (Brakel and W7-AS Team 2002) assumes that transport is enhanced at rational surfaces, e.g. by MHD activity or turbulence, and that this enhancement is reduced by magnetic shear, e.g. by decorrelation of turbulent structures. The favourable confinement close to low-order rational values of t_a corresponds to the particular property of the low-order rational numbers that their vicinity is rarefied with respect to the density of rational numbers m/n if the size of mode numbers is limited (see figure 38(right)). For the purpose of modelling neoclassical heat conductivity χ_{neo} , j_{OH} and j_{BS} are approximated by neoclassical expressions and the anomalous heat conductivity is obtained from scaling law (Ringler *et al* 1990). For simplicity each rational surface is assumed to contribute to transport with the same amplitude and only once irrespective of its degeneracy and an upper limit $m \leq m_{\max}$, are assumed. For details see Brakel and W7-AS Team (2002).

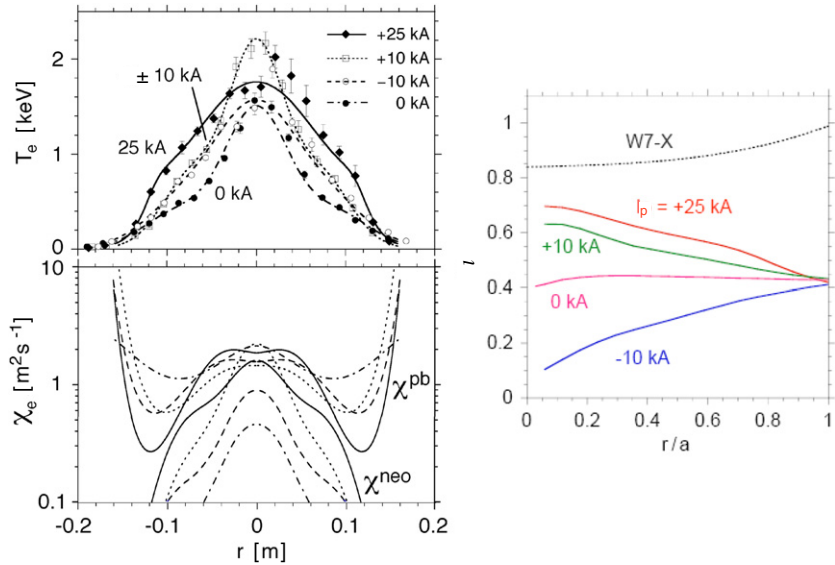


Figure 40. T_e -profiles (top) and profiles of the electron heat conductivity derived from power balance χ_{PB} and from neoclassical calculations χ_{neo} for four selected discharges at $t_a = 0.42$ but with different ohmic plasma currents: 0 kA (dash dotted line, low shear, poor confinement), +25 kA (continuous line), +10 kA (dotted line), -10 kA (dashed line) (Brakel *et al* 1997). The corresponding q -profiles are shown on the right side.

This model reproduces the experimental t -dependence of global confinement in net current-free discharges, as shown in figure 35, where the calculated electron kinetic energy is plotted together with the measured diamagnetic plasma energy. The exact positions of the confinement maxima are recovered provided the small shear of the external rotational transform $t_{ex}(r)$ is taken into account (figure 35, full line). For $t_a < 0.4$ the difference between measured plasma energy and calculated electron kinetic energy can be accounted for by the ion contribution ($T_i = 450$ eV and 280 eV for high and low confinement, respectively). For $t_a > 0.4$ the plasma radius decreases due to the 5/m islands (see section 2), whereas a constant value is used in the calculation for the full t_a -range. The dependence of global confinement on the net plasma current is reproduced by the model as well (figure 39, right, Brakel and W7-AS Team (2002)).

The empirical model of electron energy transport in W7-AS makes no assumptions about the detailed physical processes involved. It is suggested that transport is enhanced due to resonant modes at rational surfaces which do not exist close to low order rational values of the rotational transform if an upper limit is claimed for the relevant mode numbers. Fluctuation measurements show that the spectrum of small scale density turbulence strongly correlates with confinement. For details and references see section 5.4.2. Also large scale quasi-coherent MHD oscillations (Zoletnik *et al* (2005a) and section 5.4.2) located near rationals and excited, e.g., by small transport events show a dedicated dependence on t (Zoletnik *et al* 2002). However, as no correlation between their amplitude and confinement exists the quasi-coherent oscillations display the modifications in the profiles of $t(r)$ and $v_{E \times B}(r)$ rather than being themselves relevant for transport.

The argument of finite gaps in the density of finite- m resonant surfaces is a key element in theories on *ion* turbulence and on the formation of ion transport barriers at minimum

q -surfaces (Garbet *et al* (2001) and discussion in Candy *et al* (2004)). It is not clear if the arguments given there for ion turbulence also apply to electron transport. In particular electron transport in W7-AS is reduced by both positive and negative magnetic shear, whereas only negative (in the tokamak sense) or low shear is favourable to reduce ion transport in tokamaks. Evidence of sheared electric fields in the proximity of low-order rationals has been reported from the stellarators LHD (Ida *et al* 2002) and TJ-II (Estrada *et al* 2005, 2007). In tokamaks electron heat transport barriers have successfully been described by a ‘ q -comb’ model (Hogeweij *et al* 1998), which postulates a *reduction of transport* near low order rational surfaces (RTP, Lopes-Cardozo *et al* (1997), JET, Schilham *et al* (2000), TEXTOR-94, Schüller *et al* (2000)). In summary, a physics understanding of the processes that determine radial transport processes at or near rationals is still missing despite the fact that empirically successful heuristic models exist.

Radial profiles of discharges at identical boundary value t_a but different plasma currents are compared in figure 38. For the example given good confinement is obtained with $I_p = 5$ kA where the rotational transform resides within the narrow ‘resonance free’ region around $t_a = 1/2$ over a wide radial range (right). In contrast, $t(r)$ remains below this region for the low-confinement case achieved with $I_p = 0$ kA.

When the constraint of a fixed net current $I_p = I_{BS} + I_{OH}$, which defines the boundary value of the rotational transform is relaxed, i.e. $I_{OH} = 0$ and $I_p = I_{BS}$, current and rotational transform self-consistently couple to confinement which may bifurcate: high confinement sustains a correspondingly high bootstrap current which produces magnetic shear, thereby reduces transport and shifts the rotational transform away from an unfavourable vacuum field value. With low confinement the bootstrap current is not sufficient to achieve this. Such behaviour has been predicted by the transport model discussed above and is evident in the sequence of discharges at external $t_a = 0.45$ shown in (figure 41) where the plasma current is first ramped to various initial values I_{p0} by the transformer and, after a flat top phase, the external loop voltage is switched off allowing the plasma current to evolve freely. The discharge bifurcates towards low or high confinement at a critical initial current, for details see Brakel and W7-AS Team (2002).

5.3. Local heat transport

Representative examples for local power balance analysis and their comparison with neoclassical predictions have been shown in figures 12 and 13. Experiments with dimensionally similar discharges (Stroth *et al* 1993c) show that in W7AS transport has gyro-Bohm like parameter dependences indicating a more local behaviour as expected from the global scaling laws (see section 5.1). With a proper choice of the magnetic configuration, temperatures in the plasma centre can become sufficiently high that the elevated neoclassical fluxes prevail anomalous ones and the observed ion and electron heat transport can be explained neoclassically. At lower temperatures obtained for poorer confinement conditions and also generally at the plasma edge anomalous transport dominates. A key quantity is the radial electric field although it is not an external control parameter but depends on *thermal* and *heating driven* fluxes as discussed in section 3.3. For the ambipolarity condition for the radial fluxes two solutions are possible, namely electron-root conditions which may be realized in the plasma core (section 5.3.1), and ion-root conditions (section 5.3.2) which can be realized in the core but generally dominate at the plasma edge.

5.3.1. Electron-root conditions in the plasma core. For discharges with strongly localized central ECRH power deposition and high power densities P_{ECRH}/n_e a pronounced steepening

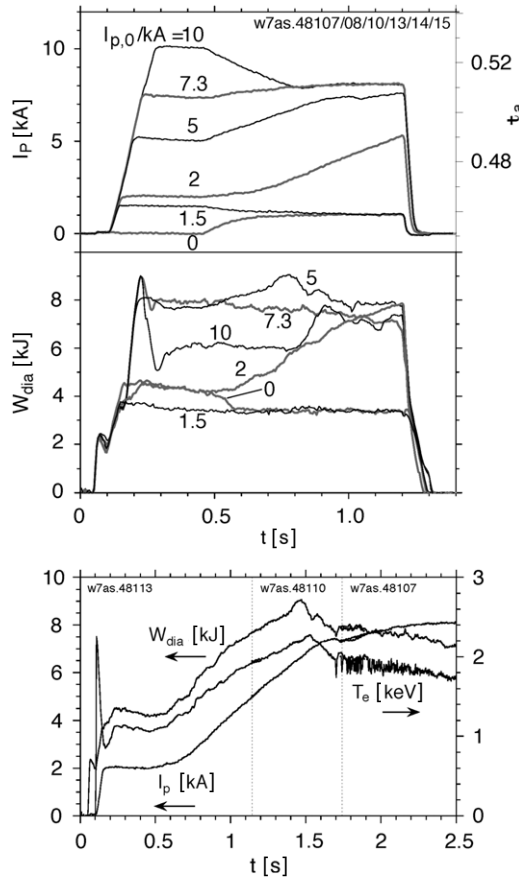


Figure 41. Evolution of plasma current (top) and diamagnetic energy (middle) for discharges with initial current control at levels I_{p0} and free running current after the external loop voltage is switched off at $t = 0.5$ s. Traces are labelled by the initial current. When starting from close to the bifurcation current the stationary high confinement regime with a bootstrap current of 8.1 kA cannot be reached within a single discharge time of W7-AS. Therefore, the expected full evolution from low to high confinement of W_{dia} , I_p and central T_e (from ECE) has been constructed from the data of the three discharges at $I_{p0} = 2, 5, 7.3$ kA by shifting their time scales such that the traces continuously match (bottom frame). The transient confinement optimum at 1.5 s is explained by a low shear t -profile and levels off when $t = 1/2$ enters the plasma from the edge. The mode activity which is evident from the central electron temperature channels correlates with the occurrence of $t = 1/2$ at $r \approx 5$ cm. ($P_{ECRH} = 400$ kW, $\bar{n}_e = 4 \times 10^{19}$ m $^{-3}$, $t_a = 0.45$).

of the temperature gradients evolves in the centre as shown in figure 17. The feature is common to helical systems as summarized in Yokoyama *et al* (2006, 2007), Wagner *et al* (2006). In small devices like W7-AS the energy loss for these conditions is dominated by the electrons and the ions are energetically almost decoupled resulting in $T_e(r) \gg T_i(r)$. An example of radial profiles is given in figure 12. The associated low electron heat diffusivities can be explained only if strongly positive values of E_r resulting from electron-root conditions of ambipolar neoclassical particle fluxes are taken into account (Maaßberg *et al* 2000b, Kick *et al* 1999). At low to density, the neoclassical electron heat flux in the electron-root region (calculated from the traditional neoclassical ordering) is significantly smaller than the one from power balance (figure 12 (lower right)). Reasons may be diagnostic limitations which enter the analysis e.g. for

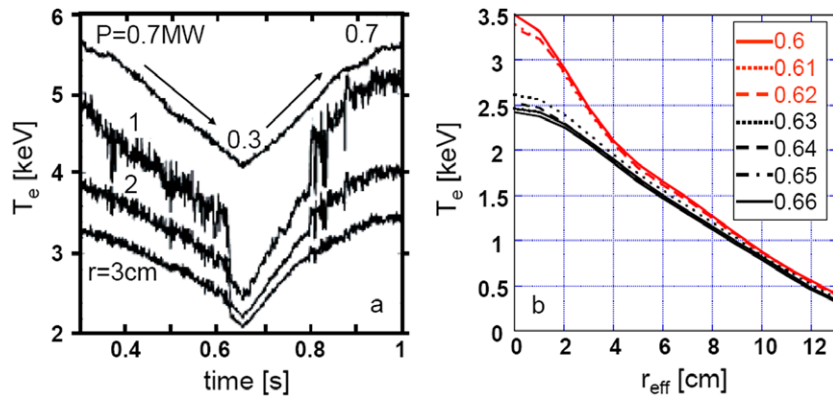


Figure 42. (Left) T_e -traces (from ECE) in a continuous power scan (uppermost trace) ([Stroth et al 2001](#)) with transition and back-transition from electron-root to ion-root. The power varies from 0.7 MW to 0.3 MW and back. The radii of the T_e -channels are given. (Right) T_e -profiles at the electron- to ion-root transition at 0.62 s plotted in 10 ms steps ([Wagner et al 2006](#)).

Z_{eff} or anomalous flux contributions or the complexity of the neoclassical analysis in the lmfp itself. In particular the traditional neoclassical approach—based on the gradient of the Maxwell distributions as the thermodynamic forces driving transport—is not sufficient to describe the highly peaked ECRH scenarios at low density as discussed in [Maaßberg et al \(2000b\)](#). At higher densities this discrepancy reduces ([Romé et al 2006](#)).

The positive electron-root was anticipated as driven by radial *thermal* particle fluxes alone ([Maaßberg et al 1993b](#)). However, convective fluxes of (ripple-trapped) supra-thermal electrons directly driven by ECRH ([Murakami et al 1998](#)) contribute to the positive E_r as can be shown by a modification of the mirror ratio ([Maaßberg et al 2000b](#)). The same conclusions can be drawn from a comparison of O₁- and X₂-mode ECR heating (see section 4.1.3 for details of these heating schemes): for X₂-mode heating with significant absorption of ripple-trapped electrons strong electron-root features with centrally peaked T_e -profiles are observed. The electron-root T_e -peak is less developed under O₁-heating conditions where only passing electrons absorb the EC power ([Romé et al 2006](#)).

Owing to the high ECRH power density available in W7-AS, the electron-root was established up to densities $\bar{n}_e = 7 \times 10^{19} \text{ m}^{-3}$. Typical values to reach electron-root conditions are $\bar{n}_e < 4 \times 10^{19} \text{ m}^{-3}$ in a density scan at $P_{\text{ECRH}} = 1.3 \text{ MW}$ or $P_{\text{ECRH}} > 0.4 \text{ MW}$ in a power scan at $\bar{n}_e = 2 \times 10^{19} \text{ m}^{-3}$ ([Maaßberg et al 2000a](#)). The attainable central $T_e(0)$ decreases with increasing \bar{n}_e and decreasing ECRH power (see figure 17). At $P_{\text{ECRH}} = 2 \text{ MW}$ and $\bar{n}_e = 2 \times 10^{19} \text{ m}^{-3}$, a maximum central value of $T_e(0) = 6.8 \text{ keV}$ was reached. However, one of the possible merits of the electron-root, the predicted strong outward convection for impurities driven by the positive radial electric field, could not be verified experimentally.

The electron-root shows a threshold behaviour. If the ECRH power is continuously scanned down (up) the transition to the electron-root occurs as a sudden drop (increase) of the core temperature where the central T_e changes by nearly 1 keV. Moreover a hysteresis in core ambipolarity both in power and in temperature is observed (figure 42) ([Stroth et al 2001](#)). Both observations are in agreement with the neoclassical expectation of a thermodynamically forbidden zone between electron and ion branch. Rapid sequences of forth and back-transitions are observed for conditions close to the threshold, i.e. at reduced P_{ECRH}/n_e ([Kick et al 1999](#),

[Stroth et al 2001](#)). They can be explained by limit cycle oscillations resulting from a strong (outward) Shafranov shift due to a very low central t -value under these conditions and a simultaneous (inward) shift of the absorption layer ([Fuchs et al 2001](#)). The latter reduces the power density in terms of P_{ECRH} divided by the number of heated particles such that the system falls below the threshold and the cycle is completed. It has been noted that the neoclassically generated $E \times B$ shear-flow layer between electron- and ion-root regions has the potential to decorrelate turbulence and thus build an internal transport barrier which also could result in the observed threshold behaviour, hysteresis and dithers ([Stroth et al 2001](#)). A reduction of turbulent activity has been observed in other helical devices (see [Wagner et al \(2006\)](#), [Yokoyama et al \(2006\)](#)). At W7-AS with increasing P_{ECRH}/n_e the poloidal coherence length of temperature fluctuations \tilde{T}_e/T_e decreases together with an increasing velocity shear as measured with the same diagnostic ([Bäumel et al 2003b](#)). For a discussion of a possible ∇E_r -related reduction of turbulent transport on top of an E_r -reduced neoclassical one see [Stroth et al \(2001\)](#), [Wagner et al \(2006\)](#).

5.3.2. Ion-root conditions and the optimum confinement regime (OC). Ion-root conditions with moderate negative or slightly positive E_r are expected in the plasma interior at higher densities with $T_e \approx T_i$ and $\nabla T_i \neq 0$. In the edge region with stronger gradients ∇T_i and ∇n the ion fluxes increase and in any case a robust ion-root solution with (often strongly) negative E_r is realized. Outside in the scrape-off layer due to the prevailing electron parallel transport to the targets, $E_r > 0$ is established. Therefore strong ∇E_r evolves at the plasma edge with the potential to improve edge confinement.

Based on these ion-root conditions a distinct confinement improvement with evolving density and temperature profiles develops within a transport timescale. The improved regime is characterized by steep density gradients and low edge densities (i.e. a narrow density profile) and high T_i values at the edge. The region of strongly negative E_r extends deep into the bulk. For historical reasons this regime has been addressed either as ‘optimum confinement (OC)’ ([Kick et al 1999](#), [Baldzuhn et al 2000](#)) referring to the fact that core transport is down to the neoclassical level or as ‘high NBI mode’ (H-NBI) ([Stroth et al 1998](#)) the latter corresponding to its access via deep fuelling supported by NBI. The regime has some common characteristics with a family of regimes that show peaked density profiles and high ion temperatures found both in helical systems such as Heliotron-E ([Ida et al 1996](#)) and CHS ([Ida et al 1999](#)) as well as in tokamak devices.

Examples for the developing OC characteristics are given in [Stroth et al \(1998\)](#): at constant \bar{n} the edge density reduces and a steep density gradient evolves with its maximum clearly inside the plasma boundary. Temperatures rise and the T_e and T_i profiles broaden developing steep gradients in the region of lower densities where $T_i \gtrapprox T_e$. Finally the maximum of ∇T is typically located outside the radius where the maximum ∇n is found ([Kick et al 1999](#), [Stroth et al 1998](#)). For profiles see figure 13. The heat diffusivity derived from power balance is reduced over the entire plasma cross-section with respect to comparable normal confinement discharges ([Stroth et al 1998](#)). In the plasma core (up to $r/a < 0.7$ where T_i is still up to 1 keV) particle flux as well as the ion heat flux are on the neoclassical level (figure 13, lower row). The electron heat flux is also reduced but may be higher than the expectations from neoclassics, however remaining within the error bars that result from the traditional neoclassical ordering ([Kick et al 1999](#), [Kreiter et al 2002](#)). For comparison in discharges with normal confinement and lower T_i anomalous fluxes prevail also in the plasma core, the expected neoclassical ones are significantly smaller ([Kick et al 1999](#)). At the plasma edge of OC discharges heat transport exceeds the neoclassical predictions by more than an order of magnitude as is the case for all confinement regimes (see figure 13(d)–(f), [Kick et al \(1999\)](#)). The increase of temperature

gradients observed there together with the development of OC characteristics indicates the strong reduction of these anomalous heat fluxes.

In the region of the steep gradients radial electric field values down to $E_r \approx -800 \text{ V cm}^{-1}$ are observed (Baldzuhn *et al* 1998b, Ehmler *et al* 2003a,b). For these strong ion-root conditions ion fluxes $\Gamma_i(E_r) \approx 0$ can be taken as first approximation such that from equation (3.2)

$$E_r \approx \frac{T_i}{e} \cdot \left[\frac{n'}{n} + \delta_{12}^i \frac{T_i'}{T_i} \right]. \quad (5.2)$$

Here $\delta_{12}^i = D_{12}^i/D_{11}^i$ is much less sensitive to E_r than the D_{ij}^i themselves. Analytic values for purely collisional plasmas are given in Maaßberg *et al* (1996). Assuming $\delta_{12} = 1$, which is a good approximation for bulk conditions inside the gradient region, E_r can be approximated by $E_r \approx \nabla p_i/(e \cdot n)$; i.e. the ion diamagnetic drift is balanced by the $E \times B$ flow. Further out the thermodiffusive contribution is more important, $\delta_{12}^i = D_{12}^i/D_{11}^i > 1$ such that one finds that the value of E_r is larger than that of $\nabla p_i/(e^* n)$ (for examples see Ehmler *et al* (2003b)). The general observation is that large negative values of E_r occur with good energy confinement and the maximum $|E_r|$ value is located at the radius where the pressure gradient is steepest. The fact that E_r at the plasma edge is close to its neoclassical expectations (Baldzuhn *et al* 1998b) although heat conductivity is anomalous indicates that the anomalous fluxes there are basically ambipolar and do not modify the neoclassically established ion-root conditions strongly. However, close to the plasma boundary the observed values of E_r can be systematically larger than the neoclassically predicted ones (for a representative example see figure 13 (upper right)). This may be due to the fact that as a consequence of the strong plasma rotation the ordering in the neoclassical theory fails (see section 3.3), but also might be an indication for non-ambipolar anomalous flux contributions (for a discussion see Baldzuhn *et al* (1998b)).

The OC-regime develops at magnetic configurations providing good confinement, with sufficient ion heating and the ingredients for a narrow density profile, namely particle sources closer to the plasma core and low recycling edge conditions. Consequently, with divertor, the OC regime became more robust. It could be obtained with similar profile characteristics either at $t_a = 1/3$ where the divertor modules act as a limiter (Kreter *et al* 2002, Ehmler *et al* 2003b) and $t_a = 0.51$ with 5/10 islands (with large plasma cross-section and island reduced by the control coils) (Kreter *et al* 2003, Ehmler *et al* 2003b) and in standard divertor configurations with increased islands at $t_a = 0.56$ (Kreter *et al* 2003). Under limiter conditions low recycling was achieved by wall conditioning. Deep fuelling is provided by the inboard limiters where the closely spaced flux surfaces allowed the recycling neutrals to penetrate deep into the confinement region. In contrast, the top/bottom limiters installed at the elliptical cross-section where the radial flux expansion is large, resulted in strong edge fuelling; a condition which suppressed the OC regime (Kick *et al* 1999). Deep fuelling is further provided by NBI (Stroth *et al* 1998). The narrow density profile is stabilized by the low edge densities themselves: they allow for a deeper penetration of recycling neutrals which shifts particle sources inward as it is confirmed by an arising high energy tail in the spectrum of CX neutrals (Baldzuhn *et al* 2000). In addition, low edge densities also result in high edge diffusion (around the LCFS with $D \propto 1/n_e$ (Grigull *et al* 1995, Maaßberg *et al* 1993a) to $D \propto 1/n_e^2$ (Heinrich *et al* 1997), see section 6), thus keeping the footpoint of the density profile down and enable strong gradients further inside. Therefore once the OC regime has been established it turns out to be rather robust, even intermediate moderate gas puffing—although it increases the central density and transiently decreases τ_E —does not affect the profile width permanently (Kick *et al* 1999, Baldzuhn *et al* 2000).

In order to develop steep ∇T_i sufficient ion heating is required. This implies matching conditions between power and density (for a qualitative orientation see figure 67): for $\bar{n} = 1 \times 10^{20} \text{ m}^{-3}$, where the maximum values of τ_E are obtained, a minimum ion heating power of $P_{\text{abs}} \approx 0.25 \text{ MW}$ is necessary; if the NBI power exceeds this value only marginally the transition to OC is delayed. With one injector only ($P_{\text{abs}} \approx 0.4 \text{ MW}$) the absorbed power reduces quickly below the threshold if the density falls below $\bar{n} = 6 \times 10^{20} \text{ m}^{-3}$ (Stroth *et al.* 1998). Increasing core radiation on the other hand defines an upper density limit for OC (e.g. for $P_{\text{abs}} = 0.35 \text{ MW}$ at $\bar{n} > 1.2 \times 10^{20} \text{ m}^{-3}$) (Stroth *et al.* 1998). An *upper power level* exists for NBI power in excess of 0.7 MW where beam fuelling cannot be balanced by particle losses anymore and density control is lost (Kick *et al.* 1998, 1996). To achieve density control under these conditions with strong NBI and improve ion heating efficiency by increased T_e one must add ECRH at $P_{\text{ECRH}} \leq P_{\text{NBI}}$. The resulting increased T_e —although increasing the ion heating (see section 4.2)—lead to broader density profiles (see section 4.1.4) (Kick *et al.* 1996). However, continuously adding ECRH degrades the characteristics of the OC regime (Stroth *et al.* 1998). Nevertheless, OC characteristics can also be achieved with ECRH alone (with central $T_i \leq 900 \text{ eV}$, Kreter *et al.* (2003)) with sufficiently high power $P_{\text{ECRH}} > 500 \text{ kW}$ and if the energy exchange between electrons and ions is high, i.e. \bar{n} close to ECRH cut-off (Baldzuhn *et al.* 2000, McCormick *et al.* 1999b).

The magnetic configuration itself seems not to be the essential element of OC, it rather enters indirectly via its influence on recycling conditions and thus the density profile (Heinrich *et al.* 1997, Baldzuhn *et al.* 1998b). (Although OC and the associated high T_i were first achieved in configurations with toroidal ripple optimized with respect to neoclassical transport (Kick *et al.* 1996). The magnetic shear does not change the OC properties significantly (Brakel *et al.* 1997). Furthermore, the ι -ranges where OC is possible differ from the sharply bounded ι_a -windows known from the quiescent H-mode (although some overlap exists, see figure 65). Discharges with degraded OC signatures—similar to those observed by continuously adding ECRH—are possible in ι -ranges next to the ‘good’ ones (Baldzuhn *et al.* 2000, Stroth *et al.* 1998).

For W7-AS the Optimum Confinement regime yields the maximum values of T_i , τ_E and $n \cdot \tau_E \cdot T_i$. Global energy confinement in OC plasmas is enhanced with respect to the ISS95W7 (W7 subset of ISS95 data) and ISS95 scalings by up to a factor of 2 and 2.5, respectively (Stroth *et al.* 1998). The highest energy confinement times of W7-AS ($\tau_E = 60 \text{ ms}$) and the maximum values of $n \cdot \tau_E \cdot T_i = 5 \times 10^{21} \text{ eV s m}^{-3}$ (#45791, Jaenicke (2003)) are obtained in this regime at $\iota_a = 1/3$ (large plasma cross-section, $a = 0.18 \text{ m}$), with moderate heating power ($P_{\text{abs}} = 0.33 \text{ MW}$) and the maximum density which could be maintained stationary under these conditions ($\bar{n} = 1.1 \times 10^{20} \text{ m}^{-3}$). Ion temperatures are limited by the upcoming neoclassical losses and the available heating power. Values of $T_i = 1.5 \text{ keV}$ (#31464, Kick *et al.* (1996)) have been obtained at moderate densities $\bar{n} = 0.6 \times 10^{20} \text{ m}^3$ with a heating mix (NBI: $P_{\text{abs}} = 0.85 \text{ MW}$, ECRH: 0.35 MW) to ensure density control despite the high density and NBI beam fuelling. With the island divertor and increased absorbed NBI power central T_i -values up to 1.7 keV were measured (Kreter *et al.* 2003).

In summary, the OC regime develops from the ion-root conditions on top of the standard ‘good’ ι_a -ranges. Confinement improves gradually—contrary to the abrupt transition to H*—which points towards a causality loop where turbulent transport is reduced by sheared flow associated with the neoclassically generated E_r but without bifurcation: increasing T_i shifts the toroidal resonance and with it the ion-root solution $|E_r| \geq |E_r^{\text{res}}| = v_{\text{th}} \cdot B_{\vartheta}$ continuously towards higher values, which in turn deepens E_r and ∇E_r reducing anomalous convective and turbulent transport, respectively. As ∇E_r and E_r are linked, the influence of the two alternative contributions is hard to distinguish (discussion in Baldzuhn *et al.* (1998b)). Indications for a

reduction of turbulent fluxes are found in a moderate decrease of the turbulence level (by about a factor of 2 despite increasing gradients) and by the change of turbulence characteristics (see references in Kick *et al* (1999), Brakel *et al* (1997)). Frequently turbulence concentrates in small ELM-like transport events (see section 5.4.2). In any case the overall temporal behaviour is in contrast to the quiescent H-mode where the transition is abrupt and turbulence amplitude is squeezed by an order of magnitude (for discussion on the relation between OC-regime and H-mode see section 7.4).

The impurity content in OC discharges increases slowly and without saturation (Baldzuhn *et al* 2000). A distinct central peaking of the radiation profiles develops in accordance with impurity transport measurements which yield a very low impurity diffusivity and rather strong inward convection as a consequence of the strongly negative E_r (Burhenn *et al* 1997, Ehmler *et al* 2002a). With impurity influx reduced—e.g. by wall conditioning—the increase of impurity radiation could be slowed down but never reduced to zero (Baldzuhn *et al* 2000).

5.3.3. Observations of anomalous transport. In stellarators at first glance the picture of anomalous transport exceeding the neoclassical predictions is more orthodox than in tokamaks. In particular, both T_e - and n_e -profiles respond to the energy and particle source profiles in a way as expected from diffusive transport models. Main experiments in W7-AS concerned the electron transport channel which is better diagnosed and for which the capabilities of ECRH could be used as a selective tool. An earlier summary is given in Stroth (1998).

Profile resilience. On- and off-axis ECRH result in peaked and flat T_e -profiles, respectively. Various T_e -profile shapes are collected in (Wagner *et al* 2006). Similar observations have been made at other helical devices (Sanchez *et al* 2005). This means that—unlike some tokamak results (e.g. Luce and Petty (1994))—the T_e -profile is not completely resilient to changes in the power deposition profile and from these results there is no need to postulate an anomalous inward heat pinch. With finite ECRH power fraction deposited in the center resulting in peaked T_e -profiles, a pinch cannot be ruled out; however, there is only room for a pinch if it is *switched on* by central heating itself (Stroth 1998). It should be stressed that in a tokamak there is always residual Ohmic heating in the centre. Hence, similar concepts may also apply to stellarator plasmas. A quantitative analysis of the W7-AS results with tokamak models gave a quite good agreement, although the critical gradient in W7-AS is steeper (Ryter *et al* 2006). The T_i -profiles in W7-AS do not show the same flexibility as the T_e -profiles (being subject to less variable deposition profiles, however). Nevertheless, for T_i no indication of profile stiffness has been observed (Wagner *et al* 2006).

Density dependence. In W7-AS τ_E increases with density in both ECRH and NBI heated plasmas (Ringler *et al* 1990), section 5.1). Although a saturation was found, the saturation density could be increased by additional heating power and thus is attributed to radiation entering the power balance analysis rather than a saturation of χ_e itself (Stroth 1998). If radiation can be overcome, e.g. by a purification of the plasma in the HDH regime, saturation vanishes and the density dependence is recovered (see section 7.6). For comparison, in tokamaks a density dependence of τ_E is only observed in low densities Ohmic discharges (LOC regime). The saturation of τ_E with density can, however, be avoided if the gas flux is switched off (IOC regime). Early experiments in W7-AS and CHS with only moderate heating power available showed a similar ‘reheat mode’ where switching off the gas flux triggered a steepening of the density gradient and a temporal increase in τ_p and τ_E (Morita and Baldzuhn 1994).

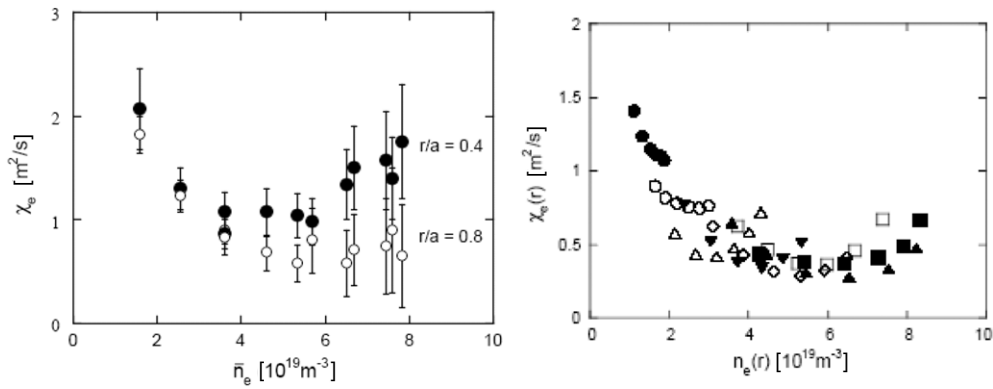


Figure 43. (Left) Evolution of χ_e obtained from a density scan. Plotted are radial averages in the core at $r/a = 0.4$, ($5 \leq r \leq 8.5$ cm) and the edge $r/a = 0.8$ ($12 \leq r \leq 15$ cm). (Right) Local χ_e as a function of the local electron density. The different symbols mark different discharges of a density scan with moderate heating power ($1.5 \times 10^{19} \text{ m}^{-3} < \bar{n} < 9 \times 10^{19} \text{ m}^{-3}$, $P_{\text{ECRH}} = 450 \text{ kW}$, $B = 2.5 \text{ T}$, $t_a = 1/3$) (Stroth *et al.* 1995b).

A density dependence of the *global* confinement time at given heating power would result from a possible local temperature dependence of χ_e . Figure 43 collects data obtained during a density scan and shows that χ_e can be well described as a function of the *local* density. This observation together with the increase of $\chi_e(r)$ radially towards the plasma edge (shown e.g. in figure 13) can only be explained by a direct dependence of χ_e on density; an implicit dependence on T_e produces decreasing diffusivities towards the edge and thus can be ruled out (Stroth 1998). The dependence of χ_e on density is lost when a critical density is surpassed (figure 43 (right)) whereas the critical density seems to depend on heating power. It is speculated that the density dependence of χ_e could be related to electrostatic turbulence (Stroth *et al.* 1995b): for given heating power the level of density fluctuations \tilde{n}/n increases towards the edge and at a given radius \tilde{n}/n decreases with increasing density, i.e. it follows the evolution of the diffusivity with both respects (section 5.4.2). For the scrape-off layer it has been shown that the measured \tilde{n}/n can be a sign of electrostatic turbulence which is able to account for the radial transport at least there outside the separatrix (section 5.4.1).

Power degradation is a robust feature observed in both tokamak and stellarator transport (section 6.1). Power degradation in W7-AS is documented in Ringler *et al.* (1990), Stroth *et al.* (1996c); for a direct comparison between W7-AS and the RTP tokamak see Peters *et al.* (1994). In W7-AS power degradation is also found in *local* electron transport, where $\chi_e(r)$ scales with the power deposited inside the respective flux surface. In the core the value of χ_e could be represented by a power law similar to that valid for the confinement time; however, in the edge power degradation seems to be stronger (Stroth 1998). The observed global dependence $\tau_E \propto P^{-0.5}$ could equally well be explained by a dependence $\chi(r) \propto T^{3/2}(r)$ or by $\chi(r) \propto \nabla T^{3/2}(r)$, the first being favoured by collisional as well as drift wave theories and the second by models using marginal stability of modes at some critical temperature gradient. Alternatively the heating power as a global parameter could be thought to affect transport directly, for example by distortion of the particle distribution function or via an additional (global, i.e. non-diffusive) loss channel of power directly to the edge. For ion transport in the plateau regime $\chi(r) \propto T^{3/2}(r)$ is expected already from neoclassics, however, power degradation is also observed under conditions dominated by anomalous transport (Ringler *et al.* 1990).

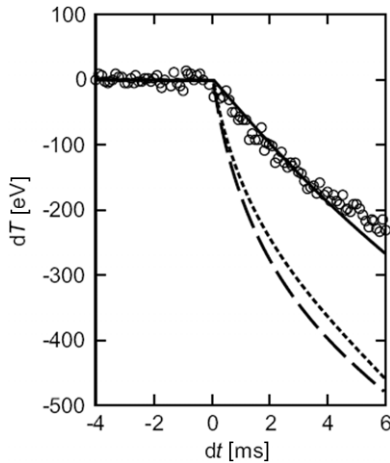


Figure 44. Simulations of the dynamic phase after decreasing the ECH power at $t = 0$ by 0.45 MW. Three models are used: $\chi_e(r)$ changes instantaneously with P (solid line), $\chi_e(r) \propto T_e(r)$ (dashed) and $\chi_e(r) \propto \nabla T_e(r)$ (dotted). The simulated changes in T_e are compared with ECE data at $r/a = 0.22$, for example (Stroth *et al.* 1996b).

On- and off-axis ECRH was applied to disentangle possible local dependences of χ_e on T_e , ∇T_e or P_{ECRH} (Stroth 1998). As expected for a purely diffusive model the power deposition in the core does not modify the electron temperature gradient at the plasma edge. This also shows that quantities related to the deposited power density such as the non-thermal power fraction, which is very different for on- and off-axis ECRH, do not sensitively determine the transport level. However, also the attempt to relate the power degradation on T_e as the leading agent fails (Stroth 1998, Peters *et al.* 1994). Formally, the observations can be reconciled with power degradation if the transport coefficient is allowed to vary with changes in heating power as a non-local quantity (up to almost linearly (Stroth *et al.* 1995b)).

Transient transport studies. Perturbative transport studies rely on the analysis of the dynamical response of plasma parameters to perturbations of the heat or particle source. In W7-AS, perturbative transport studies have been carried out by switching or modulating the ECRH power (see below) or the gas valve (see section 6.1) or injecting impurity particles through laser blow-off (see section 6.2).

Experiments with *power steps* (Stroth *et al.* 1993a, 1993b) show that the temporal evolution of the T_e -profile is slower than expected from local models which assume $\chi_e = \chi_e(r) \propto T_e(r)$ or $\chi_e = \chi_e(r) \propto \nabla T_e(r)$. An example is shown in figure 44. Only a global model where $\chi_e = \chi_e(P)$ describes the slow evolution of the temperature. Similar observations have recently also been found in tokamak experiments (Gentle *et al.* 2006). To date it has not been fully resolved whether the transient results from W7-AS can be reconciled with a strong increase of the χ_e in the core at very high heating-power densities (Stroth *et al.* 1995b, 1996b, Giannone *et al.* 1996). A heuristic model had been put forward, where the *local* diffusivity depends on the heating power deposited *inside* the respective radius (Stroth *et al.* 1993a, 1993b, 1996b). This global model introduces instantaneous χ_e changes with heating power and is able to qualitatively reconcile the different observations.

In the following the results from transport analysis using *electron heat wave propagation* stimulated by ECRH power modulation are summarized. A generalization to gas perturbation

experiments (section 6.1) is straightforward. Earlier W7-A experiments can be found in Giannone *et al* (1992), Hartfuß *et al* (1986). A review on heat wave techniques is given in Lopes-Cardozo (1995), the application to W7-AS is summarized in (Stroth 1998). The ECRH-power was modulated with an amplitude of 10–30% and the frequency scanned from 0.05 to 5 kHz. For the analysis an implicit time dependence of the modulated electron heat flux \tilde{q}_e via the quantities $T_e(t)$ and its gradient $T'_e(t)$ and an explicit time dependence $\tilde{q}_e(t)$ describing a *global* transport channel must be taken into account (Romé *et al* 1998, Gasparino *et al* 1998a). Moreover, at fairly low optical depth the absorption coefficient may be T_e -dependent. An effective on-axis power deposition profile is derived as shown in figure 19 (Romé *et al* 1997). Density modulations driven by the power modulation are disregarded; for a discussion see Gentle (1988). As in a stationary analysis the two unknown functions, namely the (time dependent) diffusion coefficient $\chi(r, T_e, T'_e)$ and the (time dependent) convection velocity $v_c(r, T_e, T'_e)$, cannot be determined from a single (time dependent) profile measurement without further assumptions.

In W7-AS the heat transport was described by a purely diffusive model i.e. assuming a vanishing convection to compare with power balance analysis results. The functional dependences of χ are then given by

$$\frac{\partial \ln \chi}{\partial \ln T'_e} = \frac{\chi^{\text{HP}}}{\chi^{\text{PB}}} - 1, \quad (5.3)$$

where $\chi^{\text{HP}} = \bar{\chi} + \partial \chi / \partial T'_e \cdot \bar{T}'_e$ is the effective ‘heat-pulse’ transport coefficient determined from the transient transport analysis and χ^{PB} is the result from stationary power balance. An error and correlation analysis is given in (Romé *et al* (1997); figure 4). Triggered by the observation of stiff profiles in tokamaks and, to some extent, in stellarators (Stroth 1998) and by the general observation of power degradation, an at least linear dependence of χ_e on T_e or T'_e was under question. According to equation (5.3) the quantity of interest is $\chi_e^{\text{HP}} / \chi_e^{\text{PB}}$ which must be well above 1 if a strong dependence of χ_e on the T'_e is present. A nonlinear dependence $\chi_e(\nabla T_e)$, as postulated by a critical temperature gradient model would yield i.e. $\chi_e^{\text{HP}} / \chi_e^{\text{PB}} > 2$, which is indeed observed in tokamaks (Peters *et al* 1994). The experimental results in W7-AS were in contradiction to this assumption (Stroth *et al* 1995a, 1995b, Peters *et al* 1994, Stroth 1998). In early experiments, the ratio $\chi_e^{\text{HP}} / \chi_e^{\text{PB}}$ was measured to be close to 1 and independent of B , t , n_e , P_{ECRH} as well as from modulation amplitude and frequency (Giannone *et al* 1992, Erckmann *et al* 1992b, Hartfuß *et al* 1994a). A typical result with $\chi_e^{\text{HP}} / \chi_e^{\text{PB}} \approx 1$ independently from the heating power is shown in figure 45 (left). Moreover, $\chi^{\text{HP}}(r)$ is independent of the modulation frequency which is also an indication against a temperature dependence of the diffusivity (Stroth 1998). A dedicated comparison of ECRH power modulation conducted between RTP tokamak and the W7-AS stellarator confirmed the different behaviour in the two devices (Peters *et al* 1994, 1995, Peters 1995): in RTP, a constant value for χ_e^{HP} was found with $\chi_e^{\text{HP}} / \chi_e^{\text{PB}} > 1$. In contrast in W7-AS the diffusivities changed with heating power with values $\chi_e^{\text{HP}} / \chi_e^{\text{PB}}$ between 1 and 2. The latter is consistent with a linear dependence of the χ_e on ∇T_e as postulated to explain the observed power degradation but still disagrees with a critical temperature gradient model. For a refined analysis extensive parameter scans have been carried out (varying P_{ECRH} , n_e , t and B_z) in order to find robust conditions, where island transport can be excluded and the best confinement is obtained (Walter 2005). The bottom line of the experiments shown in figure 45 (right), yields a ratio of $\chi_{\text{HP}} / \chi_{\text{PB}}$ between 2 and 1 depending on heating power. Taking into account results at other plasma densities, the deposited power density P/n , seems to be relevant for the observed transition to a ratio of 1 (figure 45 (right)).

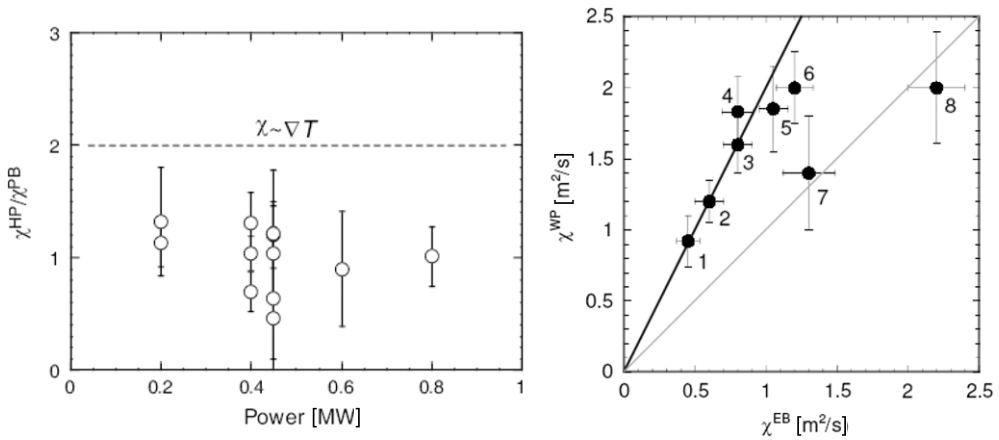


Figure 45. Ratio of heat pulse to power balance electron thermal diffusivity in W7-AS as a function of heating power (left: from Hartfuß *et al.* (1994a), right: Walter (2005)) for #42391. Numbers 1–8 correspond to about equidistant power steps between $P_{ECRH} = 0.21$ MW and 1.3 MW, the step down to $\chi_e^{HP}/\chi_e^{PB} = 1$ being between 0.8 and 0.9 MW (central density $\hat{n}_e = 4 \times 10^{19} \text{ m}^{-3}$, $B = 2.5$ T). For a dependence $\chi_e \propto \nabla T_e$ one expects $\chi_e^{HP}/\chi_e^{PB} = 1$.

An alternative method to generate transient perturbations in the electron temperature is impurity injection into the plasma edge. In W7-AS such cold-pulse experiments used carbon ablated by a laser (Walter *et al.* 1998a, 1998b). The radiation profile peaked around 13 cm and during the analysis of the temperature response; thus the plasma inside 10 cm should not be affected by the additional carbon radiation. A dip in the edge temperature is observed, which propagates inward. The response was analysed with a time-dependent transport code. It was found that a stationary value of χ_e , as obtained from a power balance analysis, was sufficient to reproduce the diffusive propagation in the core. Additional dependences on local plasma parameters were not indicated.

In summary anomalous electron energy transport in W7-AS responds to changes in the power deposition as expected from diffusive transport; profile resilience and an inward directed heat pinch—if relevant at all—play a less obvious role than in tokamaks. The density dependence of the energy confinement time results from a direct dependence of the local χ_e on the local density possibly related to electrostatic turbulence; an implicit hidden dependence on T_e can be ruled out. In order to relate the observed power degradation to a dependence of χ_e on local quantities like T_e or ∇T_e power balance experiments with varying power deposition profiles and various perturbative transport techniques were applied. The heat wave experiments resulted in $\chi_e^{HP}/\chi_e^{PB} < 2$, giving no indication for a critical gradient, and even a local model ($\chi_e^{HP}/\chi_e^{PB} > 1$) is not clearly supported. Only a global model as also suggested from the power-switching experiments allows the diffusivities to have the same value $\chi_e^{HP}/\chi_e^{PB} \approx 1$. In a heuristic model the *local* χ_e is assumed to depend up to almost linearly on the power deposited inside the respective flux surface. However the mechanism of such a non-local dependence remains open; non-thermal (heating related) ECRH fluxes do not play a dominant role. As a possible explanation for the differences in tokamaks and W7-AS it was suggested (Peters *et al.* 1994) that a heat pinch exists which increases with plasma current (discussed in Stroth (1998)) or central heating power (Ryter *et al.* 2006).

5.4. Observations on turbulence and turbulent transport

Turbulence is believed to be a main channel of anomalous transport, in particular at the plasma edge. In the scrape-off layer (SOL) the radial fluxes carried by broadband electrostatic turbulence can be calculated directly from simultaneous measurement of fluctuations \tilde{n}_e , \tilde{T}_e and $\tilde{\phi}$ (Liewer 1985). In the confinement region, these local quantities and their required phase relation have not yet been fully obtained simultaneously. Instead the strategy was to link characteristics of the observed fluctuations \tilde{n}_e , \tilde{B}_{pol} and, for the first time also \tilde{T}_e , to discharge conditions or profile changes. Simulations of turbulence in realistic 3D stellarator geometry are, due to their complexity, relatively rare (first steps in Kendl *et al* (2000), Jenko and Kendl (2002a, 2002b), Kendl *et al* (2003), Kendl and Scott (2003), Kleiber and Scott (2005), Nuehrenberg (2006)).

Frequency and poloidal wavenumber spectra of turbulence always have a broadband component indicating individual ‘fluctuation events’. The fluctuation power decays towards high frequencies and high poloidal wavenumbers (small structures) (SOL: Endler *et al* (1995b), Bleuel *et al* (2002), confinement region: Saffman *et al* (2001)). Inside the LCFS also oscillatory phenomena exist (see section 5.4.2).

The turbulent structures propagate in the poloidal direction with a common velocity dominated by the $E \times B$ velocity of the plasma, the intrinsic wave velocity of the perturbations in this rotating plasma frame can be neglected (SOL: Balbin *et al* (1992), Endler (1994)). For the confinement region even during transient phases see Hirsch *et al* (2001b, 2006). For equivalent results on tokamaks see references in Schirmer *et al* (2006). Accordingly, the poloidal propagation velocity of the perturbations reverses sign close to the LCFS, where also E_r reverses sign (velocity shear layer). Inside the LCFS $E \times B$ drift and hence the turbulence propagation is in the electron diamagnetic direction (ion-root conditions) (Konrad 1995, Hirsch *et al* 2001b, Saffman *et al* 2001). In the SOL propagation is small and in the ion diamagnetic direction due to $E_r > 0$ (Balbin *et al* 1992, Sanchez E *et al* 2000).

The perturbations are aligned along the magnetic field lines, resulting in an essentially 2D spatial structure as known from other toroidal devices (e.g. Endler (1999), Thomsen *et al* (2002a)): in the SOL with probe tips measuring on the same magnetic flux bundle with separation of 6 m along a field line correlations as high as 90% were found (Bleuel *et al* 1996, Bleuel 1998, Bleuel *et al* 2002); with separation of 32 m (2.5 toroidal turns) still a correlation of 30–35% was measured (Bleuel *et al* 1997, Bleuel 1998). Inside the LCFS, the high degree of correlation along the field lines is indicated by Doppler reflectometry which observes maxima in the autocorrelation function of small scale density turbulence (poloidal scale length ≈ 1 cm) after the $E \times B$ velocity has rotated the edge layer poloidally by $1/t$, $2/t$ of the poloidal circumference (Hirsch and Holzhauer 2004).

The LCFS represents a boundary for turbulence phenomenology (Zoleznik *et al* 1999, Bruchhausen *et al* 2004) beyond its attribute as a velocity shear layer: first in the SOL fluctuations of n_e , T_e and ϕ are always present, whereas inside the LCFS (quasi-coherent) density fluctuations strongly correlate with magnetic configuration and plasma scenarios—the LH transition or the t -dependence of confinement being obvious examples. Secondly, inside the LCFS quasi-coherent activity has a strong magnetic component correlated with the density fluctuations, whereas no correlation with magnetics is observed for SOL turbulence.

5.4.1. Turbulence and transport in the SOL. The signatures of fluctuations in the SOL are in agreement with drift-interchange turbulence with amplitudes and phases able to explain at least a significant part of the anomalous transport there. Figure 46 shows that fluctuation events

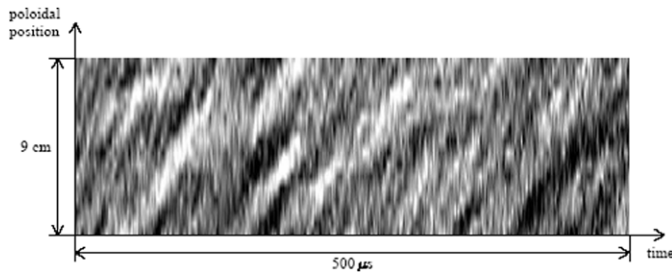


Figure 46. Raw data from the 16 channel H_α fluctuation diagnostic at W7-AS which to a good approximation displays \tilde{n} : the intensity is coded in grey scale (light: high intensity, dark: low intensity). Individual fluctuation events propagating in the poloidal direction (ion diamagnetic drift direction) with fairly uniform velocity can easily be identified as inclined structures (Bleuel *et al.* 2002).

are literally visible in the raw data of poloidally neighbouring H_α photomultiplier signals (Bleuel *et al.* 2002). The turbulent events have been characterized by their spatio-temporal correlation function yielding their typical lifetime, spatial size and propagation velocity (details in Endler *et al.* (1995a)). Statistical properties of SOL fluctuations were compared with those of other toroidal magnetic confinement devices, revealing a universal shape of power density spectra (Pedrosa *et al.* 1999, Carreras *et al.* 1999) and a general consistency with what would be expected from self-organized critical systems (Carreras *et al.* 1998).

Relative \tilde{n}_e levels are in the range of 15–60% generally increasing from the LCFS outwards into the far SOL (Bleuel *et al.* 2002). \tilde{T}_e is found to be almost in phase with $\tilde{I}_{\text{sat}} \propto \tilde{n}$ (Pfeiffer *et al.* 1998). The autocorrelation time of \tilde{n}_e is between 10 and 100 μs and systematically increases towards the wall (Bencze and Zoleznik 2005). The typical poloidal size is a few centimetre, the radial size a factor of 2 less (Bleuel *et al.* 2002, Zoleznik *et al.* 1999, 2005b); values which are also seen in the SOL of other fusion devices (Liewer 1985). In the radial–poloidal plane, the fluctuation structures are inclined. Strong evidence exists that the inclination is due to the *local* magnetic shear in W7-AS in conjunction with the high correlation of the fluctuations parallel to the magnetic field. The radial shear of the poloidal velocity may contribute to the inclination (Bleuel *et al.* 2002, Bruchhausen *et al.* 2004). The poloidal–radial tilt together with the poloidal propagation velocity result in an apparent *radial* velocity if projected onto a radial detector array (Bleuel *et al.* 1996, Bleuel 1998, Bleuel *et al.* 1998, 2002); the *radial* velocity in the plasma frame itself is close to zero.

Information on single events is obtained from conditional averaging analysis, where a condition for the signal of one probe tip is used to average over the corresponding time windows of the signals of a separate probe array (Grulke *et al.* 2001). The occurrence of single \tilde{I}_{sat} fluctuation events correlated with $\tilde{\phi}_{\parallel}$ events can be explained with the density perturbation being due to a local radial $E \times B$ drift advecting plasma of lower/higher density (for similar results in ASDEX see Theimer *et al.* (1995), Endler *et al.* (1995a)). The non-Gaussian probability distribution functions and the asymmetry (skewness) of these fluctuating quantities (Sanchez E *et al.* 2000) agree with the local poloidal propagation velocity and preferred orientation of these $\tilde{\phi}_{\parallel}$ double vortices (Thomsen 2002a).

Radial particle transport derived from triple probe measurements (probing \tilde{I}_{sat} , \tilde{E}_{pol}) shows a general radial in–out asymmetry of the fluxes and resolves single transport events with duration $<30 \mu\text{s}$ and localized as single structures in space (Bleuel *et al.* 1998), analogous to

the SOL of the ASDEX tokamak ([Endler et al 1995a](#)). On a timescale $>60\ \mu\text{s}$ the asymmetry of the in- and outward transport reveals the existence of intervals with enhanced radially outward transport, which may be related to the ELM-like transport events observed in the confinement region (see section [5.4.2](#)).

A local radial heat flux was calculated from turbulence close to the LCFS, assuming that T_i is similar to T_e . This calculated turbulent flux accounts for $\approx 30\%$ of the average heat flux through the LCFS expected from global energy balance ([Schubert 2005](#)). However, due to limitations in frequency and wavenumber bandwidth of the diagnostic, the local turbulent flux may be underestimated. From the time averaged value of the local radial heat flux a confinement time $\tau_{E,\text{turb}}$ was calculated for various plasma conditions, which shows surprisingly good agreement with global τ_E ([Bleuel et al 1999](#)).

In the SOL the turbulence parallel correlation length is larger than the connection length between the target plates and 2D numerical simulations become possible. It is expected that for such conditions the target plate boundary conditions influence the turbulence dynamics in the SOL ([Nedospasov 1989](#), [Garbet et al 1991](#), [Endler et al 1995a](#)). Numerically derived turbulence for W7-AS conditions was analysed with the same correlation techniques as experimental fluctuation data (although v_{pol} could not be treated self-consistently in the simulations); the correlation functions obtained showed good agreement ([Bleuel 1998](#), [Bleuel et al 1998](#)).

SOL turbulence can be influenced by coupling periodic electric signals by means of probe tips, where the signal propagation is detected with a toroidally separated probe array. The influence of the periodic signals on turbulence is found to be limited to a narrow spectral range around the driver frequency. The signal propagation velocity parallel to B is of the same order as the electron thermal velocity ([Thomsen et al 2001](#), [Thomsen 2002b](#), [Thomsen et al 2005](#)).

5.4.2. Turbulence and transport events in the bulk. Fluctuations of n_e , B_{pol} and T_e inside the LCFS—contrary to the SOL—show a clear dependence on the magnetic configuration and on plasma parameters:

- *t-dependence*. The amplitudes of small scale density fluctuations \tilde{n}_e (with a poloidal scale from a few centimetre down to millimetre) are strongly anti-correlated with the strong *t*-dependence of global transport. Even details of the *t*-dependence are reproduced ([Estrada et al 1994](#), [Konrad 1995](#), [Basse et al 2004, 2005](#)). CO₂-laser scattering (probing $15\ \text{cm}^{-1} \leq K_{\perp} \leq 60\ \text{cm}^{-1}$) shows that the slope of the K_{\perp} -spectrum becomes steeper in low confinement plasmas, i.e. the relative weight of larger structures increases ([Zoletnik et al 2002](#)).
- *heating power*. For a given magnetic configuration, \tilde{n}_e and \tilde{T}_e drop with increasing *heating power*, however, the associated anomalous transport in terms of electron heat diffusivity increases ([Branas et al 1995](#), [Brañas et al 1995](#), [Stroth et al 1995b](#), [Hartfuß et al 1996](#)). Thus an increasing turbulence level can neither be the only nor the dominant origin of power degradation under these conditions.
- *density*. For given heating power and radius both \tilde{n}_e at the plasma edge and \tilde{T}_e in the core decrease with density ([Branas et al 1995](#), [Brañas et al 1995](#), [Sattler et al 1994a](#), [Hartfuß et al 1996, 1997b](#), [Zoletnik et al 1999](#)) as does the heat diffusivity (see section [5.3](#)). This possibly indicates a relevance of the turbulence for this dependence ([Stroth et al 1995b](#)).
- *electron temperature*. In the core electron temperature fluctuations \tilde{T}_e were measured with correlation ECE. For a variety of plasma scenarios the dependences of \tilde{T}_e on t , n_e and P_{ECRH} can all be plotted as a hidden decrease of the mixing length of these fluctuations $\tilde{T}_e/\nabla T_e$

with the local temperature as $\tilde{T}_e/\nabla T_e \propto T_e^\alpha$ with $1 \leq \alpha \leq 3.5$ (Hartfuß *et al* 1998, Häse *et al* 1999).

Broadband density fluctuations at the LCFS have a typical relative fluctuation level of $\tilde{n}_e/n_e \approx 15\%$; it decreases towards the plasma centre typically by a factor of 10 over the outermost 5 cm in both ECRH and NBI heated discharges (Estrada *et al* 1993a, 1993b, Zoleznik *et al* 1999, Saffman *et al* 2001, Basse *et al* 2002a). The envelope of \tilde{n}_e is often modulated in time: bursts of a duration of $\approx 100 \mu s$ occur simultaneously around a flux surface (CO_2 -scattering: Basse *et al* (2005)). These bursts are related to ELM-like activity observed even under L-mode conditions as described below. Density oscillations related to the $t = 0.5$ surface have been investigated by Sanchez *et al* (1990).

Broadband T_e -fluctuations in the hot core of a fusion plasma ($0.5 < r/a < 0.75$) could be observed in W7-AS for the first time applying crossed sightline spatial decorrelation techniques to ECE radiometry (Hartfuß *et al* 1993, Sattler *et al* 1994b, Hartfuß and Häse 1997) investigating ECRH plasmas with typical $T_e(0) > 1 \text{ keV}$. The measured relative fluctuation level was $\tilde{T}_e/T_e \approx 0.3\text{--}1\%$; the lowest level corresponding to the innermost position (Sattler *et al* 1994b, Hartfuß *et al* 1996). Other correlation techniques, based on spectral decorrelation and disjoint observation volumes, have successfully been developed elsewhere, the different methods have been compared at W7-AS (Watts *et al* (1997, 2004), and references given therein).

The fluctuation structures observed with correlation ECE are poloidally elongated with a typical poloidal coherence length of about 4 cm, and a radial one of 1–3 cm. The measured poloidal propagation with $v_{E \times B}$ results in a broad spectral feature, frequency shifted by about 50 kHz and extending up to about 100 kHz (Sattler *et al* 1994b, Hartfuß *et al* 1996, Bäumel *et al* 2003b). Accordingly, the frequency spectrum is broadened if the velocity shear-layer is shifted into the probed region (Hartfuß *et al* 1996). The perturbations disappear completely in the case of flat profiles, $\nabla T_e(r) = 0$, and the T_e -fluctuations are in-phase correlated (up to 30%) with density perturbations measured at the same plasma volume where $\tilde{n}_e/n_e \approx 1\%$ (Häse *et al* 1997a, Hartfuß *et al* 1998, Haese *et al* 1998, Häse *et al* 1999). On this basis, the measured T_e and correlated n_e fluctuations are interpreted to display convective cells advecting plasma and transforming into fluctuating quantities in the presence of finite gradients ∇T_e . However, the obtained radial mixing length of the vortices is $\tilde{T}_e/\nabla T_e < 1 \text{ mm}$ only, in apparent contradiction to the measured radial coherence length of 1–3 cm. As an explanation of this discrepancy it is assumed that the structures are actually poloidally smaller and the measured $\tilde{T}_e/T_e \approx 0.3\text{--}1\%$ are due to the poloidal space averaging of the diagnostic system with a spot diameter of about 2–3 cm. This is in agreement with the observation that \tilde{T}_e/T_e increased as a stronger focussing antenna optics was used.

The *radial* phase velocity of the T_e -perturbations is directed inward and about 10 km s^{-1} (Hartfuß *et al* 1996). As for structures in the SOL, this apparent radial velocity could be due to the poloidal $v_{E \times B}$ of a radially–poloidally tilted structure projected on the radial ECE sightline. However, in order to explain the apparent large inward velocity the corresponding structures should be radially elongated in contradiction to measurements with a 2D imaging system (Bäumel *et al* 2003b). High amplitude radially elongated ‘streamer’ vortices displaying ETG modes have been predicted by Jenko and Kendl (2002a, 2002b) for the investigated W7-AS e-root discharges with strong ∇T_e . The observed decrease of the *poloidal* coherence length with P_{ECRH} can be attributed to an increasing velocity shear as observed by the 2D correlation radiometer (Sattler *et al* 1994b, Hartfuß *et al* 1996) and a 2D imaging system (Bäumel *et al* 2003b).

A second low frequency T_e -perturbation with $f < 15 \text{ kHz}$ resembles an outward propagating (on a diffusive timescale) T_e -profile perturbation ($\tilde{T}_e/T_e \approx 1\%$, radial coherence

length around 5 cm) probably caused by the central ECRH, either due to a fluctuating power level similar to active perturbation experiments but at a much lower level, or due to the electron wave absorption process itself (Hartfuß *et al.* 1996). Accordingly, the perturbation exists even if ∇T_e is flat and not correlated with a density perturbation (Sattler *et al.* 1994b, Hartfuß *et al.* 1996, Häse *et al.* 1999).

Magnetic activity beyond coherent MHD is observed in broad frequency bands extending up to 500 kHz associated with bursting Alfvén activity (section 9.4 and examples in figures 100–102) and together with ELMs (section 7.3, and figure 64). A quasi-coherent MHD activity was observed in High Density H-mode conditions (Belonohy *et al.* 2007a). Transient quasi-coherent oscillations with a few maxima only occur associated with ELM-like activity and are described below.

Turbulent fluxes cannot directly be inferred from this limited information. However, a strong correlation of turbulence dynamics with changes in gradients is observed at the H-mode transition and for single events such as ELMs (see section 7.3, Hirsch *et al.* (1996b)). Moreover, *transient transport events* (Hirsch *et al.* 1998b, Zoleznik *et al.* 2005a) can be identified for nearly all plasma conditions, except in the quiescent H-mode, including limiter discharges, different heating scenarios and also with only moderate edge pressure gradients. With respect to duration (duration of a turbulent burst about $\approx 200 \mu\text{s}$, (Basse *et al.* 2005, Pokol *et al.* 2007)) and spectrum of \tilde{n}_e and \tilde{B}_{pol} and transport (intermittent n_e - and T_e -profile flattening followed by an inward propagating coldpulse (Pokol *et al.* 2005)), they resemble small ELMs but the pivot point of the intermittent ∇T_e flattening is less ‘edge-localized’ and shifted deeper inside the plasma under conditions where the pressure gradient is shifted correspondingly (Hirsch *et al.* 1998b, Zoleznik *et al.* 2005a). All changes in turbulence and gradients are closely linked in space and time, thus a causality loop could not be inferred either in single ELMs (Hirsch *et al.* 1996b) or by correlation techniques down to diagnostic limitations of a few ten microseconds (Zoleznik *et al.* 2005a). The correlated observations at different diagnostic locations (magnetic probes, beam emission spectroscopy, scattering, ECE at high-field- and low-field side) support the picture that the event affects the whole flux surface (Zoleznik *et al.* 2005a). Like ELMs the strength of these events depends on the rotational transform (see figure 66 for comparison); in particular they appear close to values where good confinement can be reached (Belonohy *et al.* 2007a). ELM-like phenomena also have been reported from TJ-II (Garcia-Cortes *et al.* 2000, Alejaldre *et al.* 2002) and LHD (Watanabe *et al.* 2003).

As a prominent feature associated with transport events *quasi-coherent transient oscillations* occur highly correlated in \tilde{n}_e and \tilde{B}_{pol} (Zoleznik *et al.* 1999) with frequencies of around 20–30 kHz and a few maxima only, i.e. a lifetime of 100–200 μs . Perturbation amplitudes measured at the plasma edge are typically $\tilde{n}_e/n_e \approx 3\text{--}50\%$, $\tilde{B}_{\text{pol}}/B = 10^{-3}$ (Zoleznik *et al.* 1999, 2002). Lithium beam emission spectroscopy (BES) shows that they occur at least in the first 2–3 cm inside the LCFS without affecting the SOL. The poloidal mode number (inferred from magnetics) is determined by the next major rational ($m = 2, 3$, i.e. poloidal wavelength 30–50 cm), the perturbations rotate with the $E \times B$ velocity of the plasma frame resulting in the observed 20–30 kHz (e.g. Anton *et al.* (1998), Zoleznik *et al.* (1999), Pokol *et al.* (2004, 2007), Polol *et al.* (2003), Papp *et al.* (2005)). Spectra and radial extent of quasi-coherent activity are supposed to be attributed to rationals; their modification during the t variation being the consequence of the evolution of the profiles of t and $v_{E \times B}$ (Zoleznik *et al.* 2002, Pokol *et al.* 2007, Papp *et al.* 2005). Usually multiple frequencies are observed in the spectrum and their amplitudes can be modulated sometimes in a correlated way, depending on discharge conditions. As the poloidal mode numbers of the different frequency components are usually

identical, the different frequencies are believed to come from different radial positions through the radial change of the $v_{E \times B}$ profile (Zoletnik *et al.* 2002, Pokol *et al.* 2007, Papp *et al.* 2005). Stronger individual events can be identified as being directly linked to ELM-like behaviour or ELMs; for an example see figure 64. Correlation analyses show the simultaneous signatures of transport events and quasi-coherent perturbations even if individual events are hard to depict. The simultaneous occurrence of quasi-coherent activity and increase in the power of millimetre-scale density turbulence is shown in Basse *et al.* (2005), the simultaneous transient flattening of ∇T_e followed by an inward propagating cold pulse in (Zoletnik *et al.* (2005a), Papp *et al.* (2005) and figure 47). It is assumed that these quasi-coherent oscillations represent a damped harmonic oscillation subsequent to a localized transport event which suddenly had changed the local pressure profile. The perturbation of the plasma edge equilibrium extends along the field lines and relaxes after 100–200 μs , corresponding to the density relaxation along a flux surface after several $2 \cdot \pi \cdot R / v_{\text{th}}^{\text{ion}}$ ion transit times.

Both the quasi-coherent oscillations and the (associated) concentration of transport in separable events change highly reproducibly during confinement changes e.g. induced by varying t (Zoletnik *et al.* 2002, Pokol *et al.* 2004). However, the observed changes in amplitude or repetition rate of the events are *not* generally correlated with τ_E itself in a quantitative way, indicating that these phenomena are not generally responsible for the *average* anomalous transport at the edge (Zoletnik *et al.* 1999).

6. Particle and impurity behaviour

The operational limits of W7-AS plasmas turned out to be essentially affected by the properties of particle and impurity transport. In the following section global scalings and local transport quantities as well as the experimental efforts to influence transport properties are described.

6.1. Particle confinement

6.1.1. Stationary particle balance analysis. The particle transport analysis is based on measured profiles of $n_e(r)$, $T_e(r)$ and $T_i(r)$. All particle and energy sources (sinks) are calculated using fits to these experimental data from different diagnostics. The reliability of the particle transport analysis depends significantly on the quality of these profile data, in particular at the outer radii. The (1D) radial particle balance equation for stationary conditions

$$\nabla \Gamma = S_p$$

is solved for the flux-surface averaged particle flux density, Γ . The particle sources, $S_p(r)$, from the recycling and the gas valve (typically used for feedback control of the line density) were calculated by the DEGAS code (Heifetz *et al.* 1982, Sardei *et al.* 1991) in the early phase of W7-AS and by the EIRENE code (Reiter *et al.* 2005, Fiedler *et al.* 1996, Heinrich *et al.* 1997) later; an additional NBI contribution to $S_p(r)$ (i.e. the birth profile) is estimated by the FAFNER Monte-Carlo code (Penningsfeld *et al.* 1996).

Since experimental measurements of the particle fluxes are generally not available, the neutral densities cannot be determined only from the recycling modelling (for given edge temperatures). Consequently, absolutely calibrated H_α -measurements at the dominant recycling zones were compared with the equivalent line-integrated H_α -signals simulated in both codes. This calibration technique allowed for the estimation of the neutral gas profile as well as the ion charge exchange (CX) losses. At W7-AS, however, a sufficient H_α documentation of the major part of the vessel was lacking, so that the particle sources could be estimated only for discharges where the limiter was responsible for the main recycling fluxes.

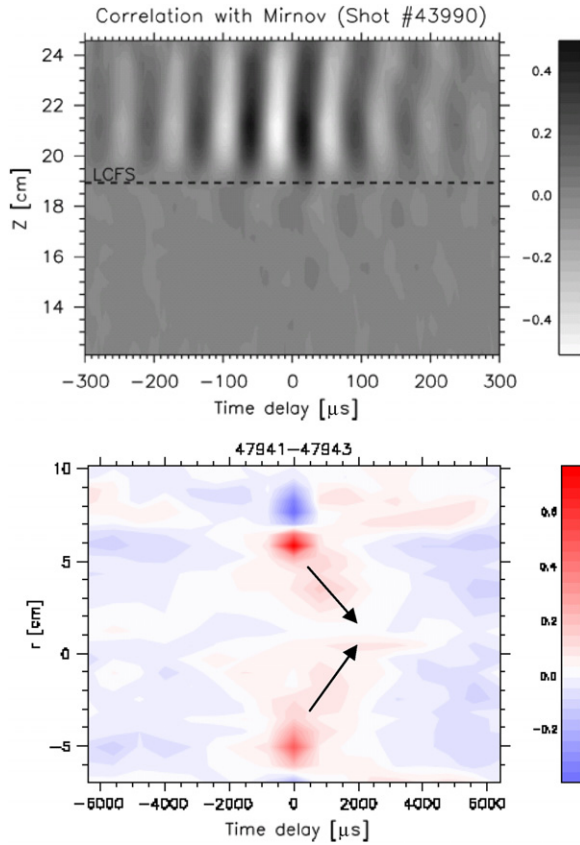


Figure 47. Signatures of transport events and associated quasi coherent activity. (Top) Normalized correlation between signals from Li-beam emission spectroscopy (displaying \tilde{n}_e) and a magnetic probe (\vec{B}_{pol}). The horizontal axis gives the time lag, the vertical distance along the Li-beam coordinates displaying a radial range around the LCFS (upper part of figure: confinement region). (Bottom) Spatio-temporal correlation of the T_e -perturbations. Positive time lag means delay relative to the reference channel at $r = 6$ cm on the low-field side top of figure, the LCFS is at about 8 cm. The transport event appears as an intermediate flattening of the T_e -profile closely inside the LCFS all along the flux surface (low field side and high field side) followed by an inward propagating cold perturbation (Zoletnik *et al.* 2005a).

The neutral distribution from recycling consists of a very low-energy component (roughly the surface temperatures) which is ionized very close to the target and a high-energy component related to the plasma temperatures at the edge. In front of the target, a sheath potential of roughly $2.5 T_e(a)$ (Reiter *et al.* 2005) develops increasing the energy of ions which strike the target. Within the target, these ions are elastically scattered by the target atoms and slowed down by electron collisions; see e.g. Behrisch and Eckstein (1986) for a detailed description. A significant part of the ions are backscattered into the plasma with reduced energy (the others are implanted in the target). Only this fast ion component contributes to the particle sources in the bulk part of the plasma.

At the outer radii, electron impact ionization significantly reduces the neutral inward flux. The rate coefficient for electron impact ionization, $\langle \sigma v \rangle_e$, has a maximum about 100–200 eV but falls for higher T_e , whereas the rate coefficient for CX-collisions, $\langle \sigma v \rangle_{\text{cx}}$, increases with

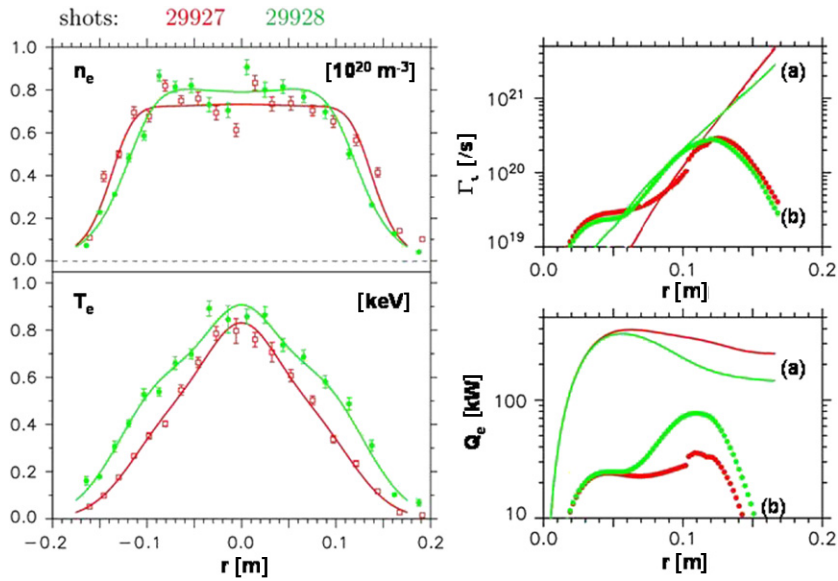


Figure 48. n_e and T_e -profiles (on the left) and particle (upper right) and electron energy fluxes (lower right plot) for ECRH discharges (500 kW) with only slightly different $t_a \cong 0.345$ for shot 29927 and 0.340 for 29928. The solid lines on the right represent the fluxes from the particle and energy balance, and the full circles the neoclassical predictions for both discharges.

T_i up to about 2 keV. (Ion impact collisions are negligible for fairly low ion energies.) With dominating CX-collisions (the average neutral energy becomes close to $3/2T_i$), the neutrals can penetrate deeper into the plasma before they are ionized. Consequently, the bulk plasma is sensitive to the energy distribution of the neutrals entering the plasma and (with respect to the recycling) on the edge ion and electron temperatures. All these processes are implemented in both the DEGAS and EIRENE Monte-Carlo codes. By integrating the particle balance equation, the particle fluxes are estimated and compared with the neoclassical fluxes which are calculated from the DKES database by using the fits to the measured densities and temperatures profiles and by including the ambipolar radial electric field (see section 3.3).

Additional neutral sources have to be considered when using a supersonic gas jet (Yao and Baldzuhn 2003) or pellet injection as fuelling technique (Baldzuhn *et al* 2003c, Baldzuhn and Sandmann 1993, Baldzuhn *et al* 2003a, 2004, Lyon *et al* 1997). The determination of pellet deposition profiles is subject of complex pellet codes (Lengyel *et al* 1999) and was experimentally supported by investigation of carbon test pellets in W7-AS (Bakhareva *et al* 2005, Kuteev *et al* 2003, Ushakov *et al* 1999). However, density and heating scenarios with locally enhanced carbon pellet ablation (Timokhin *et al* 2004, Sergeev *et al* 2006) were identified. This might correlate with the existence of suprathermal electrons in W7-AS (Ledl *et al* 2004) and has to be taken into account with respect to fuelling efficiency.

6.1.2. Particle transport in the plasma core. For ECRH discharges an example for particle and electron energy transport analysis is shown in figure 48. The two discharges at the same line averaged density differ only slightly by the edge value of $t_a \cong 1/3$. Due to the t_a -dependence of confinement (see section 5.2) a good energy confinement in particular at the outer radii is found with the lower t_a -value (#29928, in green). For both examples the neoclassically predicted

particle fluxes are well consistent with the particle balance for the intermediate radii, although the neoclassical electron heat flux is much lower than the one from the energy balance. At the outer radii with low temperatures, the strongly temperature dependent neoclassical transport coefficients are by far too small to fit the fluxes from particle and power balance with the experimental profiles, i.e. transport is ‘anomalous’. At the innermost radii, the neoclassical particle flux exceeds the particle balance one. This is a general tendency in pure ECRH discharges with fairly peaked T_e -profiles at least for the ion-root scenario. Due to the strong inner particle flux and the absence of central particle sources significantly hollow density profiles are predicted in these cases from a purely neoclassical treatment. However, with central ECRH flat density profiles are observed and only a tendency to become slightly hollow with increasing P_{ECRH} . For the electron-root with strong positive E_r , the expected neoclassical fluxes are strongly reduced and might be consistent with the observed particle balance taking into account the uncertainties in particular of the recycling modelling which is sensitive on the edge T_i and T_e .

For the discharge with slightly lower t_a and good confinement (#29928) the associated narrow n_e -profile points towards the Optimum Confinement regime found in particular for pure NBI or combined heating (see section 5.3). The higher edge temperatures in these discharges with narrow density profile have a fairly strong impact on the energies of the inward neutral flux and stabilize the narrow n_e -profile: although the edge neutral density is lower, the neutrals penetrate much deeper into the bulk thereby leading to a higher particle flux for $r \leq 12$ cm. This leads to a bifurcation in the edge density profile as described in the context of the optimum confinement regime (see section 5.3). The equivalent bifurcation character also can be found at fixed $t_a \approx 1/3$ but by a slow variation of the line-averaged density (Heinrich *et al.* 1997).

NBI and combined NBI+ECRH. At W7-AS the NBI constitutes a significant central particle source with roughly $2.5 \times 10^{20} \text{ s}^{-1}/\text{MW}$ power. For comparison the total particle fluxes at the edge were typically several 10^{21} s^{-1} . Beam fuelling usually prevents quasi-steady-state operation with NBI alone, because an increase of the plasma density is observed, which introduces an enhanced impurity radiation and finally leads to a thermal roll over of the plasma (Ringler *et al.* 1987). An exception is the HDH mode, as discussed in section 7.7. Density control despite the central particle fuelling of NBI could be achieved with combined heating by ECRH and NBI. An example of particle balance analysis in discharges with combined heating (830 kW NBI and 330 kW ECRH absorbed power) is given in figure 13. In these discharges the ambipolar neoclassical particle fluxes are in good agreement with the particle balance up to two-thirds of the plasma radius (both the ion and electron energy flux agree with the energy balance in this region). Again, at the outer radii with low temperatures, the neoclassical fluxes are much too low. Experiments combining different ECRH and NBI power levels showed, that the density can be controlled by adding a comparable amount of ECRH power to the NBI power (Erckmann *et al.* 1993a, 1993b, 1995a). An example with time traces shown in section 4.1.4, figure 21 demonstrates that global density control is lost and recovered as ECRH is switched off and on, respectively. In those conditions where the density can be controlled the radial profiles of T_e and n_e show a high similarity to profiles obtained with ECRH only. The density profiles then remain broad and flat and the temperature profile is strongly peaked. In contrast, if the density control is lost the n_e -profiles become peaked and the T_e -profiles are more similar to purely NBI heated plasma profiles, i.e. the central part of the T_e -profile flattens, but T_e is only slightly reduced at the outer radii. In most cases a change of recycling sources or the modification of the NBI particle source are negligible such that the central density increase reflects the improvement of the particle confinement. Neoclassical calculations with the flattened T_e -profile lead to a reduction of the ambipolar particle flux of

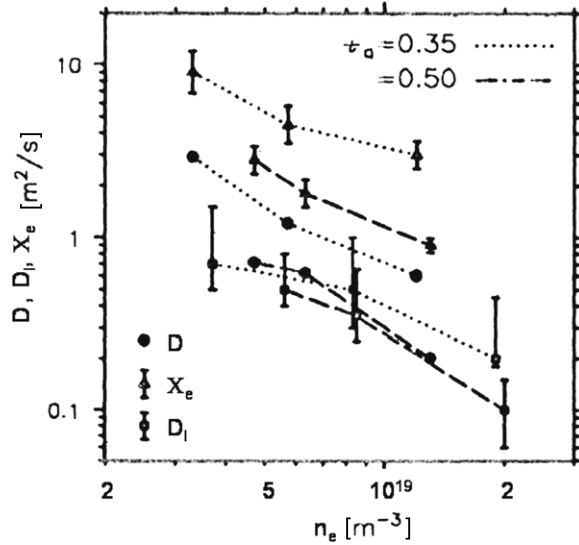


Figure 49. Particle diffusivity, D , and electron heat diffusivity, X_e , versus local density, n_e ($0.8a$), and impurity diffusivity, D_I (obtained by the laser ablation technique), versus central density for ECRH discharges (70 GHz, 2nd harmonic) at W7-AS: $t = 0.35$ at 550 kW ECRH power (dotted lines) and $t_a = 0.5$ at 180 kW (dashed lines).

up to 50% in the central region. For such examples, this so-called ‘ECRH density pump out’ is a purely neoclassical effect determined by the change in the T_e -profile.

The local diffusivity, D was evaluated from a purely diffusive ansatz for ECRH heated discharges at 1.25 T and 2.5 T with values for the edge rotational transform $t_a \approx 1/3$ and 1/2, where good confinement properties are found (see section 5.2). In all cases, D showed a strong increase towards the plasma edge (Sardei *et al* 1990), as was found for the experimental electron heat diffusivity derived from power balance analysis (Kuehner *et al* 1990). A clear ECRH power dependence of the particle diffusivity in the outer confinement region was observed (Ringler *et al* 1990). Lower values of the diffusivities were found at full field operation. The results show that, at least in the outer confinement region, D scales positively with the heating power and negatively with B . As an overview the density dependences of particle diffusivity D , heat diffusivity χ_e from power balance (both at 80% of the plasma radius) as well as the impurity diffusivity, D_I , (from Al ablation) are compared in figure 49 (Maaßberg *et al* 1993a). All these transport coefficients scale roughly with n_e^{-1} , with $D/D\chi_e$ ($r/a = 0.8$) values ranging between 0.1 and 0.3. Experiments disclosing lower edge density as a prerequisite for improved confinement properties reveal a $D \propto n_e^{-2}$ dependence (Heinrich *et al* 1997) for each confinement regime but with lower absolute values for the high confinement case. The latter difference could be resolved by assuming a $(n_e \cdot T_e)^{-1}$ -dependence. However, the different n_e -scaling is not understood and the T_e -dependence has to be carefully interpreted as some additional parameter affecting D .

6.1.3. Transient particle transport analysis of the bulk plasma. The transient particle balance was analysed both for gas feed modulation experiments and for ECRH discharges in which the power deposition was switched from on-axis to off-axis, resulting in a flattening of the T_e -profile. The (transient) particle sources, S_p , are estimated by the EIRENE code and a

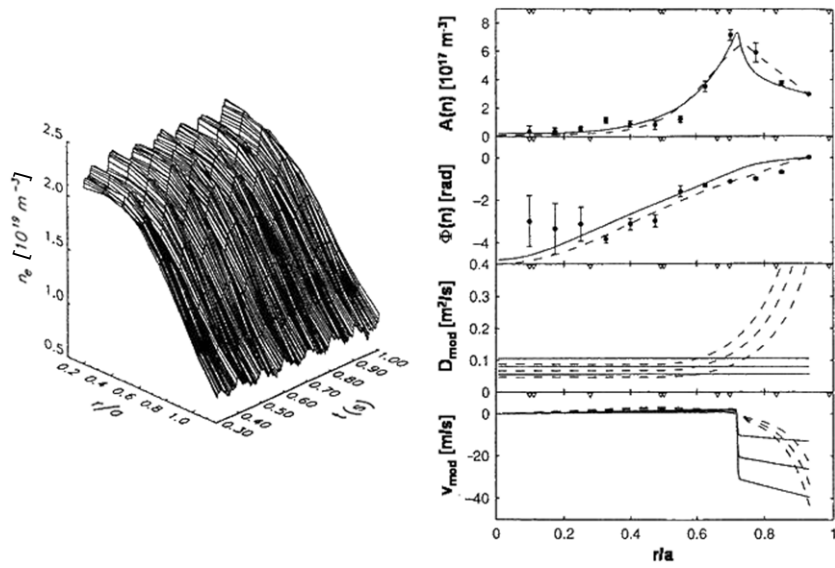


Figure 50. Gas feed modulation experiments. (Left) Temporal evolution of the electron density profile (#36120) during modulation of the gas feed (10 Hz). (Right) Density perturbation amplitudes and phases (circles with error bars) and two models for the transport coefficients D_{mod} and v_{mod} as indicated in the frames below (model 1: solid curves, model 2: dashed curves) (Koponen *et al* 2000a).

non-classical particle pinch term, v , is included in the ambipolar particle flux density

$$\Gamma = \Gamma_e = -n_e \cdot \left(D_{11}^e \frac{n'_e}{n_e} + D_{12}^e \frac{T'_e}{T_e} - v \right)$$

with D_{11}^e and D_{12}^e being the on- and off-diagonal elements of the transport matrix, respectively. Whereas the diffusion coefficients and the pinch term cannot be resolved for the stationary analysis, the transient analysis might allow for additional conclusions, in particular on the existence of a significant pinch term. However, a straightforward estimation of both terms is not possible in the strict mathematical sense as it is discussed in section 5.3. A 10-channel interferometer (Geist *et al* 1997) combined with a fast profile reconstruction algorithm (Koponen and Dumbrais 1997) was used to analyse the density-profile evolution

$$\frac{\partial n_e}{\partial t} = -\nabla \Gamma_e + S_p$$

during the dynamic phases discharges. Gas feed modulations with frequencies of 10–100 Hz and amplitudes of 1–5% were applied in discharges with $(0.5\text{--}3) \times 10^{19} \text{ m}^{-3}$, $B = 1.25 \text{ T}$ as well as 2.5 T , and ECRH powers of 180–1300 kW (Koponen *et al* 2000a). The temperature gradient driven particle flux, $-n_e \cdot D_{12}^e \cdot T'_e / T_e$ was not treated independently, but (partly) included in the convective modelling. The density modulation amplitudes and phase shifts were approximated by least-squares fitting models of the transient diffusion coefficients, D_{mod} , and convection velocities, v_{mod} . Figure 50 shows the results of this analysis for an ECRH discharge with on-axis power deposition. Either a constant D_{mod} and a step-like v_{mod} (continuous lines in figure 50) or a purely anomalous diffusive ansatz $D \propto n_e^\alpha$ leading to $D_{\text{mod}} = D$ and $v_{\text{mod}} = -\alpha \cdot D \cdot n'_e / n_e$ (dashed lines) were used. In the plasma centre, the particle transport is mainly diffusive except for high ECRH power where an outward convection becomes significant allowing for slightly

hollow density profiles (this effect is equivalent to the T'_e driven flux omitted in this analysis). The strong inward pinch at the outer radii in model 1 supports the density dependent diffusivity of model 2. For both models, the experimental modulation amplitudes and phase shifts are fitted quite equivalently in this example. A regression of the constant diffusivity obtained from all the gas feed modulation experiments yielded $D_{\text{mod}} \propto n_e^{-1.18 \pm 0.13} \cdot T_e^{0.69 \pm 0.22} \cdot B^{-0.51 \pm 0.22}$. The n_e -dependence of this scaling is in good agreement with the stationary particle balance analysis, and the T_e -dependence is also roughly equivalent to the power dependence.

The impact of the (off-diagonal) thermo-diffusivity, $-n_e \cdot D_{12}^e \cdot T'_e/T_e$, was analysed for a discharge in which the ECRH power deposition was switched from on-axis to off-axis and with an additional moderate on-axis deposition in the late phase (Koponen *et al.* 2000b, Stroth 1999). The central T_e -profile changed from peaked to flat, and the n_e -profile from flat to slightly peaked. EIRENE simulations showed that the particle source profile was rather similar in these scenarios. The neoclassical estimate of D_{12}^e was used in time dependent 1D transport simulations with the ASTRA code (Pereverzev and Yushmanov 2002), and an additional convection, v , was adjusted to fit the measured density evolution. The diagonal diffusivity was assumed to scale like $D_{11}^e \propto 1/(r)$ with values typically much larger than the neoclassical ones. An inward convection, $v < 0$, was always needed to compensate the diffusive outward fluxes for the three scenarios in these discharges. The density peaking is possible only when the electron temperature profile is flat. Thus an additional inward convective flux is found in both types of transient particle balance analysis.

6.1.4. Particle transport in the SOL. In the SOL region, the magnetic field topology of W7-AS led to a 3D dependence of the plasma transport. Nevertheless, for purely limiter-dominated configurations ($t < 0.4$) the limiters introduced large-size flux bundles of uniform connection lengths (typically 1, 2, 3 toroidal turns for the standard operation range of ($t \approx 1/3$), which were poloidally decoupled to a good approximation. In this case, the cross-field transport was essentially radial. Parallel losses, on the other hand, could be parametrized by parallel particle confinement time τ_{II} for sufficiently low plasma densities and high temperatures, which implies small longitudinal gradients of the plasma parameters. With this approximation (1D model), least-square fits of radial profiles (measured with Langmuir probes) yielded D values which were best correlated with $D \propto (P_{\text{heat}} - P_r)^{0.85} \langle n_e \rangle^{-1.1}$ where the global parameters non-radiated heating power and averaged density are used (Sardei *et al.* 1992, Grigull *et al.* 1992, 1995). Both the density scaling and the absolute values of D in the SOL matched quite well to those found at the periphery of the bulk plasma from particle equilibrium balance, which gives no indication for different particle transport mechanisms in the density region and in the SOL of W7-AS.

6.2. Impurity confinement

The impurification of plasmas by contact with plasma facing components might be acceptable at low concentrations but can severely limit the machine performance if the impurity content overbalances the equilibrium between impurity radiation losses and heating power. Basically, the impurity content is determined by three mechanisms: the impurity confinement of the core plasma, the impurity sources from the wall and the impurity transport in the edge plasma, which controls the ‘insulation’ of the core from being fed by the intrinsic impurities from the wall. The main part of this section concentrates on the impurity transport in the plasma core. Cases where the global impurity behaviour is affected by particular processes at the plasma edge (H , H^* , HDH) are summarized in section 6.2.4 at the end of this section.

As pointed out in section 3.5, particle transport properties of the background ions cause ambipolar radial electric fields E_r which can be expressed in first order by means of the ion density and temperature gradients as the fundamental thermodynamic driving mechanisms for impurity transport. In the ‘tracer’ approximation E_r is not affected by impurity fluxes. Strength and polarity of the ambipolar fields depend on the stellarator specific transport regimes (v -, $1/v$ -, \sqrt{v} -regime) in the long mean free path range (Galeev *et al* 1979) caused by the three-dimensional magnetic topology. Consequently, certain transport features different from those typically known from tokamaks appear in the stellarator: e.g. contrary to tokamaks where the ‘temperature screening’ of impurity ions is a beneficial mechanism against impurity accumulation, for stellarators all driving forces are predicted to principally support accumulation in the standard ion root (Maaßberg *et al* 1999). Only in low-density scenarios at W7-AS positive ion- or electron-roots can be established in the central plasma as a tool to flush out impurities.

It is therefore essential to proof the experimental evidence for these prospects and to elucidate to what extent the neoclassical predictions can be applied to W7-AS. For this purpose, the dependence of impurity transport on global plasma parameters was investigated (Burhenn *et al* 2004, 2005) as well as local transport coefficients derived and compared with the neoclassical model implemented in the radiation and transport code SITAR (W7A-Team and NBI-Group 1985). After discussing these detailed studies the last part of this section will deal with the general consequences of the observed impurity transport properties.

6.2.1. Impurity transport analysis. Contrary to the modelling of stationary impurity profiles which can only provide local information about the ratio of convective to diffusive fluxes, transient impurity sources offer the possibility to distinguish between both processes. Therefore, impurity transport in W7-AS was investigated by means of the impurity gas-oscillation technique (Unger 1995) but most commonly by analysis of laser blow-off (LBO) experiments (Ledl 1995, Burhenn *et al* 1999) injecting a short pulse (<1 ms) of mostly aluminium as tracer ions in concentrations which neither perturb the global plasma parameters nor affect the aluminium transport coefficients. The temporal behaviour of the spectral emission of different ionization states of the tracer ions after the injection pulse was monitored by VUV, x-ray and visible spectrometers depending on the ionization states—the latter providing the source function of the tracer beam.

The impurity confinement time as derived from the temporal decay of the radiation emitted by the highest ionization states is a global transport quantity. Local transport coefficients were evaluated from the total temporal and spatial radiation evolution measured by the soft-X camera system after the injection (Burhenn *et al* 1999, Weller *et al* 1991). Due to lack of intensity, this method is restricted only to the inner two-thirds of the plasma while for the outer region effective values for the transport coefficients have to be assumed. Uncertainties due to Abel inversion and the iterative procedure taking into account transport in the derivation of the total tracer density evolution from the energy integrated intensity make an exact estimation of the error difficult. From the simulations, an accuracy within a factor of 2 is reasonable.

The studies were partially supported by carbon edge density profiles from Li-beam CXRS measurements (Ehmler *et al* 2002a) and Z_{eff} -values (IR, soft-X camera, Thomson scattering optical set-up and visible to NIR (Krychowiak *et al* 2003)). The experimental data were compared with predictions by SITAR: the expressions for the impurity fluxes

$$\Gamma_I^Z = -D_I \frac{\partial n_I^Z}{\partial r} + v_I \cdot n_I^Z, \quad \frac{\partial n_I^Z}{\partial r} = -\frac{1}{r} \frac{\partial}{\partial r} (r \Gamma_I^Z) + Q_{\text{sources}} + Q_{\text{sinks}}$$

(diffusion coefficient D_I , convective velocity v , both independent of Z) are still based on neoclassical and Pfirsch–Schlueter transport for axisymmetric devices and are therefore of limited applicability. The only modification is the reduction of the impurity fluxes by a factor of 2 in order to account for the ‘effective’ elongation of the flux surfaces (partial drift optimization) compared with a classical stellarator ([Grieger et al 1992](#)). However, first efforts to account for the stellarator specific features indeed indicate a noticeable impact on the impurity transport coefficients and stresses the necessity for consideration of these properties in future codes. Additional to the implemented transport model, SITAR is able to perform transport calculations with a predefined set of transport coefficients or a combination of both.

6.2.2. Impact of global plasma and operational parameters on impurity transport. A scaling law for the impurity (aluminium) confinement time $\tau_I \propto a^{2.4} \cdot \hat{n}_e^{1.2} \cdot B^{0.3} / P_{ECRH}^{0.8}$ with a being the plasma radius and \hat{n}_e the central electron density was derived for plasmas with central densities lower than $5 \times 10^{19} \text{ m}^{-3}$ ([Burhenn et al 1995](#)). The use of P_{ECRH} as a scaling quantity might contain some hidden dependence on ion temperature and collisionality as well as the ion temperature gradients which on their part are determined again by the coupling between ECRH power and ion temperature at different densities. However, the ion temperature was available only for a couple of shots considered in the scaling law. The impact on the scaling due to a spatially varying origin of the emission along radial positions with different confinement properties when changing the temperature could be excluded by comparison of discharges with different densities and heating powers but the same electron temperature. The remarkably strong dependence on heating power P_{ECRH} and density \hat{n}_e which has also been observed at TJ-II ([Hidalgo et al 2005](#)) is a trend which is typically not expected from neoclassical simulations and might point to additional impact of plasma turbulence on impurity transport. No isotope effect and only a weak and therefore ignored dependence on the rotational transform t was observed, except for dedicated limiter plasmas with rather small and well defined aperture ($a = 12 \text{ cm}$), excluding any uncertainties in plasma size introduced by the corrugated last close flux surface at high rotational transform ([Brakel et al 1993](#)). The energy confinement time $\tau_E \propto a^{2.21} \cdot R^{0.74} \cdot \bar{n}_e^{0.5} \cdot B^{0.73} \cdot t_{2/3}^{0.43} / P_{ECRH}^{0.54}$ ([Stroth et al 1996c](#)) with major radius R , average density \bar{n}_e and rotational transform at two-thirds of the plasma radius, $t_{2/3}$, as well as the particle diffusion coefficient $D \propto \hat{n}_e^{-1.18} \cdot B^{-0.51} \cdot \hat{T}_e^{0.69}$ (or alternatively using P_{ECRH} instead of \hat{T}_e : $D \sim \hat{n}_e^{-1.8} P_{ECRH}$) ([Koponen et al 2000a](#)) with central electron temperature \hat{T}_e and density \hat{n}_e show the same trends for the density and heating power dependence, supporting the assumption of turbulent transport being a dominant factor.

Regardless of the transport mechanism (classical or turbulent (gyro-bohm)), a dependence on the toroidal magnetic field according to $1/B$ or $1/B^2$ is expected but surprisingly missing ($\propto B^{0.3 \pm 0.2}$). Hence, two similar NBI, i.e. non-resonant, heated plasmas at 2.5 and 1.25 T central magnetic field strength were compared ([Burhenn et al 2000](#)). Indeed, the impurity diffusion coefficient D_I shows values that are a factor 3 or 4 larger for the case of 1.25 T compared with 2.5 T. However, the inward convection v_I is also increased, so that, finally, the global impurity confinement times do not change.

The most important impact on impurity transport with respect to the machine performance is given by the unfavourable density dependence of the impurity confinement time. Stationary radiation levels can usually be sustained at densities below $5 \times 10^{19} \text{ m}^{-3}$ without problems. Beyond that density the increasing confinement time can reach values close to a second or even more and the intrinsic impurity radiation starts to rise continuously throughout the pulse length. Depending on the impurity flux level from the walls, this can lead to a degradation of the plasma energy by excessive radiation losses at highest densities, being most critical and pronounced in ELM-free H-modes (H^*).

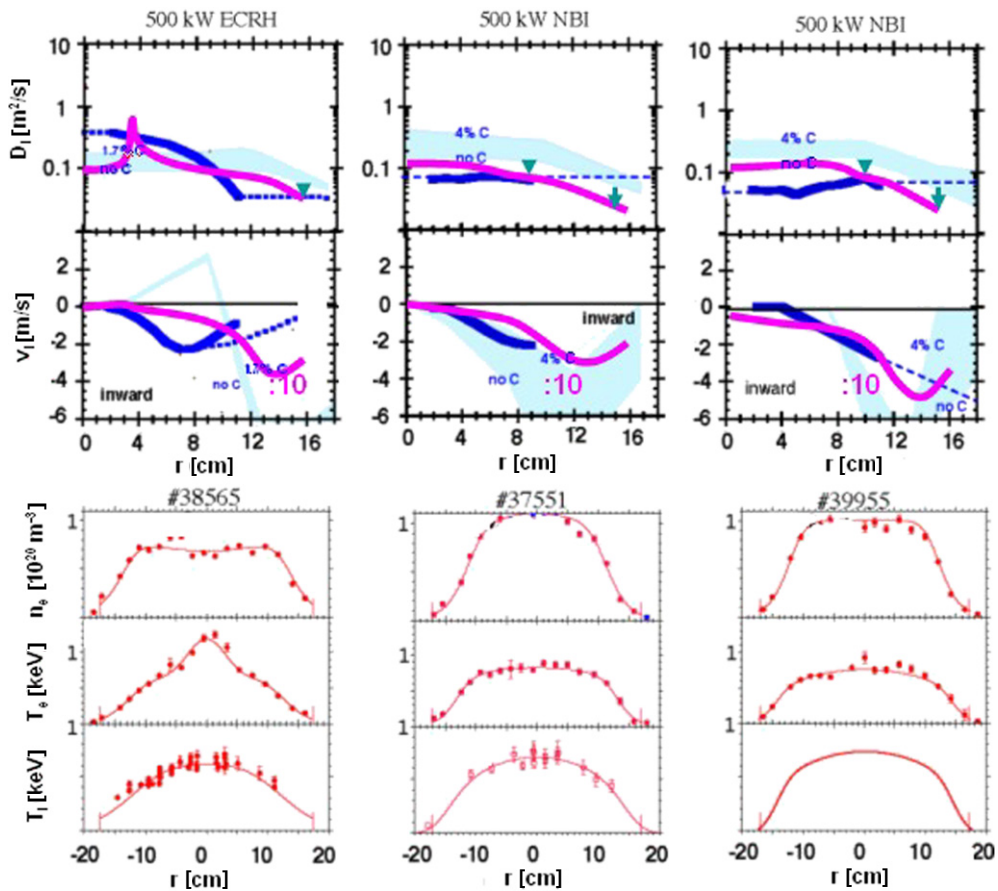


Figure 51. Comparison of impurity confinement in ECRH (left) and NBI (middle and right) heated plasmas; top: comparison of experimental (blue lines) and predicted (shaded areas: traditional neoclassics, magenta lines: 3D stellarator magnetic field included) local transport coefficients (dotted lines are extrapolated in order to match the time traces); bottom: profiles of plasma density and temperature.

Local transport coefficients were derived and compared for medium ($3.5 \times 10^{19} \text{ m}^{-3}$) and high central density ($7 \times 10^{19} \text{ m}^{-3}$) ECRH plasmas (Burhenn *et al.* 1997, 1998). Although at high density a slight peaking of the T_i -profile is observed in the plasma centre, the similar shape of electron density and ion temperature profiles points to no essential change of the ambipolar electric field and the convection velocity, respectively, at these two densities. Within the error bars, this was confirmed by electric field measurements using CXRS. But a clear reduction of the radial profile of the diffusion coefficient by a factor of 2–3 in the high density case (latter shown in figure 51 (left)) was found. A similar trend was observed in TJ-II (Zurro *et al.* 2003). At low density, the higher diffusive transport leads to small confinement times (figure 52 (left), curves (2)) and a shorter time scale for achieving stationarity (figure 52 (right), curves (2)). The increase of radiation at high density (figure 52 (right), curves (1)) and the long confinement time (figure 52 (left), curves (1)) are compatible with smaller diffusion, in particular at the edge, where the reduced impurity fluxes cause longer time scales for achieving steady-state radiation profiles (here: stationarity predicted at 1.7 s, beyond the end of the pulse). The

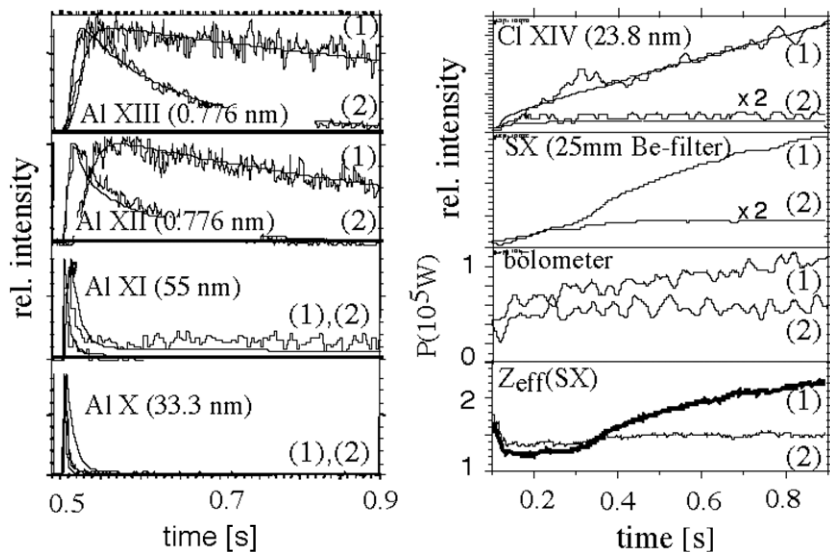


Figure 52. Time traces of aluminium radiation after LBO (left) and intrinsic impurity radiation (right) in a high (1) ($7.0 \times 10^{19} \text{ m}^{-3}$, see figure 51 (left), #38565–38569) and medium (2) density ($3.5 \times 10^{19} \text{ m}^{-3}$, #38705–38709) 500 kW ECRH plasma together with simulations for intrinsic Cl XIV (right top: smooth lines) using experimentally derived D_I , v_I -profiles (for the high density case see figure 51 (left)).

final level of total radiation is then defined by the effective impurity influx which might be acceptable if it is kept small such as by wall conditioning, and proper choice of inboard materials (Brakel *et al* 1992, Ehmler *et al* 2002b), ELM activity or HDH specific screening mechanisms (Feng *et al* 2005a) or reduction of the wall load by active edge radiation cooling (Hildebrandt *et al* 1997).

Therefore, the different temporal evolution of the intrinsic impurities at different densities can be explained by changes in transport alone, without any peculiarities in impurity source rates. This was experimentally confirmed by a constant source of fluorine injected into a high density flat-top discharge (Burhenn *et al* 2000). The fluorine radiation in the plasma core indeed starts to rise continuously, evolving to a fluorine density profile which is clearly shrunken in the gradient region where $(v_{I,\text{inward}}/D_I)$ is high and thus indicating impurity accumulation. Temporal and radial evolution agree well with predictions using the experimentally derived transport coefficients for the high-density case (figure 51(left)).

In contrast to tokamaks, which reveal increasing anomalous diffusion coefficients towards the plasma edge, peaked profiles were measured in W7-AS and TJ-II (Zurro *et al* 2004). This means that the inverse dependence of D_I on density in W7-AS is not reflected in the radial profile of D_I .

Access to higher densities was achieved by NBI heating as ECRH is applicable only below its cut-off density of $1.2 \times 10^{20} \text{ m}^{-3}$ for 140 GHz gyrotron frequency. Figure 53 shows the dependence of the impurity and energy confinement time on plasma density for different heating scenarios (pure ECRH, pure NBI, combined heating ECRH + NBI). The unfavourable scaling of the impurity confinement time (but favourable of the energy confinement time) on density in ECRH plasmas is continued when going to higher density NBI plasmas (dark grey shaded region). Both ECRH- and NBI-heated plasmas in the overlapping high density

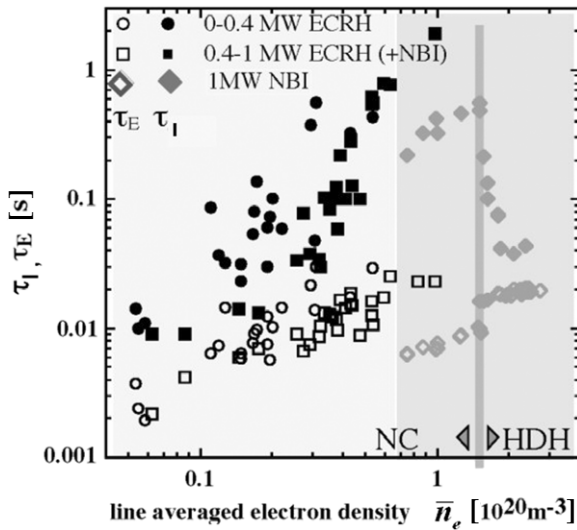


Figure 53. Energy and impurity confinement times versus electron density in normal confinement (NC) ECRH and NBI plasmas, and during the HDH transition (dark shaded region). The discontinuity at the boundary of the two shaded regions is due to smaller plasma apertures in the divertor configuration at $t_a = 1/2$.

region show comparable and extremely long impurity confinement times often suffering from impurity accumulation and loss of density control at highest densities.

Besides density, the heating power also reveals a strong impact on the impurity confinement. Discharges with similar medium density show a degradation of impurity confinement at higher ECRH heating power. This is characterized by shorter decay times after impurity injection and a factor of 2–3 enhanced diffusion coefficients nearly throughout the entire plasma cross-section (Burhenn *et al.* 2004), respectively. This might possibly be an indication for enhanced turbulent transport at increased heating power in agreement with the observed power degradation of energy confinement.

Nevertheless, the observed power degradation of impurity confinement might be a tool to prevent accumulation in high density plasmas up to a certain degree. Figure 54 shows the beneficial impact of increased ECRH heating power on the temporal behaviour of impurity radiation in W7-AS. At higher density a higher heating power level is necessary in order to avoid accumulation. With an applied averaged ECRH power density of about 1 MW m^{-3} accumulation of impurities in a plasma with central density of $8 \times 10^{19} \text{ m}^{-3}$ can be avoided.

6.2.3. Comparison with neoclassical predictions. In spite of an obviously substantial contribution of turbulent transport, in particular at low density, the impact of the underlying neoclassical transport properties should come to the fore, somehow, especially when provoking them by drastic alterations in the main thermodynamic driving mechanisms. One way is the variation of the ambipolar electric field and its impact on the inward convection for impurities by exerting influence on the density and temperature profile shape using on- and off-axis ECRH deposition (Erckmann and Gasparino 1994). Indeed, compared with plasmas with off-axis ECRH launch the strongly peaked electron temperature in the on-axis case causes moderate positive ambipolar fields in the core plasma, resulting in shorter impurity confinement times (Erckmann *et al.* 1995a). Uncertainties in the profile data to that time do not allow for the

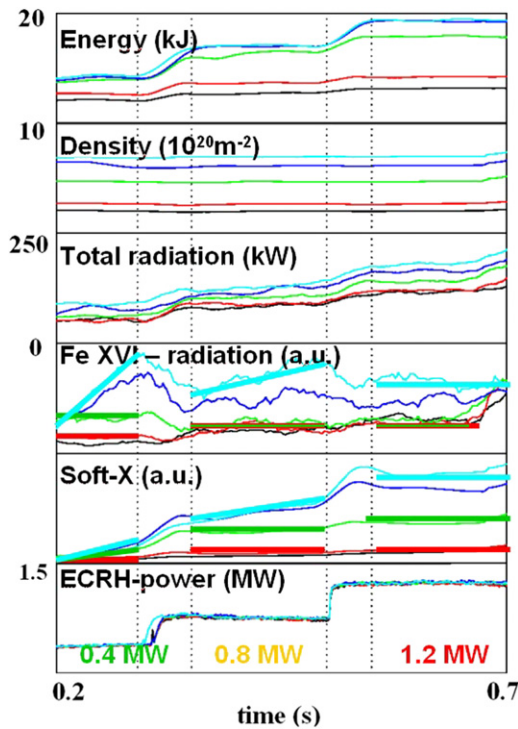


Figure 54. Evolution of impurity radiation in plasmas with different density and ECRH heating power (#43133, 43134, 43140, 43143 and 43144).

conclusion that off-axis ECRH deposition typically results in clearly peaked density profiles. Nevertheless, there is evidence for slightly raised central densities in the off-axis case being consistent with an increase in impurity confinement time. When going to high density NBI heated plasmas, the density profiles partially tend to become peaked. Besides the density dependence of D_I , the long confinement times in those plasmas are therefore assumed to be additionally affected by inward transport inferred by the density gradients.

Another way is to establish either a positive ‘ion-root’ or an ‘electron-root’ in order to produce a positive ambipolar electric field, which should flush out impurity ions. This was demonstrated at W7-AS for the case of helium (Hirsch *et al* 1995a, Baldzuhn *et al* 1997a, Baldzuhn 1998). Unfortunately, the electron root appeared only in an extremely restricted narrow zone in the plasma centre ($r = 1\text{--}3\text{ cm}$), where the helium density profile, indeed, becomes moderately hollow. The effect was expected to appear more distinctly but is in agreement with the high diffusion coefficients derived from aluminium laser blow-off experiments (assumption $D_{\text{He}} = D_{\text{Al}}$), which smears out the radial helium distribution. Due to the strong localization of the effect no remarkable change in aluminium confinement time—which was anyhow short at these low densities—was measured. Moreover, the role of the counteracting negative electric field of the ion-root, present in the outer half of the plasma, has additionally to be considered.

In spite of similarly long impurity confinement times in the overlapping density region for both NBI and ECRH plasmas, there are typical differences in the radial profiles of the local transport parameters for both heating scenarios (Burhenn *et al* 2004). ECRH-heated plasmas reveal comparatively high diffusion coefficients in the central plasma region with low

values at the plasma edge, whereas NBI-heated plasmas exhibit rather flat D_I -profiles with strongly increasing inward convection v_I towards the plasma boundary (figure 51(top)). The comparison of the predicted and measured diffusion coefficients shows a severe discrepancy in the sense that the experimental values in the edge region of high-density ECRH plasmas, and even more pronounced, over the entire plasma in high-density NBI discharges, fall below the predicted ones by a factor of 3–8. This is not the case for low-density plasmas where the measured transport is typically higher than the predictions. At present, it is not clear whether this deviation is a problem of stellarator specific features, which are not considered in the existing model (see section 3). As a first step to test the influence of stellarator specific transport properties on the predicted confinement, the impact of the ambipolar radial electric field produced by the ambient plasma on monoenergetic transport coefficients was calculated by the DKES code in full three-dimensional magnetic topology and inserted in figure 51(top). An additional background impurity species was not considered in this first approach. The diffusion coefficients—in fact—tend to drop towards the plasma edge, where the electric fields become large, and seem to slightly better approach the experimental data. The high inward convection in the presence of the comparable low diffusion coefficients is qualitatively in agreement with the observed accumulation.

6.2.4. Improved confinement regimes. ELM-free H-modes (H^*) could be established at higher densities and were afflicted with extremely long impurity confinement times and strong accumulation. The resulting radiation losses generally cause a fast degradation of the plasma energy and were responsible for the transient nature of this mode (McCormick *et al* 2003c, 2002). However, the change in the impurity confinement time when entering this mode from a normal confinement mode appears not always as spectacular as expected, because the impurity confinement is already long in normal confinement plasmas at this density (see section 6.2.2). As in tokamaks, a beneficial mechanism to reduce the central level of accumulation in H^* plasmas in the face of long impurity confinement might be the onset of ELM activity which acts instantaneously on the edge confinement and seems to reduce the effective impurity influx to the core. The bulk radiation reacts slowly on the time scale determined by the transport coefficients and tends to saturate. Nevertheless, the processes involved during ELMs are quite complex (Weller *et al* 2001) and the impact on impurities needs more detailed analysis.

With the island divertor (Grigull *et al* 2003b, Jaenicke *et al* 2002b) a transition to a stationary high density H-mode (HDH) (see section 7.5) at even higher densities than for H^* -mode plasmas could be established: beyond a NBI heating power dependent threshold density ($(1.5\text{--}2.1) \times 10^{20} \text{ m}^{-3}$), the impurity confinement time drops sharply by more than a magnitude down to values comparable to the energy confinement time (figure 53). Simultaneously, the energy confinement time rises by nearly a factor of 2. Unlike the impurity behaviour in high-density normal confinement plasmas below the threshold, the degraded impurity confinement, the screening of impurity influx and the improved density control in HDH now permit access to stationary high-density operation up to densities of $4 \times 10^{20} \text{ m}^{-3}$. At the transition from normal confinement to HDH-mode, the plasma density profile changes from a peaked one to an extremely flat profile with steep edge gradients (figure 55). The plasma temperature profile does not essentially change. In order to explain the low and stationary radiation level in HDH, two beneficial effects have to be considered separately. First, the high edge density in HDH reduces the edge temperature in such a manner that impurity influx is effectively screened by friction with outstreaming plasma ions (Feng *et al* 2005a). Second, laser blow-off transport analysis indicates a degraded impurity core confinement in HDH caused by a reduced inward convection (Burhenn *et al* 2002). The diffusion coefficient

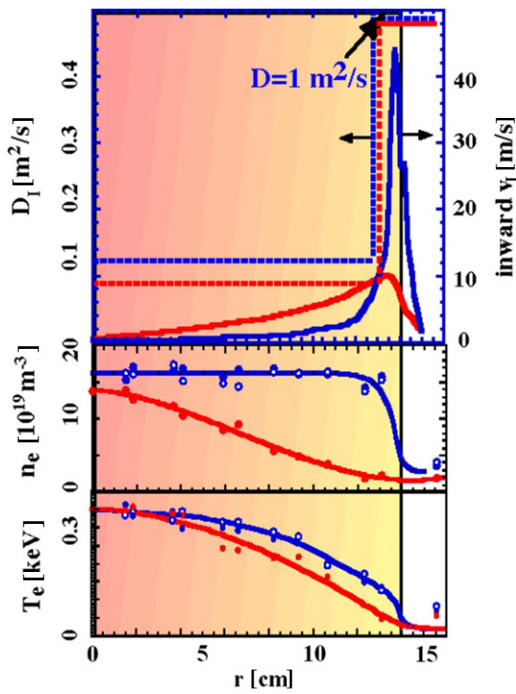


Figure 55. (Top) Transport coefficients for a NC (red) and HDH (blue) plasma with 1 MW NBI heating power. The shaded region is the confinement region of the plasma with separatrix around 14 cm. (Middle and bottom) Density and temperature profiles.

does not change very much. The latter is qualitatively in agreement with the traditional picture that flattening of density profiles reduces the central inward flux in the presence of nearly unchanged outward directed fluxes (temperature screening). However, this approach ignores the classical prediction of large inward convection at the plasma edge where strong density gradients evolve during flattening of the central profiles. Contrary to tokamaks where anomalous transport dominates the plasma edge such inward fluxes might be of importance in stellarators. Moreover, in standard ‘ion-root’ plasmas, negative temperature gradients do not screen impurity influx but support accumulation.

Coupling the inward velocity to the local radial electric field as a driving mechanism (Ida *et al* 2003, Burhenn *et al* 2002) supports the reduction of the inward convection in the HDH core plasma, but in fact reveals a strongly increasing inward convective velocity at the plasma edge (figure 55). The reason is the steep pressure gradient in the boundary of HDH plasmas from which large negative radial electric field strengths and, consequently, large inward convective velocities are derived. In spite of the reduced central inward convection, this enhanced inward velocity layer at the plasma edge implies now long confinement times, which are in contradiction to the small experimental ones. Consequently, the diffusion coefficient, which was assumed radially constant, had to be artificially increased at the plasma edge (in the region of the high inward convection layer) in order to match the short experimental confinement times. This is compatible with Li beam-CXS measurements of C^{6+} density profiles showing a step-like drop at the plasma edge in HDH which could only be successfully reproduced under the assumption of enhanced edge diffusion figure 55 (Ehmler *et al* 2002a, Burhenn *et al* 2004).

Neoclassical predictions for HDH and normal confinement by SITAR ([Burhenn et al 2003](#)) show remarkable similarities to the experimentally derived transport coefficients in figure 55, in particular, the strong rise in the edge inward convective velocity in HDH. In fact, simulated time traces of injected aluminium ions reveal long decay times for both high density normal confinement (as expected: due to the high central inward convective velocity) as well as for HDH (due to the strong edge inward velocity). The only way to match the short experimental confinement time in HDH was the introduction of an artificial edge layer with enhanced diffusion at the location where the inward convection is high. Depending on the size and extension of this diffusive zone, nearly any decay time can be produced. Consequently, each change in transport in this edge localized region—either by turbulent transport, mode activity, frequent ELM activity or other mechanisms—will affect the global impurity confinement.

However, still no definite evidence for enhanced turbulent transport or mode activity at the plasma edge in the HDH regime was found. Nevertheless, the strong sensitivity of the impurity confinement to the relative location of such a diffusive layer with respect to the inward velocity layer points to the key role of edge transport for the global confinement properties of impurities. This is supported by comparison of HDH and the ELM-free H-mode (H^*) ([McCormick et al 2003a](#), [Burhenn et al 2004, 2002](#)) which—besides certain differences in the absolute central density—both reveal quite similar density and electron temperature profiles. Nevertheless, the H^* -mode—opposite to the HDH—mode—reveals an extremely long impurity confinement time, indicating that the core plasma is not exclusively responsible for the global impurity confinement but, moreover, additionally the edge plasma properties.

A more extensive analysis of the HDH feature is the subject of further theoretical approaches ([Igitkhanov et al 2002, 2006](#)).

6.3. Density limit

In the following section the general consequences of the transport phenomena at high density (investigated in detail previously) for the achievement of high-density machine performance are described. In contrast to tokamaks, current-free stellarators do not suffer from current-associated disruptions and show no indications for an ‘absolute’ density limit. Instead the limit is determined by radiation losses, basically controllable by heating power and therefore ‘soft’. Naturally, the stellarator has to distinguish between a density limit for quasi-stationary plasmas and a systematically higher density limit, which can be achieved in transient discharges.

As mentioned, the time constant for reaching steady state with respect to the local radiated power is determined by the transport coefficients of the impurity ions. The key values for stationary radiation are determined by the ratio of the inwards pinch velocity and the diffusion coefficient: the time constant for reaching steady state, the peaking of the final impurity ion density profile and, for a given impurity source strength, the central value of impurity concentration at steady state ([Fussmann 1986](#)). At low densities stationarity can be reached rather fast and discharges can be sustained with a low and constant level of radiation loss. In contrast at high densities, a steady increase of radiation and a peaking of the impurity density profile (accumulation) with long equilibrium times partly in excess of the pulse length takes place. If the total core radiation level exceeds 50–60% of the input power, degradation of the plasma energy is observed, leading to even enhanced radiation losses and, finally, to the termination of the pulse by radiative collapse. The critical plateau density above which radiation losses are no longer stationary and the diamagnetic energy begins to decrease throughout the pulse duration represents a density limit for the achievement of stationary high density plasmas. Its quantification depends on the actual intrinsic impurity content and species,

and hence on machine condition and experimental scenarios. Beyond this limit if the impurity sources are large, a radiation collapse can take place already long before the final stationary radiation level has been established. In these cases the achievable pulse length becomes a function of the density. In transient discharges or density ramp-up experiments, those values where denoted as a ‘density limit’ at which the maximum diamagnetic energy starts to drop by radiation cooling during the course of the pulse. However, these values represent upper estimates for the stationary density limit, because the thermal collapse would also happen in stationary discharges at slightly lower density but, due to the long transport time scale, correspondingly later (possibly not within the pulse duration).

Time dependent simulations of the bolometer ([Giannone et al 2002b](#)) and soft x-ray radiation were carried out ([Giannone et al 1999](#)) using density and temperature profiles, ASTRA ([Pereverzev and Yushmanov 2002](#)), STRAHL ([Behringer 1987](#)) and simple assumptions about the impurity flux at the boundary and the measured impurity transport coefficients. The combination of a simple two-point model for the plasma edge with ASTRA allowed time dependent simulations of the density and temperature in front of the limiter being essential for the power balance at the plasma edge.

6.3.1. Limiter discharges. W7-AS limiter discharges are stationary at low and medium density. At high constant line integrated electron density a maximum in diamagnetic energy is reached until with rising total radiated power (reinforced by a peaking of the impurity ions ([Giannone et al 1999](#)) the diamagnetic energy falls. Finally the discharge terminates or recovers. ECRH power ramp down experiments confirm that the density limit in stellarators is determined by the power balance of input power and radiated power ([Giannone et al 2000b](#)). When the radiated power approached the total input power, the plasma underwent disruption-free contraction. Apparent differences in total radiated power in discharges with NBI, ECRH or combined heating could be understood in terms of the difference in temperature evolution of each discharge.

A magnetic field and power scan was carried out for NBI heated plasmas. These results were compared with an empirical stellarator scaling law for density limit discharges with peaked central radiation ([Itoh and Itoh 1988](#), [Sudo et al 1990](#)):

$$n_{\text{dl}} \propto 0.25 \left(\frac{PB}{a^2 R} \right)^{0.5}, \quad (6.1)$$

where the line integrated density, n_{dl} (10^{20} m^{-3}), is expressed in terms of the magnetic field, B (T), deposited NBI power, P (MW), minor radius, a (m) and major radius, R (m). The pre-factor depends on impurity species, concentration and transport and successively increases by improved wall conditioning, wall coating (boronization) and installation of carbon divertors. For the devices W7-A, Helitron-E, CHS and W7-AS, the square root dependence of the density limit on power and magnetic field could be verified ([Grigull et al 1998](#), [Giannone et al 2000a](#)). However, in W7-AS and LHD, densities higher than predicted by this scaling law were achieved in discharges with strong edge radiation (e.g. the partially detached HDH-mode in W7-AS as shown in figure 56). They have a density limit scaling with only slightly different parameter dependences but a different pre-factor. This clearly demonstrates that the pre-factor and the density limit, additionally, depend strongly on the radial location of the radiation emission. As mentioned, central radiation losses beyond 40–50% of the input power severely affect the power balance by reduction of the net heating power whereas nearly 70–90% power loss at the plasma edge can be accepted in partially detached HDH divertor plasmas without thermal instability. At even higher density the plasma completely detaches and collapses.

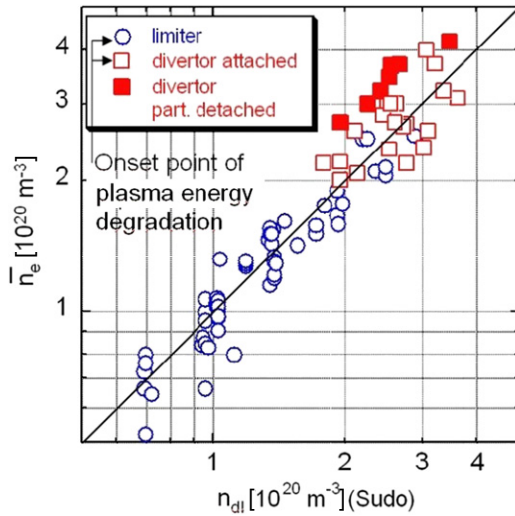


Figure 56. Maximum densities of NBI discharges in W7-AS for limiter, attached divertor and partially attached divertor scenarios versus the density limit according to [Sudo et al \(1990\)](#). Filled squares: quasi-stationary discharges.

6.3.2. Divertor discharges. The unfavourable density dependence of impurity transport connected with impurity accumulation is also valid for plasmas at high rotational transform (around $t_a \approx 1/2$) in which the separatrix is formed by an island chain at the boundary of the plasma instead of by limiters. Beyond a certain density and in special windows of the edge rotational transform, these magnetic configurations, moreover, allow achievement of H-mode plasmas which also initiate a radiation collapse if they are ELM-free. H-mode plasmas with strong ELM activity reached an equilibrium state with respect to the radial profiles of radiated power within the duration of the discharge (2 s). These observations suggested that the latter scenario, as in tokamaks, could be one path to steady-state confinement in stellarators ([Giannone et al 2000b](#)).

At densities below the HDH threshold ([Giannone et al 2002a](#)) in discharges at 1.25 T, a series of oscillations in the radiated power and diamagnetic energy was observed. This cycle of plasma cooling, decrease in diamagnetic energy, impurity loss, subsequent plasma reheating and increasing total radiated power was also observed in limiter plasmas and at LHD ([Giannone et al 2000b](#), [Takeiri et al 1999](#), [Nakamura et al 2002](#), [Peterson et al 2001](#)) and is an instructive example of a periodically perturbed power balance.

In contrast to discharges at densities below the HDH-threshold or limiter discharges, where centrally peaked radiation profiles increasing with time ultimately led to a radiation collapse, divertor discharges in the HDH regime show steady-state hollow radiation profiles. One important condition for the avoidance of a thermal instability and thus the achievement of stationary operation is the sustainment of at least partial detachment. Under this condition, the SOL is still able to be supplied with heating power by fast parallel conductivity. With the onset of total detachment this is only possible by the smaller radial transport channel, leading to an imbalance of the local power balance and hence to a radiation collapse.

From magnetic field and power scans of NBI heated plasmas for density limit discharges in the HDH configuration, the experimentally measured density limit was compared with predictions made by an empirical density limit scaling law derived from power balance

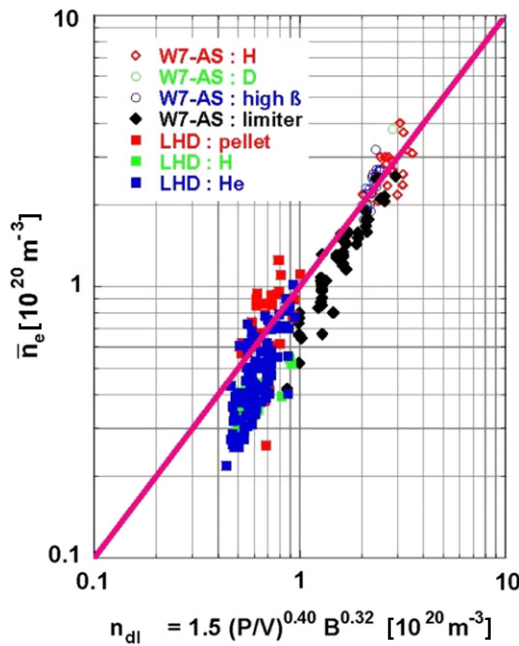


Figure 57. Comparison of achieved and predicted values of line integrated densities, \bar{n}_e , for density limit discharges in LHD and the divertor configuration of W7AS with the scaling law derived from edge radiation dominated plasmas. The predicted maximum of line integrated density, $n_{dl}(10^{20} \text{ m}^{-3})$, is expressed in terms of the magnetic field, B (T), deposited NBI power, P (MW) and plasma volume, V (m^3).

considerations for edge radiating plasmas. Combining the power balance considerations for discharges with dominant edge radiation (Wobig 2000), as found in the divertor HDH mode, with the stellarator energy confinement time scaling law ISS 95 (Stroth *et al.* 1996c), expressions were derived for the expected values of the maximum line integrated density (Giannone *et al.* 2003):

$$n_{dl} \propto \left(\frac{P}{V} \right)^{0.4} B^{0.32} t_{2/3}^{0.16}, \quad (6.2)$$

where the line integrated density, n_{dl} (10^{20} m^{-3}), is expressed in terms of the magnetic field, B (T), deposited NBI power, P (MW), rotational transform at two-thirds of the plasma radius, $t_{2/3}$, and plasma volume, V (m^3). Introducing the plasma volume and neglecting the weak t -dependence, this scaling law basically reproduces quite similar parameter dependences to the expression for centrally peaked radiation profiles (equation (6.1)) but with a higher pre-factor. This clearly points out the edge radiation to be more advantageous with respect to power balance. Figure 57 shows the comparison between this heuristically derived scaling law and the experimental results from the stellarators W7-AS and LHD (Peterson *et al.* 2004). Even the high beta discharges in W7-AS at magnetic field $B < 1.25$ T, which also showed HDH signatures and dominant edge radiation, followed the predicted scaling. In this diagram, the density limit values of line integrated densities for limiter discharges are also displayed for comparison. Of course, these values tend to lie below the predicted density limit scaling for the HDH mode. The line integrated densities achieved in the HDH mode are significantly larger than the Greenwald density limit for tokamaks.

At the density limit, the HDH plasma detaches completely and starts to collapse. Modelling with EMC3EIRENE for a detached HDH-plasma predicts radial field line compression on the low field side and a higher heat flux into the island SOL than on the high field side ([Feng et al 2003a](#)). This leads to a poloidally asymmetric temperature distribution in the islands, and the lower temperature on the high field side favours the carbon radiation. The line integrated measurements of the bolometer cameras in the vicinity of the divertor were consistent with this prediction. Tomographic inversion of the two main bolometer cameras showed that a poloidally asymmetric feature appeared and grew as the density limit was approached.

A scaling for the maximum β as limited by radiation and power balance in the plasma boundary can be derived from the definition of plasma beta, β , substituting of the energy confinement scaling ISS 95 ([Stroth et al 1996c](#)) for τ_E including a factor 2 enhancement factor for the HDH mode and substituting of n_{dl} using equation (2) ([Giannone et al 2003](#)):

$$\beta = 1.38 \times 10^{-2} a^{-0.19} R^{-0.46} P^{0.66} B^{-1.11} t_{2/3}^{0.51}. \quad (6.3)$$

The parameters are the minor radius, a (m), major radius, R (m), magnetic field, B (T), deposited NBI power, P (MW) and rotational transform at two-thirds of the plasma radius, $t_{2/3}$. Substituting typical values for W7-AS with $P_{\text{NBI}} = 3$ MW, $a = 0.155$ m, $t = 0.52$, $R = 2.1$ m and $B = 0.9$ T predict $\beta = 2.3\%$, constrained by density limit and boundary radiation considerations. In comparison, $\langle \beta \rangle$ values of 3.4% were attained in W7-AS beta limit experiments (see section 10.3, [Weller et al \(2001, 2002b\)](#)). However, this prediction must be understood as a simple estimate, since details of the impurity transport coefficients and impurity concentrations will finally decide the achieved beta limit.

6.4. Summary

In the core of NBI plasmas particle transport is basically neoclassical. However, for low-density ECRH discharges, the experimental fluxes in the plasma centre are generally larger than predicted. In contradiction to neoclassical theory, a particle inward pinch is indicated, which might be assigned to turbulent transport or nonlinear ECRH-plasma interaction. Towards the edge, the experimental fluxes exceed the neoclassical ones, approaching each other at high density. Strongly peaked temperature profiles in the case of on-axis ECRH deposition imply degradation of particle confinement by thermodiffusion and allow for stationarity—if added with comparable power—even in high density NBI plasmas, which usually suffer from loss of density control. The scaling of the particle diffusion coefficient (positive with heating power, negative with magnetic field and density) gives no indication for different particle transport mechanisms in the density gradient region and in the SOL of W7-AS. Similar scaling was found in the plasma core, revealing the electron temperature as a more appropriate scaling quantity than the heating power ([Koponen et al 2000a](#)).

Impurity transport scales with global plasma parameters similarly to energy and particle transport and is assumed to be governed by turbulent transport at low density with increasing neoclassical character at high densities. For densities below $5 \times 10^{19} \text{ m}^{-3}$ quasi-stationary plasmas with constant radiation losses could be sustained instantaneously. The unfavourable density dependence leads gradually to accumulation beyond this density on a time scale, which can be larger than the pulse length. The final stationary radiation level is then determined by the impurity source strength and might be acceptable if the sources are kept low. A technical way to reduce the accumulation is the utilization of the heating power degradation of impurity confinement or the establishment of an ELM phase in H-mode plasmas. High density NBI plasmas are typically afflicted with strongly peaked radiation losses which lead to a degradation

of plasma energy—and a termination of the pulse duration by a radiation collapse. This defines a ‘soft’ density limit in W7-AS which is basically controllable by heating power. In contrast to tokamaks, the current-free W7-AS stellarator showed no indications for an ‘absolute’ density limit.

The appearance of the divertor HDH mode beyond a power dependent threshold density provides access to stationary operation up to densities of $4 \times 10^{19} \text{ m}^{-3}$. Besides an improved energy confinement, the impurity confinement is beneficially degraded in HDH by reduction of the central inward pinch causing edge dominated radiation losses. Expressions for the density limit for peaked and edge dominated radiation profiles were derived whereas edge localized radiation losses allow for higher density limits (e.g. HDH). Comparison of the HDH and H* modes points to the relevance of edge transport for the final understanding of the impurity behaviour in the HDH mode. The consideration of stellarator specific impurity transport properties additional to the usual transport models for axisymmetric devices appears to be highly relevant for future modelling and understanding of stellarator transport. The absence of temperature screening of impurities—as a neoclassical tool for purification—is not predicted for stellarators in the standard ion root or at least only for highly collisional regimes of the background gas. The shielding effect of positive electric fields on impurity ions was principally demonstrated at W7-AS but without influence on the overall confinement due to the restriction to the plasma centre. Consequently, operational regimes with mainly positive radial electric fields in relevant collisionality regimes, HDH mode like bifurcations or the controlled utilization of other purifying mechanisms (e.g. ELMs) have to be explored at W7-X.

7. H-mode regimes

The first stellarator experiment to achieve a transition into the H-mode was W7-AS in 1992 ([Erckmann et al 1992a, 1993d](#), [Wagner et al 1994a](#)). Since then H-mode related phenomena have been observed in several helical devices (a summary is given in [Wagner et al \(2006\)](#)). Most characteristics of the quiescent H-mode (H*) in W7-AS (section 7.1) are identical to those well known from tokamaks, demonstrating that the H-mode is a generic regime of toroidal confinement (for a discussion see [Wagner \(2007\)](#) and references therein). In particular, a layer of strongly reduced turbulent transport occurs and disappears on a fast ($<100 \mu\text{s}$) timescale just inside the last closed flux surface. The abrupt change of plasma and turbulence characteristics there and the existence of a back-transition indicate a bifurcation phenomenon. The close correlation in the dynamics of turbulence and flows supports the picture of turbulence suppression by sheared flows ([Biglari et al 1990](#)) as a basic element of the transition physics (section 7.2). In W7-AS a strong poloidal flow velocity develops in the H-mode at the plasma edge and the associated $v_\theta B_\phi$ term deepens the well in E_r , which already exists before the transition as a consequence of the ion-root conditions of neoclassical fluxes. This development of a strong and remaining $v_\theta B_\phi$ is in contrast to tokamak observations where, in the fully developed H-mode, E_r is balanced mainly by the ion pressure gradient; the $v \times B$ term, however, is considered to play the role of a trigger right at the transition. ELMs (section 7.3) break the transport barrier also in W7-AS; they define the edge dynamics for a variety of regimes. The quiescent H-mode can be reached in selected configurations only. Besides this configuration dependence, the operational range of H-mode regimes (section 7.4) is characterized by the absence of a clear power threshold and the appearance of H-mode related phenomena early in the discharge. This and the apparent importance of poloidal flows v_θ are indications that stellarator-specific conditions, discussed in section 7.8, facilitate the spin-up of sheared flows and thus the H-mode transition.

Two more regimes of improved edge confinement with H-mode related characteristics exist: the standard ion-root optimum confinement regime (OC, see section 5.3.2) develops at medium densities with inward shifted density gradients (low recycling fluxes) and broad T_i -profiles. It has large negative values of E_r as well and thus edge gradients ∇E_r , which even exceed those observed in H^* . OC often shows grassy ELMs. In contrast to the quiescent H-mode, the OC regime evolves gradually on a transport timescale without a sudden transition (or back transition) and has no layer of complete turbulence suppression.

With the divertor a new regime, the high density H-mode (HDH), was achieved (Grigull *et al* (2001b), McCormick *et al* (2002), sections 7.5–7.7). It is obtained at a power dependent threshold density in excess of $1.5 \times 10^{20} \text{ m}^{-3}$ either after an ELM phase or starting from a quiescent H-mode, respectively. Its key elements are favourable energy confinement, high separatrix densities which allow divertor operation and, in particular, the purification of the plasma from impurities. The latter enables quasi-steady-state conditions and detached divertor operation, thereby offering favourable conditions as an operational regime for future stellarators.

7.1. The quiescent H-mode

The transition to a quiescent H-mode (H^*) (figure 58) is marked by the sudden and nearly complete suppression of turbulence at the first few centimetres inside the confinement region (figure 58, lowest trace). The power of broadband magnetic- and density fluctuations ($50 \text{ kHz} < f < 600 \text{ kHz}$) measured by magnetic probes, microwave- and laser-scattering (Holzhauer *et al* 1996, Holzhauer and W7-AS Team 1996, Basse *et al* 2003) and reflectometry (Estrada *et al* 1993b, 1994, Brañas *et al* 1995, Hirsch *et al* 1996b) drops by more than an order of magnitude within about $100 \mu\text{s}$. Outside the LCFS fluctuations remain unaffected on this fast timescale. This reduction of turbulence constitutes a transport barrier in the outermost 3–4 cm of the confinement region where gradients of n_e , T_e and T_i immediately start to rise (figures 58(c)–(e)). Particle and heat fluxes to the divertor targets reduce as indicated by the drop in H_α -light (figure 58(a)) and by target probes (Grigull *et al* 1999a). The global energy confinement time obtained as $\tau_E = \frac{W_{\text{dia}}}{P_{\text{heat}} - \partial W / \partial t}$ increases by up to a factor 1.65 (McCormick *et al* 1999b) (figure 58(b)). The increased particle confinement is displayed indirectly by a reduction of feedback controlled gas puff (with the danger to lose density control).

In the fully developed H-mode (i.e. after 2–3 confinement times) edge pedestals have developed both for T_e and T_i (figure 59, temporal evolution in figure 58). As quite steep ∇n_e exist already prior to the quiescent H-mode (see section 6.1) the transition results in a rise of the edge density gradient by 40–60% (figure 58(b)) rather than in a pedestal structure (Kocsis *et al* 1995, Hirsch *et al* 1996b); the separatrix density falls (Kocsis *et al* (1995), McCormick *et al* (1999b) and figure 58(c)). If the quiescent phase can be stabilized over a sufficient time, density fall-off lengths $(\nabla n/n)^{-1}$ as short as 1 cm have been observed (Knauer *et al* 1999). Due to a strongly increased impurity confinement (see bolometer signal in figure 58(b)) a radiative zone develops inside the transport barrier, for example see figure 74. After a few confinement times (50–100 ms) H^* suffers from excessive radiation losses which ultimately lead to a back-transition to an ELM state or a radiative collapse (figure 58(a) and section 6.3). An alternative is to access the HDH regime by ramping up the density as described in section 7.7.

As a characteristic signature of the H-mode, the gradient of the radial electric field, ∇E_r (obtained from spectroscopy, see section 3.3) increases just inside the separatrix (figure 58(f)). Profile examples $E_r(r)$ are given in Hirsch *et al* (2006) and Wagner (2007). Prior to the

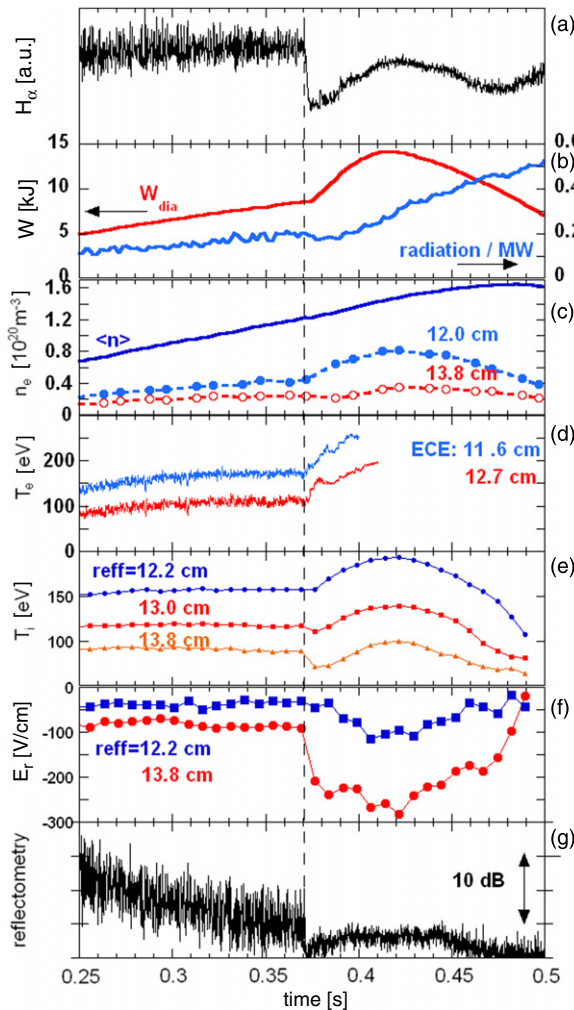


Figure 58. Discharge which undergoes a transition to the quiescent H-mode during a preprogrammed density ramp (#45265, $B = 2.5$ T, $t_a = 0.56$, separatrix at $r = (14 \pm 0.5)$ cm, 0.4 MW NBI heating): (a) H_α from a target, (b) energy and radiated power, (c) average density (interferometry) and edge densities from Li-BES. (d) edge T_e close inside the separatrix (from ECE, the plot ends when the inner time trace reaches cut-off). (e) edge T_i traces (passive spectroscopy). Right after the transition T_i decreases at the separatrix but increases inside the barrier, (f) E_r close inside the separatrix obtained from the Doppler shift of impurity lines (BIV-emission) and (g) reflectometry signal as uncalibrated monitor of turbulence at $r = 13.4$ cm (note the log scale).

H-mode the negative values of $E_r(r)$ inside the radius with maximum gradients are close to neoclassical predictions for the ion-root which can be approximated by $E_r \approx \nabla p_i/(e \cdot n)$ (section 5.3.2, equation (5.4)). Further out where $\delta_{12}^i = D_{12}^i/D_{11}^i > 1$, the thermo-diffusive contribution is more important and thus the neoclassically calculated electric field becomes $E_r \geq \nabla p_i/(e \cdot n)$ (Ehmller *et al.* 2003b). For a discussion of possible additional anomalous flux contributions close to the very edge see section 5.3.2, figure 13 and Baldzuhn *et al.* (1998b). After the L-H transition ∇p_i increases over the outermost 4–6 cm, by about 50% at its maximum. The well in $E_r(r)$ deepens at the same radii where pressure gradients steepen

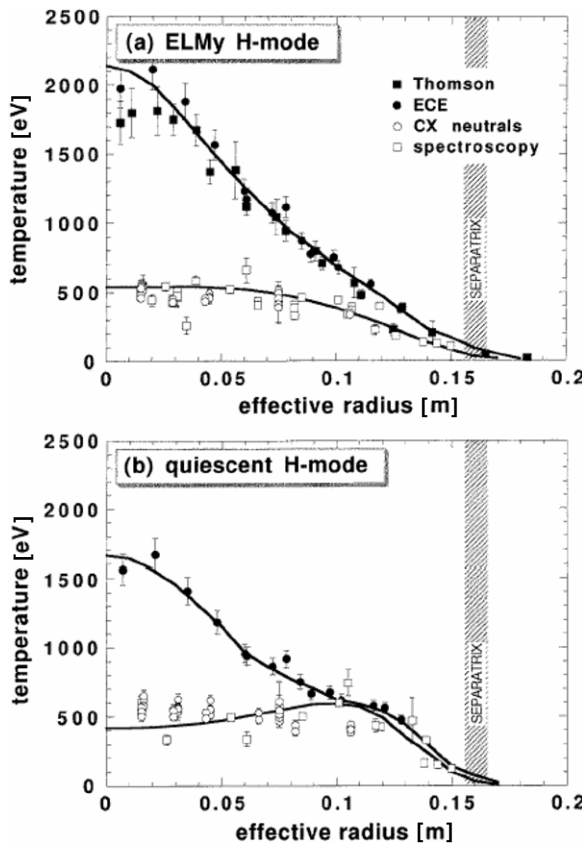


Figure 59. Electron (closed symbols) and ion temperature profiles (open symbols) measured before the transition ((a), top) and within the fully developed H^* ((b), bottom). Discharge #40365 heated by 200 kW ECRH, $B_{\text{tor}} = 2.5$ T, $t_a = 5/10$ island edge, no divertor yet. The quiescent H-mode (b) is achieved by a 20% increase in the line averaged density, thus the central T_e is lower than in the ELMy prephase (Hirsch *et al.* 1998a).

(Wagner *et al.* 2006) but by a factor of up to 2 more than expected from the increase in $\nabla p_i/(e \cdot n)$ alone (Grigull *et al.* 2001a, Wagner *et al.* 2005). Figure 60 shows an example discharge which undergoes two H-phases at well separated discharge conditions with a density ramp in between. Already before the H-mode one observes $E_r \geq \nabla p_i/(e \cdot n)$ (figure 60(b)) in agreement with the general W7AS observations for this probed position $r = a - 3.8$ cm close to the separatrix (see section 5.3.2). During the two H-phases marked by dashed lines, $E_r(r)$ decreases more than expected from the change of $\nabla p_i/(e \cdot n)$ alone. In the fully developed H-mode the radial electric field $E_r = \nabla p_i/(e \cdot n) - B_\theta \cdot v_\phi + B_\phi \cdot v_\theta$ is balanced by the diamagnetic term and in addition by a strong contribution from *poloidal* rotation of the bulk ions (Hirsch *et al.* 2006, Wagner *et al.* 2006). The contribution of *toroidal* rotation $B_\theta \cdot v_\phi$ can be neglected in W7AS due to (i) the large aspect ratio $B_\theta \ll B_\phi$ and (ii) damping of toroidal flows by the toroidal ripple of the linked mirror concept (section 3.1) effective, in particular, at the plasma edge (Hofmann *et al.* 1994). This importance of a $B_\phi \cdot v_\theta$ contribution to the radial force balance of the bulk ions even in the fully developed H-mode seems to be in contrast to tokamak observations. There in the established H-phase E_r is stabilized mainly by the ion

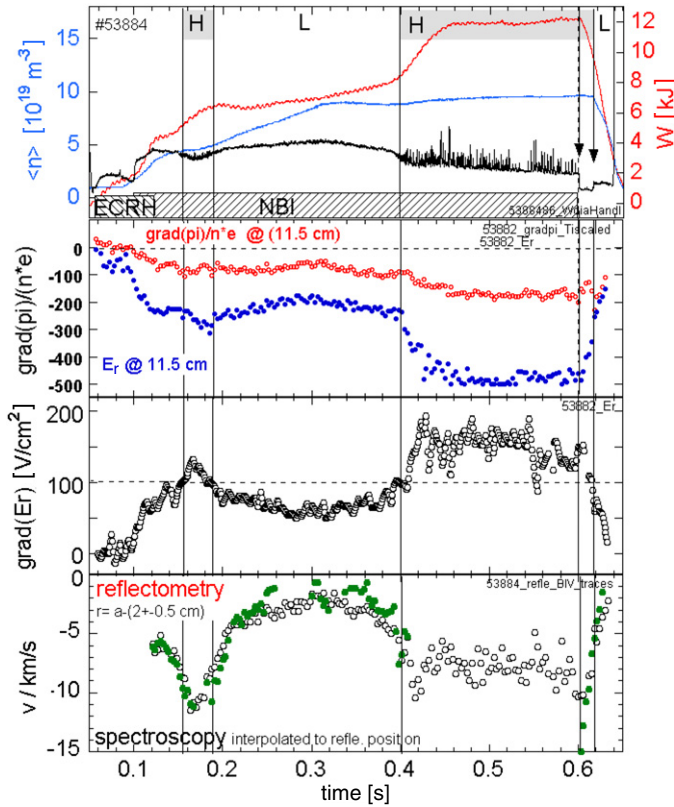


Figure 60. Discharge with two H-phases interrupted by a density ramp. (Top) Energy content, W , line average density, heating and H_α -radiation. H-mode transitions and back-transitions are marked by dashed vertical lines. (Below) Development of radial electric field E_r and diamagnetic component $\nabla p_i(e \cdot n_e)$ at the radius with maximum values of E_r at $r = a - 3.8$ cm. (Below) ∇E_r at radius $r = a - 2$ cm, where the maximum gradient develops. The horizontal line indicates that H-mode transitions and back-transitions all occur at a value of $E_r = -100$ V cm $^{-2}$. (Bottom) Propagation velocity of density turbulence (Doppler reflectometry, filled circles) and $E \times B$ velocity (open circles). The latter is interpolated to the cut-off layer radius which shifts radially by about 1cm during the discharge depending on the density profile. Note that in the post-heating H-phase ndl and $\nabla p_i/(e \cdot n_e)$ remain nearly constant. Details in (Hirsch *et al* 2006).

pressure gradient (Schirmer *et al* 2006, Wagner 2007, Kim *et al* 1994) and the $v \times B$ term is considered to play the role of a trigger at the transition only.

7.2. The H-mode transition

Dithering transition. The transition to the quiescent H-mode is often accompanied by a dithering between turbulent and quiescent phases as also observed in other devices (Zohm 1996). The turbulent phases appear as bunches of ELM events rather than stationary L-states (the events occur in a rapid sequence with separation $\Delta t < 500 \mu\text{s}$ such that their signatures in H_α overlap) and develop towards individual single ELMs as shown for example in figure 61 (Hirsch *et al* 1998a, Grigull *et al* 2001a, Gadelmeier *et al* 2004). During the short quiescent intervals edge turbulence is already indistinguishable from that of the fully developed H* (Holzhauer *et al* 1996, Hirsch *et al* 1998a, Basse *et al* 2003). Edge gradients

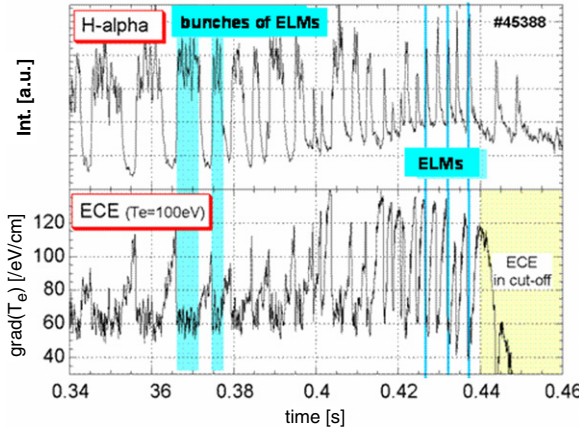


Figure 61. Dynamics during a transition to a quiescent H-mode. During the plotted time interval a feedback controlled density ramp $0.8 \times 10^{20} \text{ m}^{-3} < \bar{n} < 1.6 \times 10^{20} \text{ m}^{-3}$ is performed; $t_a = 0.569$; $P_{\text{NBI}} = 0.4 \text{ MW}$ (more traces in Hirsch *et al* (2000), Grigull *et al* (2001a)). (Top) H_α signal from a limiter. (Bottom) ∇T_e obtained from neighboured ECE channels at $r = a - 1 \text{ cm}$, where in H^* the maximum of ∇T_e occurs. The average T_e at this position remains nearly constant ($T_e = 100 \text{ eV}$) until H^* is reached. ECE signals are running into cut-off at 0.44 s. For a study comparing turbulence during and between the ELMy intervals see Basse *et al* (2002c, 2001). The dynamics of a transition during density flattop is similar but with less violent ELMs (Hirsch *et al* 2006).

∇T_e and ∇n start to rise without measurable delay right at the end of the turbulent burst with resolution down to the diagnostic limits of $20 \mu\text{s}$ (Hirsch *et al* 1996b). ∇T_i is difficult to diagnose on that timescale. The values of ∇p_i and ∇E_r averaged over 10 ms increase with the percentage of quiescent phases in the same interval (Grigull *et al* 2001a). During the time window shown in figure 61 the steepening of ∇T_e becomes faster (lower trace) as the edge pedestal is less perturbed by ELMs and thus the particle and heat losses are quickly compensated from the core. Finally the achievement of a quiescent H-mode exceeding a few milliseconds is equivalent to the suppression of ELMs rather than a final L–H transition. The bifurcation to the first short H^* interval early in this phase is often difficult to identify.

Bifurcation character. The existence of abrupt transitions, back-transitions and rapid oscillations between two states indicates the bifurcation of transport properties (in contrast to the continuous development towards and from the OC regime). For the discharge shown in figure 60 the second back-transition occurs after heating has been switched off with some dwell time $\Delta t_{\text{H-L}}/\tau_E = -\ln(0.5)$ (Wagner 2007). Up to this post-heating back transition, marked by the sudden increase of turbulence, the edge gradients remain nearly on their H-mode level and decay rapidly thereafter; the different slopes of dW/dt and $d\bar{n}/dt$ confirm the change in global energy- and particle confinement. As this post-heating back-transition shows no dithering and can be free of ELM activity it is easier to diagnose than the transition into the H-mode. A detail of time traces is plotted in figure 62. The monitor for small-scale magnetic turbulence (selecting $f > 200 \text{ kHz}$) shows that the bifurcation itself can be as fast as $\approx 10 \mu\text{s}$ (Wagner 2007). Spectroscopy measurements for several identical discharges are collected in figure 63. A distinct jump of the radial electric field by $\Delta E_r \gtrsim +90 \text{ V cm}^{-1}$ is observed for the innermost position probed with the diagnostic (in total five radial channels) at $r = a - 3.8 \text{ cm}$ corresponding to the radius with the maximum values of $|E_r|$. Further outside ($r = a - 2.0 \text{ cm}$), at the maximum of ∇E_r , a clear jump of E_r cannot be resolved.

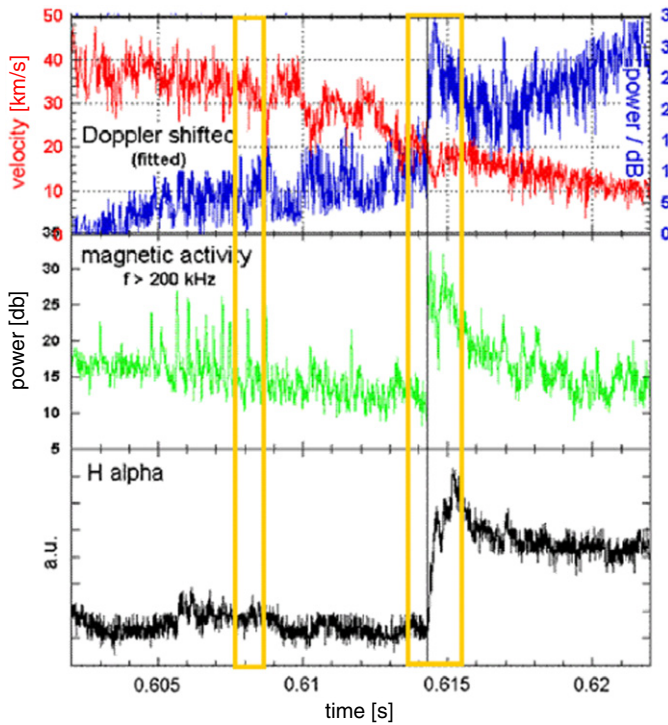


Figure 62. Post-heating back-transition marked by the increase of the H_α signal (bottom). The time window is a zoom to the post-heating back-transition shown in figure 60; heating ended at 0.600 s. At the back transition the power of the magnetic activity (middle) measured with a Mirnov coil followed by a high-pass filter with $f > 200$ kHz increases within $<40\ \mu\text{s}$. The top trace shows turbulence propagation velocity v_\perp (red) and (blue) monitor for turbulence amplitude (returned microwave power, displaying the roughness of the reflecting layer: note the log scale) measured with Doppler reflectometry. Temporal resolution $<10\ \mu\text{s}$, reflecting layer at $r = a - 2\ \text{cm}$ (radius of maximum ∇E_r), the antenna tilt angle selects perturbation wavelength of 0.7 cm (diagnostic details in Hirsch and Holzhauser (2004)).

E_r -profiles for this type of discharge measured from active and passive CXRS at He, C⁶⁺ and BIV impurities, respectively, are given in Wagner (2007).

Threshold conditions. The existence of a critical condition for the bifurcation is indicated by the evolution of edge parameters T_i , T_e , n_e (and their gradients) prior to the L–H transition (during density ramps (Grigull *et al.* 2001a) as well as during \bar{n} -flattop conditions) and by their development towards the post-heating H–L back-transition (Hirsch *et al.* 2006). Prior to the L–H transition ∇p_i and $E_r \approx \nabla p_i/(e \cdot n)$ both increase. The relevance of a critical pressure gradient could be indicated by the observation that for fixed heating power a quiescent H-mode is established roughly for a condition $n_e^{\text{edge}} \cdot T_e^{\text{edge}} = \text{const.}$ despite different heating methods and t_a -values (Grigull *et al.* 2001a). However, prior to the post-heating back-transition ∇p_i remains rather unaffected due to the superior H-mode confinement whereas a strong spin-down of $v_{E \times B}$ is measured indicating the latter as the critical quantity (Wagner *et al.* 2002, Hirsch *et al.* 2006). This corresponds to the observation that during the H-mode a strong $E \times B$ rotation develops which decays after the heating has been terminated while the H-mode edge profiles are still maintained.

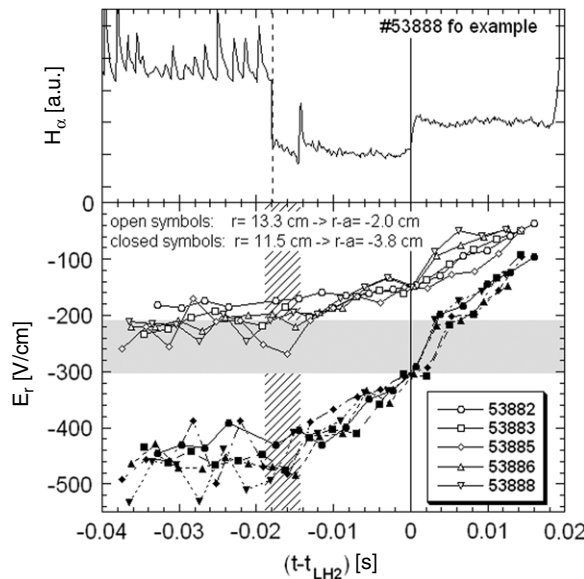


Figure 63. Development of E_r towards the post-heating back-transition measured with passive impurity spectroscopy (species: BIV) at the radius of the minimum of the $E_r(r)$ profile ($r = a - 3.8$ cm, closed symbols) and at the maximum of ∇E_r at $r = a - 2$ cm (open symbols). Data from five identical discharges with time and E_r normalized to the H-L back-transition as determined from H_α (an example of H_α for one of the discharges is shown as the uppermost trace). The absolute time of the transitions in the individual discharges scatters by ± 2 ms. The time window where NBI heating is switched off is therefore marked by a vertical bar. The H-phase has ELMs resulting in a larger scatter of the data; there is also an ELM in the post-heating H-phase of the H_α -example.

Figure 60 shows that the transitions to the H-mode as well as the corresponding back-transitions both occur at the same value of $|\nabla E_r| = 100 \text{ V cm}^{-2}$ despite the different plasma densities. Values for different types of discharges scatter between $|\nabla E_r| \gtrsim 50-100 \text{ V cm}^{-2}$. No indication for a hysteresis between L-H and H-L transition has been observed with respect to this quantity (Hirsch *et al* 2006). Experiments in the heliac TJ-II (Pedrosa *et al* 2005) demonstrated the development of an edge $E \times B$ sheared flow which is expected to increase when the turbulent drive for rotation (Reynolds-stress) is large enough to overcome the flow damping (Carreras *et al* 2006). In this case E_r is expected to be dominated by the $v \times B$ term as it is the case of W7-AS. Moreover, an inverse energy cascade towards large zonal flow structures is expected. An indication for the latter is a finite level of bicoherency (displaying three-wave-coupling) as it is indeed found in edge density fluctuations during the W7-AS H-mode (Diamond *et al* 2000). L-mode turbulence for comparison are difficult to interpret due to diagnostic limitations (reflectometry) in the case of high turbulence amplitudes. The high level of bicoherency remains throughout the H-phase—as the $v \times B$ term does—in contrast to observations at the DIII-D tokamak (Moyer *et al* 2001), where a finite bicoherency appears transitorily right at the L-H transition facilitating the bifurcation before the $\nabla p_i/(e \cdot n)$ term develops and stabilizes the new mode (see section 7.1).

In W7-AS the observed values $|\nabla E_r| \gtrsim 100 \text{ V cm}^{-2}$ are close to the values expected to decorrelate turbulent cells (Biglari *et al* 1990). However, experimental growth rates and radial correlation length of turbulence as required to prove the criterium for shear flow decorrelation (Biglari *et al* 1990) have not been measured. Finally, we note that a critical *macroscopic* ∇E_r alone cannot be a sufficient condition for the turbulence suppression as discharges in the OC

regime often show much larger values of ∇E_r or $|E_r|$ which lead neither to a nearly complete turbulence suppression as in the H-mode nor to a transport bifurcation as displayed by the abrupt L–H or H–L transitions. It is speculated that on top of the *macroscopic* ∇E_r , the level of self-generated *microscopic* zonal flows, and thus the *fluctuating local* ∇E_r , is the decisive element for the bifurcation.

Turbulence and flows. Measurements in the edge barrier with fast diagnostics agree with the paradigm of turbulence suppression by sheared flows: the propagation velocity of density turbulence perpendicular to the magnetic field, v_\perp (measured with Doppler reflectometry) tightly follows the $E \times B$ velocity which is obtained from spectroscopy down to the millisecond timescale of the latter diagnostic (figure 60, lowest trace). This relation maintains in the H-mode as far as sufficient tracer turbulence is available (Hirsch *et al.* 2006). Stationary radial profiles of $v_\perp(r)$ and $v_{E \times B}(r)$ obtained during the flattop phases of standard L-mode discharges confirm this result, indicating that the intrinsic phase velocity of the edge turbulence in the plasma frame is small (Hirsch *et al.* 2001b). This has also been observed at the tokamaks AUG (Schirmer *et al.* 2006) and Tore Supra (Hennequin *et al.* 2005) (see section 5.4). Doppler reflectometry measurements in the edge layer (figure 60 (bottom)) show a strong correlation between the turbulence amplitude \tilde{n} and the turbulence propagation velocity v_\perp (presumably displaying the $v_{E \times B}$ shear) (Hirsch *et al.* 2006): in figure 62 a rising turbulence level \tilde{n} can be observed already in the post-heating H-phase. During the whole plotted time interval the spin-down of the propagation velocity (and thus $v_{E \times B}$) correlates with an increase of \tilde{n} (note the log scale for \tilde{n}). The general strong correspondence between \tilde{n} and v_\perp is broken at the H-mode transition itself, where a sudden jump of \tilde{n} by more than an order of magnitude is observed within $<200\ \mu\text{s}$. The turbulence overshoots and settles at a level about one order of magnitude higher than during the H-mode. For the probed layer corresponding to the radius where ∇E_r is maximum ($r = a - 2.0\ \text{cm}$) no significant discontinuity for v_\perp is observed, in agreement with spectroscopy where a distinct jump in E_r occurs only deeper in the plasma at the maximum values of $|E_r|$ (figure 63). On a *fast timescale* ($<100\ \mu\text{s}$) \tilde{n} and v_\perp are modulated in a correlated way with typical frequencies of about 10 kHz, possibly indicating zonal flows and GAM activity (Hirsch *et al.* 2006).

7.3. ELMs

The ELM phenomenology depends on the magnetic configuration, the proximity to conditions for a final transition to H* and on ∇p . Enforcing the drive for ∇p , either by increasing heating power or increasing ∇n by gas puffing, results in stronger but more irregular ELMs. Thus a dependence of an ‘ELM repetition frequency’ on heating power or edge parameters cannot be inferred. Quasi-periodic ELMMy H-modes with repetition frequencies of 1–2 kHz occur at moderate heating with \bar{n}_e and t_a close to the operational conditions of the quiescent H-mode. The energy loss per ELM estimated from profile changes was $<4\%$; thus a major part of the non-radiative flux across the separatrix is carried by ELMs. The energy confinement resides at the level of a turbulent state. (Hirsch *et al.* 1998b). Violent single ELMs with pronounced spikes in the H_α signatures occur during the degradation phase of H* characterized by increasing radiation and decreasing edge temperatures. They are likely driven by resistive interchange or ballooning modes (Weller *et al.* 2006), see section 10.8).

A single ELM—for examples see (figure 61, $t > 400\ \text{ms}$ and figure 64)—shows the basic features also observed in tokamaks (Hirsch *et al.* 1996b, Holzhauer and W7-AS Team 1996, Hirsch *et al.* 1998a, 1998b)—tokamak ELMs are reviewed in Zohm (1996), Connor (1998), ITER Physics Expert Groups (chapter 2) (1999): it is a distinct event of about $200\ \mu\text{s}$ associated

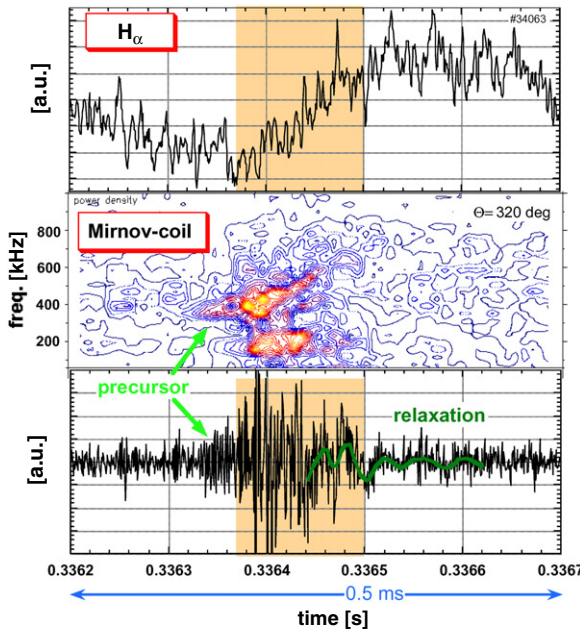


Figure 64. Sequence of MHD activities during an ELM event: (1) quasi-coherent precursor activity, (2) burst of broadband fluctuations, (3) low-frequency (20–60 kHz) relaxation of plasma equilibrium (Weller *et al* 2001).

with a burst of strongly enhanced density and magnetic fluctuations (their power increases by more than an order of magnitude within 20–50 μ s) which immediately expels particles and heat from the outermost 4–5 cm inside the LCFS (Kocsis *et al* 1995, Hirsch *et al* 1996b, 1998b, Grigull *et al* 1999a). A consecutive cold pulse propagates inward on a diffusive timescale (Holzhauer *et al* 1996, Volpe *et al* 2003b). The pivot point of the transient flattening of ∇T_e and ∇n_e is mostly situated in a narrow (± 0.5 cm) layer, located 1–3 cm inside the LCFS (Hirsch *et al* 1998a). Density fluctuations show up first at the innermost radial position accessible to the reflectometer—typically 3–4 cm inside the LCFS, about the top of the temperature pedestal—and expand radially outward with a few hundred metres per second. The increase in fluctuation power is almost independent of the radial position in contrast to the time averaged fluctuation level in turbulent discharges which decreases from the LCFS inward (Estrada *et al* 1993b, Brañas *et al* 1995, Branas *et al* 1995), (see section 5.4.2). Magnetic fluctuations show a broad spectrum with characteristic frequency bands (figure 64) and occur nearly simultaneously for all poloidal and toroidal coil positions down to the limit to measure the fluctuation power, $< 3 \mu$ s, indicating a global character of the ELM (Holzhauer *et al* 1996). Preceding the actual ELM, magnetic probe arrays often show a short period (about 50 μ s) of growing quasi-coherent precursor activity ($f \approx 150$ –400 kHz, see figure 64) with poloidal mode numbers $m > 4$. Assuming a propagation with $v_{E \times B}$ one estimates $m \approx 10$ (Hirsch *et al* 1996b). During and after the ELM, a low-frequency relaxation of the perturbed plasma equilibrium results in a transient oscillation of density and magnetic field with only a few observable periods (figure 64 and section 5.4.2 for details) (Anton *et al* 1998, Zoleznik *et al* 1999, 2002, Pokol *et al* 2007).

In the SOL the fluxes induced by an individual ELM as measured with probes show a fine structure similar to observations in the ASDEX Tokamak (Endler *et al* 2002). The

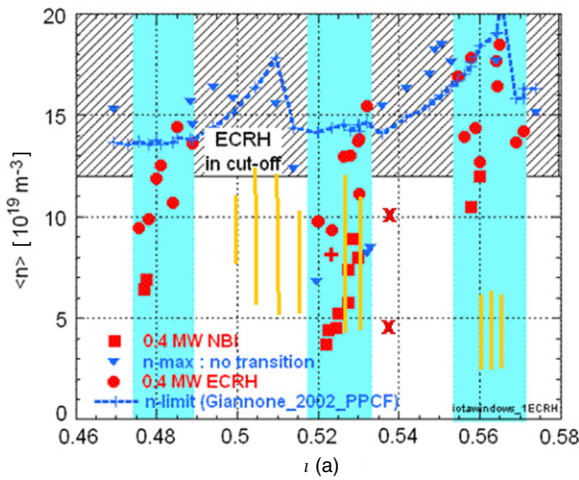


Figure 65. Operational range for the quiescent H-mode (duration exceeding 10 ms) with respect to edge topology as characterized by a nominal edge rotational transform ‘ $\iota(a)$ ’ calculated from the ratio of currents in the external field coils. The actual rotational transform at this plasma boundary is determined from the respective island chain and changes in a non-monotonous way with the control parameter $\iota(a)$. The quiescent state is obtained by a feedback controlled density ramp with $\iota(a)$ kept constant. Densities where a transition to H^* is observed are indicated for 0.4 MW NBI heating (squares) and 0.4 MW ECRH (dots). Triangles indicate maximum densities either close to the density limit (Giannone *et al* (2002a), dashed line) or achieved with ECRH without a transition to H^* (Hirsch *et al* 2000). The yellow hatched areas mark conditions where the OC regime has been achieved.

power deposition onto the targets (Gadelmeier *et al* 2004) reaches up to 25 MW m^{-2} during pronounced single ELMs (with an uncertainty by a factor of two arising from surface morphology) which is about the values reported for tokamaks. The relative intensity of the footprints for the different divertor legs (inner versus outer strike point and upper versus lower divertor) changes during an ELM by up to a factor of 4, possibly indicating drift effects (Thomsen *et al* 2002b).

7.4. operational conditions

Magnetic edge topology. The quiescent H-mode is obtained only in three sharply defined windows of the edge rotational transform ι_a (figure 65) where at sufficiently high density and low to moderate heating power H^* is practically unavoidable (Wagner *et al* 1994b, Hirsch *et al* 1996b, Grigull *et al* 1999b). These quite narrow windows ($\Delta\iota/\iota \gtrsim 1\%$) are highly reproducible, independent of the heating (ECRH or NBI), the gas program, the toroidal magnetic field and did not change with divertor installation. They do not correlate with the strong dependence of electron energy transport on ι_a (figure 35). The spatio-temporal structure of ELMs—and thus the divertor heatload—also depends sensitively on ι_a as shown in figure 66. This offers an intrinsic knob for ELM mitigation in a low-shear stellarator and is reminiscent of the geometry dependence of ELMs in tokamaks (triangularity, x-point to target distance (Stober *et al* 2001)) or on the impact of helically resonant magnetic edge perturbations (Evans *et al* 2004).

Several reasons have been discussed for the strong impact of edge magnetic topology:
(1) The plasma minor radius is as large as possible but keeping a separatrix configuration

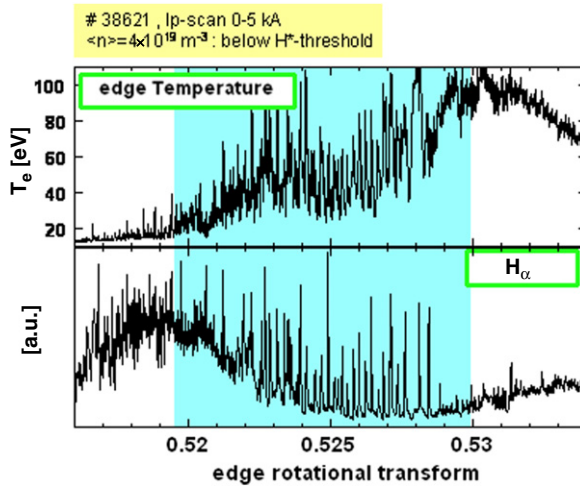


Figure 66. ELM phenomenology (T_e from ECE measured 1–2 cm inside the separatrix and H_α -monitor) as t_a is scanned across an H-mode window during 150 ms. Line average density and heating power are kept constant at values right below conditions where H^* occurs. The marked range shows t_a values where slightly higher densities result in an immediate transition to H^* (see figure 65) (Hirsch *et al.* 1997).

defined by the inner separatrix of the island chain, however, with targets located right behind the x-point. In this configuration the connection length decreases to a value of some metres within a radial distance of $\Delta r \approx 1$ cm outside the LCFS. This allows for strong shear in E_r around the separatrix displayed by a distinct maximum in the space potential measured with probes already at low densities, i.e. *before* a transition to a quiescent H-mode occurs (Wagner *et al.* 1994b). (2) In two of the three t_a windows viscous damping terms for poloidal plasma rotation resulting from the vicinity of helical edge islands (see Shaing (1993)) are minimized such that a high flow velocity can be expected (Wobig and Kisslinger 1997, 2000). Both explanations do not hold for the third window found in the 5/9 island-divertor configuration where the flux surface corrugation is strong and the distance between x-points and the target is rather large. Please note that the edge topology also modifies conditions for the penetration of neutrals and the loss orbits for thermal ions both of which could modify the stabilization of the barrier (with ∇E_r as a measure of its strength). A clear picture is hampered as up to now all magnetic edge properties have been obtained from vacuum flux geometries and not from true 3D equilibria, where finite pressure would induce an ergodic edge layer (Geiger and Suzuki 2006, Reiman *et al.* 2007) (see section 10.4).

Density. The H-mode operational space with respect to absorbed heating power and average density is shown in figure 67 which selects t_a inside one of the H^* operational windows. Quiescent (H^*) plasmas with durations exceeding a confinement time are obtained at moderate heating power $P_{\text{abs}} \leq 1.5$ MW during density ramps. Divertor installation did not modify these conditions. From detailed observations and a comparison with different heating schemes it is tentatively concluded that rather than the plotted line average density the decisive parameter is the edge density, respectively, its gradient. An operational diagram in terms of edge parameters e.g. ∇n_e^{edge} and ∇T_e^{edge} is hampered by the lack of finite- β edge equilibria (necessary for diagnostic mapping) including the dominant island structures (Grigull *et al.* 1999b, Hirsch *et al.* 2000, Grigull *et al.* 2001a).

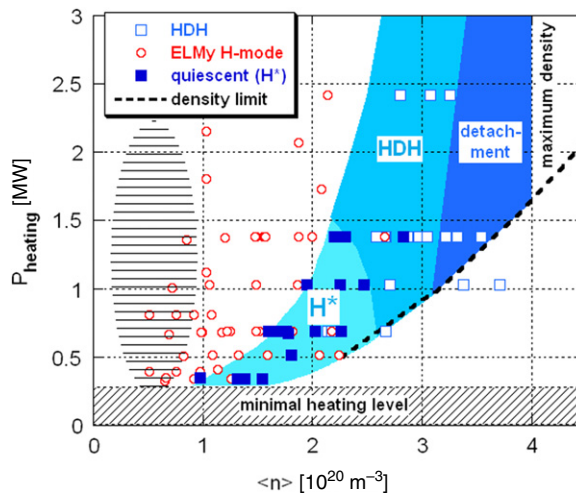


Figure 67. Survey of the H-mode operational space in an absorbed power versus average density plane selecting the t_a -window with 5/9 plasma edge (divertor configuration but slightly varying island size) derived from both, density ramp experiments and under stationary conditions. Circles indicate ELMy H-modes with either periodic activity or bunches of ELMs. The density limit (dashed line) is calculated from [Gianrone et al \(2002a\)](#). The horizontally hatched area indicates for which conditions the OC regime often characterized by grassy ELM-like events can develop, however, taking into account a wider range of configurations.

Lack of a power threshold behaviour. The H-mode operational space shown in figure 67 differs from the power threshold behaviour reported from tokamaks and the heliotrons CHS ([Toi et al 1996](#), [Akiyama et al 2005](#)) and LHD ([Watanabe et al 2003](#)) where at given density a minimum absorbed NBI power is required for a transition. Such a behaviour is consistent with the existence of a critical pressure gradient at the plasma edge. In contrast, in W7-AS increasing the heating power needs an *increasing* density to stabilize the ELMs and thus to allow for quiescent H-mode with a duration exceeding a few ms. At a given density a quiescent H-mode therefore can be achieved only *below* and not above a certain power threshold ([Grigull et al 2001a](#)). A transition to a quiescent H-mode can already be obtained with ECRH heating power *reduced* down to 300 kW (at a density $\bar{n} = 8.9 \times 10^{19} \text{ m}^{-3}$ and $t_a \approx 5/9$ separatrix edge). In this case the power flux across the separatrix is a factor of 3–4 lower than calculated from tokamak power threshold scaling (using ITER99 which includes smaller devices ([ITER Physics Expert Groups \(chapter 2\) 1999](#))). Moreover, ELMs or ELM-like phenomena and short interspersed H*-phases (duration $\approx 1 \text{ ms}$) are observed even at lower power levels and lower densities and even under limiter edge conditions e.g. at $t_a \approx 1/3$ ([Hirsch et al 1998b, 2006](#), [Zoletnik et al 2005a](#)), see section 5.4.2).

H-mode and optimum confinement regime. Optimum confinement can be realized in a wider range of t_a (i.e. where configurations with ‘good’ confinement exist) and without such sharply bounded windows as for the H-mode (compare figures 65 and 35). OC is obtained only at medium densities (figures 65 and 67). If the density is increased the favourable OC characteristics are lost as a broader density profile together with increasing core radiation results in a general reduction of T_i at the edge and an associated reduction

of $|\nabla E_r|$ (Balduhn *et al* 2000, Stroth *et al* 1998, McCormick *et al* 1999b). From such a regime the H-mode with its *sudden* turbulence suppression and subsequently developing $E \times B$ rotation can be obtained by continued gas puff: the maximum of ∇n_e is shifted further towards the separatrix, dithering and ELMs appear and finally a transition to H^* is reached provided an appropriate t_a -value has been chosen. Vice versa, OC can *develop* from a quiescent H-mode provided the latter has been realized at sufficiently low density delaying a radiation collapse (Kick *et al* 1999): if during H^* the gas puff is stopped (and recycling is sufficiently low, e.g. due to wall conditioning) ∇n and thus the maximum of ∇E_r shift deeper into the core until the quiescent phase is terminated by ELMs. This ELM activity contributes to the further narrowing of the density profile supporting the development of OC conditions—inward shifted ∇n , strong ∇E_r extending deep into the bulk and broad T_i -profiles yielding superior confinement.

7.5. Achievement of the HDH mode

Without divertor a loss of density control as well as a high level of radiation were an inherent characteristic of higher densities on W7-AS, which therefore could only be achieved transiently in a steep \bar{n}_e -ramp (McCormick *et al* 1999b, 2001, Burhenn *et al* 2004), (section 6.3). Surprisingly, with divertor fast \bar{n}_e -ramps paved the way to a steady-state high energy confinement regime which was characterized by density control and no impurity accumulation (Grigull *et al* 2001b, McCormick *et al* 2002, Jaenische *et al* 2002b). This high density H-mode (HDH) regime became the workhorse of divertor operation for \bar{n}_e beyond a power-dependent threshold density \bar{n}_e^{th} , whereby both attached and detached plasmas could be realized and the density limit (see section 6.3) considerably extended. The HDH regime was attainable only with NBI heating, since the threshold density exceeded the ERCH (140 GHz, X2) cut-off density of $1.2 \times 10^{20} \text{ m}^{-3}$. HDH can exist in a wide variety of magnetic configurations ($t_a = 5/8, 5/9, 5/10$) over a wide range of x-point to target distances, including limiter plasmas as well if the heating power is sufficiently high. Thus a divertor configuration is not an imperative prerequisite. In fact, all high- β studies were carried out under limiter conditions, but display essentially HDH characteristics (section 10.3 and Weller *et al* (2003)). HDH was also achieved under limiter conditions at full field (2.5 T) for $t_a \approx 5/9$ with $P_{\text{abs}} \sim 2.5 \text{ MW}$ where the control coil currents were reversed (as for high- β studies) to smooth the peripheral island structure, thereby placing the core plasma solidly in contact with the target plates (McCormick *et al* 2003c). In section 7.8 only the $t_a = 5/9$ standard divertor configuration (SDC defined in section 8.3), where most investigations took place, will be considered. For this configuration below \bar{n}_e^{th} a normal confinement regime (NC) exists, which in strong contrast to the HDH mode exhibited poor energy confinement time, τ_E , strong ELM activity and at higher densities radiation increasing continuously with time, often leading to radiation collapse. Section 7.9 details results of operation at a slightly lower value of t_a (0.561 versus 0.567), where the quiescent H-mode was extant as a prelude to HDH.

7.6. Properties of the HDH mode

NC and HDH regimes are shown in figure 68 where the temporal behaviour of three discharges with flattop densities near \bar{n}_e^{th} are depicted. Two of the discharges differ less than 2% in density (1.68 and $1.705 \times 10^{20} \text{ m}^{-3}$, #55596 and 95, respectively) and are below \bar{n}_e^{th} , whereas the third discharge (#55598) is established at $\bar{n}_e = 1.95 \times 10^{20} \text{ m}^{-3} > \bar{n}_e^{\text{th}}$. All discharges have the same initial gas puff waveform (shown along with H_α) and initially attain the same stored energy W , thereby implying strong similarities in n_e - and T_e -profiles. However, due to marginal

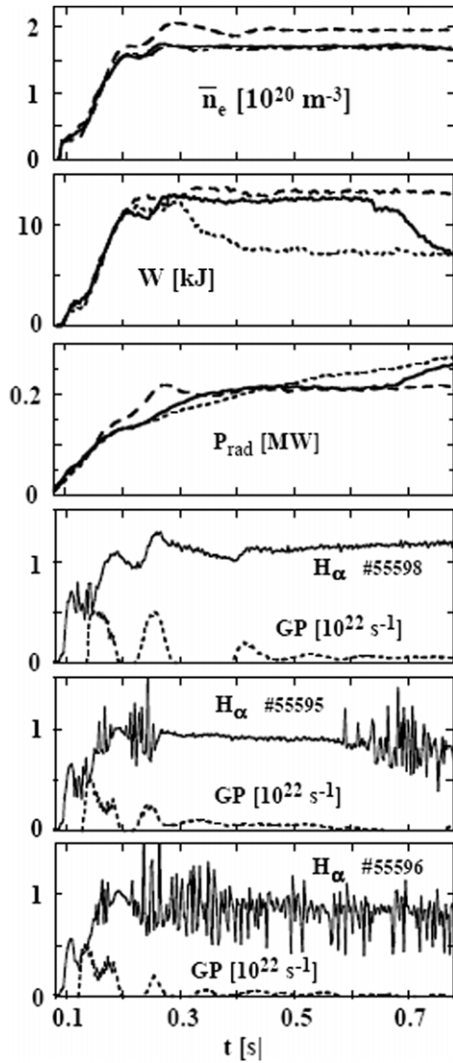


Figure 68. Temporal behaviour of: line-averaged density n_e , stored energy W , global total radiated power P_{rad} , and H_α from the divertor module region and gas puff (GP) rate. The NC->HDH transition density is slightly in excess of $1.7 \times 10^{20} \text{ m}^{-3}$ for this series. Standard divertor configuration (SDC): $t_a = 0.567$, $a = 11.8 \text{ cm}$, x-point distance to target plate $\sim 3.8 \text{ cm}$; $B = -2.5 \text{ T}$; $P_{\text{abs}} \cong 0.7 \text{ MW}$. Electron fuelling rate from NBI is $\sim 1 \times 10^{20} \text{ s}^{-1}$.

differences in the successive gas puff corresponding to the different densities, W is either maintained (HDH) until cessation of NBI heating (around 1 s) or continues for several 100 ms before lapsing to lower W (NC) or suffers a transition to the same lower W within 100 ms ($1.68 \times 10^{20} \text{ m}^{-3}$). The NC-phases are accompanied by ELM activity, seen in the H_α traces. In contrast, the higher confinement phases are essentially ELM-free. Another principal difference of the two regimes is the behaviour of P_{rad} : at $\bar{n}_e = 1.68 \times 10^{20} \text{ m}^{-3}$ P_{rad} increases throughout, whereas for $\bar{n}_e = 1.71 \times 10^{20} \text{ m}^{-3}$ P_{rad} attains constancy over most of the high- W phase. Finally, for $\bar{n}_e > \bar{n}_e^{\text{th}}$, P_{rad} is stationary, in strong contrast to the dramatic increase in P_{rad} seen in quiescent H-modes (figure 58).

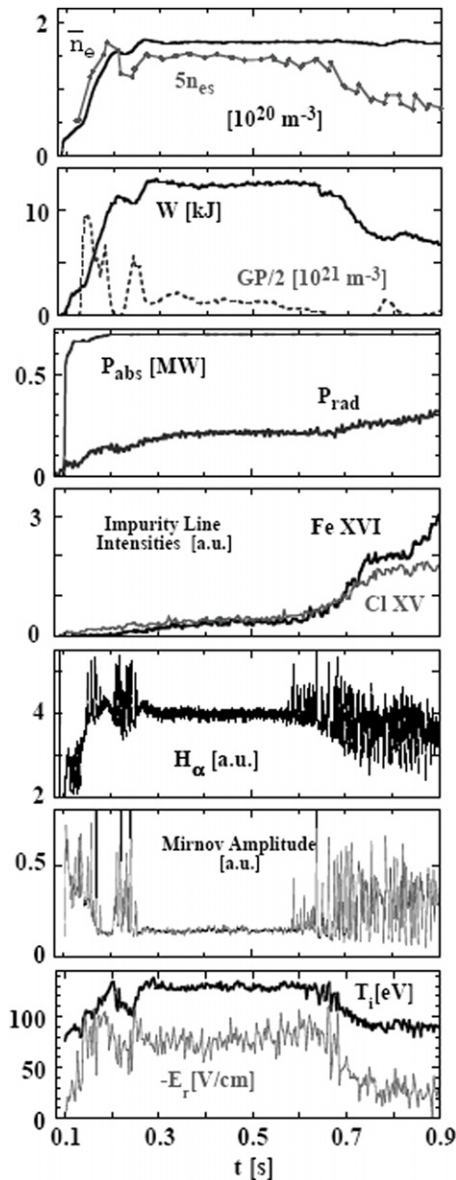


Figure 69. Temporal behaviour of n_e and n_{es} , W and gas puff, P_{abs} and P_{rad} , impurity line intensity of Fe and Cl along a central chord, H_α and Mirnov activity, ion temperature T_i and radial electric field E_r (derived from passive observation of a BIV line along a chord in the density gradient region). HDH-like conditions exist over $\sim 0.3\text{--}0.6$ s, after which confinement decays to NC. #55595.

A comparative study of NC-HDH for the same setup conditions is shown in figure 58 which analyses #55595 in more detail. \bar{n}_e is maintained constant via the indicated gas puff waveform regulated by feedback. The H_α - and Mirnov-coil traces attest to little activity over most of the high-confinement phase, in contrast to NC. Concomitant with HDH is both a higher radial electric field E_r and ion temperature T_i at the edge, as to be expected if a transport barrier

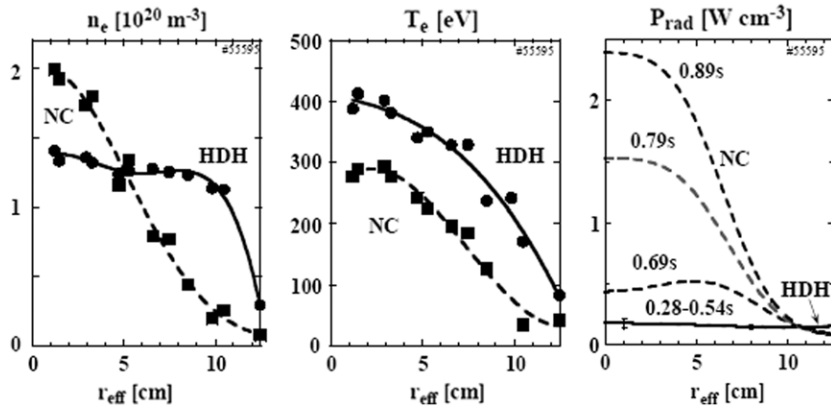


Figure 70. n_e -, T_e - and P_{rad} -profiles for the HDH- and NC-phases of #55595. The n_e - and T_e -profiles are averaged over $\sim 0.28\text{--}0.53$ s (HDH) and $0.78\text{--}0.88$ s (NC). The error bars for the P_{rad} HDH profile give the standard deviation at those radii over the indicated time span. P_{rad} HDH increases at larger r_{eff} .

is established there. In clear contrast to a quiescent H-mode, the global radiation during HDH remains constant (compare figure 58 and figure 69) and starts to increase in time only in the final NC phase as do impurity lines of Fe and Cl. The separatrix density n_{es} develops strictly in parallel to W over a wide parameter range (McCormick *et al* 2007), i.e. one obtains high n_{es} for the HDH phase and lower n_{es} for NC, marking a very characteristic change in the shape of the density profile. n_e - and T_e -profile differences between NC and HDH are documented in figure 70: NC exhibits a peaked n_e -profile, whereas HDH is flat with a steep gradient at the edge (here not resolved), indicating the particle transport barrier. The T_e -profiles are similar in form but higher for HDH, with some hint of a pedestal. The most striking difference is that for NC the P_{rad} -profiles are peaked and increase in amplitude with time, while the HDH profiles are hollow and stationary.

Impurity confinement was examined via Al-laser ablation (section 6.2.4, Burhenn *et al* (2004), McCormick *et al* (2002, 2003c)). Figure 71 gives $\tau_{\text{Al}}(\bar{n})$ for a series of steady-state discharges for hydrogen (top row) and deuterium (bottom row) with $P_{\text{abs}} \gtrsim 1.4$ MW, in contrast to τ_E . For H^+ discharges over all the power levels investigated the threshold density scales as $\bar{n}_e^{\text{th}} \propto 1.67 \cdot P_{\text{abs}}^{0.28}$ (10^{20} m^{-3} , MW) for the standard divertor configuration, being $\bar{n}_e^{\text{th}} \propto 1.8 \times 10^{20} \text{ m}^{-3}$ for $P_{\text{abs}} \gtrsim 1.4$ MW, as depicted. Considering the H^+ discharges first, τ_E increases more than a factor of two and τ_{Al} decreases markedly when $\bar{n}_e > \bar{n}_e^{\text{th}}$. The international stellarator scaling ISS95 (Stroth *et al* 1996c) follows the NC points, whereas the W7-AS scaling lies somewhat above (not shown). Below \bar{n}_e^{th} the τ_E associated with transient attainment of HDH conditions, as illustrated in figures 58 and 59, yield a curve blending smoothly with the steady-state values above \bar{n}_e^{th} . This underlines the fact that the NC->HDH threshold density does not represent an abrupt jump in confinement, rather it represents the boundary beyond which HDH conditions can be sustained. Further, τ_E scales almost linearly through these points up to $\bar{n}_e = 2.2 \times 10^{20} \text{ m}^{-3}$ where τ_E begins to saturate. This is in dramatic contrast to the ISS95 where $\tau_E \propto \bar{n}_e^{0.5}$ (Stroth *et al* (1996c), section 5.1). Beyond $\bar{n}_e = 3 \times 10^{20} \text{ m}^{-3}$ with the onset of partial detachment (section 8.4) τ_E drops, due to encroachment of the radiation profiles into the core region, leading to a drop in T_e globally as well as n_e at the edge as illustrated in figure 72. The fractional radiation $P_{\text{rad}}/P_{\text{abs}}$ increases with density throughout, being about 50% at the onset of partial detachment and

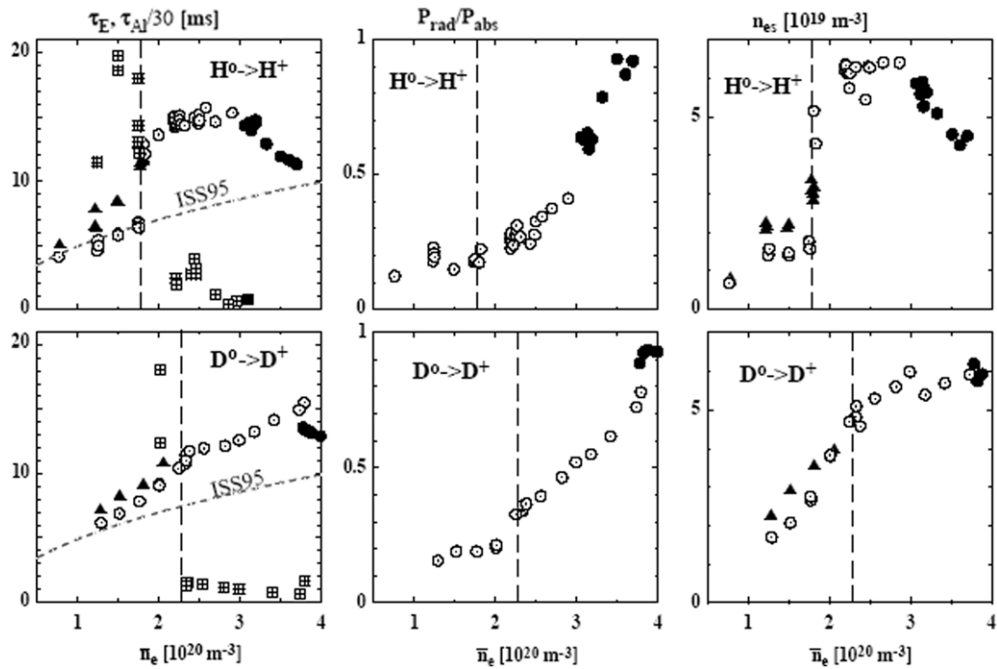


Figure 71. (Left column) Energy confinement time τ_E and 1/e falloff time τ_{Al} of laser-ablated Al versus \bar{n}_e for $H^0 \rightarrow H^+$ (top row) and $D^0 \rightarrow D^+$ (bottom) quasi-stationary discharges (each point is a separate discharge). τ_E^{ISS95} scaling is indicated. The vertical dashed lines denote the NC \rightarrow HDH transition densities. (Middle column) Fractional radiation P_{rad}/P_{abs} . (Right column) Separatrix density n_{es} . The solid triangles denote transitory HDH confinement. Otherwise, open symbols represent attached- and solid circles detached-plasmas. SDC, $B = -2.5$ T, $P_{abs} \cong 1.4$ MW.

around 90% at the highest values. The separatrix density n_{es} follows the same pattern as τ_E (McCormick *et al* 2007), attaining particularly high values in HDH and being $\sim 6 \times 10^{19} \text{ m}^{-3}$ at the peak. These properties of HDH, the combination of both high n_{es} and high radiation in quasi-steady-state, are those which enable stable operation under detached conditions on W7-AS.

Since from the beginning of divertor experiments H^+ was used in preference to D^+ in order to mitigate impurity production at the target plates, only a small subset of discharges exists with D^+ . As shown in figure 71, they obviously follow a different operational characteristic with \bar{n}_e : this is no major change in confinement at the NC \rightarrow HDH transition, rather τ_E grows almost linearly with \bar{n}_e up to detachment, in particular if one considers the transient HDH points. This arises as a result of deviating n_e - and T_e -profiles. In NC the peaked n_e -profiles develop a pedestal not seen for H^+ with increasing \bar{n}_e , and at the transition into HDH where $n_e(r)$ takes on the same form as for H^+ the increase in $T_e(r)$ is less (McCormick *et al* 2003c). This may represent a genuine isotope effect, not otherwise seen in other regimes on W7-AS, or it may be only an expression of the more shallow power deposition profiles for D^+ . In any case, τ_{Al} plummets to low values at the transition and P_{rad}/P_{abs} is similar to H^+ for the attached situation. However, since n_{es} is generally lower (in the same fashion as τ_E), a higher radiation fraction is necessary ($\sim 80\%$) before detachment ensues.

Typical n_e -, T_e - and P_{rad} -profiles comparing NC and attached/detached HDH conditions are displayed in figure 72 ($P_{abs} \cong 1.4$ MW, $H^0 \rightarrow H^+$). The profile form behaviour is the

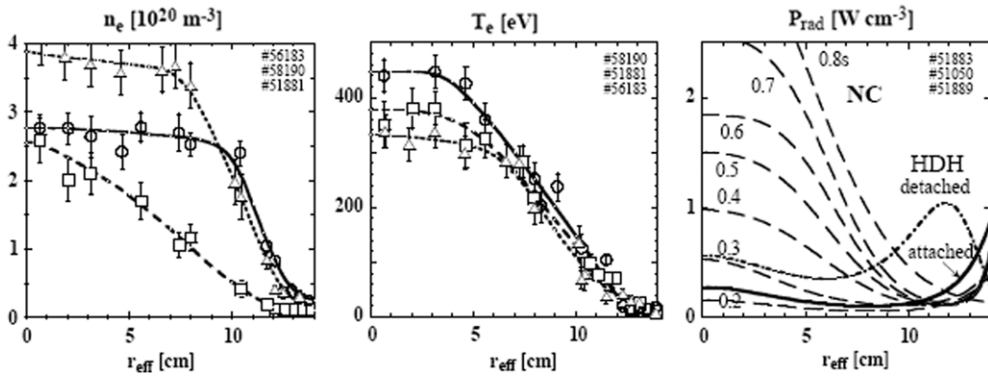


Figure 72. n_e -, T_e - and P_{rad} -profiles for NC and for HDH attached and detached conditions. SDC, $B = -2.5 \text{ T}$, $P_{\text{abs}} \cong 1.4 \text{ MW}$, $\text{H}^0 \rightarrow \text{H}^+$. #51881 ($n_e = 1.5 \times 10^{20} \text{ m}^{-3}$, $P_{\text{rad}}/P_{\text{abs}} \cong 14\%$), #51890 ($2.5 \times 10^{20} \text{ m}^{-3}$, 25%), #56183 ($3.26 \times 10^{20} \text{ m}^{-3}$, 66%), #51883 (0.8 s: $1.76 \times 10^{20} \text{ m}^{-3}$, 34%); #51889 ($2.45 \times 10^{20} \text{ m}^{-3}$, 23%); #51050 ($3.65 \times 10^{20} \text{ m}^{-3}$, 71%).

same as for the lower power discharge of figure 70 for NC and HDH (attached). Now, since n_e for the HDH profile is higher, only a moderate increase in T_e over the NC case is registered. For the moderately detached situation T_e is lower over the entire profile, which in combination with the slightly lower edge density leads to a P_{rad} -profile now shifted somewhat into the core region. This tendency becomes more pronounced at higher densities, at least for H^+ plasmas, thereby leading to a lower stored energy. For D^+ both the decrease in T_e and shrinking of the n_e - and T_e -profiles are far less evident (McCormick *et al.* 2003c).

7.7. Transition from quiescent H-mode to HDH

For the standard divertor configuration the normal confinement state is characterized by ELM activity in the density ramp phase (figure 58) until attainment of HDH conditions; a quiescent H-mode H^* is not obtained. In contrast, discharges with a 5/9 configuration where t_a is shifted more towards the centre of the H-mode window (see section 7.4) permit access to the H^* and the HDH states under almost identical conditions (McCormick *et al.* 2003a, 2003b).

In the discharge depicted in figure 73 the density is ramped up until attainment of H^* , and then after a 60 ms plateau is increased again until the HDH mode is solidly established. The entrance into H^* is marked by cessation of ELM activity (seen in H_α), followed by a rapid increase in P_{rad} as well as in FeXVI line radiation. The constant \bar{n}_e during H^* was enabled by He glow-discharge cleaning to promote pumping by the carbon divertor target plate (not necessary for HDH). Even so, H^* could not be maintained longer without rapid evolution into radiation collapse (Brakel *et al.* 2002). Over the H^* period the P_{rad} profiles progress from flat to hollow with rapidly increasing edge radiation. The 2nd \bar{n}_e -ramp to HDH stops the increase in P_{rad} and the FeXVI intensity diminishes to zero by the end of the ramp. As shown by figure 74 HDH again leads to the characteristic hollow P_{rad} profile, constant in time and peaked strongly to the outside. No falloff in intensity of laser-ablated AlXII radiation can be observed over H^* , whereas the decay time is $\sim 100 \text{ ms}$ for HDH (Burhenn *et al.* (2003) and section 6.2.4). The n_e - and T_e -profiles for H^* and HDH are similar in form (McCormick *et al.* 2003a, 2003b). The lower values of T_i and E_r for HDH most likely imply a weaker edge pressure gradient, although this cannot be certain since the measurements are derived from passive BIV emission whose radiating shell may experience a

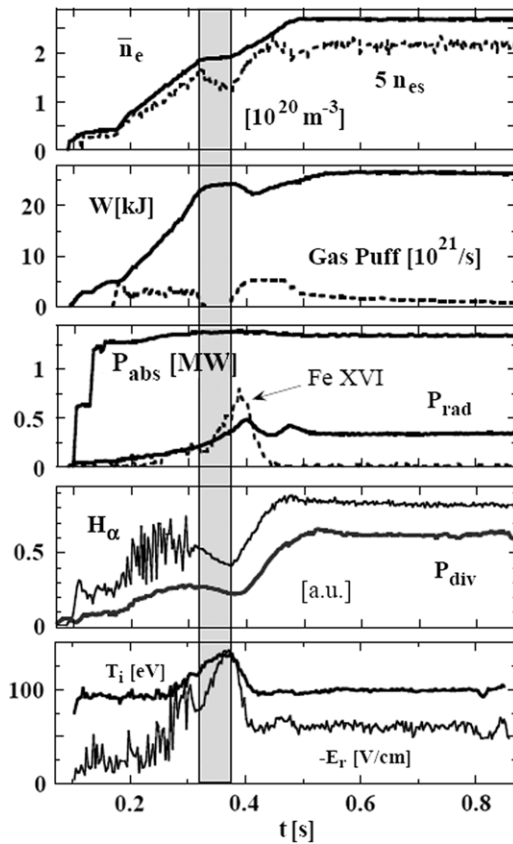


Figure 73. Temporal behaviour of a discharge with an \bar{n}_e -ramp passing an ELM phase to H* (shaded region) and then further to HDH (>0.5 s). n_e and n_{es} ; stored energy W and gas puff rate; P_{abs} , P_{rad} and intensity of FeXVI along a central chord; H_α from divertor region and sub-divertor neutral pressure P_{div} . Ion temperature T_i and radial electric field E_r , both derived from passive observation of a BIV line along a chord in the density gradient region. $t_a = 0.561$, $a = 14.2$ cm, x-point distance to target plate ~ 0.8 cm; $B = -2.5$ T; $P_{abs} \cong 1.4$ MW, $H^0 \rightarrow H^+$, electron fuelling rate from NBI is $\sim 2 \times 10^{20} \text{ s}^{-1}$.

spatial shift during the \bar{n}_e -ramp. The sub-divertor pressure P_{div} , which is a good indicator of particle transport to the target plates (McCormick *et al* 2005), increases more strongly than n_{es} over $H^* \rightarrow$ HDH. This may be an indication of increased cross-field transport across the separatrix and thus a less steep density gradient, supporting the potential trends documented by T_i and E_r .

In HDH the collisionality $\nu^* = v_{ii} \cdot R/v_{th} \cdot t_a$ for impurities and H^+ is higher in comparison with H^* by about a factor of two resulting from the lower $T_e(r)$ and higher $n_e(r)$ values. Impurities are highly collisional over the entire cross-section in both regimes. For the background ions $\nu^*(H^+)$ is typically around 0.2–0.3 in the plasma centre, i.e. they are marginally collisionless but they are always collisional at the edge. Thus, there is not a clear change from one collisionality regime to another, although it cannot be excluded that the differences in ν^* might be related to the change in impurity transport. In any case, the HDH mode could never be established under low-collisionality conditions. Efforts to reduce ν^* by increased heating power (increase of T_e) within an established HDH discharge produces a back

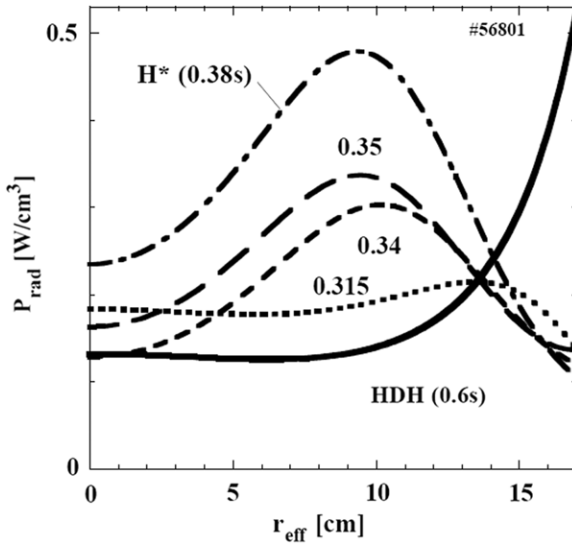


Figure 74. P_{rad} profiles for the H^* and HDH phases of figure 80. The separatrix is around 14.2 cm.

transition to NC conditions. Generally, the increase of n_e^{th} with power also means that any increase in heating power must be accompanied by an increase in density to maintain HDH, thereby somewhat negating attempts to decrease collisionality in that fashion.

7.8. Discussion on H-mode physics in W7-AS

The lack of a clear power threshold behaviour for the conventional H-mode and H-mode related phenomena—strong ∇E_r , short interspersed H^* phases, ELM-like events—observed early in the discharge and in wide ranges of operational space may indicate that there are stellarator specific conditions which facilitate the spin-up of sheared flows and thus the occurrence of an H-mode barrier layer. Both (i) the precondition given by the neoclassically determined E_r and (ii) the physics of flows and turbulence in a 3D drift-optimized configuration may contribute.

(i) The ion-root E_r -values in W7-AS discharges with steep edge gradients are determined (for a wide variety of T_e) by the strong decrease of ion fluxes with E_r values right above the *toroidal* resonance of the ion orbits $|E_r| \geq |E_r^{\text{res}}| = v_{\text{th}} \cdot B_\vartheta$ where v_{th} is the ion thermal velocity. Helical resonances as discussed in [Shaing \(1993\)](#) do not play a role in the W7-AS configuration ([Maaßberg et al. 1993b](#)). Outside the separatrix in the scrape-off layer parallel electron losses lead to $E_r > 0$ such that a strong ∇E_r exists inside the separatrix, pinned by these boundary conditions to the plasma edge. With typical edge values for T_i and the rather large aspect ratio of $A \cong 11$ (i.e. low B_ϑ) and $|E_r^{\text{res}}| \approx v_{\text{th}} \cdot B_\vartheta$ one estimates $\nabla E_r \cong -100 \text{ V cm}^{-2}$ as it is indeed measured for many types of discharges with good confinement already prior to the H-mode transition. This neoclassically determined sheared E_r may constitute a biasing precondition for a transition.

(ii) In 3D drift-optimized configurations global and zonal flows possibly governing the physics of the H-mode transition are expected to differ significantly from the axisymmetric case. Dissipative effects for poloidal flows such as magnetic pumping depend sensitively on the 3D edge topology ([Wobig and Kißlinger 1995](#), [Wobig and Kisslinger 1997](#)). A preferred flow direction is expected in quasi-symmetric configurations—a field where investigations

only recently started (Kleiber and Scott 2005, Nührenberg 2006). The geodesic curvature, κ_G , which is one of the optimization quantities in quasi-isodynamic configurations, also regulates the poloidal viscosity and governs the energetic coupling between zonal flows and geodesic acoustic modes (Sugama and Watanabe 2006). Calculations of drift Alfvén turbulence indicate much stronger zonal flows for the quasi-isodynamic W7-X than for a tokamak (Kendl *et al.* 2003, Nührenberg 2006). Such a coupling mechanism would also lead to an t_a -dependence in H-mode accessibility. In this context it is interesting that Heliotron-J—a device which also has a rather low magnetic shear and follows quasi-isodynamicity as an optimization principle—shows (1) a t_a -dependence in H-mode quality and (2) a gradual development into the H-mode with density, i.e. H-mode like phenomena already at the very beginning of the discharge provided a small minimum density (about $1 \times 10^{19} \text{ m}^{-3}$) is exceeded (Sano *et al.* 2004, 2005).

For both the quiescent H-mode and HDH a sufficiently high density or a density ramp is necessary. For HDH a fast \bar{n}_e -ramp at the beginning of the discharge concurred with the initiation of NBI; however, HDH could also be forced by strong puffing in a fully developed ELM-NC discharge (Grigull *et al.* 2001b, McCormick *et al.* 2002). Experiments with inner sector limiters showed that a hard gas puff could at least transiently enhance the edge density for a given \bar{n}_e (McCormick *et al.* 1999b). It has been demonstrated theoretically that the density increase at the edge can occur faster than typical diffusive times (Igitkhanov *et al.* 2004). Thus a working hypothesis is (McCormick *et al.* 1999a, 1999b, Grigull *et al.* 2001a), that a hard puff forces the formation of an H-mode-like n_e edge profile, which leads to a deepening of the well of negative E_r close to the plasma edge, sheared poloidal flow and suppression of turbulence. Beyond a certain threshold mean density \bar{n}_e^{th} (possibly reflecting a threshold edge density as the local parameter behind) the situation becomes self-sustaining without the driving mechanism of a strong gas puff. The shift of \bar{n}_e^{th} to higher values with higher power (figure 67) may reflect that more central fuelling associated with NBI (leading to peaked, NC-like profiles) must be compensated by stronger edge fuelling, resulting in higher \bar{n}_e . Another approach to the density dependence of the H-modes is addressed by a simplified model where the momentum balance of a multi-species plasma is considered in cylindrical geometry, but with a helical magnetic field (Sünder and Wobig 2006). With increasing density a layer of both reduced viscosity and increased driving forces (turbulent Reynolds stresses) resulting from the radial particle flux is shifted more and more to the edge region. The effect is to produce flat n_e -profiles with a steep density gradient at the edge, as is generally observed for H-modes on W7-AS.

The fact that a quiescent ELM-free H-mode H^* was restricted to well-defined t_a -windows and, e.g., not accessible in the standard divertor configuration illustrates the importance of boundary conditions, yet not understood. Transitions between H^* and HDH could only be obtained with carefully selected t_a values at the edge of the t_a -window towards SDC conditions.

The above discussion does not explain why the quiescent H-mode exhibits strong impurity accumulation, whereas HDH does not. For normal confinement the impurity accumulation can be directly related to its peaked density profiles for which neoclassical confinement predicts the effects observed (section 6.2). In the case of H^* and HDH the n_e -profiles have the same form and impurities are driven to the vicinity of the edge transport barrier in both cases. The inward directed E_r associated with both regimes (figures 69 and 73) contrives to confine impurities inside the barrier such that they accumulate with a hollow radiation profile as observed for H^* . To counteract this influence it is necessary to postulate enhanced impurity diffusion for HDH in the steep gradient region (Ida *et al.* 2003, Burhenn *et al.* 2004), whereby core transport processes remain the same.

From the EMC3-EIRENE code calculations (Feng *et al.* 2006a) a strong retention effect on the target-released carbon impurities is predicted for high-density low- T conditions in the

scrape-off layer. This corresponds to the reduction of the inward-directed thermal force below the outward-directed friction force, which ultimately reflects the reduction of the parallel ion heat conductive transport in favour of the cross-field transport. However, this effect explains neither the access to HDH under limiter conditions nor the sudden flushing out of impurities at the transition from H to HDH.

It should be noted that the enhanced D_α H-mode (EDA) of the C-Mod tokamak has properties similar to HDH, e.g. flat n_e -profiles with steep edge gradients, some overlap of the edge T_e - and n_e -ranges (and thus the associated collisionality v^*) and steady-state, ELM-free operation without impurity accumulation (Greenwald *et al* 1999, Basse *et al* 2004). The impurity transport behaviour is consistent with a strong inward neoclassical impurity pinch in the density gradient region, which to some extent is counteracted by a larger diffusion coefficient for the EDA H-mode in comparison with normal ELM-free H-modes which exhibit accumulation (Pedersen *et al* 2000). A quasi-coherent mode (QC) is thought to promote impurity flushing (Snipes *et al* 2001, Mossessian *et al* 2002, Mazurenko *et al* 2002). Indeed, for the W7-AS HDH discharge of (figure 73) a quasi-coherent mode is also present during the HDH phase reacting even to the temporal modulations in P_{rad} at the beginning of HDH (Belonohy *et al* 2007a, 2007b). However, this mode seems to be absent in other discharges with HDH characteristics in contrast to the case of C-Mod where the QC mode, thought to be a resistive x-point ballooning mode, is clearly seen and localized in the density pedestal region. Note that in W7-AS the HDH mode can also be obtained with limiter plasmas where the x-points are behind the target plates. Thus a consistent and clear signature of an unknown mechanism postulated to expel impurities from the edge region in HDH but not in H* has not yet been found, in spite of intensive investigations with a variety of diagnostics (McCormick *et al* 2003c, Bäumel *et al* 2003a).

7.9. Conclusion on H-modes in W7-AS

The classical quiescent H-mode achieved under stellarator conditions is of high value for general physics understanding of H-modes in toroidal confinement (Wagner 2007). The Optimum Confinement regime, on the other hand, is well-suited as a testbed for drift optimization under collisionless high- T_i conditions, which can be established in a wide radial range of the core plasma. However, both regimes suffer from low separatrix densities not compatible with divertor operation and from enhanced impurity confinement—conditions inappropriate for an integrated baseline scenario towards high-confinement, steady-state operation. ELMy H-modes with optional ELM mitigation possibly using the sensitive configuration dependence of ELMs in low-shear stellarators are an option to be explored. In this frame the discovery of the HDH-mode on W7-AS was vitally important, as it combines superior energy and low impurity confinement with n_{es} that allow successful divertor operation. As a regime at densities above the Greenwald limit of most tokamak devices it has been demonstrated that quasi-steady-state, high density, high confinement and robust high power operation under ELM-free conditions is feasible over a wide range of divertor-compatible operational conditions ($n_e \approx 1.5\text{--}4 \times 10^{20} \text{ m}^{-3}$, n_{es} up to $8 \times 10^{19} \text{ m}^{-3}$, P_{abs} (co-, counter-NBI) $\approx 0.7\text{--}2.8 \text{ MW}$, $P_{\text{rad}}/P_{\text{abs}}$ up to 90%, $B_\varphi \approx 0.7\text{--}2.5 \text{ T}$, $\langle \beta \rangle$ up to 3.1% (Weller *et al* 2003), attached/detached plasmas). Moreover, as a working horse of divertor physics in W7-AS, the HDH regime has delivered the edge conditions (high n_{es} , high P_{rad} at the edge) necessary for divertor studies and comprehensive validation of the EMC3/EIRENE code over the entire spectrum of relevant divertor conditions (section 8.5). Whereas salient features of the HDH regime are reasonably documented, the physics understanding of specific HDH characteristics is at a phenomenological level. The dominant attribute of impurity

flushing may be modelled by postulating enhanced impurity diffusion in the gradient region where E_r is large and negative, but there is no understanding or even information as to what this mechanism might be. It may well be that the HDH-mode is one of a generic family of ‘high collisionality’ ELM-free H-modes with some form of enhanced (impurity) transport at the edge, meaning that HDH will be restricted to the high-collisionality corner of operational space. Consequently, at this level it is not possible to extrapolate to other devices.

8. Plasma edge and divertor physics

8.1. Introduction

The development of adequate divertor solutions for controlled plasma exhaust is one of the key issues for present and next-step larger stellarators. However, in contrast to the extensive experience gained with divertors in tokamaks over the last few decades (see e.g. [Pitcher and Stangeby \(1997\)](#), [ITER Physics Expert Groups \(1999, 2007\)](#), [Schneider et al \(2006\)](#)), related research on stellarators is in its absolute infancy. An overview of efforts in this regard is given in [König et al \(2002, 2004\)](#). A divertor option compatible with stellarator configurations is the so-called island divertor (ID) which utilizes the flux diversion by intrinsic or externally induced magnetic islands at the plasma edge. This concept was initially proposed in the 1970s for tokamaks as a low-current alternative to the poloidal field divertor ([Karger and Lackner 1977](#)). An advantage is that, due to the small resonant perturbation fields of $\Delta B_r/B_\varphi \approx 10^{-4}\text{--}10^{-3}$ needed for the formation of islands, topological parameters of the islands governing the flux diversion can basically be controlled by low-current auxiliary coils. A series of plasma edge studies included dedicated pre-experiments verifying in particular the flux diversion by boundary islands as well as the performance of newly installed control coils ([Grigull et al 1990](#), [Sardei et al 1992](#), [Hildebrandt et al 1992](#), [Grigull et al 1992](#), [Brakel et al 1992](#), [Sardei et al 1995](#), [Hildebrandt et al 1995](#), [Grigull et al 1996, 1997](#), [Zebisch et al 1997](#), [Sardei et al 1997](#), [Weller et al 1997b](#), [McCormick et al 1999b](#), [Herre et al 1999](#), [Herre 1999](#), [König et al 2001](#), [McCormick et al 2001](#)). Finally the in-board limiters of W7-AS were replaced by an ID at the end of 2000 ([Kisslinger et al 1993](#), [Grigull et al 2001b](#), [Brakel et al 2002](#)). The aim was to perform first proof-of-principle experiments with the perspective of future application in the larger W7-X stellarator ([Kisslinger et al 1993](#), [Renner et al 2000, 2002](#)). The most prominent result associated with the installation of the divertor was the discovery of the HDH mode (see section 7.6, [Grigull et al \(2001b\)](#), [McCormick et al \(2002\)](#)), whose properties enable, besides other improvements, promising divertor plasma regimes ([Grigull et al 2002, 2003b](#), [McCormick et al 2003c](#)). Thus a database of edge/scrape-off-layer (SOL)/divertor experience has been compiled which may serve both as a basis for future W7-X divertor studies and as reference material for validation of the 3D edge transport code EMC3-EIRENE ([Feng et al 1999c](#), [Reiter et al 2005](#)).

This section gives an overview of the edge and divertor plasma phenomenology and, as far as presently understood, of the underlying physics. Section 8.2 first introduces the ID concept and compares basic topological characteristics with those of tokamak poloidal field divertors. Section 8.3 describes the W7-AS edge magnetic field topology, the divertor arrangement and the diagnostics equipment. Section 8.4 presents the main experimental results by following a route from general performance aspects to more specific details. Section 8.5 outlines the development of the EMC3-EIRENE code as an essential part of the ID studies and relates, as far as presently possible, modelling results to experimental findings. Beyond that, it also

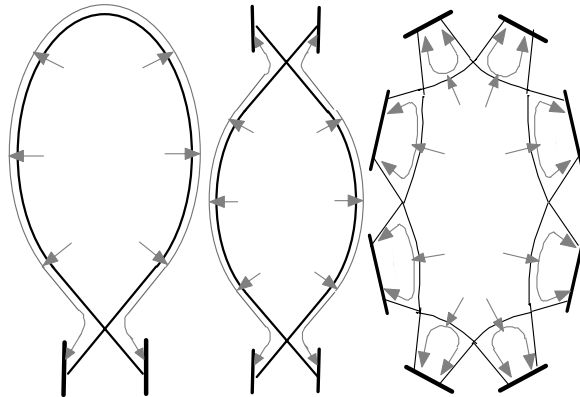


Figure 75. From left to right: schematics of single-null and double-null tokamak divertors and of an island divertor. Projections of energy and particle flow directions to targets (thick solid lines) are indicated by grey arrows. Mode numbers of boundary islands in stellarators vary from machine to machine.

addresses certain ID features which, due to the shutdown of W7-AS in 2002, could not yet be addressed experimentally.

8.2. The island divertor concept

In divertor configurations, particles and energy leaving the confinement region are guided along open field lines to targets remote from the core plasma (flux diversion). Thus unfavourable penetration of sputtered impurities and recycling neutrals into the core is prevented, and the targets are potentially protected against thermal overload by means of enhanced radiation from the edge. Density control is enabled by active pumping of neutrals entering the sub-divertor region. In tokamaks, divertor configurations are realized by introducing additional poloidal fields which tear the nested flux surfaces at the edge apart by forming a separatrix with x-points at the top and bottom ('double-null') or on one side only ('single-null' configuration). In low-shear stellarators, magnetic islands at the edge provide a natural separatrix configuration, figure 75. With respect to the symmetry of the different devices, divertor targets and baffles in tokamaks are axisymmetric, while those in stellarators have to be toroidally finite and three-dimensionally shaped in order to avoid leading edges. Topological parameters relevant for the flux diversion are the field line connection lengths L_c inside the SOL from the stagnation plane to the targets and the geometrical target-to-core distance. In tokamaks, L_c scales as $R/N t$ with R being the major radius, N the number of x-points and t the rotational transform within the SOL. In IDs, the respective lengths are determined by the internal rotational transform t_i inside the islands and, hence, by the magnetic shear τ' at the position of the n/m resonance, $L_c \propto R/n t_i$ with $t_i = r_i \tau'$. Symbols m, n, r_i denote the poloidal and toroidal mode numbers and the radial size of the islands, respectively. Consequently, connection lengths, in particular in low-shear stellarators, are typically larger than in tokamaks, despite multi-island structures. The target-to-core distance is limited by the radial extension of the islands which scales as $r_i \propto (R b_{mn}/n t')^{1/2}$, with b_{mn} being the resonant radial perturbation field normalized to the toroidal field. Large low-shear stellarators with low poloidal mode number generally favour the formation of large islands. In the large helical device (LHD), a heliotron with strong shear, a local island divertor (LID) configuration (Morisaki *et al.* 2005) is realized by choosing the lowest- $m, n/m = 1/1$ island generated by additional perturbation fields. In W7-X, an ID

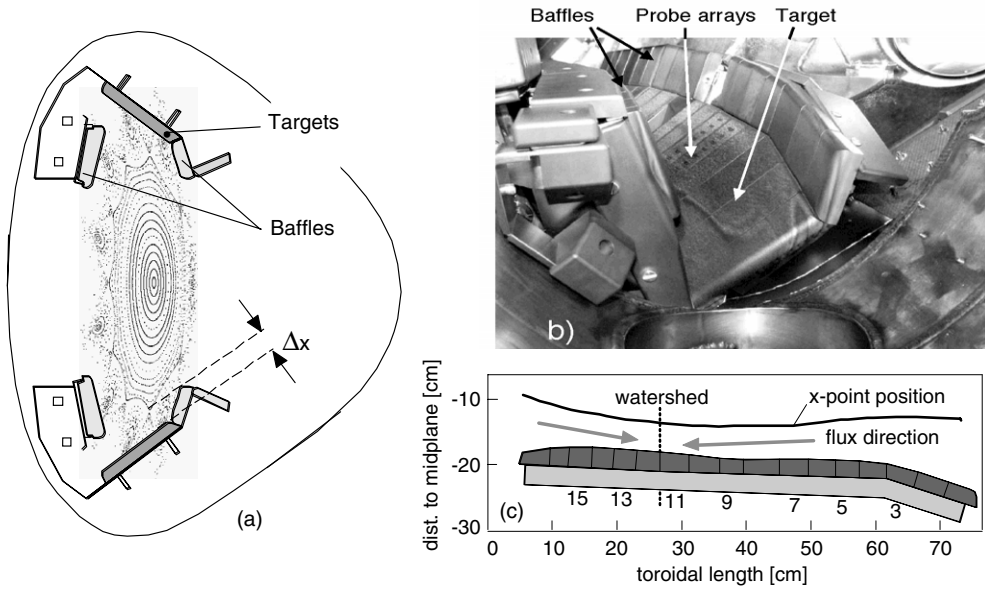


Figure 76. (a) Elliptical plasma cross-section with island divertor modules. Such modules are installed at the top and bottom of each of the five elliptical planes. Δx denotes the minimum separation between x-points and targets. (b) Photograph of a bottom divertor module. (c) Toroidal cross-section of a bottom target, x-point positions, and tile numbers for orientation. The watershed separates fluxes coming from the upstream high field side (left) from those from the low field side (right). Numbers indicate target tiles for orientation. Tiles 5 and 6 and 13 and 14 are equipped with flush-mounted poloidal Langmuir probe arrays.

configuration will be formed by relatively large 5/5 intrinsic boundary islands. Principally, the islands could be arbitrarily enlarged by increasing b_{mn} , but—due to the limited space between main plasma and first wall—in general only at the expense of the confining plasma cross-section. Because of this latter restriction, target-to-core distances have to be considerably shorter, at least in low-shear devices with multiple x-points, than those in tokamak divertors which need extended space only at the bottom (single-null) or top and bottom (double-null) of the configuration. Although both tokamak poloidal divertors and IDs are governed by the same basic physics, these topological differences considerably affect the weights of contributing physics processes. Smaller target-to-core distances basically ease the penetration of recycling neutrals into the core and enhance, in combination with longer connection lengths (small field line pitch $\Theta = i_0 a / R$), the perpendicular-to-parallel transport ratio in the island SOL (for details see section 8.5). The main issue with respect to the ID experiments on W7-AS was whether at all and to what degree such configurations are appropriate for divertor operation in the sense mentioned above.

8.3. The W7-AS island divertor

Divertor configuration. In W7-AS, the intrinsic, symmetry preserving $m/n = 5/8$ to 5/10 boundary islands form natural ID configurations. The divertor was optimized for 5/9 islands but works as well with 5/8 or 5/10 islands. It consists of five identical (top-bottom) module pairs arranged at the elliptical cross-sections, figures 76(a) and (b). Each module is composed of a 3D shaped, inertially cooled carbon fibre compound (CFC) target intersecting

the islands, and of baffles (isotropic graphite). The target toroidal position closest to the x-points ('watershed') generally separates fluxes coming from the upstream high-field side from those from the low-field side, as is schematically indicated in figure 76(c). Radial positions and size of the islands and, hence, field line connection lengths L_c to the targets as well as the minimum separations Δx between x-points and targets can be varied within relatively large ranges by fine-tuning of t (by adjusting the planar/modular coil currents) as well as by auxiliary coil currents I_{cc} controlling the $B_{5,n}$ perturbation field magnitude (see section 8.4.2, figures 85(a) and 5). Most data have been obtained in the so-called standard divertor configuration (SDC) at $B_\varphi = -2.5$ T, a vertical field of $B_z = -0.01$ T, $t_a = 5/9$ and $I_{cc} = 3.5$ kA. If not explicitly mentioned otherwise, the data presented in the following sections refer to NBI discharges ($H^0 \rightarrow H^+$ injection) at these settings. The corresponding vacuum field connection length L_c from an upstream reference position (1 cm outside the main plasma separatrix at the equatorial inboard side of a triangular symmetry plane) to the target is about 90 m. The target-to-x-point minimum distance Δx is about 4 cm. At an averaged equilibrium plasma pressure of $\beta \approx 1\%$, which is typical for HDH discharges with $P_{NBI} = 2$ MW (absorbed power $P_{NBI}^{\text{abs}} = 1.4$ MW), these values are estimated to be reduced to about 40 m and 2.6 cm, respectively. However, these latter values, resulting from recent HINT2 equilibrium code calculations (Suzuki *et al* 2006), need to be considered as preliminary since certain assumptions on pressure and current distributions at the edge need further validation.

Divertor specific diagnostics. About 65% of the target tiles are instrumented with thermocouples (target tile calorimetry). Two opposite (top and bottom) divertor modules are equipped with target-integrated, flush-mounted poloidal Langmuir probe arrays, four visible range CCD cameras with interference filters and two IR-thermography cameras (McCormick *et al* 1999a). The probe arrays are placed at target tiles 5, 6, 13 and 14 (see figure 76(c)). The cameras (both visible and IR) look from their top and bottom positions through the plasma onto the respective opposite target plates. The top divertor is additionally equipped with a spectrometer tangentially imaging the SOL range between target tiles 8, 9 and main plasma separatrix ('SOL spectrometer', see section 8.4, figure 83(a)). The equivalent range at the bottom divertor is imaged by an 8-channel bolometer array ('divertor bolometer').

8.4. Experimental results

8.4.1. General performance. The divertor modules generally improved the impurity and recycling behaviour in W7-AS. Impurity radiation from the core was reduced, and density control became much easier. Both effects are primarily ascribed to the considerably enlarged coverage of the plasma surface by carbon which more effectively screens the plasma from medium- to high-Z impurities, in addition to enhancing the transient pumping capability. As already mentioned, the most important achievement was the access to the HDH mode. Its properties enabled very high line-averaged densities to be attained under controlled, quasi-stationary conditions with high separatrix densities and edge radiation fractional levels, permitting access to stable detachment scenarios (downstream temperature $T_{ed} < 10$ eV, details in next sub-section). This is exemplarily demonstrated in figure 77 which compares time traces of net current-free HDH discharges (attached and detached) with a normal confinement (NC) discharge with \bar{n}_e being slightly below the HDH mode threshold density. In contrast to NC discharges, which generally suffer from impurity accumulation in the core (oxygen, iron, chlorine), both attached and detached HDH regimes typically show more or less strong

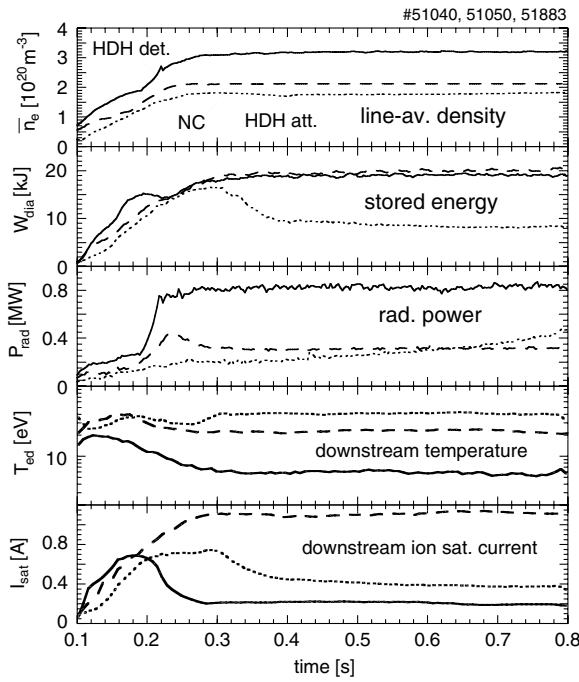


Figure 77. Comparison of typical time traces from net current-free, normal confinement (NC), HDH attached, and HDH detached discharges. Standard divertor configuration (SDC, see text), NBI $H^{\circ} \rightarrow H$ injection, absorbed NBI power $P_{NBI}^{\text{abs}} = 1.4$ MW. Downstream peak parameters were obtained from Langmuir probe arrays at target tiles 13 and 14, bottom divertor (peak 2, see more below figure 80).

edge radiation only (mainly from carbon) with radiated power fractions up to about 90% during detachment (see section 7.7). They can be sustained quasi-stationary over many energy confinement times. In most cases, the pulse lengths were limited to about 1.5 s only by the NBI performance and not yet by outgassing of plasma facing components and subsequent loss of density control. Power accountabilities $(P_{\text{rad}} + P_{\text{cal}})/P_{NBI}^{\text{abs}}$ were typically at about 50–70% for attached, and close to 100% for detached discharges. Here P_{cal} are convective losses from target tile calorimetry (scaled up to full coverage by thermocouples) and P_{rad} radiation losses inferred from two bolometer cameras at a triangular plane (not covering radiation from the divertor regions). Stable detachment needs a rather high upstream density and is found to be always partial in the sense that it extends over most of the target areas apart from a small region, figure 78. In agreement with the number of island fans impinging on the targets, the strike zones on the targets basically form up to three poloidally separated lines which helically more or less extend along the targets (Hildebrandt *et al* 2003b). Due to the specific SOL topology, the plasma at the outer strike line on target tiles 1–6 stays permanently attached, but at reduced power load. At partial detachment, considerable neutral compression within the sub-divertor region is observed (McCormick *et al* 2005), which is a precondition for active particle pumping. Prior to detachment, the development of the strike zones on the targets with increasing density shows, however, a multi-faceted picture, and the existence of finite density ranges with stable partial detachment is restricted to specific configurational settings. Details are described in the following sub-section.

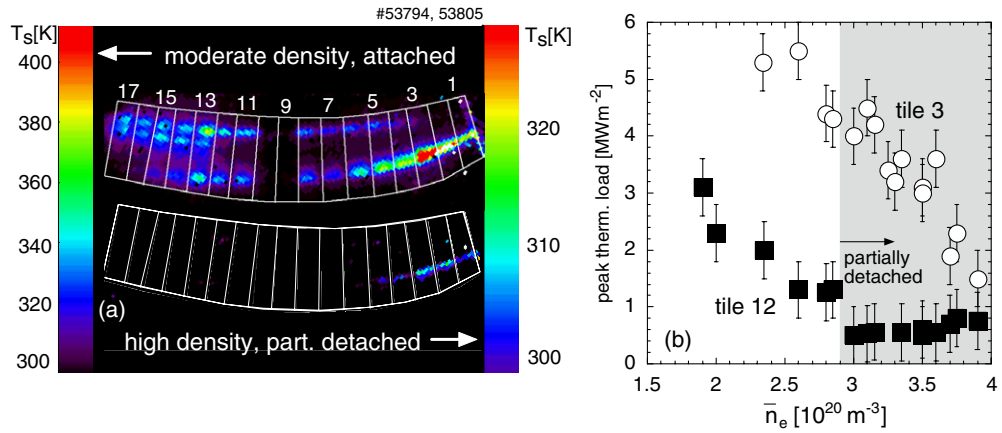


Figure 78. Target thermal load from thermography. SDC, H → H⁺ injection, $P_{\text{NBI}}^{\text{abs}} = 1.4 \text{ MW}$. (a) Contours of target surface temperatures T_s for attached and detached HDH scenarios. Stable detachment is always partial meaning that the plasma detaches from most of the surface apart from a small region (bottom right). (b) Peak thermal loads on target tiles 3 and 12 as functions of \bar{n}_e .

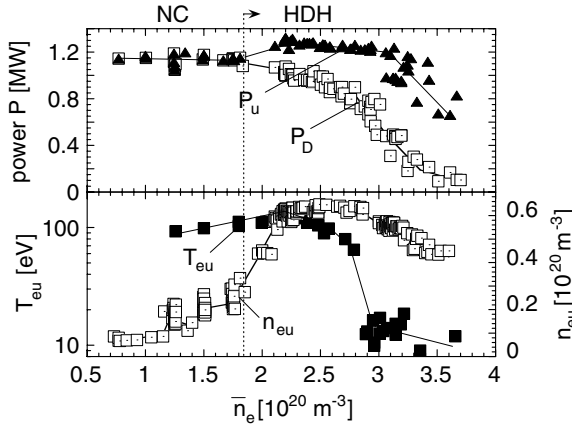


Figure 79. SOL and upstream plasma parameters as functions of \bar{n}_e . SDC, H^o → H⁺ injection, $P_{\text{NBI}}^{\text{abs}} = 1.4 \text{ MW}$. (a) (Top) Net powers $P_u = P_{\text{NBI}}^{\text{abs}} - P_{\text{rad}}^{\text{core}}$ flowing across the main plasma separatrix and $P_D = P_{\text{NBI}}^{\text{abs}} - P_{\text{rad}}$ flowing to the divertor. The radiated power P_{rad} does not include radiation from the target proximity. (b) (Bottom) Electron temperatures T_{eu} and densities n_{eu} at the upstream separatrix position.

8.4.2. Edge and divertor plasma phenomenology.

Upstream conditions. The SOL parameters are governed in detail by the magnetic field structure and divertor geometry as well as by the parameters at the upstream separatrix position. Typical trends of the latter at fixed NBI power are shown in figure 79, which plots $P_{\text{NBI}}^{\text{abs}} - P_{\text{rad}}$, the power flowing across the separatrix $P_u = P_{\text{NBI}}^{\text{abs}} - P_{\text{rad}}^{\text{core}}$ (with $P_{\text{rad}}^{\text{core}}$ being the core radiated power), the separatrix values of electron temperature T_{eu} , and density n_{eu} as functions of \bar{n}_e . T_{eu} was obtained shot by shot from a dedicated edge Thomson scattering system at the high-field side of a triangular plane, whereas n_{eu} was measured by a Li-beam. The accuracies of the upstream absolute values in figure 79 suffer somewhat from uncertainty with respect to the

exact radial position of the separatrix, but the tendencies can be taken as representative. T_{eu} measured at the high-field side basically reflects the course of P_u , but shows a steeper decrease towards highest densities than expected from two-point modelling which assumes parallel energy transport alone (Schneider *et al* 2006). The extremely low values at detachment are consistent with strong carbon radiation from that region (see below). However, the observation of permanent attachment at target tiles 1–6 predicates a considerably weaker drop of T_{eu} at the low-field side. Although such in/out asymmetry could not be experimentally verified due to the lack of diagnostics at appropriate positions, we assume that more compressed flux surfaces at the low-field side, in particular in the range of the elliptical planes, lead to an enhanced cross-field energy flux and, consequently, to a higher upstream temperature (see also section 8.5). The variation of the upstream density n_{eu} with \bar{n}_e reflects respective n_e radial profile modifications—strong broadening at the NC \diamond HDH transition and slight shrinking again at detachment. This is found to be correlated with the n_e -dependence of the edge-to-core ratio of the refuelling rate by recycling neutrals (section 8.5).

Strike zone structure. Basically, the strike zones should concentrate along helical lines, reflecting the intersection lines of the islands' separatrix with the targets. According to 'field line diffusion' calculations it follows that target tiles 1–11 should be intersected by flows along the island fans B and D, and tiles 12–17 only by the flow along fan C (figure 80). Complementary fans as well as fan A should be mutually shadowed by other target modules. However, as the figure also shows, the strike lines indicated by ion saturation current poloidal profiles from the Langmuir probe arrays exhibit considerable deviations from this simple picture, including a top/bottom asymmetry as well as a regime (NC/HDH) dependence. These deviations are not yet understood in detail, but the asymmetry inverts to a large extent with B -field reversal (Grigull *et al* 2003a), thus indicating superimposed plasma drift effects (Feng *et al* 1998). From the number of sharp peaks we conclude that the basic 5/9 island structure remains preserved also at finite β . Nevertheless, uncertainties exist concerning the details of the real equilibrium island structure, the occurrence of considerable drift effects and the fact that slight misalignments of the targets relative to the magnetic field cannot be fully excluded.

Downstream plasma characteristics. Notwithstanding this restriction, the leading order development of the downstream parameters in dependence on the upstream values can be characterized for the basic divertor scenarios introduced in section 8.4.1 in somewhat more detail. Figure 81 exemplarily shows peak values of downstream ion saturation current densities $j_{s\parallel}$, (particle fluxes), electron temperatures T_{ed} and densities n_{ed} from the Langmuir probes at four positions (see peak numbers in figure 80) as functions of the upstream density n_{eu} . The data were obtained from flat-top discharges as well as discharges with slow density ramps or stepwise increased density and are averaged over time intervals of 50 ms. Peak 1 and 2 positions can be taken to some extent as representative of the strike zones developing to detachment, those shown for the peak 3 and 4 positions for the zone with permanent attachment. As is basically expected from particle and power balance considerations in the SOL, T_{ed} monotonically decreases with increasing \bar{n}_e and n_{eu} and, at further increased \bar{n}_e , even with falling n_{eu} due to decreasing power influx P_u and increasing radiation from the SOL. Peaks 1 and 3 are characteristic for normal confinement (NC) discharges. At the transition to HDH regimes, peak 1 splits into peak 2 and a neighbouring peak, peak 3 shifts to the peak 4 position (see figure 80), both being connected with a discontinuity in the courses of the maximum $j_{s\parallel}$ and n_{ed} values of the profiles. At line-averaged densities exceeding the value

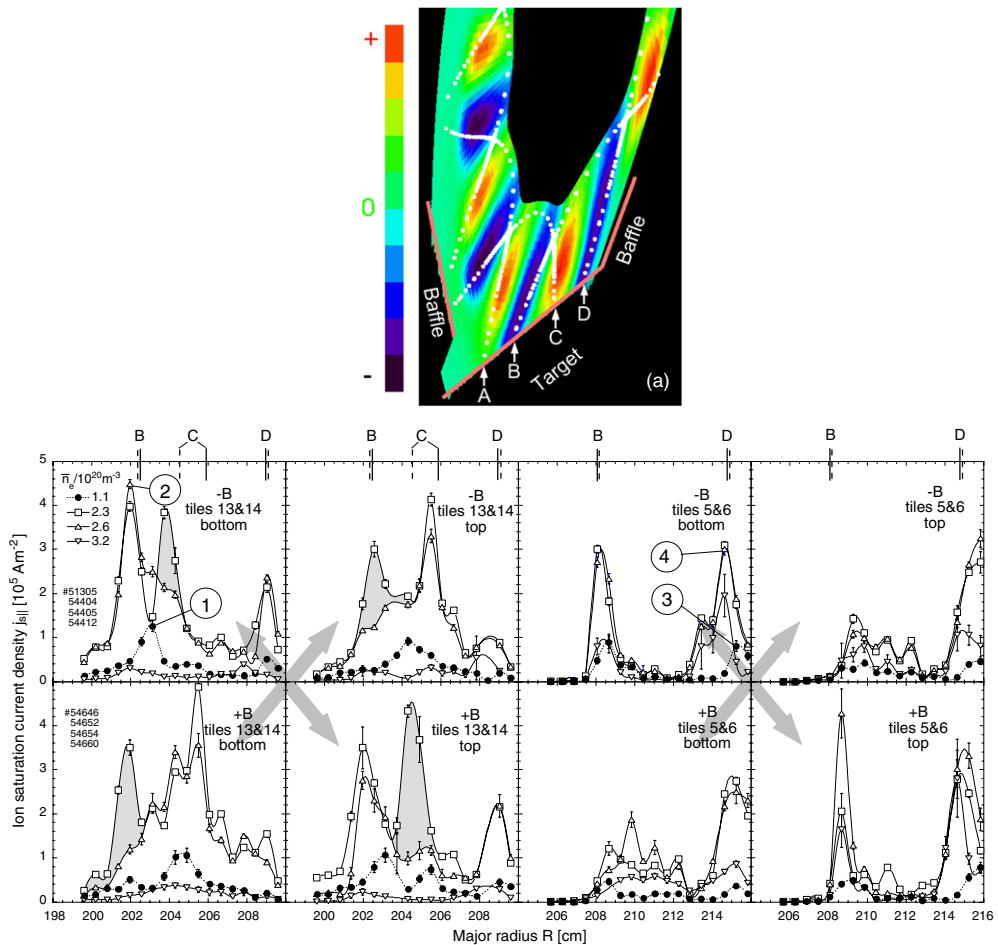


Figure 80. Strike line poloidal positions and top/bottom asymmetries. (Top) Particle fluxes from EMC3-EIRENE code simulation, SDC (vacuum magnetic field). Blue and red colours indicate flows in negative (−) and positive (+) directions with respect to B-fields. (Bottom) Ion saturation current poloidal profiles from target-integrated Langmuir probe arrays at target tiles 13 and 14 and 5 and 6 at negative and positive magnetic field directions, $H^0 \rightarrow H^+$ injection, $P_{NBI}^{\text{abs}} = 1.4 \text{ MW}$. Letters and short lines at the top indicate island fan positions corresponding to the left figure for the vacuum magnetic field (full lines) and an equilibrium configuration with $\langle \beta \rangle \approx 1\%$ (dashed lines, HINT2 code result). The measured profiles show a top/bottom asymmetry which widely inverts with B -field reversal as is accentuated by grey shaded areas and arrows. Encircled numbers indicate peaks which are exemplarily analysed in more detail in figure 81.

where n_{eu} is maximum, the maximum T_{ed} at tiles 13 and 14 (peak 2) drops to below 10 eV, and the corresponding $j_{s\parallel}$ and n_{ed} values become strongly reduced, thus indicating the approach to detachment. A characteristic difference from tokamak divertors is that both the particle flux and the downstream density typically start to decrease already prior to detachment at downstream temperatures well above 10 eV. Peak 4 parameters develop similarly, but stay at considerably higher values in the high- \bar{n}_e range thus indicating permanent attachment. This difference and, hence, the partial character of detachment, becomes plausible when assuming hotter regions of the island SOL at the low-field side of the elliptical cross-section ranges. Field lines (and flux tubes) starting from the upstream stagnation plane have, after finally

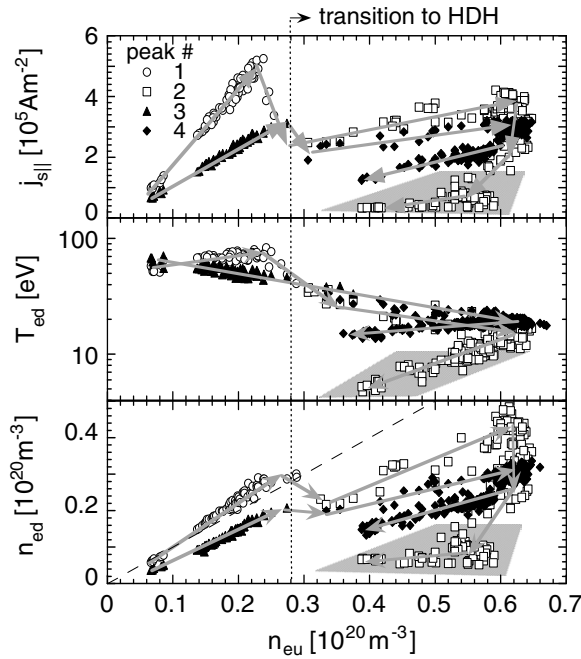


Figure 81. Downstream local parameters from target-integrated Langmuir probes. Peak values of the ion saturation current density $j_{s\parallel}$, the electron temperature T_{ed} , and the density n_{ed} as functions of the upstream density n_{eu} . SDC, $H^o \rightarrow H^+$ injection, $P_{NBI}^{\text{abs}} = 1.4$ MW. Peaks 1–4 correspond to the positions indicated in figure 80 by respective encircled numbers. Grey arrows indicate the directions of increasing \bar{n}_e . The dashed line in the bottom figure indicates $n_{ed} = n_{eu}$. Peak 2 develops to detachment (hatched ranges, $T_{ed} < 10$ eV, reduced particle flux), whereas the peak 4 data indicate permanent attachment even at highest \bar{n}_e values.

passing through this hotter island region, short connection to the strike region with permanent attachment (one magnetic field period) but long connection to detachment regions (eight field periods). This picture is supported by EMC3-EIRENE results (section 8.5) and probably explains—analogously to the inboard/outboard asymmetries observed in tokamak divertors—the different detachment behaviour. In contrast to a tokamak divertor SOL which is dominated by parallel transport, and deviating from earlier results in separatrix configurations bounded by limiters on W7-AS (Grigull *et al* 1996), a well pronounced high-recycling regime (with n_{ed} strongly exceeding n_{eu} in consequence of pressure constancy along field lines) prior to detachment is not observed, figure 81(bottom). Assuming this holds for all strike zones, a considerable loss of parallel momentum in this geometry at T_{ed} values still well above about 5 eV is indicated, where momentum losses due to charge exchange (CX) are not yet effective (ITER Physics Expert Groups 1999). EMC3-EIRENE code simulations support this assumption and relate this effect to friction between counter-streaming particle flows within the island SOL as well as cross-field particle and momentum transport into shadowed regions between the discontinuous targets. Such behaviour is predicted to be generic for the ID configuration of W7-AS (section 8.5).

The course of downstream parameters at the top divertor show similar features up to the onset of partial detachment. In order to abstract from changing peak positions and different local developments shown in figure 80, figure 82 compares relative courses of the total ion saturation currents (from Langmuir probe arrays) and total H_α -intensities (from CCD cameras

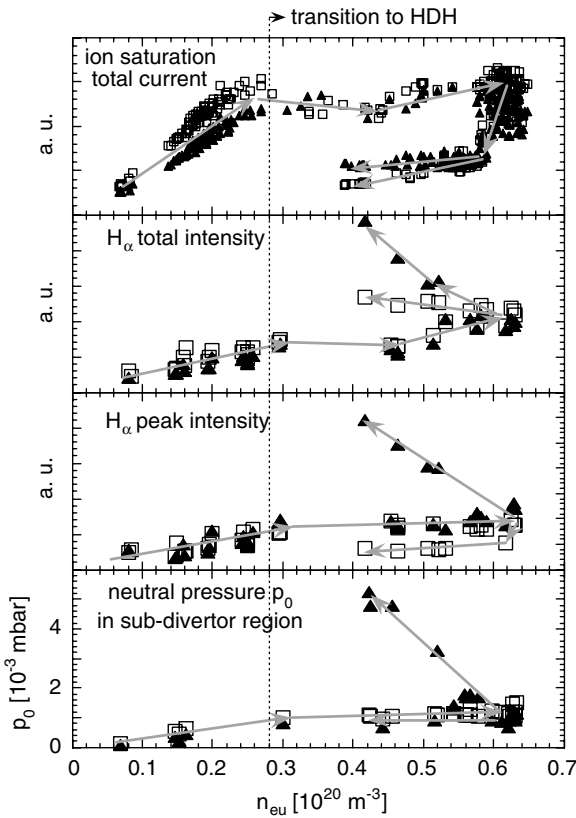


Figure 82. Particle fluxes and neutral pressures, SDC, $H^0 \rightarrow H^+$ injection, $P_{NBI}^{\text{abs}} = 1.4$ MW. From top to bottom: ion saturation total currents, H_α total intensities, local maximum H_α intensities, and neutral pressures in the sub-divertor regions at top (solid symbols) and bottom (open symbols) divertors as functions of the upstream electron density n_{eu} . At partial detachment (rollover of n_{eu}), the currents (fluxes onto the targets) strongly decrease, whereas the total H_α -intensity top/bottom asymmetrically increases due to increasing contributions from the volume. The neutral pressure reflects the courses of the H_α signals. The strong increase during detachment from the top divertor is associated with the occurrence of volume recombination in that region (see next figure).

imaging the top and bottom targets) in dependence on the upstream density. We note that, with the transition to HDH, the data from both diagnostics indicate a less steep increase of the particle flux than of the upstream density. The absolute level is typically about twice that of the quiescent H-mode (H^*), section 7.1. At partial detachment, the currents (which directly represent the particle fluxes onto the targets) strongly decrease, whereas the total H_α -intensity increases due to increasing contributions from the volume. In that range, where the ionization-to-excitation rate becomes temperature dependent, the figures show a pronounced top/bottom asymmetry: both the total as well as the maximum local H_α -intensities from the top divertor region are much higher than those from the bottom region. Neutral particle densities near the wall outside the divertor regions are typically at about 10^{-4} mbar. At partial detachment, the pressure in the top sub-divertor region increases up to about 5×10^{-3} mbar, whereas the pressure in the bottom region even slightly decreases, figure 82 (bottom), thus reflecting the asymmetry of the H_α -radiation. Both asymmetries, that of the H_α -intensities and that of the neutral compression, are found to be inverted at reversed B -field direction (McCormick *et al* 2005). The increasing

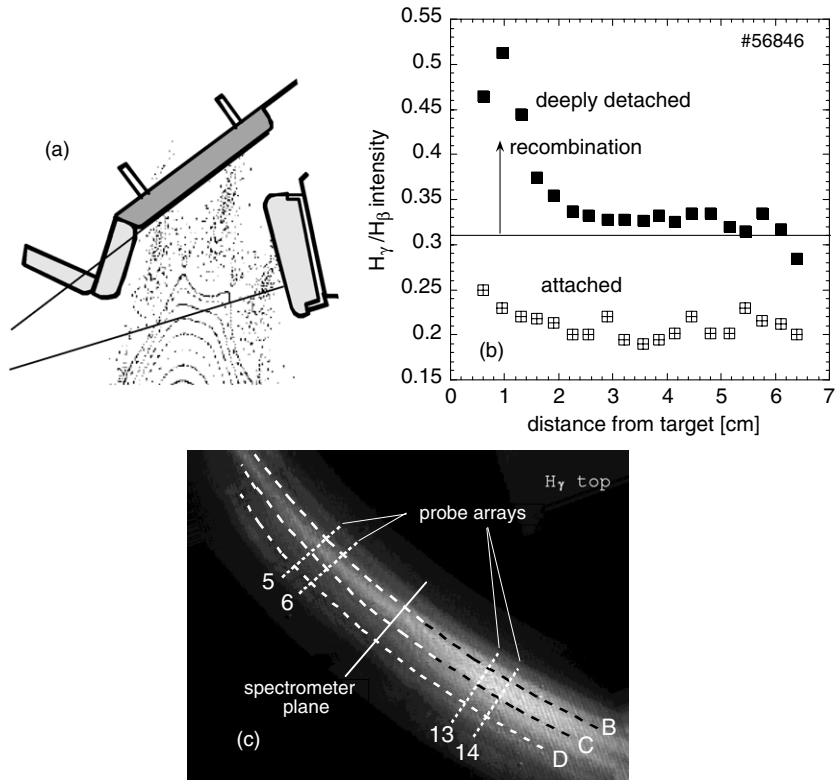


Figure 83. Indication for volume recombination near the top target. (a) Viewing angle of the SOL spectrometer. (b) H_γ/H_β intensity ratios from the SOL spectrometer as functions of the distance from the divertor target for attached (crossed squares) and deeply detached (solid squares) divertor plasmas. Values above 0.31 indicate volume recombination. (c) Camera view of H_γ -emission from the top target region. Dashed lines indicate island fan positions according to figure 80(a).

neutral compression at detachment is probably caused by an increased neutral density in the target and the divertor slit region due to volume recombination. This presupposes T_{ed} values below about 1.5 eV. Although such low values could not be verified by probe data, which tend to overestimate very low downstream temperatures due to kinetic effects (Strangeby 1995), the high ratio of the H_γ/H_β -intensities from the SOL spectrometer shown in figure 83 gives such evidence (Wenzel *et al.* 2003, Ramasubramanian *et al.* 2004, Wenzel *et al.* 2004). Further support is gained by an analysis of Balmer line broadening indicating the existence of a cold, condensed plasma layer in that region (Wenzel *et al.* 2003, Ramasubramanian *et al.* 2004). Bottom camera views of strong H_γ -emission indicate that the recombination zone extends over a broad target range, figure 83(c). Although data from the SOL spectrometer are available only for the top divertor at negative B -field there is indirect indication from the neutral pressure that volume recombination occurs at the top target only, and that this asymmetry also inverts with B -field reversal.

Impurity radiation. There is evidence from the two bolometer arrays at the triangular plane and from spectroscopy that the radiative losses from HDH discharges (attached as well as partially detached) are dominated by carbon radiation from the edge. Sputtering from

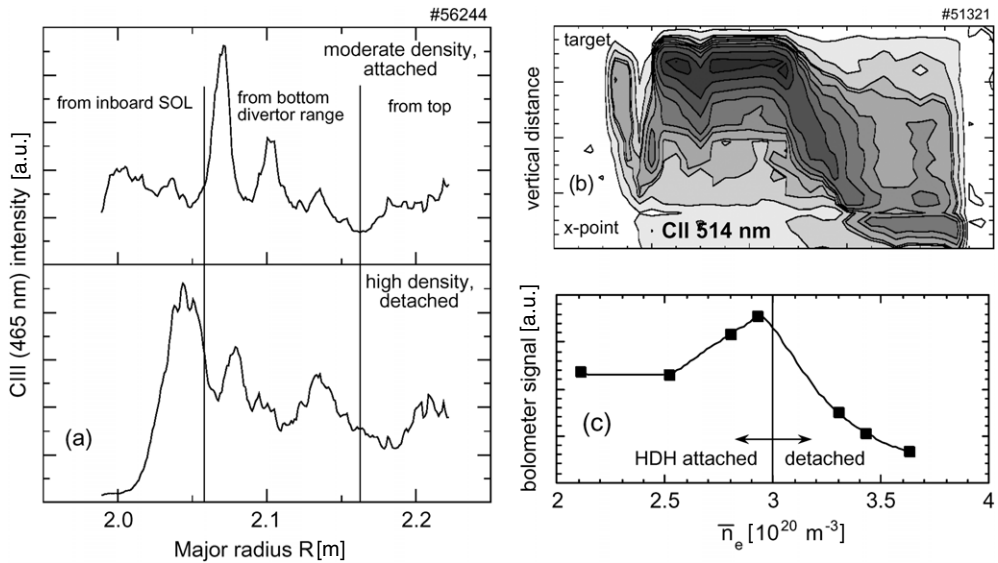


Figure 84. Carbon radiation, SDC, $H^0 \rightarrow H^+$ injection, $P_{NBI}^{\text{abs}} = 1.4 \text{ MW}$. (a) CIII line radiation radial profiles at a toroidal position of target tile #5, bottom divertor. The profiles were obtained from a top camera looking vertically through the plasma onto the bottom target. CIII radiation source ranges were allocated by means of the peak radial positions combined with a comparison of peak line curvatures from the total camera view with field line curvatures in these ranges. (b) Line-of-sight integrated contours of the CII line radiation over the range between target and x-point from the SOL spectrometer (see figure 93(a)). At 0.5 s, the discharge was driven to partial detachment by ramping \bar{n}_e from 2.3 to $3.1 \times 10^{20} \text{ m}^{-3}$. (c) Signal from the divertor bolometer channel closest to the bottom target versus \bar{n}_e . In combination, the figures indicate that the carbon radiation lifts, at detachment, off from the targets and becomes enhanced at the inboard SOL.

divertor targets is probably the primary source of this carbon. Unfortunately, the available set-up of bolometer arrays and cameras was not suited for tomographic reconstruction of detailed poloidal distributions of the radiation sources considering the multi-island structure at the edge. Measurements of line-integrated radiation profiles (Ramasubramanian *et al* 2004, Wenzel *et al* 2004, 2002, Thomsen *et al* 2004, Wenzel *et al* 2005) yield a picture which is not unique and difficult to interpret in detail. The top CCD camera shows, however, multi-stripe structures of the CII and CIII line radiation which, via the curvatures and radial positions of the individual stripes, can be approximately assigned to the x-point proximities (detached discharges) or the strike lines on the bottom target (attached discharges) (Ramasubramanian *et al* 2004, Wenzel *et al* 2005, 2002, Thomsen *et al* 2004). Combining in particular respective CIII line radiation radial profiles with vertical profiles from the SOL spectrometer and the divertor bolometer (Giannone *et al* 2003) indicates that partially detached discharges show nearly vanishing radiation from the detached region of the divertor, figures 84(b) and (c), but enhanced radiation in particular from the inboard SOL, figure 84(a). Considering the cooling rate of the carbon emission, which is maximum at about 10 eV (Strangeby 2000), this result is, as already mentioned, consistent with the low T_e -values measured at the inboard upstream position.

Parameter range for stable detachment. In accord with basic energy balance considerations, threshold densities for the onset of partial detachment increase with NBI power: for hydrogen

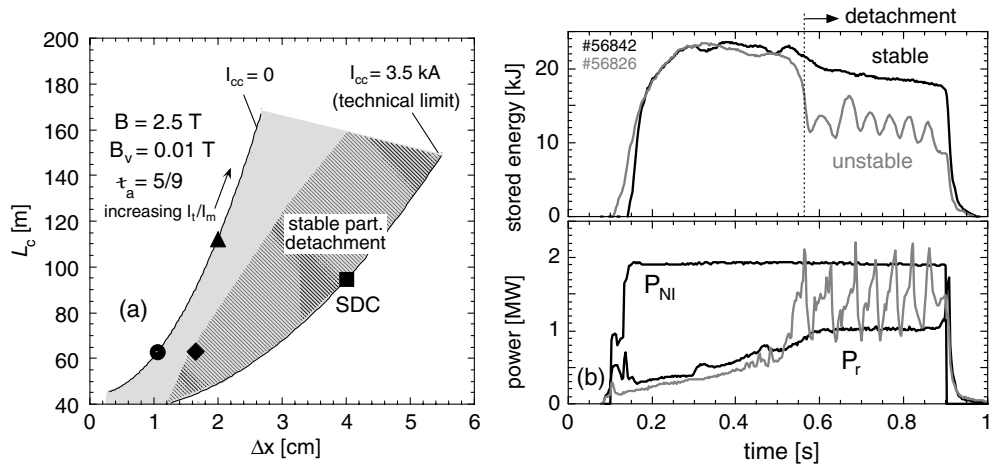


Figure 85. Existence of stable partial detachment. (a) Accessible range of field line connection lengths L_c from upstream stagnation plane (1 cm outside main plasma separatrix) to targets, and minimum separations Δx between targets and x-points (see figure 76(a)), vacuum magnetic field, $\tau_a = 5/9$. Within the shaded range, L_c and Δx can be independently varied by adjusting the toroidal/modular coil current ratio I_t/I_m and control coil currents I_{cc} . SDC indicates the standard divertor configuration (see text). The hatched area indicates the existence range of stable partial detachment. Symbols denote specific settings analysed by code calculations (section 8.5). (b) Examples for discharges with density ramps leading to stable partial detachment (black) or instability (grey, example for a ‘breathing’ discharge).

plasmas with 1, 2 and 3.5 MW $H^0 \rightarrow H^+$ injection (0.7, 1.4 and 2.5 MW absorbed), detachment starts at $\bar{n}_e^{\text{thr}} = 2.3, 3.0$ and $3.6 \times 10^{20} \text{ m}^{-3}$, respectively. Corresponding n_{eu}^{thr} values are 0.4, 0.6 and $0.76 \times 10^{20} \text{ m}^{-3}$. In deuterium plasmas ($D^0 \rightarrow D^+$ injection), respective threshold densities are slightly higher (McCormick *et al* 2003c), but it is not yet clear whether this isotope effect is simply related to different NBI deposition profiles, or whether it reflects a more fundamental difference in transport. Increasing \bar{n}_e beyond a certain higher limit at fixed heating power generally leads to complete detachment. The radiation belt then becomes unstable and moves into the core, and the discharge begins to ‘breathe’ (periodically enhanced core radiation and subsequent recovery) or even becomes terminated, often via MARFE formation at the inboard side (Wenzel *et al* 2002, Thomsen *et al* 2004, Wenzel *et al* 2005, Thomsen *et al* 2003a,b). The existence of a finite density range with stable partial detachment between attached HDH scenarios and radiation induced collapse is found to be restricted to configurational settings with sufficiently large field line pitch inside the islands and separations Δx between x-points and targets (sufficient flux diversion) which is shown in figure 85(a). The tendency is evident although the absolute values for L_c and Δx shown in the figure need to be corrected for finite-beta effects—a task for the future. Moving from right to left in the hatched range of the figure, the power flux onto the region with permanent attachment becomes reduced, and the density range for stable detachment shrinks. For configurations to the left of the hatched range discharges immediately switch from stable attachment to complete detachment and instability with increasing density, figure 85(b). At these settings where the ratio of Δx to the SOL thickness is too small—short Δx as well as long L_c lower this ratio—the scenarios become limiter-like: flux diversion becomes negligible, and the differences of the connection lengths mentioned above lose their importance for the downstream temperatures. Consequently, the energy channels to the targets

become more homogeneous, thus explaining the absence of a finite density range with partial detachment.

8.5. Modelling and theoretical assessment

This section presents a theoretical analysis and discussion of the island divertor physics in W7-AS, based mainly on 3D simulations using the EMC3/EIRENE code, which was motivated by and developed in close interaction with the W7-AS divertor problems. Theoretical efforts made so far have been mainly concentrated on examining and understanding the basic transport features of the island divertor associated with the specific 3D island divertor topologies. In particular, it was aimed at identifying the elementary similarities and differences in SOL physics between the well-developed poloidal-field divertor in tokamaks and the first island divertor in an advanced low-shear stellarator within the Wendelstein line. Topics addressed are not restricted within the frame of the experimental investigations shown in the foregoing section, meaning that there exist certain theoretical issues open for further experimental verifications. Key divertor function elements, such as particle flux enhancement, neutral screening, impurity retention, thermal power removal via impurity line radiation and detachment are presented within a self-consistent physics frame and assessed with respect to tokamak divertors. Owing to the existing uncertainties in equilibrium configurations (vacuum field used in simulations) and in drift effects (not yet self-consistently treatable in the present code version), comparison with experiment is usually done by checking the relevance and consistency in general trends and in leading-order effects. Additionally simple models guide to the leading physics and the dominating mechanisms behind 3D code findings.

8.5.1. Development of the EMC3 code. 3D SOL transport modelling was realized on the W7-AS island divertor by developing and applying a new 3D fluid code—EMC3 (edge Monte-Carlo 3D) (Feng *et al* 1999c, 2004b). Alternative 3D approaches were used to study plasma edge cooling via impurity injection in the edge islands (Naujoks *et al* 1997). Based on early 2D models of an island divertor (Herré *et al* 1997, 1999) EMC3 development began with a rather simple fluid model including only the heat conduction process for electrons, taking however, from the very beginning, into account the fully 3D edge structure of magnetic configurations and divertor installations. Thus, code applications to specific devices were possible and were done during the whole code development process. The physics model in the code was improved gradually by separating the energy transport between ions and electrons (Feng *et al* 1997), by implementing the momentum balance and continuity equations (Feng *et al* 1999c), by coupling the EIRENE code (Reiter *et al* 2005) for neutral transport and by including a trace-impurity fluid model (Feng *et al* 2001). After the substantial extension of the physics model, the code was numerically switched from magnetic to finite-flux-tube coordinates by developing and implementing a new reversible field line mapping technique (Feng *et al* 2002, 2005b). This technical improvement opened the code application range to arbitrary configurations including stochastic fields. The whole code development/application process was accompanied by checks and benchmarking in physics and numerics with analytical models (Feng *et al* 1997, Kobayashi *et al* 2004a, 2007a) and with the B2 code as well (Feng and Kisslinger 2000). Numerically, the EMC3 code employs a new advanced Monte-Carlo technique for the treatment of highly anisotropic 3D fluid transport processes in arbitrary magnetic topologies (Feng *et al* 2000). Both EMC3 and EIRENE are fully parallelized.

After extensive applications to the divertor physics of W7-AS (Feng *et al* 2004a, 2005c, 2006a), the code has been recently implemented for the island divertor of W7-X (Sharma *et al* 2005, 2006), the local and helical divertors of LHD (Kobayashi *et al* 2007b,

Morisaki *et al.* 2005), the ergodic divertor of TEXTOR-DED (Kobayashi *et al.* 2004b) and the start-up limiters of ITER—also a problem necessitating a 3D analysis (Kobayashi *et al.* 2007a, Sardei F *et al.* 2007).

8.5.2. Transport characteristics: island divertor versus tokamak divertor.

Perpendicular-to-parallel transport ratio. The connection length and the island size determine the respective parallel and perpendicular transport scale lengths in the SOL (Feng *et al.* 1999a). In the following, we compare the perpendicular-to-parallel transport ratio between tokamaks and W7-AS. For convenience, we introduce the field-line pitch Θ which, in a tokamak, is defined by $t_a a/R = B_p/B$ (a = minor radius) and takes a typical value of 0.1. In W7-AS, the divertor-relevant field-line pitch is determined by the internal rotational transform $t_i = r_i t'$, i.e. $\Theta = t_i a/R$ and can only reach a value of about 0.001. For energy transport, the condition for the parallel heat conduction flux to dominate over the perpendicular one is $T_e > (\chi n_e \Theta^2 \kappa_e)^{2/5}$ (Feng *et al.* 1999b). Assuming, for example, $\chi n_e = 1 \times 10^{20} \text{ m}^{-1} \text{ s}^{-1}$, satisfying the above criterion requires a temperature of about 36 eV in W7-AS and 1 eV in a tokamak divertor, respectively. This means that, while the energy transport in a tokamak SOL is governed by the parallel heat conduction, in the island divertor the cross-field transport competes with the parallel one and even becomes dominant in low-temperature regions where $T_e < 36 \text{ eV}$, presenting a complex transport pattern inside the islands. For particle and momentum transport, if a classical parallel convection and an anomalous cross-field diffusion are assumed, the ratio of the parallel to the perpendicular transport time scale is given by $\tau_{\parallel}/\tau_{\perp} = 2D/\Delta x \Theta V_{\parallel}$ with Δx indicating the target-to-core distance limited by the radial island size. For $V_{\parallel} = 8 \times 10^4 \text{ m s}^{-1}$ (sound speed of a hydrogen plasma with $T_e = T_i = 36 \text{ eV}$) and a diffusion coefficient $D = 1 \text{ m}^2/\text{s}$, the ratio of $\tau_{\parallel}/\tau_{\perp}$ takes a value of about 0.6 in W7-AS with $\Theta = 0.001$ and $\Delta x = 4 \text{ cm}$. This value drops down to 1×10^{-3} when Θ increases to 0.1 and Δx to 20 cm, like, e.g. in a tokamak like ASDEX-Upgrade.

An extended two-point model. In order to better understand the role of cross-field transport in the island divertor, the tokamak two-point (2P) model has been extended to cover the island divertor by including cross-field transport terms (Feng *et al.* 2006a, 2006b). This was achieved by strongly reducing the island geometry. The extended 2P model includes an energy transport equation

$$T_{\text{up}}^{7/2} = T_{\text{d}}^{7/2} + \frac{7q_{\parallel}L_c}{2\kappa_e} - \frac{7\chi(n_{\text{eu}} + n_{\text{ed}})}{4\kappa_e\Theta^2}(T_{\text{up}} - T_{\text{d}}) \quad (8.1)$$

and a pressure balance equation

$$p_{\text{up}} = 2p_{\text{d}}(1 + f_{\text{m}}) \quad (8.2)$$

with the Bohm-boundary condition at targets

$$n_{\text{ed}}c_{\text{sd}}\gamma T_{\text{d}} = q_{\parallel}, \quad (8.3)$$

where subscripts ‘up’ and ‘d’ mean respective up- and downstream and n_{eu} and n_{ed} are the up- and downstream densities. The other symbols have their usual meanings. The last term in equation (8.1) stands for the cross-field heat conduction from both ions and electrons and disappears for large Θ as in tokamak cases. f_{m} in equation (8.2) represents a momentum loss which, in a tokamak, is mainly caused by ion–neutral collisions active only at low divertor temperatures ($\lesssim 5 \text{ eV}$) under detachment conditions. Before detachment, the pressure is usually

conserved along the field lines. In contrast, for the island divertor in W7-AS, EMC3/EIRENE code simulations have predicted strong momentum losses and a consequent significant pressure drop along the field lines already at low density, high temperature conditions in the absence of an intensive plasma–neutral interaction. The underlying mechanisms have been studied in detail and understood as a result of counter-flow frictions in the island SOL and of momentum trapping in the shadowed regions between the discontinuous divertor plates (Feng *et al.* 1999b). This geometry-related momentum loss determines the basic island divertor transport features deviating from the standard divertor transport picture for tokamaks. In order to reveal the geometric correlation, f_m was derived for a simplified island geometry (Feng *et al.* 2006a):

$$f_m = \frac{D}{2\Theta C_{sd}} \left(\frac{1}{\lambda_\Gamma} + \int \frac{n_e V_{II}/n_{ed} c_{sd}}{(\Delta y/2)^2} dx \right). \quad (8.4)$$

The first term in the parentheses accounts for the momentum trapping in the divertor shadowed region, with λ_Γ being a characteristic decay length of the parallel particle flux in the divertor shadow. The second one represents the momentum loss caused by friction between counter-flows. The integration of the normalized parallel particle flux is performed over x (radial direction) from the inner separatrix to the target. The existence of counter-flows has been implied in the integral by applying stagnation boundary conditions on the interfaces between the counter-flows (see figure 80 (top)). Δy indicates the poloidal width of the flow channel limited by the interfaces. The momentum loss is relevant in W7-AS because of the small Δy (~ 4 cm on average) and the small Θ . If $\Theta \rightarrow \infty$, f_m vanishes and equations (8.1)–(8.3) reduce to a standard two-point model for tokamaks. Aiming at illustrating the consequences of the geometry-related momentum loss, we assume here that both λ_Γ and the second term in the parentheses in equation (8.4) remain unchanged in the island SOL and leave a more precise assessment to the 3D code. Under this constraint, f_m can be expressed as $f_m = \alpha/T_d^{1/2}$, with α being introduced as a free parameter representing the strength of the momentum loss. Then, for a given $q_{||}$ one can determine n_{ed} , T_{eu} and T_{ed} by equations (8.1)–(8.3) using n_{eu} , as an independent variable. For $q_{||} = 0.5 \text{ MW}/(4\pi^2 a R \Theta)$ and $\chi = \chi_e + \chi_i = 3 \text{ m}^2 \text{ s}^{-1}$, the results are shown in figures 86 and 87. Figure 86 shows the n_{eu} -dependence of n_{ed} for different momentum loss strengths with $\alpha = 0, 2, 5$ and 10 . The dashed curve shows the standard two-point model results without cross-field transport for reference. The sharp change in curve slope at $n_{eu} = 1 \times 10^{13} \text{ cm}^{-3}$ indicates the transition to a high recycling regime. The small difference between the $\alpha = 0$ curve and the standard case arises from the slight drop of T_{eu} due to the cross-field heat conduction included in the extended model, which will be discussed later in some detail. With increasing α the curves become flatter and flatter. For $\alpha > 5$, n_{ed} remains below n_{eu} and the sharp transition from low to high recycling predicted by the standard two-point model disappears. Figure 87 compares the evolution of upstream and downstream temperatures with increasing n_{eu} between the standard case and the extended model with $\alpha = 5$. The extended model shows a much more moderate change of T_{ed} with n_{eu} because of the weaker n_{eu} -dependence of n_{ed} , as shown in figure 86. As a consequence, the detachment transition is shifted to extremely high n_{eu} -values (see section 8.5.5). T_{eu} changes its slope once decoupled from T_{ed} as it does in the standard two-point model. However, it does not reach a plateau. Indeed, it decreases slightly due to the increased contribution from the cross-field heat conduction. At high n_{eu} , T_{eu} changes its slope once again. In this n_{eu} -range, the cross-field heat conduction flux tends to dominate over the parallel one, leading to a strong drop of T_{eu} with n_{eu} . The significant contribution of the cross-field heat conduction to the energy transport in the islands has an important effect on impurity transport, which will be discussed in section 8.5.4.

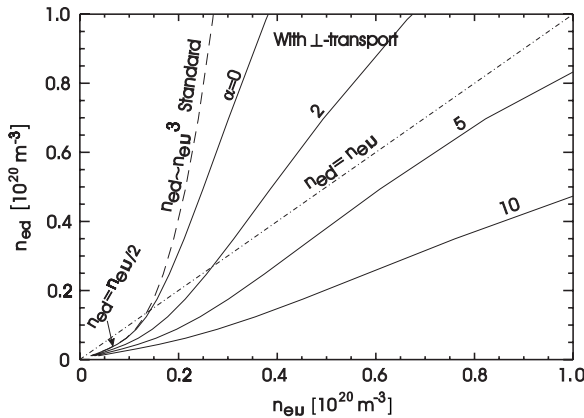


Figure 86. Downstream density versus separatrix density: comparison between the standard two-point model and the extended two-point model with different strengths of momentum loss resulting from cross-field transport.

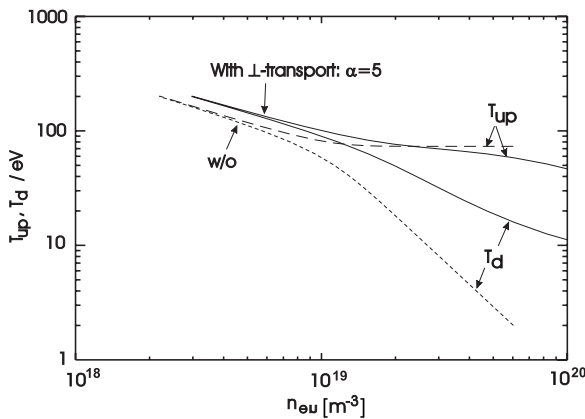


Figure 87. Upstream and downstream temperatures versus separatrix density: comparison between the standard two-point model and the extended two-point model with $\alpha = 5$.

3D simulation results. Island divertor transport in W7-AS has been extensively studied using the EMC3/EIRENE code for realistic island configurations based on the vacuum field. We first show an example with $P_{\text{SOL}} = 200 \text{ kW}$ for pure hydrogen plasmas without impurities (Feng *et al* 1999a). In the absence of impurity radiation, the reduced SOL power allows an examination of linear and nonlinear transport processes within a more reasonable n_{eu} -range. Shown in figure 88 are the n_{eu} -dependences of the downstream density, the upstream and downstream temperatures and the momentum loss factor f_m (see equation (8.4)). The 3D code confirms the basic results predicted by the extended two-point model: firstly, significant momentum losses already set in at low densities, high temperatures without an intensive neutral gas interaction. Secondly, as a consequence of the first point, n_{ed} is almost linearly coupled with and remains smaller than n_{eu} . Thirdly, a significant contribution of the cross-field heat conduction to the energy transport in the islands usually leads to a drop of T_{eu} at high density conditions.

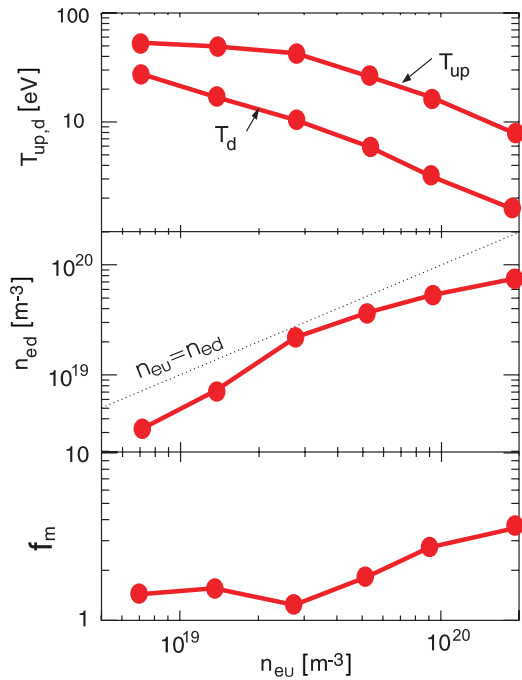


Figure 88. EMC3/EIRENE simulation results for pure hydrogen plasmas with $P_{\text{SOL}} = 200 \text{ kW}$. From top to bottom: upstream and downstream temperatures, downstream density and momentum loss factor f_m as a function of n_{eu} . Here, the upstream density and temperature are the averaged values on the LCFs, while those at downstream are averaged within the power channels onto targets. The downstream temperature defined in this way reflects the average thermal energy of electrons before entering the sheath.

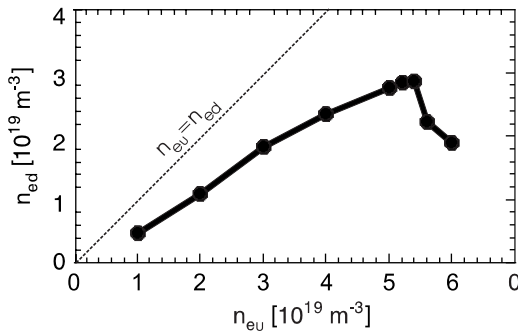


Figure 89. A density scan taking the intrinsic carbon impurity into account. n_{eu} increases almost linearly with n_{eu} until the ionization front detaches from targets leading to a roll-over of n_{ed} .

In order to make a comparison with experimental results, the intrinsically released carbon impurities have to be taken into account. An upstream-density scan was performed using the EMC3/EIRENE code (Feng *et al* 2004a) using $P_{\text{SOL}} = 0.85$ to 1 MW as given by the experiments (figure 89). The roughly linear relation between n_{ed} and n_{eu} found in the code simulations throughout the density range up to rollover confirms the previous code predictions without impurities (see figure 89). In addition, the code shows a rollover of n_{ed} already before detachment transition. In tokamaks, a significant reduction of the particle flux to the

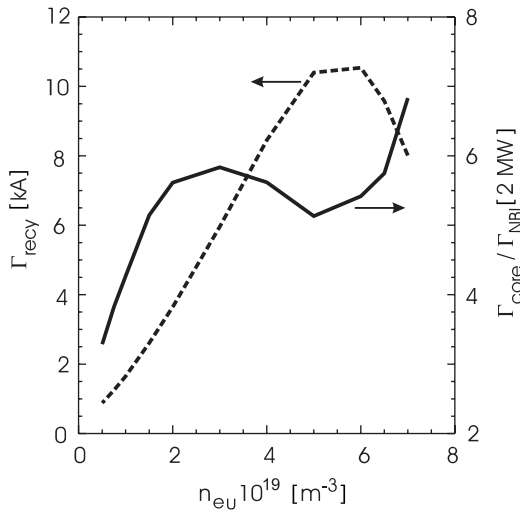


Figure 90. Dependence of total recycling flux Γ_{recy} and the neutral flux penetrating into the core (core-fuelling rate) Γ_{core} on the separatrix density n_{eu} . Γ_{core} normalized to the NBI-source. EMC3/EIRENE calculation (hydrogen, SDC, $P_{SOL} = 1.2$ MW, 2% carbon sputtering, $D = 0.5 \text{ m}^2 \text{ s}^{-1}$ for both carbon and hydrogen and $\chi_i = \chi_e = 3D$).

target is usually an indication for onset of detachment. This requires intensive ion–neutral collisions which can only be realized at low downstream temperatures ($\lesssim 5$ eV). For W7-AS, the momentum loss contribution from the charge-exchange (CX) neutrals was examined by switching off the corresponding term in the 3D code. The resulting effect on downstream density is below 10% in the given parameter range. Thus, there must be a different reason for the earlier onset of n_{ed} -rollover in the island divertor. The 3D code shows that the downstream density decreases once the ionization zone moves inwards due to temperature effects (see also the next section). The inward shift of the ionization front causes a radial inward extension of the parallel plasma flow, leading to an enhancement of the momentum loss due to counter-flow friction. This could be qualitatively understood from equation (8.4) showing that a broadening of the radial flow profile increases the momentum loss factor f_m .

8.5.3. Neutral screening. The open island divertor in W7-AS with relatively small islands has generally a weak neutral screening efficiency. In addition, a strong local density rise at downstream under high-recycling conditions cannot be established in W7-AS. Thus, in order to improve the island neutral screening efficiency, the upstream density has to be strongly increased to increase the overall density in the islands.

Figure 90 shows the dependences of the total recycling flux Γ_{recy} and the neutral flux penetrating into the core (core-fuelling rate) Γ_{core} and the separatrix density n_{eu} (Feng *et al.* 2005a) as calculated by the 3D code. The upstream density is increased until the plasma approaches detachment; neutral transport in detached plasmas will be discussed in section 8.5.5. Γ_{core} is normalized to the NBI-source in order to show the relative importance of the core fuelling by the recycling neutrals. The high Γ_{core} -values explain why a divertor-relevant SOL plasma (high density, low temperature) in W7-AS was always concomitant with a high core density. For $n_{eu} < 2 \times 10^{19} \text{ m}^{-3}$, the islands are transparent to the recycling neutrals so that Γ_{core} increases with the n_{eu} as a consequence of the rising total recycling flux Γ_{recy} . Increasing n_{eu} decreases the neutral penetration length and leads to a shift of the ionization

front towards the targets. Around $n_{eu} = 2 \times 10^{19} \text{ m}^{-3}$, the island screening (decrease of neutral penetration length) effect compensates the source (increase of Γ_{recy}) effect and stops the growth of Γ_{core} . After this point, Γ_{core} even drops slightly due to the gradually improved island screening efficiency until the downstream temperature drops below the ionization energy of the recycling neutral gas. Then, the strongly reduced ionization activity makes the islands transparent again for the recycling neutrals. In this case, Γ_{core} increases quickly with n_{eu} . Impurity radiation strengthens this process.

The recycling neutrals provide the main fuelling source for the core (see figure 90), which should be reflected by the core density. Comparing the Γ_{core} -curve shown in figure 90 and the experimental n_{eu} -curve shown in figure 79, one sees a clear correlation between the calculated core-fuelling rate and the measured \bar{n}_e . Following the rollover of Γ_{core} , \bar{n}_e flattens for n_{eu} -values from $(2\text{--}6) \times 10^{19} \text{ m}^{-3}$ and recovers when the islands become transparent again for the recycling neutrals.

In addition, recent numerical studies on the recycling-induced CX-neutral transport have shown that a dense, cold island can efficiently protect the iron-wall from physical sputtering by CX-neutrals in different ways, (a) by moving the CX-neutrals to a low energy spectrum band, (b) by reducing the divertor-well leakage and (c) by moderating the interaction between the core plasma and the wall recycling neutrals (Feng *et al* 2007).

8.5.4. Impurity retention. EMC3/EIRENE code simulations have shown that, by enhancing the recycling flux and lowering the island temperature, the impurity flow velocity, which is determined by the balance between thermal force and friction, can be turned from inwards to outwards-directed (Feng *et al* 2005a). This impurity flow reversal in the island SOL has a strong impact on the density distribution of the target-released carbon impurity. The dominating thermal force comes from ions due to their weak classical conductivity with respect to electrons. As known from classical theory, the ratio of friction to thermal force is determined by the ratio of the ion classical convective to conductive heat flux (Igitkhanov 1988). Therefore, increasing the plasma flow and reducing the conductive heat flux both favour the impurity retention in the islands. The estimations made in section 8.5.2 for the energy transport based on electrons can be extended to ions. For ion energy transport, the cross-field heat conduction builds also a bypass through which the classical heat conductive flux can, under high-density, low-temperature conditions, be strongly reduced, leading to a significant reduction of the related thermal force.

In general the cross-field heat conduction becomes dominant if

$$n/T_i^{5/2} > k_i \Theta^2 / \chi_i. \quad (8.5)$$

Because of the rather small pitch angles $\Theta (\sim 10^{-3})$ this condition can be met in W7-AS. For example, assuming that $\chi_i = 2 \text{ m}^2 \text{ s}^{-1}$ and $n = 5 \times 10^{19} \text{ m}^{-3}$, satisfying the above condition requires $T_i \leq 120 \text{ eV}$. For attached hydrogen plasmas with $P_{NBI}^{\text{abs}} = 1.4 \text{ MW}$, the measured T_{eu} take a typical value of about 100 eV (see figure 79). For $n_{eu} = 4 \times 10^{19} \text{ m}^{-3}$, the EMC3 code, with the input parameters given in section 8.5.3, provides $T_{eu} \approx 90 \text{ eV}$ and $T_{iu} \approx 100 \text{ eV}$, with showing no significant difference between electron and ion temperatures as it is typical for high density conditions. Once equation (8.5) is established upstream, the cross-field heat conduction will dominate the ion energy transport throughout the islands. Then, the classical conductive heat flux is strongly reduced and thereby the related thermal force. This transition from thermal-force-dominated to friction-dominated impurity transport is shown in figure 91. One sees a sharp decrease of the carbon density (normalized to the total carbon yield) at the separatrix when the friction becomes dominating over the thermal force for the $n_{eu} > 2 \times 10^{19} \text{ m}^{-3}$.

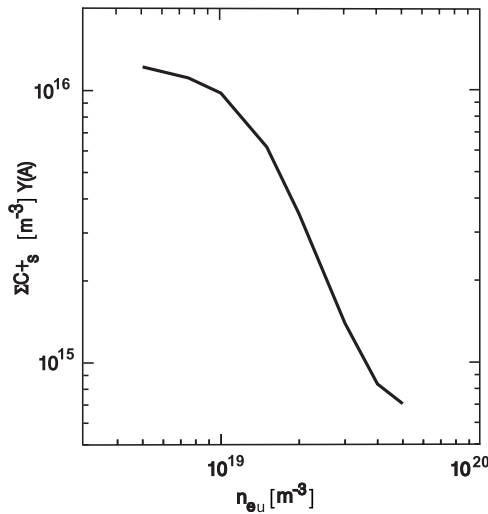


Figure 91. Carbon separatrix density as a function of n_{eu} . The carbon density at the separatrix drops quickly once the friction becomes dominating.

As shown in equation (8.5), the effective reduction of the parallel conductive heat flux is associated with the—stellarator-specific—small internal field-line pitch of the islands. On the other hand, a small field-line pitch also increases the perpendicular-to-parallel transport ratio for impurities; finally the island impurity flushing effect will vanish when $\Theta \rightarrow 0$ (Feng *et al* 2006a). As already estimated in section 8.5.2, the parallel convection and the cross-field diffusion play a comparable role for particle transport in the W7-AS islands. This obviously holds for impurities as well, as for friction-dominated impurity transport the parallel velocity is for impurities and main ions about the same. A larger field-line pitch will increase the parallel-to-perpendicular transport ratio and thereby improve the impurity retention effect of the edge islands. This, however, would shift the transition condition to even higher densities and lower temperatures.

8.5.5. Detachment.

Detachment transition. The absence of a high recycling regime in W7-AS shifts detachment transition to rather high n_{eu} values. The transition condition has been analysed based on 1D radial energy transport model (Feng *et al* 2004a). The threshold island density is found to scale with the heat flux $q_u = P_{SOL}/4\pi^2 Ra$, the carbon concentration C and the cross-field conductivity χ as

$$n \propto \left(\frac{q_u^2}{C \chi} \right)^{1/3} \quad (8.6)$$

For a roughly linear coupling between upstream and downstream densities as found for W7-AS, the above scaling holds for both downstream and upstream densities. Scaling equation (8.6) indicates that, for a given q_u , the carbon concentration and the cross-field heat conductivity play a less important role than the plasma density in triggering detachment.

The condition for detachment transition was examined in upstream density and carbon sputtering coefficient space using the EMC3/EIRENE code (Feng *et al* 2001). With a SOL

power of 1 MW ($D = 0.5 \text{ m}^2 \text{ s}^{-1}$ and $\chi_e = \chi_i = 3D$), detachment occurs at $n_{eu} = 8 \times 10^{19} \text{ m}^{-3}$ with 1.3% carbon sputtering. When n_{eu} is decreased by 25% down to $6 \times 10^{19} \text{ m}^{-3}$, the sputtering coefficient has to be increased by more than a factor 2 up to 3.1% in order to achieve detachment. These results are consistent with the parameter sensitivity analysis given by equation (8.6) if the carbon concentration C there is replaced by the sputtering coefficient.

In addition, the code shows an abrupt change in radiation level at detachment transition which allows an easy, clear identification of the detachment regime in both simulations and experiments. The abrupt change in radiation level has been understood to be associated with a thermal instability due to the two-branch characteristic of the carbon cooling rate function (Feng *et al.* 2004a).

Features of detached plasmas. After detachment transition, the radiation zone lifts from the targets and the radiation distribution in the islands is determined by the local balance between energy transport and radiation. The island topology enters directly the energy transport and thereby can influence the radiation distribution in the island SOL. Indeed, divertor experiments have demonstrated a high sensitivity of the global performance of a detached plasma to the island geometry (see section 8.4.2). The observed geometry-related detachment stability motivated a detailed numerical study to reveal the underlying mechanisms (Feng *et al.* 2003b, 2005c). Four configurations (see figure 85(a)) were chosen for the numerical investigations. Two of them are located in the stable $\Delta x - L_c$ range and the other ones are taken from the unstable region. The upstream density n_{eu} is used as a detachment trigger in the simulations and ramped up throughout the detachment phase until the radiation layer enters the core. Other code input parameters like the SOL power, transport coefficients and boundary conditions were fixed. The ‘numerical experiments’ showed that, for each selected configuration, there exists a certain finite n_{eu} -range where the radiation layer can be stabilized in the island SOL, although the n_{eu} -window is clearly narrower for the configurations which are experimentally unstable (Feng *et al.* 2005c). This result deviates from the experiments in so far as the latter do not exhibit any stable detachment outside the hatched range of figure 85(a). The reason for this deviation is probably that the two input parameters in the code, P_{SOL} and n_{eu} , are not control parameters in experiments. This difference between simulations and experiments suggests, however, that the observed detachment instability is triggered from the SOL, but then governed by the SOL–core interaction as will be discussed later in some detail.

The 3D code shows that the location of the carbon radiation zone at detachment is influenced by the fine structure of the islands. For the two stable configurations with large islands (square in figure 85(a)) or field-line pitch (rhombus), a carbon radiation belt is formed on the inboard side of the torus and is kept outside the LCFS, leaving a warm region for the recycling neutrals. Figure 92 shows the typical location of the carbon radiation and the distribution of the hydrogen ionization source including molecule contributions for the standard divertor configuration. The flux surfaces in W7-AS, as in standard tokamaks, are more compressed on the low-field side than on the high-field side. The resulting weaker cross-field heat flux on the high-field side favours impurity radiation and plasma condensation. The low-field side and the divertor recycling region are relatively radiation-free so that the power fraction entering the islands on the low-field side can be transported down to the divertor region to sustain the recycling process. This is reflected by the in/out asymmetry in the T_e -contour shown in figure 92. The existence of such a power channel has been detected by the target thermography (see figure 78). The power channel leaves a hot spot at its termination on the target, which agrees well with the code results (see the lower picture in figure 92).

In contrast to the inboard-side-radiation picture for a stable partial detachment configuration, the EMC3/EIRENE predicts an intensive X-point-Marfe-like radiation

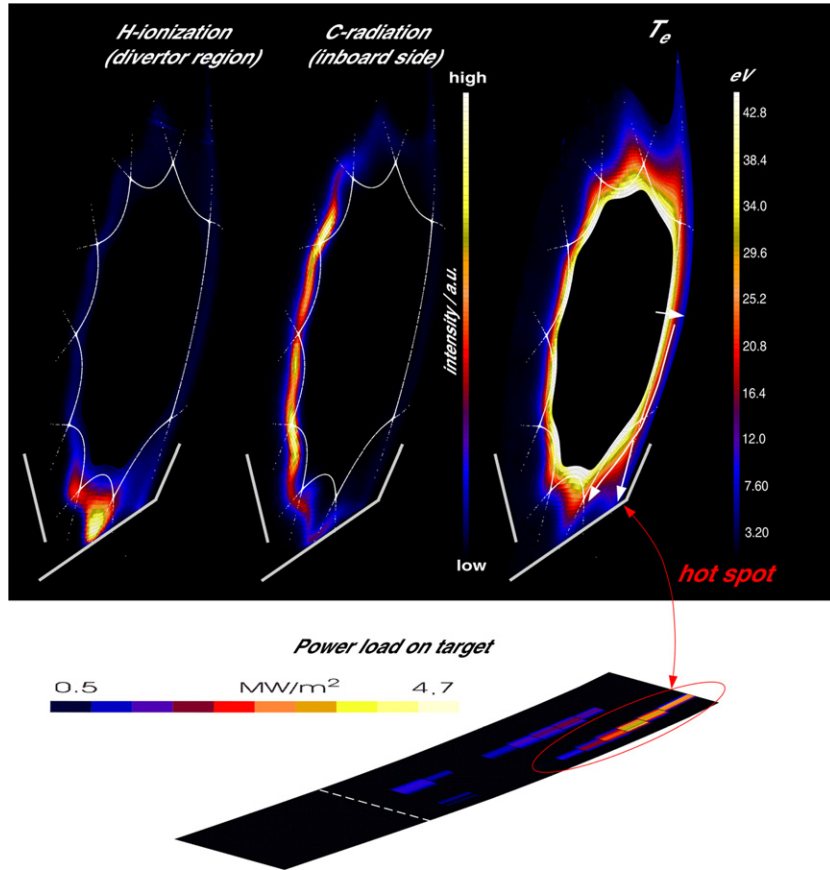


Figure 92. Typical distribution patterns of (top left) hydrogen ionization and (top middle) carbon radiation in a stable partial detachment for the W7-AS standard divertor configuration (square in figure 85(a)), calculated by EMC3/EIRENE. The temperature on the low-field side is higher than on the high-field side (top right). A radiation-free power channel on the low-field side transporting energy down to the recycling region is schematically indicated by arrows. The power channel leaves a hot spot on the target (bottom) which has been detected by the target thermography (see figure 78(a)).

distribution for the two unstable configurations with small islands (circle in figure 85(a)) or small field-line pitch (triangle) in the detachment phase before the radiation layer moves into the core with increasing density. The left picture in figure 93 shows the carbon radiation distribution for the island configuration marked by a circle in figure 85(a). Now, the radiation layer stays in the divertor region and cools down the recycling zone. It is not yet clear why the radiation prefers the divertor region in this case. An intuitive explanation can be attempted as follows. A larger connection length, i.e. a smaller field-line pitch, obviously increases the radial width of the parallel power channel carrying the energy from the position of preferential radial outflux (the low-field side) to the region of preferential radiation loss (the high-field side). On the other hand, a smaller target-to-core distance reduces the radial space available for this channel. Both effects will result in a depletion of the parallel power channel available for the inboard-side radiation in favour of the power intercepted by the target. Indeed, the 3D code shows a lower radiation fraction for the divertor radiation pattern than for the inboard radiation distribution (Feng *et al.* 2005c). This consideration is further supported by the fact

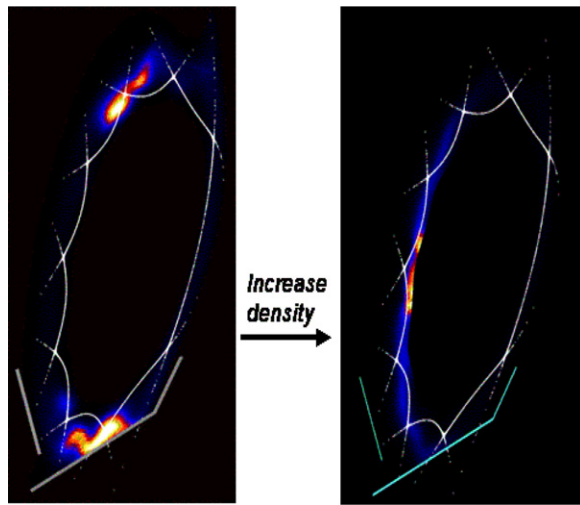


Figure 93. EMC3/EIRENE shows that a small island size (circle in figure 85(a)) or field-line pitch (triangle) results in an intensive, divertor-localized radiation (left, using the small island configuration as an example) in the initial detachment phase. However, independent of the island configurations, once plasma approaches a density limit, a strongly localized radiation zone appears on inboard midplane (right).

that, once the radiation layer goes into the core with increasing n_{eu} , all the four configurations, despite their different paths through a detachment regime, converge to one radiation pattern, i.e. a strongly localized intensive radiation zone appearing on the inboard midplane (see the right picture in figure 93). This is consistent with the experimental observations for plasmas approaching density limit (Thomsen *et al* 2003b, 2004, Wenzel *et al* 2005).

A possible drive of the detachment instability. Core and SOL plasmas are strongly coupled through the recycling neutrals. The location of carbon radiation has a strong impact on the island neutral screening efficiency, which is shown in figure 94. The divertor radiation location, compared with the inboard side radiation case, results in a much higher sensitivity of the core neutral penetration flux to n_{eu} and to P_{SOL} as well. A simple stability analysis shows that a rapid growth of the neutral penetration flux with reduced P_{SOL} can drive an instability (Feng *et al* 2005c). The growth rate of this instability is proportional to $|\partial \Gamma_{recy} / \partial P_{SOL}|$, which is much larger for the divertor radiation than for the inboard-side radiation. Note also the smaller detachment ranges for those configurations (Feng *et al* 2005c). In addition, the simple model shows that decreasing n_{eu} has a stabilizing effect on the detached plasmas. Although there is no experimental evidence to show that the observed detachment instability is really driven by the recycling neutrals, the simultaneous and corresponding drop in P_{SOL} and n_{eu} through a stable detachment (see figure 79) supports this theory.

8.6. Conclusion

Accounting for the importance of a controlled plasma exhaust, the edge plasma investigations on W7-AS culminated in proof-of-principle experiments on a modular island divertor as well as the development and application of a Monte-Carlo-based 3D edge transport code. The outstanding result of the experiments was that, in contrast to limiters, a chain of not too small

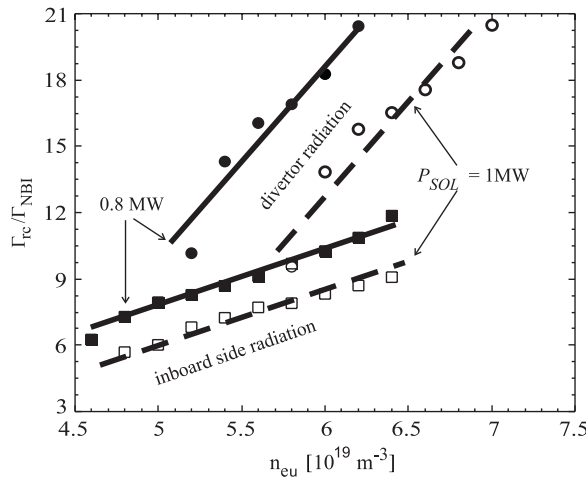


Figure 94. Calculated neutral gas penetration flux into the core as a function of n_{eu} , P_{SOL} for the two selected configurations marked by square and circle symbols in figure 85(a). Open symbols indicate the higher power case. The lines guide the eye. The location of carbon radiation has a strong impact on the island neutral screening efficiency.

boundary magnetic islands intersected by targets provides favourable operational conditions with strong radiation from the edge, a finite density range with stable partial detachment and adequately reduced power load on the targets, and a considerable neutral compression in the sub-divertor region. The threshold density for the onset of detachment increases with heating power. At too small field line pitch inside the islands or too small target-to x-point distances (too small islands), discharges with increasing density immediately switch from stable attachment to complete detachment and radiation instability, often via MARFE formation.

The SOL parameters in detail show a multi-faceted picture. The deposition patterns on the targets are top/bottom asymmetric due to plasma drift, and the development of the up- and downstream parameters with increasing density deviates considerably from that in a typical tokamak SOL. The present understanding of these details is impeded by the occurrence of drift effects and the uncertainty with respect to the exact equilibrium magnetic field structure at the edge. Due to these uncertainties, respective simulations with the EMC3-EIRENE code had to be restricted to basic physics features in model configurations, not aiming at the exact reproduction of local experimental data. Drift effects have not yet been included self-consistently. The results nevertheless explain at least qualitatively the observed tendencies including the essentials of the detachment phenomenology. Most of the specific features are consequences of a considerable contribution of cross-field transport within the SOL due to the small field line pitch inside the islands. This can also be shown by simplifying model approaches. Beyond this, the simulations predict a positive impact of the cross field transport bypass on the impurity screening capability of islands which, however, needs validation by future experiments. The partial character of stable detachment and the stabilization of the main radiation zone at the upstream inboard SOL region are finally attributed to the stabilizing effect of a hotter region at the upstream low field sides of the elliptic planes in consequence of an enhanced cross-field energy transport due to radially more compressed flux surfaces and islands at these regions. Although there is no direct experimental evidence; both the experimental and code results strongly suggest the existence of such inboard/outboard temperature asymmetry. At very small islands (vanishing flux diversion) the stabilizing effect of the island topology

is lost, and the density range with stable detachment shrinks to zero consistent with the experiments.

Although these studies mark a first step only, we mean that the results are rather promising concerning the island divertor potential for controlled plasma exhaust in stellarators. It is, nevertheless, worthwhile to finally point at a critical element of the concept. The SOL scenarios and hence the divertor performance are considerably influenced by details of the edge magnetic field configuration. For this reason, the exact knowledge and control of the actual equilibrium edge configuration—a deficit in the present study—are essential for future application. In contrast to tokamaks, this is a challenge at least for low-shear stellarators. As large boundary islands can be introduced by relatively small superimposed resonant fields, their structure is very sensitive to perturbations due to plasma currents and/or error fields. Progress regarding this specific problem and for island divertors in general is expected from future island divertor studies on the W7-X stellarator together with further completion of the 3D edge code.

9. MHD stability

9.1. Introductory remarks

The ideal stability limit provides a hard operational limit in tokamaks. Therefore, its counterpart in stellarators, mainly due to pressure-driven interchange and ballooning modes, serves as an important reference for comparison with experimental data. The predicted stability limits for the W7-AS standard configuration are around $\langle\beta\rangle \leq 2\%$ (Nührenberg and Zille 1984, 1987, Cooper 1995). Some characteristics of pressure driven modes in W7-AS are described in section 9.2, whereas the relation to the achievable plasma β is discussed in section 10.

The elimination of current driven instabilities such as kink and tearing modes as well as internal and major disruptions by net current-free operation represents an inherent advantage of stellarator devices. The existing OH transformer is utilized for configuration control and for investigations of various issues including the effect of magnetic shear on confinement and MHD stability. The assessment of potential detrimental effects associated with significant toroidal currents in W7-AS is the main scope of section 9.3.

A major concern in reactor-scale fusion plasmas are Alfvén instabilities driven by resonances with fast particles such as fusion born α -particles or energetic ions present during NBI and ICRH heating. The Alfvén spectrum in W7-AS is expected to differ with respect to a typical tokamak case due to non-axisymmetry and magnetic shear characteristics. The peculiarities of NBI driven global Alfvén modes will be described in section 9.4.

9.2. Pressure driven modes

In most cases pressure driven instabilities in W7AS appear in an intermediate range of beta (typically below $\langle\beta\rangle \approx 2-2.5\%$) as low frequency ($<10\text{ kHz}$) quasi-coherent oscillations around low order resonances of the rotational transform $t = n/m$ (Weller *et al* 1992, Jaenickel *et al* 1992, Weller *et al* 1994a, 1998, 2001, 2002b). The radial eigenfunctions obtained from x-ray tomography and from MHD code calculations correspond to global modes extending over a large fraction of the plasma radius centered in a region of large pressure gradient. The connection between global mode activity and low-order rational surfaces is illustrated in figure 95. In the two cases with different external rotational transform, large amplitude pressure driven modes have been observed during the transition to high beta. It can be seen that the plasma pressure induces noticeable shear in the t profiles, particularly at low

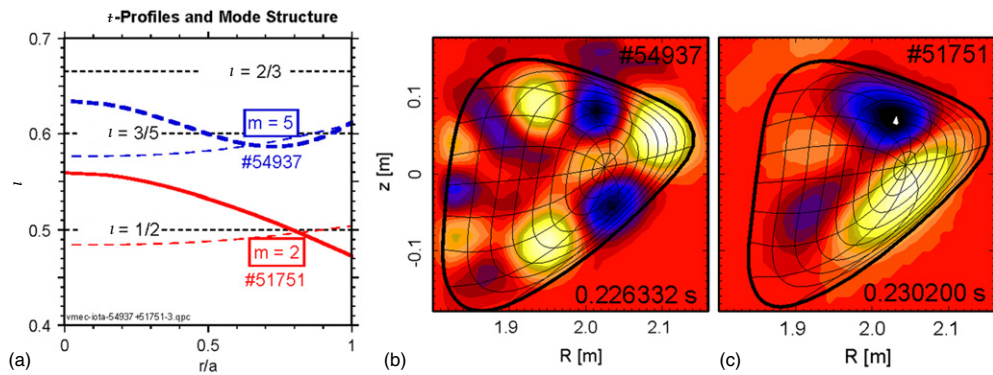


Figure 95. Observation of pronounced activity by pressure driven low frequency global modes at intermediate $\langle\beta\rangle$ in discharges with different external rotational transform ($t_{ext} = 0.52$ in #51751, $t_{ext} = 0.63$ in #54937). The thin dashed lines represent the vacuum configurations, the thick lines the finite- β ι -profiles. In both cases, $\langle\beta\rangle$ reaches significantly higher values after the phase of transient MHD activity. The poloidal mode structure of the rotating perturbation is deduced from tomographic reconstructions of perturbed x-ray emissivities (b, c). The $m = 2$ and $m = 5$ mode structures are resonant at the rational surfaces $\iota = 1/2$ and $\iota = 3/5$, respectively, in the ι -profiles as predicted by VMEC (a). A strong ballooning effect is seen at the outboard side.

external iota. The mode frequency is in the range of several kHz, and the poloidal structure and radial location correspond to the particular rational surfaces at $t = 1/2$ and $3/5$, as expected from the equilibrium reconstruction. The mode structure is obtained from x-ray tomography (10 cameras, 320 channels, Görner *et al* (1997, 1998b), Weller *et al* (1999b)) and analysis of magnetic signals using singular value decomposition (SVD) methods (Anton *et al* 1997). Strong ballooning behaviour is seen in both the x-ray and the magnetic data. This could be due to the increase of curvature in the good and bad curvature regions due to the Shafranov shift (see also section 10), which is typically in the range 15–25% of the effective plasma radius under these conditions. The mode displacement, therefore, can be considered to consist of a rotating part which is amplified in the region of bad curvature. The temporal evolution is then characterized by non-harmonic waveforms, particularly in the case of the Mirnov coils which pick up time and space derivatives of the mode displacement. Consequently, the frequency spectra can contain many harmonics. Up to seven were found in the Mirnov wavelet spectrograms. The x-ray signals are a direct measure of the radial displacement and do not depend on frequency leading to a reduced content of higher harmonics (Weller *et al* 2007).

The described phenomena resemble the so-called edge harmonic oscillations in tokamaks (EHO, Burrell *et al* (2002), Sutrop *et al* (2005)) or edge harmonic modes in the Large Helical Device (EHD, Toi *et al* (2004)). In W7-AS, the occurrence of these modes is clearly linked to a low- n global mode exhibiting strong ballooning behaviour which again is associated with high beta and large pressure gradients.

The linear ideal MHD stability properties, in particular the local stability boundaries according to the ideal (Mercier) and resistive interchange criteria, as well as the stability against ideal global low- n modes, have been examined for selected cases using the JMC (Nührenberg and Zille 1987), CAS3D (Schwab 1993, Merkel and Nührenberg 1996, Nührenberg 1999a, 1999b) and TERPSICHORE (Anderson *et al* 1990) codes. All these 3D stability codes use as input MHD equilibria as prescribed by the 3D free boundary equilibrium code VMEC (Hirshman *et al* 1986a), mostly assuming parabolic pressure profiles. In many cases, the STELLOPT optimizer tool (Strickler *et al* 2002) was used to reconstruct

VMC-based equilibrium solutions complying with experimental data and geometrical constraints ([Zarnstorff et al 2004](#)). In general, the stability limits for global modes coincide with those evaluated by the Mercier criterion and are roughly consistent with experimental data. The high-n ideal ballooning stability boundary deduced from field line ballooning studies with the COBRA ballooning code ([Sanchez R et al 2000](#)) is correlated with the Mercier criterion (see also section [10.6](#)). In cases of pronounced violation of the local ballooning criterion, corresponding unstable localized perturbations have been found by CAS3D which was set up for high radial resolution and a large number of perturbation harmonics ([Nührenberg 2001](#)).

The threshold for resistive interchange modes has been assessed with the JMC code by neglecting the shear stabilization term (see section [2.4](#)). Generally a wider unstable region towards the plasma boundary is found encompassing the Mercier unstable region (see figure 11 in [Geiger et al \(2004b\)](#)). Investigations of the stability boundaries of resistive ballooning modes by the GARBO code ([Kaiser 1993](#)) revealed a significant effect due to resistivity in W7-AS, whereas the ideal limit persists in W7-X due to the stabilizing effect of compressibility. Further results concerning pressure driven modes and the role of resistivity are presented in section [10](#).

The experimentally observed self-stabilization effect at higher beta resembling second stability behaviour is likely due to a combination of three stabilizing effects: (i) the increase of the magnetic well and shear (Shafranov shift), (ii) a radial shift of the relevant rational surface away from the steep pressure gradient, and (iii) a local flattening of the pressure profile by the perturbed field. In many cases the observed saturation amplitudes stay below a transport relevant level, or the discharges are very quiescent, even if the ideal linear stability is violated. The threshold for mode induced transport corresponds typically to magnetic perturbations with $\tilde{B}/B > 10^{-4}$ at the plasma edge. This is derived from correlations between magnetic fluctuations and plasma signals indicating global and local deterioration of the confinement. Also, this is a typical threshold found by field line tracing in the case of resonant field perturbations producing magnetic island widths of more than 5–10% of the plasma radius. Similar properties of magnetic perturbations were also found in the Large Helical Device, LHD ([Weller et al 2006, Watanabe et al 2004a, 2004b](#)).

Besides of coherent MHD modes weak turbulent MHD activity was found under various conditions in W7-AS ([Anton et al 1998, Basse et al 2002b](#)). A detailed discussion is beyond the scope of this section.

9.3. Current induced MHD-effects

The emergence of current carrying compact quasi-axisymmetric stellarators, which can be considered to be hybrids between drift-optimized stellarators and advanced tokamaks ([Zarnstorff et al 2001](#)) has prompted studies of current induced effects. Former experiments in the ohmically heated W7-A stellarator ([Jaenische and WVII-A Team 1980](#)) have shown that $m = 2$ tearing modes and hence major disruptions could be stabilized with modest external helical fields providing a rotational transform $t_{\text{ext}} \geq 0.15$ and accordingly a fraction $t_{\text{ext}}/\iota(a) \geq 0.3$, where t_{ext} is the external rotational transform and $\iota(a)$ the total rotational transform at the plasma edge. This effect has been attributed to the improved positional stability and the shift of the relevant rational surface away from the steep current gradient region.

9.3.1. Experiments. In W7-AS a variety of different current density and rotational transform profiles have been realized in order to assess the operational limits imposed by current driven instabilities ([Weller et al 2000, Sallander et al 2000](#)). Diagnosing these instabilities, on the

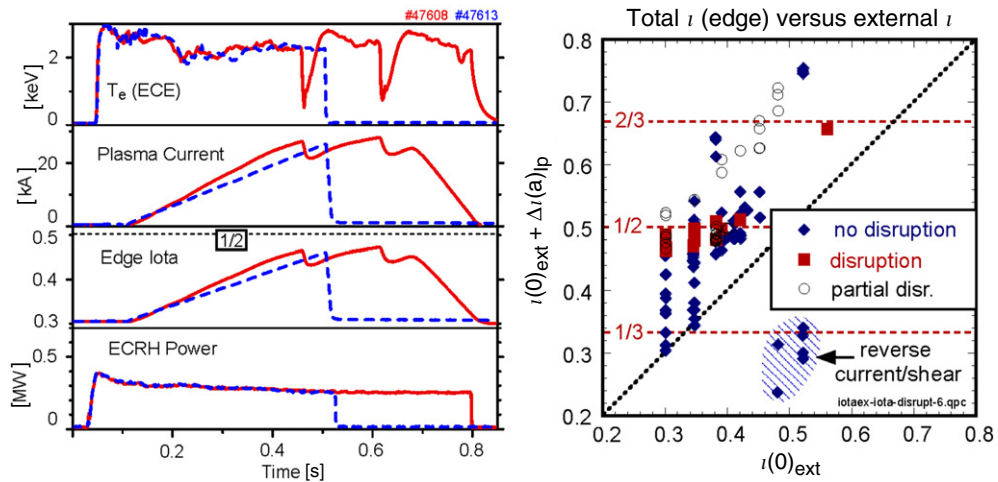


Figure 96. Soft disruptions during OH current ramps in ECRH heated plasmas. The waveforms (left) show the time evolution of the central electron temperature, the plasma current, the edge iota and the heating power for two cases. In each case, the thermal collapse occurs when the $\iota = 1/2$ surface is close to the edge. The database of 137 shots (right) covers different heating scenarios (ECRH, NBI and ECRH + NBI). The experiments with reversed current drive are below the dotted line representing the currentless case. The shots are classified according to the absence of disruption-like events, and the occurrence of large or small disruptive effects, respectively. The strongest effects are connected with the formation of the $\iota = 1/2$ surface in the outer plasma region. The vacuum iota is approximated here by its central value, which is directly given by the coil currents.

other hand, provides a tool to derive information on the current profiles, which has in particular been exploited in the case of ECCD experiments. In experiments with inductive currents we have created different low order rational surfaces varying the ratio $\iota_{\text{ext}}/\iota(a)$. The most important effects are disruption-like events associated with tearing modes at rational surfaces, most strongly at $\iota = 1/2$ and less pronounced at $\iota = 2/3$. Figure 96 shows strong transient thermal crashes during OH current ramps in ECRH heated discharges. The magnitude of the related drop of the OH current depends on the degree of plasma cooling down. The operational diagram shown in the right part of the figure contains a database of 137 shots covering different heating scenarios (ECRH, NBI and ECRH+NBI). The shots are represented by the boundary values of the rotational transform achieved for different values of the external rotational transform. The experiments with reversed current drive, which were performed in order to access the rational surfaces $\iota = 1/3$, $1/4$ and $1/5$ with significant currents (≥ 10 kA), are below the dotted line representing the currentless case. The shots are classified according to the absence of disruption-like events, and the occurrence of large or small disruptive effects, respectively. The strongest effects are connected with the formation of the $\iota = 1/2$ surface (Jaenische *et al.* 1994, 1992) in the outer plasma region in the presence of currents exceeding ≈ 10 kA (corresponding $\Delta\iota_1/\iota > 0.15$).

The disruptive events are provoked by tearing modes which initially rotate with frequencies of a few kHz and which slow down as the perturbation starts growing. Typically, these precursor modes are locked completely when the collapse takes place.

Frequently, the growth rate of $m = 2$ modes during NBI heating is comparable with the rotation frequency and the modes get almost immediately locked. This leads ultimately to a fast crash (within ~ 0.1 ms), indicating a direct contact of the large $m = 2$ islands with the

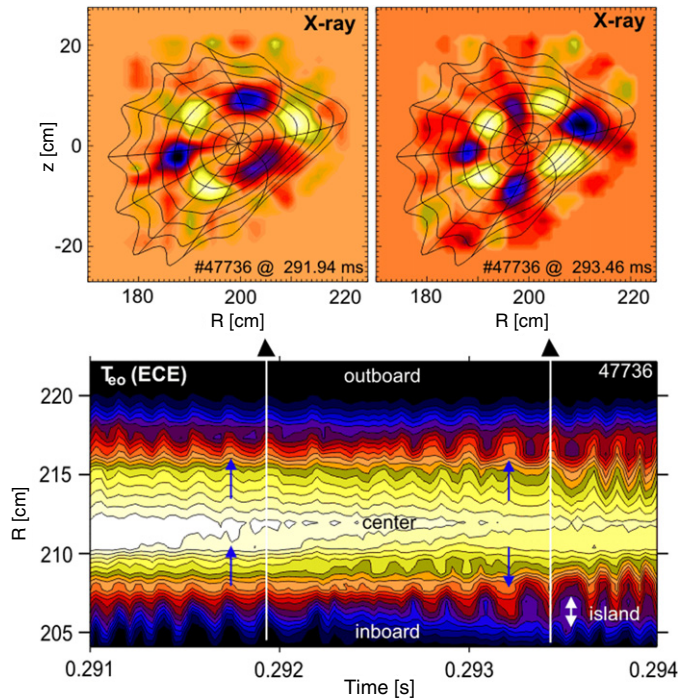


Figure 97. Example of a discharge with inductive current drive (30 kA), ECRH heating at 2.5 T and $t_{\text{ext}} = 0.48$. Tearing modes appear around 0.3 s, when the plasma current has reached ≈ 20 kA. At this time the rational surfaces $t = 2/3$ and $t = 3/4$ are at $r/a \approx 0.83$ and $r/a \approx 0.63$, respectively. The outward movement of these surfaces during the current ramp causes a transition of $(m, n) = (3, 2)$ to $(4, 3)$ modes as revealed by x-ray tomography (top). The electron temperature contours in the horizontal midplane from ECE (bottom) clearly exhibit the transition from odd to even m modes, which both cause a local flattening of the T_e -profiles. In the case of the $(4, 2)$ mode, a tearing type displacement is inferred from the anti-phase oscillations of the T_e -contours around the position indicated by the double arrow.

limiters or the break-up of the magnetic surfaces. The last conjecture is substantiated by the measured energy and pitch-angle resolved distribution of the energetic ions observed during the crash by the fast ion loss detector (Werner *et al* 2000, 2001). The measured distribution of the lost ions agrees with the calculated slowing down distribution of the injected beam ions. This cannot be explained by increased loss cone effects but rather by a field structure connecting the plasma interior with the limiter. The current decays typically on a timescale of ≤ 5 ms. In most cases, the decay is only partial, presumably because the equilibrium is maintained by the stellarator field. Typically, values of $\tilde{B}/B_0(r = a) \geq 0.1\%$ are reached for the magnetic perturbation at the plasma edge before the collapse.

Tearing mode activity and disruptive events observed at other rational surfaces proved to be weaker compared with the $t = 1/2$ case. The formation of $t = 2/3$ and $t = 3/4$ in the plasma reached by current drive and increased external transform is frequently accompanied with the appearance of tearing modes with corresponding mode numbers $(m, n) = (3, 2)$ and $(4, 3)$. In a few cases a thermal collapse has been observed as well. Figure 97 shows a transition between a $(m, n) = (3, 2)$ mode and a $(4, 3)$ mode within a time of ≈ 1 ms. This observation is consistent with the expected formation of an $t = 3/4$ surface at a current level of ≈ 19 kA during the current ramp, and the outward movement of both the $t = 2/3$ and $t = 3/4$

surfaces with increasing current. The transition from an even to an odd mode can be clearly seen in the ECE temperature contours. The island widths, w , of the observed rotating modes are estimated from the experimental data to reach values corresponding to about $w/a \approx 1/3$ of the plasma radius resulting in a local flattening of the profiles.

9.3.2. Non-inductive current drive. Additionally, experiments with non-inductive current drive were conducted in order to particularly investigate the effect of the bootstrap current on the MHD stability ([Weller et al 2001](#), [Sallander et al 2000](#)). This was accomplished by using combined heating with 0.5 MW of ECRH and 1 MW of NBI (co-injection), resulting in a maximum plasma current of ≈ 20 kA ($\approx \Delta t_1 = 0.1$) that could be achieved without using the OH transformer. The major part is attributed to the bootstrap current, and there is also a significant contribution of a beam driven Ohkawa current ([Marushchenko et al 2002](#)). The current could be driven beyond critical values associated with the major resonances $t = 1/2$ and $t = 2/3$, and the current ramp was only transiently affected by MHD effects at rational surfaces.

In W7-AS, an intense electron cyclotron current drive programme (ECCD, [Erckmann and Gasparino \(1994\)](#)) including co- and counter-ECCD under on- and off-axis launch was performed resulting in a variety of current profiles ([Maaßberg et al 2005](#), [Erckmann et al 1995b](#), [Marushchenko et al 2004](#)). With on-axis co-ECCD, peaked current densities were generated which led to the formation of $t = 1$ as predicted by equilibrium calculations using simulated ECCD current profiles ([Marushchenko et al 2004](#)). The existence of $t = 1$ was experimentally verified by the observation of sawtooth oscillations preceded by $(m, n) = (1, 1)$ mode activity close to the plasma centre ([Müller et al 1995](#), [Büchse et al 1993](#)). The tearing mode activity at $t = 1/2$ observed under similar conditions typically consists of rotating (2,1) modes saturated on comparably low amplitudes without provoking a disruptive-like event. This activity is a useful marker of the $t = 1/2$ position. In the case of on-axis counter-injection, a strongly reversed shear configuration without any current driven MHD activity could be established. Very quiescent discharges were also obtained in discharges where the bootstrap current was locally compensated and flat t -profiles could be retained. Important factors impacting the stabilization of tearing modes are the contribution of external rotational transform, shear formation or avoidance of major rationals, and (local) current compensation.

9.3.3. Stability calculations. Similarly to the earlier examination of W7-A current profiles ([Jaenicke and WVII-A Team 1980](#)) a stability analysis on the basis of a delta-prime (Δ') calculation was performed for a few typical W7-AS cases. The contribution of the bootstrap current to the total current density was roughly estimated on the basis of an axisymmetric model ([Brakel and W7-AS Team 2002](#), [Hinton and Hazeltine 1976](#)). In most cases, the t -profiles were evaluated in the approximation of equilibria calculated without taking the toroidal current self-consistently into account (i.e. flux geometry effects are neglected). Then the contribution of the toroidal current to the rotational transform Δt_1 was added. The Δ' -code solves the tearing mode equation for the perturbed helical flux function ψ in cylindrical tokamak geometry ([Furth et al 1973](#)). Therefore, the analysis may be considered to yield an estimate of the lower stability limit, since stabilizing contributions due to toroidal geometry effects and pressure induced curvature effects are neglected. The tearing mode stability index Δ' , with $\Delta' > 0$ in the unstable case, denotes the discontinuity of ψ'/ψ across the resonant surface and is sensitive to the local current density gradient. The external helical field does not directly enter into the stability calculation but indirectly via the t -profile. The size of the magnetic islands

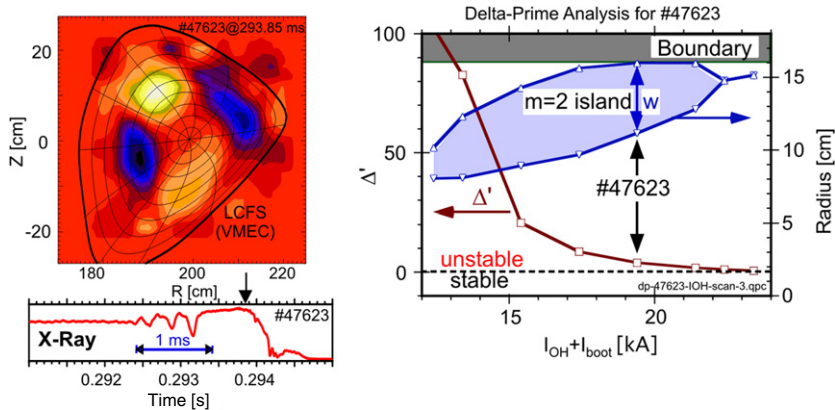


Figure 98. Growing $(m, n) = (2, 1)$ tearing mode causing a soft disruption during an OH current ramp in an ECRH heated discharge. The perturbed x-ray intensity (upper left) results from tomographic reconstruction of Fourier filtered signals. Just prior to the thermal collapse the rotation of the mode stops (see bottom left figure). The Δ' -analysis based on estimated OH and bootstrap current profiles yields instability throughout the current ramp (right). Here, the total current consists of the sum of OH and bootstrap currents; no ECCD was applied. At the time of the disruption the predicted island comes into contact with plasma facing components.

associated with the tearing mode, and hence the strength of the magnetic field perturbations, can be assessed by using the nonlinear dependence of Δ' on the island width w , where $\Delta'(w)$ is taken across the island and the saturated island size is inferred from the condition $\Delta'(w) = 0$.

In contrast to the results concerning ohmically heated plasmas in W7-A, the calculations for W7-AS current profiles predict unstable modes in a wide parameter range even for cases with the highest values of t_{ext} . An example of a Δ' -analysis is given in figure 98 referring to a case of an OH co-current in an ECRH discharge where an almost complete thermal collapse occurred. The calculation predicts unstable $(m, n) = (2, 1)$ tearing modes in conjunction with a width of the respective island of $w \approx 5$ cm extending up to the limiter. This is in agreement with an island width of 4–6 cm estimated from the tomographic mode reconstructions. The predicted values for $\tilde{B}/B_0(r = a)$ are generally significantly smaller than the experimental values (roughly by a factor of 10). This discrepancy might be due to neoclassical drive (Zohm *et al* 1997) or nonlinear effects. The figure contains a numerical scan of the external rotational transform showing that the current profile of #47623 is expected to be unstable almost in the entire range, where $\iota = 1/2$ is present in the plasma. The case where a disruption was observed coincides with the prediction of islands extending to the limiter. The nonlinear evolution of the magnetic islands has been assessed in this case by using the classical resistive MHD Rutherford equation $\tau_{\text{res}}/r_s \cdot dw/dt = r_s \cdot \Delta'(w)$ (Rutherford 1973), where $\tau_{\text{res}} = \mu_0 r_s^2 / (1.22\eta)$ is the resistive time at the radius of the rational surface r_s and η is the neoclassical resistivity. Using the initial value $\Delta'(0) = 4.7$, the Rutherford equation yields $dw/dt = 28 \text{ cm ms}^{-1}$ in the linear phase of the island growth which is consistent with the experimental value of $dw/dt = 17 - 25 \text{ cm ms}^{-1}$ as derived from x-ray data.

The most relevant cause for the different stability behaviour in W7-AS as compared with W7-A is the increased contribution of the bootstrap current in W7-AS, which leads to broader current densities and steeper gradients at the rational surfaces near the edge. Furthermore, additional heating (ECRH, NBI) in W7-AS leads to current profiles differing from those obtained in OH discharges of W7-A. The typical current profiles are characterized by noticeable gradients extending throughout the plasma from the hot plasma region to the edge. Therefore,

a proper radial shift of the relevant resonant surfaces by means of superimposing an external helical field does not provide an effective way of stabilization, unless the resonance is expelled from the plasma.

In W7-AS, toroidal currents of opposite direction can be driven, which are associated with normal and reversed shear of the total rotational transform. Therefore, W7-AS is well suited for studies of neoclassical tearing mode physics (Zohm *et al* 1997). Also, magnetic islands can be present due to the stellarator field harmonics, which may serve as seed islands of neoclassical modes (Hegna 1998). Actually, almost no tearing mode activity was found in the reversed OH-current (reversed shear) configurations. Qualitatively, this could be indicative of neoclassical stabilization. A definite conclusion, however, cannot be drawn, since the experimentally observed stability behaviour in normal and reversed shear configurations was well consistent with predictions based on the classical Δ' -analysis. The bootstrap current appears to play a key role in the reversed shear case as well, since it compensates the inductive current in the outer region, resulting in enhanced stability without necessarily involving neoclassical effects.

9.4. Fast ion driven Alfvén instabilities

First observations of alpha-particle-driven toroidal Alfvén eigenmodes (TAE) were made in the TFTR tokamak (Nazikian *et al* 1997). Most of the experimental investigations (Wong 1999), however, refer to plasmas with energetic particle populations, which originate from the heating by neutral beam injection (NBI) or ion cyclotron resonance heating (ICRH). Alfvén eigenmodes (AEs) have frequently been observed in NBI low- β heated plasmas. In particular in cases with a relatively large fraction ($>10\%$) of resonant energetic particle energy in the slowing down distribution, they are typically the origin of the most prominent and relevant MHD-activity found in W7-AS.

9.4.1. Low-shear coherent GAE modes. During neutral beam injection in W7-AS pronounced MHD activity is observed, which is attributed to global Alfvén eigenmodes resonating with ions of the slowing down distribution (Weller *et al* 1993, 1994b, 1994c, Weller *et al* 1995, 1998, Ringler *et al* 1987, Teo *et al* 1998, Weller *et al* 2001). In most cases net-current-free plasmas were investigated injecting almost tangentially up to about 1.5 MW at 50–55 kV in co- and/or counter-direction. Usually hydrogen was injected into a deuterium target plasma ($H \rightarrow D$), but $D \rightarrow D$ injection has been used occasionally in order to study fast particle effects by monitoring the beam–target neutron rates.

The rotational transform at the plasma edge was typically slightly above the main resonances at $t = 1/3, 1/2$, where the confinement is good due to the reduced number of possible resonances (Brakel and W7-AS Team 2002). Therefore, the shear Alfvén continua (AC) defined by the simple dispersion relation, $\omega^2 = (k_{\parallel} \cdot v_A)^2$ with $k_{\parallel} = (m \cdot t - n)/R$, v_A Alfvén speed, poloidal and toroidal mode numbers m, n do not extend to the zero frequency limit since k_{\parallel} remains finite. In the gaps below the Alfvén continua weakly damped global Alfvén eigenmodes (GAE) of both helicities, $n/m > 0$ and $n/m < 0$, can exist. In the first case the mode helicity is in the same direction as the equilibrium field, and relatively low frequency GAEs in the range 10–40 kHz typically appear. The mode numbers correspond to low order values of m and n with the ratio n/m closest to the value of the rotational transform at the location of the mode. Toroidal coupling between modes of the same toroidal mode number n and adjacent poloidal mode numbers m and $m \pm 1$ is very weak due to low shear, and therefore, toroidicity induced Alfvén eigenmodes (TAE) as in tokamaks are not important. Low frequency GAEs appear mostly as continuous coherent oscillations on signals of various

diagnostics. The mode frequencies scale with the Alfvén speed as concluded from scans of the magnetic field and mass density variations. The particle drive is inferred from transient mode behaviour at the time, when a neutral injector is switched off. The decay of the mode activity corresponds to the slowing down of fast particles below the resonance velocity, and is therefore much faster than the decay of the plasma pressure. The propagation of the GAE modes is in the direction of the fast ion diamagnetic drift (opposite to the case of the other modes), and this is consistent with the excitation mechanism, relying on free particle energy which is tapped from the fast ion density gradient. The condition for the drive to overcome the fast particle velocity space damping is approximately given by $\omega_{*,i,fast}/\omega_{GAE} > 1$ ([Li et al 1987](#)).

The spatial structure of GAE obtained from x-ray tomographic reconstructions usually extends over a large fraction of the plasma radius. In the case of single peak spectra, the mode structures are consistent with the lowest mode numbers to be expected. Frequently, however, two or more peaks appear in the Alfvén spectrum, which are associated with different toroidal mode numbers but similar pitch n/m , or with nodes in their radial eigenfunction, respectively. The second effect shows the global waveguide mode structure of the GAEs.

In many cases, particularly at high magnetic field, the velocity of the injected ions does not reach the Alfvén speed. Excitation of GAEs then occurs via $m \pm 1$ sideband resonances because of toroidal coupling and particle drift effects. The sideband resonance, which is at $v_A/3$ in the TAE case, can be as low as $v_A/10$ for GAEs because k_{\parallel} can be different by this factor for m and $m \pm 1$.

The basic features of energetic particle driven GAEs could consistently be described with the 2D MHD code FAR coupled with a gyrofluid model for the fast ions ([Spong et al 1992](#), [Weller and Spong 1993](#), [Spong et al 1994a](#), [Weller et al 1995](#)). The FAR code also predicts GAE modes, similar to those in W7-AS, to be the most important modes in tokamaks with q-profiles containing extended regions of low or reversed shear ([Spong et al 1994b](#)). Conversely, TAE modes have been observed in W7-AS in cases of increased shear (see next sub-section). In addition, frequency spectra and GAE mode structures have also been investigated with the CAS3D code taking the 3D ideal MHD equilibrium as provided by the VMEC code into account.

In quasi-stationary discharges coherent GAE activity does not seem to cause significant losses. Typical saturation amplitudes of the magnetic perturbations are about $\tilde{B}/B \leq 10^{-4}$, which seem to be in a sub-critical range. Only in transient phases at the start of NBI, where the velocity distribution can be more unstable, plasma energy losses in combination with larger mode amplitudes have been found ([Weller et al 1997a, 1999a, 2001](#)).

9.4.2. Modes in the TAE gap. Small amounts of shear lead to stabilization of GAEs, as inferred from cases with different plasma beta. Calculations with the FAR gyrofluid code show that increased continuum damping may cause the stabilization. In order to study the common underlying physics of GAE modes under low shear conditions and TAE modes at increased shear we have used OH-current drive to modify shear, including cases with positive and negative shear. In particular, at higher shear TAE gaps become accessible as in tokamaks, and TAE modes could be identified, which are characterized by a single pair of two adjacent poloidal harmonics ([Görner et al 1998a](#)). Figure 99 shows a comparison of experimentally derived mode perturbations (from x-ray tomography, left) with mode structures obtained from CAS3D modelling (perturbed pressure contours and even parity radial displacement components, middle). Whereas GAE structures consist of a single poloidal mode harmonic, the experimentally observed mode structure shown in this figure changes from $m = 5$ in the plasma core to $m = 6$ at the boundary, in accordance with the structure due to the

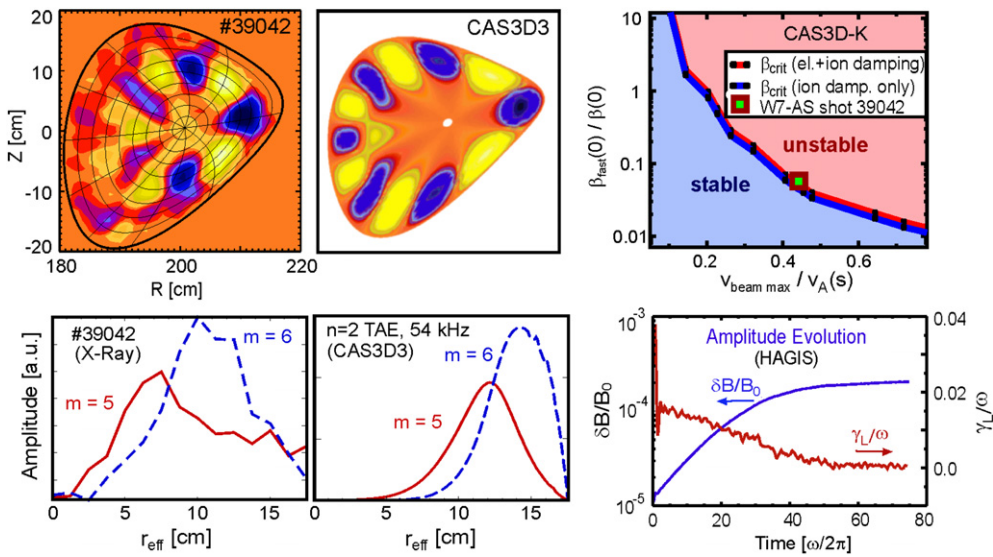


Figure 99. TAE modes in W7-AS in the presence of enhanced shear generated by small (5 kA) OH driven current. The variation of the t -profile between $\approx 2/5$ (centre) and $\leq 2/6$ (edge) favours the formation of a $n = 2$ TAE around 50–60 kHz with main poloidal harmonics $m = 5$ towards the inside and $m = 6$ in the outer part of the plasma (even parity mode). The mode structure obtained from x-ray tomography (perturbed x-ray emissivity and its poloidal Fourier decomposition, left) is compared with the perturbed pressure distribution and radial eigenfunctions predicted by the CAS3D code (middle). The right part contains a linear stability diagram obtained by CAS3D-K (top). The two close lines at the stability boundary refer to cases differing in the inclusion of the electron damping term. The nonlinear evolution of the mode amplitude, as predicted by HAGIS using the CAS3D eigenfunctions, is shown underneath. The experimental case is close to marginal stability consistent with relatively low saturation amplitude.

expected coupling between the $(m, n) = (5, 2)$ and $(6, 2)$ harmonics in this case of increased shear.

In the right upper part of the figure, a stability diagram is shown obtained with the CAS3D-K code (Könies 2000, 2005), which is a perturbative linear stability code based on a hybrid MHD-driftkinetic model. It uses MHD eigenfunctions and frequencies from the CAS3D code and takes energetic particles into account by a generalized energy integral. The diagram was generated by using measured profiles and the calculated fast ion distribution function for discharge #39042 (left) and by varying the stability parameters $\beta_{o,\text{fast}}/\beta_{o,\text{therm}}$ (ratio of central fast ion beta and thermal beta) and $v_{\text{beam,max}}/v_{A0}$ (ratio of maximum neutral beam injection velocity and central Alfvén speed). CAS3D-K predicts case #39042 (represented by a single square symbol) to be marginally unstable.

In addition the self-consistent nonlinear interaction of the mode with fast particles has been studied with the guiding centre particle following code HAGIS (Pinches *et al.* 1998) for this case of (weak) TAE activity. In order to make HAGIS available for stellarator configurations toroidal averages of the W7-AS equilibrium and of the linear MHD eigenmode, which was taken from the CAS3D calculation, were used. Relatively small saturation amplitudes of $\tilde{B}/B \approx 2 \times 10^{-4}$ at the radial position, where the mode amplitude peaks, have been obtained causing only a negligible effect on the fast particle distributions (Weller *et al.* 2001). The results of the HAGIS calculation are roughly consistent with the magnetic measurements, which give low values of $\tilde{B}/B(r = a) \leq 1 \times 10^{-6}$ at the plasma edge, and with the absence of

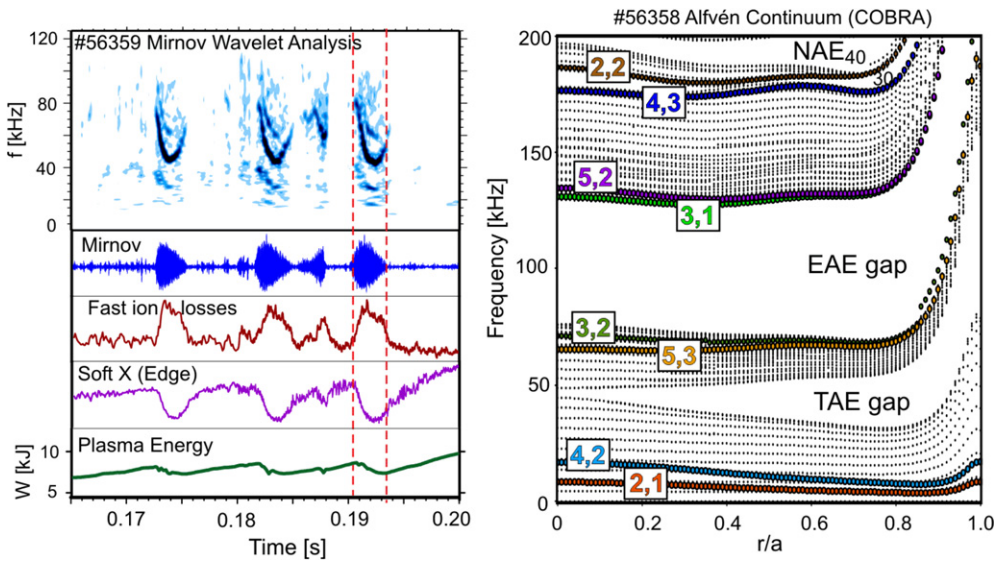


Figure 100. Alfvén instabilities during density/plasma energy ramp up causing fast particle and thermal losses. (Left) Mirnov activity, fast ion loss signal (EFIP), edge SX-signal and diamagnetic energy (W7-AS #56359 at 1.2 T, $t(a) \approx 0.51$). Right: Alfvén continuum spectrum as predicted by the COBRA code showing resonances (black dots), prominent gaps and branches of low (m, n) resonances (coloured circles). The strongest mode harmonic in the magnetic data chirping down from 70 to 40 kHz corresponds to $(m, n) = (4, 2)$ located in the edge region as inferred from x-ray profiles.

MHD induced losses. The temporal evolution of the perturbed magnetic field and the growth rate according to the HAGIS calculation are included in the lower right part of the figure.

A regime of bursting GAE and TAE modes correlated with noticeable effects on the fast ion confinement was found at low electron collisionality achieved with combined ECRH and NBI heating. During the bursts fast downward frequency sweeping is observed. Fast particle losses in this case have been inferred from data obtained with deuterium injection using the neutron rate as a measure of the fast particle density since beam-target reactions are the dominating neutron production process. The magnitude of the stationary neutron flux was found to be significantly lower than predicted. This indicates MHD induced losses and/or charge exchange losses of energetic ions of the beam slowing down distribution. Evidence of the first process is obtained from the observed correlation between relaxations of the D-D neutron rate and soft x-ray signals with the MHD bursts (Weller *et al.* 1997a, 2001). The CAS3D code was used to identify the modes as TAE modes, which were caused by internal shear induced by compensating a relatively large bootstrap current distribution with a centrally peaked Ohmic current.

Figure 100 contains another case, where bursting modes are correlated with fast ion and thermal losses during the plasma ramp-up phase. The dominating mode harmonics as found by a Mirnov signal analysis based on a generalized Lomb periodogram method (Zegenhagen *et al.* 2006a) was $(m, n) = (4, 2)$. The energetic ion losses were detected by a scintillator-based escaping fast ion probe (EFIP, Werner *et al.* (2001)). The mode frequency, sweeping down from 70 to 40 kHz, is close to the TAE gap as follows from the comparison with the Alfvén continuum spectrum (right part of figure) calculated by the COBRA Alfvén continuum code (Kolesnichenko *et al.* 2000, 2001). However, a clear

mode identification was not possible. In a similar case at lower rotational transform (W7AS #34723), the mode was classified as a non-conventional GAE with frequency above the AC (NGAE, [Kolesnichenko et al \(2007a, 2007b\)](#)). In order to explain the observed losses a novel mechanism of mode induced anomalous electron heat conductivity and thermal crashes was proposed ([Kolesnichenko et al 2005a, 2005b, Kolesnichenko et al 2006](#)).

9.4.3. Alfvén modes in higher gaps. The Alfvén instabilities observed in the lower frequency range ≤ 70 kHz (GAE, TAE, EAE) have counterparts in tokamak configurations. However, the Alfvén spectra at higher frequencies differ clearly due to non-axisymmetric magnetic field harmonics in stellarators. In particular, additional gaps in the continuum spectrum and corresponding Alfvén eigenmodes occur, which are absent in axisymmetric geometry. Whereas the ellipticity induced AE (EAE) in both devices are generated by the average plasma elongation, the most important non-axisymmetry induced modes are helical Alfvén eigenmodes (HAE, [Nakajima et al \(1992\)](#), [Kolesnichenko et al \(2001, 2007b\)](#)) due to rotating field harmonics. In addition, the periodicity of the magnetic field along the toroidal direction gives rise to so-called mirror induced Alfvén eigenmodes (MAE). These modes may be present in tokamaks as well if the toroidal ripple due to the finite number of toroidal field coils is sufficiently large. The characteristic frequencies ω^* of these modes are approximately determined by intersections of the cylindrical continuum branches, given by $\omega^* = |\mu t^* - \nu N_p| v_A^*/2R \equiv k_{\mu,\nu}^* \cdot v_A^*$ with $t^* = (2n + \nu N_p)/(2m + \mu)$. Here, the superscripts (*) denote the radial location of the crossing point of the branches with mode numbers (m, n) and $(m + \mu, n + \nu N_p)$. The indices μ, ν of the coupling parameters $\varepsilon_B^{\mu\nu}$, given by the corresponding harmonics of the equilibrium field

$$|B| = B_0 \left[1 + 0.5 \sum_{\mu\nu} \varepsilon_B^{\mu\nu}(\psi) \cos(\mu\theta - \nu N_p \phi) \right],$$

describe the type of the gap (e.g. TAE by $(\mu, \nu) = (1, 0)$, HAE₂₁ by $(\mu, \nu) = (2, 1)$, MAE₀₁ by $(\mu, \nu) = (0, 1)$). N_p is the number of toroidal field periods. Besides the effects on the Alfvén spectra the non-axisymmetric field components also lead to a new variety of wave-particle resonances resulting from different sideband harmonics in the drift orbits of passing and trapped particles ([Kolesnichenko et al 2002](#), [Kolesnichenko et al 2002, 2006](#)). In general, the resonance condition can be written as $\omega = [(mt - n) + j(\mu_r t - \nu_r N_p)] v_{\parallel}^{\text{res}} / R$ with $j = 0, \pm 1$, or if $\omega = \omega^*$ and $k_{\parallel m,n} \equiv (mt - n)/R \approx k_{\mu\nu}^*$ is used for ‘gap’ modes, the resonance velocity is given by $v_{\parallel}^{\text{res}} = v_A^* [1 + 2j(\mu_r t^* - \nu_r N_p)/(\mu t^* - \nu N_p)]^{-1}$. A unique feature of non-axisymmetric field harmonics is also the possibility of gap crossings connected with additional effects on the Alfvén continuum and on eigenmodes, e.g. anti-balloonning behaviour as found in W7-AS ([Yakovenko et al 2007](#), [Zegenhagen et al 2006b](#)).

The excitation of high-frequency Alfvén instabilities (≤ 500 kHz) in W7-AS is mostly correlated with Alfvén speeds below the maximum beam ion velocity. Figure 101 shows an example of the characteristic transition from low frequency to high frequency bursting modes, occurring as soon as the full injected ion velocity normalized to the volume averaged Alfvén speed exceeds unity ($v_{\parallel,\text{max}}/\langle v_A \rangle > 1$). In this shot the range $0.5 \leq v_{\parallel,\text{max}}/\langle v_A \rangle \leq 1.8$ is covered by a density ramp. When $v_{\parallel,\text{max}}/\langle v_A \rangle$ is slightly above unity, Alfvén modes in the GAE and TAE range ≤ 50 kHz are seen in the Mirnov wavelet spectrogram. Later with increasing magnitude of $v_{\parallel,\text{max}}/\langle v_A \rangle$, the unstable modes are characterized by multiple frequencies in the range of 40–250 kHz which are particularly strong during the short phase of increased NBI power. Further on during the density ramp all the instabilities disappear, but they

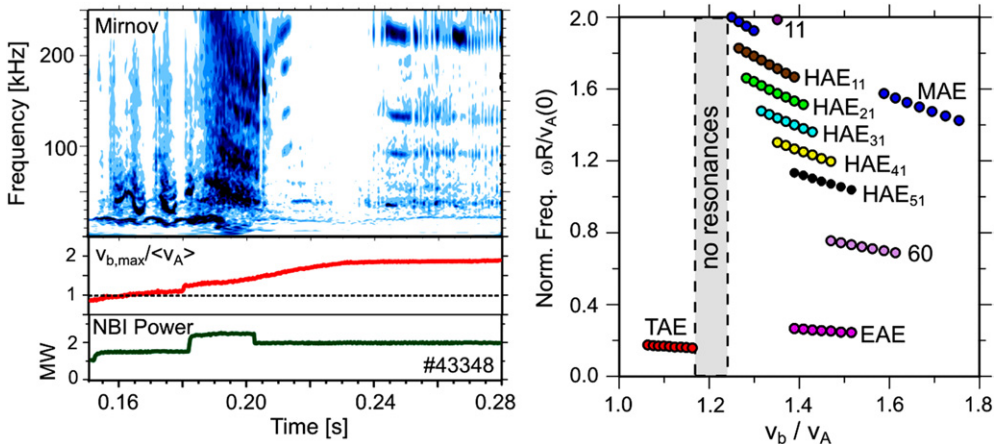


Figure 101. Change of the AE-frequency spectrum depending on the fast ion content and the Alfvén speed. (Left) Mirnov wavelet spectrogram, ratio of maximal beam velocity and averaged Alfvén speed and NBI power (W7-AS #43348, $\langle\beta\rangle \leqslant 1.3\%$) at 1.2 T, $t(a) \approx 0.31$). A density ramp drives $v_{beam,max}/\langle v_A \rangle$ above unity causing excitation of higher frequency modes. The theoretically calculated dependence of the destabilized Alfvén spectrum on v_{beam}/v_A (right) is in qualitative agreement with the experimental data. The mode denoted by 60 refers to a higher order AE with coupling parameters $(\mu, \nu) = (6, 0)$.

show up again around the maximum value $v_{||,max}/\langle v_A \rangle \approx 1.8$ where the mode at ~ 230 kHz is dominating. This behaviour could qualitatively be explained by the evolution of wave-particle resonances (Lutsenko *et al* 2002, Kolesnichenko *et al* 2004). For this the structure of the Alfvén continuum was calculated with the code COBRA, and Alfvén eigenmodes as predicted by the BOA-E code (Lutsenko *et al* 2002) were used. The magnitudes of the resonance velocities were taken into account as described above. The fast ion drive was modelled by considering only fast ion velocities above a threshold at $0.9 \times v_{||,max}$, since it strongly grows with the particle energy. The Alfvén continuum in the high frequency range is typically found to consist of very wide gaps with the resonances squeezed in narrow bands, and therefore, a number of weakly damped modes could be identified. The result of the calculations is shown in the right part of the figure, where the frequencies of unstable modes are plotted as a function of $v_{||,max}/\langle v_A \rangle$. The multiple modes at higher frequencies correspond to HAEs with different coupling parameters being sequentially excited and stabilized again in the range of $v_{||,max}/\langle v_A \rangle$ coinciding with a quiescent phase as seen in the experiment. Close to the maximum resonance velocity (in the stationary phase of the discharge) the dominant mode is predicted to be a MAE corresponding to the strong spectral line around 230 kHz.

In the high- β regime the averaged Alfvén speed overlaps with a significant part of the fast ion distribution due to low magnetic field and high densities. Nonetheless, the discharges are mostly stable, because the slowing down times of the fast ions are short in these high collisional plasmas, resulting in relatively low fast ion pressures compared with the total plasma pressure ($\langle\beta_{fast}\rangle/\langle\beta_{tot}\rangle < 0.1$ typically). Only in transient phases during stepping up the NBI power, a variety of Alfvén eigenmodes are destabilized (Weller *et al* 2003, Kolesnichenko *et al* 2003). A comparison of observed frequencies for such a case with code predictions is shown in figure 102. Several Alfvén modes up to 250 kHz are destabilized during a 30 ms time interval (Mirnov spectrogram, middle). The multiple modes are very likely TAEs and EAEs, as well

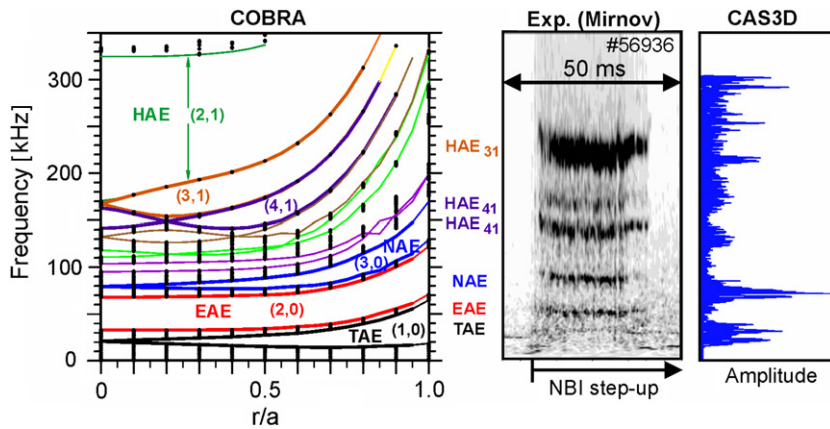


Figure 102. Alfvén continuum spectrum predicted by the COBRA code (left) for a case of transient activity of NBI driven Alfvén instabilities (middle). Dots show the calculated continuum frequencies for several radii. The calculated boundaries of major gaps labelled by the respective poloidal and toroidal coupling numbers are shown with solid lines (in particular, the TAE gap is (1,0), the EAE gap is (2,0), the HAE gap is (2,1), etc.). The observed frequencies (middle) correspond to global eigenmodes found with the BOA-E code. All the higher gap modes are excited during a transient overshoot of the fast particle drive (fast ion beta relative to the thermal beta) after a step-up of the NBI power. The right part contains a filtered response function calculated by the CAS3D code as a measure of resonances due to global modes.

as HAEs of different types with coupling parameters of $(\mu, \nu) = (3, 1)$ and $(4, 1)$. This is inferred from Alfvén calculations of AC spectra and Alfvén eigenmodes by several 3D MHD codes including COBRA, CONTI (Könies 2003) and STELLGAP (Spong *et al* 2003) for the AC, and CAS3D and BOA-E for AEs. CAS3D also yields the AC (Nührenberg 1999b), which was found to be in close agreement with all the other Alfvén continuum codes. The left part of the figure contains the result of the COBRA code. The right part gives the result of the CAS3D code, which evaluates the response with respect to global modes in a special spectral modus, where forced free-boundary ideal modes are excited by an oscillating magnetic field containing sufficient poloidal and toroidal harmonics. Again, the Alfvén continuum at higher frequencies is characterized by very compressed continuum resonances with wide gaps in between. This is typically the case when the gap widths (determined by the magnitude of the corresponding field harmonics) are comparable with the distance of adjacent gaps (Yakovenko *et al* 2007).

An extensive study of Alfvén instabilities was made covering the last ~ 2300 shots of W7-AS (Zegenhagen 2006). The majority of the shots were dedicated to high density discharges in divertor and high- β configurations with a vacuum rotational transform in the range $\tau = 0.45\text{--}0.55$. For the cases where instabilities were found, a data analysis was performed including: (i) a mode analysis (based on the generalized Lomb periodogram method), (ii) an analysis of correlations between magnetic probe signals and fast escaping ion data, (iii) an equilibrium analysis (with STELLOPT) using measured electron temperature and density profiles, (iv) a comparison of the observed mode frequencies and mode numbers with the calculated Alfvén continuum for mode classification, (v) and an evaluation of the stability parameters $v_{\parallel,\max}/\langle v_A \rangle$ and $\langle \beta_{\text{fast}} \rangle/\langle \beta_{\text{tot}} \rangle$. The distribution function of the fast ion distribution was calculated using the Monte-Carlo Code NEUTRALBEAM (Werner 2005) for the NBI birth profile and the Fokker-Planck code DFNBI (Maaßberg 2004) for the slowing down

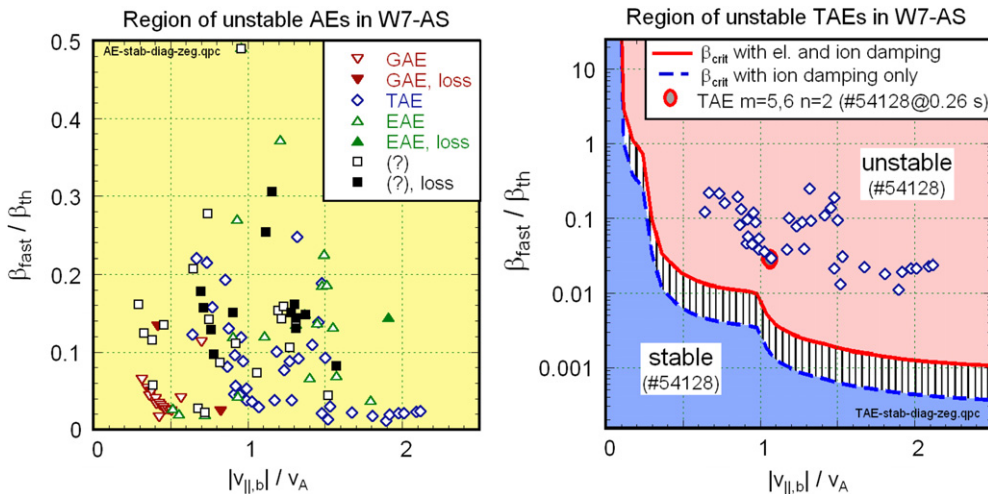


Figure 103. Range of unstable NBI driven Alfvén eigenmodes characterized by the stability parameters $\beta_{\text{fast}}/\beta_{\text{therm}}$ and $v_{\parallel,\text{beam}}/v_A$. The database was compiled from a restricted number of shots of the last experimental campaign in W7-AS. The different symbols indicate different types of AEs as identified by consistency checks of observed mode numbers and frequencies with predictions based on 3D Alfvén continua spectra calculated by the COBRA code. The cases where fast particle losses were observed are marked by solid symbols. In a number of cases no identification was possible (left). The subset of observed unstable TAE mode cases is plotted in a stability diagram for a particular shot obtained with a local model for growth and damping rates (Kolesnichenko *et al.* 2001, Könies 2005).

distribution. The final database contained only 133 cases of Alfvénic instabilities which were analysed. Figure 103 shows an operational diagram (left), where each case is represented by a symbol in the $\langle\beta_{\text{fast}}\rangle/\langle\beta_{\text{tot}}\rangle$ versus $v_{\parallel,\text{max}}/\langle v_A \rangle$ plane. For a few cases further studies were made using the CAS3D-K code in order to compare the data with linear stability predictions. In the right part of the figure, the subset of observed unstable TAE mode cases is plotted in a stability diagram for a particular shot obtained with a local model for growth and damping rates (Kolesnichenko *et al.* 2001, Könies 2005).

Although in previous analyses some evidence of stellarator AEs was found (see previous figures), no clear identification of HAEs or MAEs could be made in this database. A part of the unidentified modes may be due to energetic particle modes (EPM, Chen (1994), Zonca and Chen (1996)), since $\langle\beta_{\text{fast}}\rangle/\langle\beta_{\text{tot}}\rangle$ is relatively large, the frequencies are in the expected range and correlations with energetic ion losses were found. Most of the modes could be consistently attributed to TAE and EAE modes excited through resonances at $v_{\parallel} = v_A$, $v_A/3$. The GAEs were found to be weakly damped and exclusively excited through sideband resonances in the sub-Alfvénic regime. In most cases no impact of mode activity on the fast particle confinement was found.

9.5. Discussion

An important result of stability studies in W7-AS consists of the absence of fast disruptive instabilities even close to operational limits. The plasma reaction occurs mostly via slow transitions to increased transport. Although the local ideal MHD stability tends to underestimate the stability found in W7-AS (similarly as in the Large Helical Device, LHD), the linearized ideal MHD analysis still provides a useful reference. The observed pressure driven

mode activity is mostly correlated with the predicted unstable regions. The data suggest that relevant MHD modes are absent, if Mercier stability is ensured.

The Ohmic transformer in W7-AS as well as the ECCD system have proven to be very useful tools for the investigation of current driven modes, for realizing configurations with different rotational transform and for configuration control. However, additional operational limits are introduced by current driven MHD modes causing thermal collapses, in particular at $t = 1/2$.

Alfvén modes excited by fast resonant particles represent the most prominent instabilities in a wide parameter range. Stellarator field harmonics (helical or mirror components) cause a new variety of continuum gaps and global modes (HAE, MAE) as well as of particle-wave resonances. The analysis of these modes in W7-AS and their effect on the fast particle confinement will provide a good basis to assess the role of Alfvén instabilities in W7-X and a Helias type reactor.

10. High- β operation

10.1. Introductory remarks

Achieving high plasma pressure in stationary conditions without disruptive activity is a key challenge for developing fusion energy. The processes that limit the accessible β values are investigated in order to develop an understanding of 3D high- β plasmas and the expected operating limits for new experiments. Here β defined by $\langle \beta \rangle = 2\mu_0 \langle p/B^2 \rangle$ is the volume averaged plasma pressure normalized to the magnetic field pressure, and therefore is a measure for the efficiency of the magnetic confinement concept. A plasma β in the range of about $\langle \beta \rangle = 5\%$ is required for an economically attractive fusion reactor. In order to achieve this goal sufficiently good plasma equilibrium and stability properties of the magnetic configuration have to be achieved. In particular, the Pfirsch–Schlüter currents result in critical β -values above which the confinement is deteriorated by equilibrium changes and/or effects of pressure driven MHD instabilities. Therefore, it is essential to minimize the Pfirsch–Schlüter currents by exploiting 3D shaping of the plasma. Experimental verification of the optimization principle is also an important goal of the W7-AS high- β program. The demonstration of the reactor capability of an extensively optimized stellarator ([Wobig 1999](#)) will be explored in Wendelstein W7-X, which is presently under construction ([Grieger et al 1992](#), [Grieger and W7X Team 1998](#), [Beidler et al 1990](#)). A comparison of high- β results in W7-AS with those achieved in the large helical device (LHD) can be found in [Weller et al \(2006\)](#), [Watanabe et al \(2004c\)](#).

10.2. Formation and optimization of high- β discharges

The limitation of the available heating power requires ([Weller et al 2006](#)) low magnetic field operation at maximized densities to access the high- β regime. Under these conditions electron cyclotron wave heating cannot be applied unless advanced heating scenarios based on mode conversion into electron Bernstein modes via the OXB-process are used ([Laqua et al 1999, 2003a, 2003b](#)). Plasma heating thus relies on neutral beam injection (NBI). Before installation of the divertor the plasma was bounded by limiters, and high power NBI (up to 3.4 MW 50 keV hydrogen or deuterium injected by two beam lines) has resulted in loss of particle control and early termination of the plasma by radiation collapse ([Weller et al 1989, 1991](#), [Burkhardt et al 1998](#), [Jaenicke et al 2000](#)). This effect could be mitigated to some extent by increased graphite shielding of plasma facing

components (PFC) and boronization of the vacuum vessel. Only in cases of magnetic fields with $B \leq 1$ T, where the particle confinement deteriorates, quasi-stationary discharges could be established with $\langle \beta \rangle \leq 2.3\%$ (Hofmann *et al* 1996, Weller *et al* 1998, 2001). After installation of the island divertors, the high- β performance of W7-AS has greatly improved (Weller *et al* 2002a, Jaenicke *et al* 2002b, Weller *et al* 2002b, 2003, Weller 2003, Geiger *et al* 2004b, Zarnstorff *et al* 2004), mainly because of two major beneficial effects. Firstly, improved impurity control could be achieved due to the substantially increased graphite coverage at the plasma boundary. Boronization was only occasionally required, but glow discharge cleaning had to be applied frequently in order to keep control of the plasma density.

Secondly, configurations with higher rotational transform could be exploited by using the control coils for edge configuration control. High-iota configurations are preferable because the equilibrium β -limit (for a classical stellarator) is approximately $\langle \beta \rangle_{EL} \approx (a_{eff}/R) \cdot t^2$, and in addition the global confinement shows a weak favourable t -dependence. However, with increasing iota the modular field harmonics involve perturbations at the $t = 5/m$ resonances with lowest m and hence larger decay lengths towards the magnetic axis. The associated formation of island chains or stochastic field regions at the edge causes a progressive reduction of the effective plasma radius associated with reduced confinement. Smooth flux surfaces can be restored using the divertor control coils at high rotational transform ($t < 0.45$). In contrast to proper island divertor configurations (Grigull *et al* 2001b) the coils are energized to suppress edge islands and maximize the plasma volume resulting in better global energy confinement. This is important in high- β operation, because the plasma temperature has to be kept above a critical value to avoid a thermal collapse. In addition the value for the equilibrium β -limit increases linearly with the inverse aspect ratio.

The vertical field B_z was optimized in order to centre the plasma between the inner and the outer divertor plates in the high- β phase, thereby maximizing the plasma volume. In most cases a constant B_z was used. This pushed the vacuum configuration against inboard vessel installations and scraped off a large part of the plasma cross-section. During the evolution of high- β plasmas the plasma is shifted horizontally outward and expands in size (Geiger *et al* 1996). Consequently, during the plasma start-up phase, unfavourable conditions with regard to beam absorption and confinement have to be accepted. According to 3D equilibrium calculations iota at the edge is decreased with increasing plasma β leading to changes of the edge resonances. The appearance of edge islands and their compensation by the control coils has also been deduced from flattened temperature regions and from the footprints of H_α light and heat deposition on the divertor target plates. By applying proper control fields, a transition from narrow H_α structures (due to islands intersecting the target plates) to broad patterns typical for smooth flux surfaces aligned with the target plates is observed.

Another essential improvement was achieved by aligning the previously counter-injecting NBI beamline into co-direction. The expected beneficial effect at low magnetic fields, i.e. the reduction of fast ion orbit losses, could be qualitatively verified by measurements with the lost ion scintillator plate detector (section 4.2.1, Werner *et al* (2001)). The transition from balanced to all co-injection results in toroidal currents up to ≈ 3 kA, which are compensated by OH current drive. This may cause ambiguities of the t -profile, which are very difficult to resolve, given the experimental errors of the profile data (Geiger *et al* 2003). The toroidal rotation induced by the beams remains below about 10% of the thermal ion velocities due to the relatively large plasma viscosity owing to the field variation in the toroidal direction (Baldzuhn *et al* 1998b).

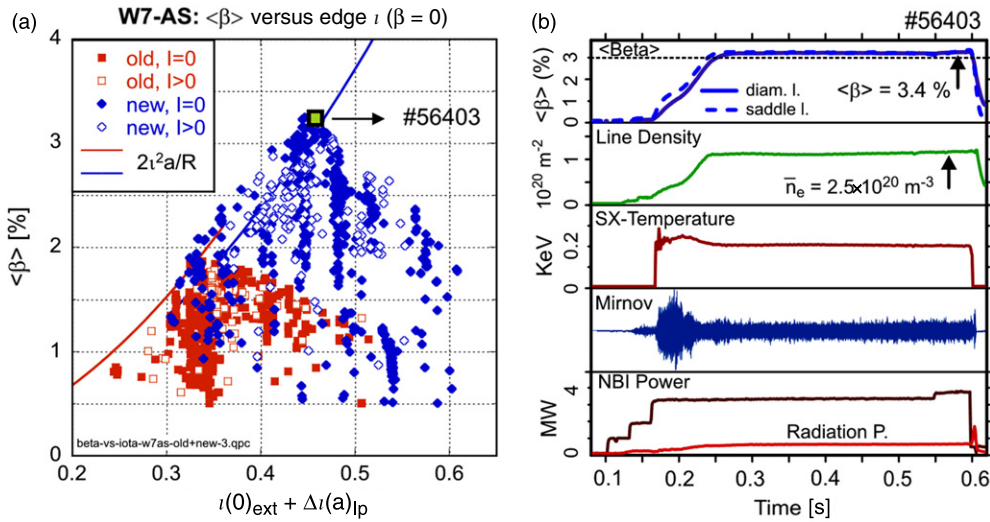


Figure 104. (a) Comparison of volume-averaged β (approximate values from diamagnetic energy) achieved before (red squares) and after (blue) installation of divertor modules in W7-AS as a function of the total rotational transform. Discharge #56403 with the so far highest value of $\langle\beta\rangle$ ($\approx 3.4\%$ from a detailed equilibrium analysis) is marked in the plot. (b) The time evolution of this shot (at $B = 0.9$ T and $t_{ext} = 0.5$) exhibits a MHD-quiescent quasi-stationary discharge with a flat top at $\langle\beta\rangle \approx 3.2\%$ (peak value 3.4%) corresponding to about 70 confinement times. The diamagnetic energy agrees with the energy derived from saddle coils which detect the field of the Pfirsch–Schlüter currents (top traces). Below the line integrated electron density (HCN interferometer), the central electron temperature (x-ray two-foil analysis), the injected NBI power and the radiated power are given.

10.3. Confinement and operational limits

A significant extension of the operational space could be achieved under the optimized conditions as described in the previous section. Figure 104(a) compares approximate β -values from diamagnetic loop measurements before and after installation of the divertor systems. At low rotational transform ($\iota < 0.4$) the experimental points are bounded by the lines representing the equilibrium limit in W7-AS according to $\langle\beta\rangle_{EL} \approx 2(a_{eff}/R) \cdot \iota^2$. This corresponds to a critical Shafranov shift reaching values of 50% of the plasma radius. At this value a significant destruction of flux surfaces has to be expected. Actually, data of the campaigns before and after the installation of the divertor are shown causing the difference between the two β -limits due to different aspect ratios. Maximum b was found in the range $\iota = 0.4\text{--}0.5$ with magnetic fields of $B = 0.8\text{--}1.1$ T. The deterioration at higher rotational transform is attributed to resonant field perturbations (islands), which cause a shrinkage of the confinement region and which cannot fully be compensated by the control coils.

The right part of the figure 104(b) shows time traces of an optimized high- β discharge reaching up to $\langle\beta\rangle = 3.4\%$ with a central value of $\beta_0 \approx 7\%$. Good agreement was obtained between the plasma energies derived from the diamagnetic loop and the saddle coils indicating the presence of an isotropic pressure distribution. The analysis of the flux signal due to the Pfirsch–Schlüter current measured by the saddle coils was achieved by comparison with the calculated response of model equilibria by the DIAGNO code (Gardner 1990). The fast ion pressure due to the tangentially injected neutral beam ions is expected to be in the range of $\leq 10\%$ of the thermal pressure under the present high collisionality conditions. For the case

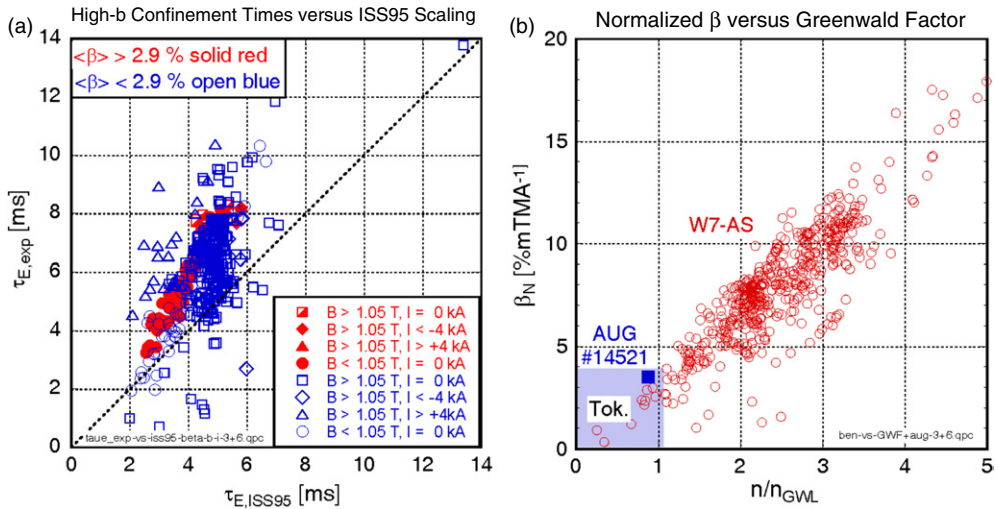


Figure 105. (a) Comparison of measured energy confinement times with the ISS95 scaling for a high- β database. The cases with highest β -values are marked by solid symbols. (b) The normalized β -values are plotted versus the line averaged densities normalized to the Greenwald density. The shaded area marks the range accessible in tokamaks. The solid symbol represents a typical AUG dataset (courtesy of H Zohm).

shown on the right, the ratio of the fast ion pressure and the thermal pressure is $\langle\beta_{\text{fast}}/\beta_{\text{th}}\rangle \approx 4\%$, the collisionality parameter in the plasma centre is $\varepsilon^{3/2} \cdot v^* \approx 1$, the volume averaged slowing down time is $t_{\text{sl}} \approx 1.2$ ms and the global confinement time is $\tau_E \approx 5$ ms exceeding the empirical ISS95-scaling ($\tau_{E,\text{ISS95}} \approx 3.7$ ms) (Stroth *et al* 1996c, Yamada *et al* 2005). The discharge is stationary over a period corresponding to about $70 \tau_E$. The radiated power with $P_{\text{rad}}/P_{\text{abs}} \leqslant 25\%$ is relatively low, and the radiation profiles stay peaked at the plasma boundary throughout the discharge. Impurity confinement times with $\tau_I/\tau_E < 2$ have been found in comparable discharges by injection of laser ablated iron tracer impurities (Weller *et al* 2003). The MHD activity is very weak throughout the whole flattop phase. The discharge exhibits all the features of the high density H-mode regime (HDH) observed for the first time in W7-AS island divertor configurations at higher magnetic field and lower NBI power (section 7.6).

The confinement properties and operational space characteristics have been evaluated for a database of ≈ 530 cases (including a number of shots during low- β phases) for which 3D equilibrium VMEC (Hirshman *et al* 1986a, 1990) code calculations were available. In figure 105(a), a comparison between the experimental confinement times and the ISS95 scaling is presented. The W7-AS high- β data are centered well above this scaling and better fit the W795 scaling (Stroth *et al* 1996c), exclusively derived from W7-AS low- β data. It is remarkable that this scaling is recovered even close to operational limits without evidence of degradation at the highest β -values (data points with $\langle\beta\rangle \geqslant 2.9\%$, marked by solid red symbols). It should also be noted that the data set contains a number of cases where the equilibrium b -limit has been approached as inferred from a Shafranov shift exceeding a significant fraction of the plasma radius and as indicated by saturation of β with increasing heating power. Also, most of the maximum- β discharges have densities within $\pm 20\%$ of the values predicted by the W7-AS density limit scaling (Giannone *et al* 2000a, 2000b, Giannone *et al* 2002a), since the favourable density scaling

is exploited to maximize β . The density limit itself is defined by the density beyond which the global confinement starts to degrade and the plasma eventually runs into a radiative collapse.

In most cases the high- β discharges were heated by hydrogen injection into hydrogen target plasmas ($H^0 \rightarrow H^+$). With deuterium injection ($D^0 \rightarrow D^+$), the achievable β was lower by up to $\sim 20\%$, and steady state was more difficult to attain, mainly due to increased impurity influx. The database includes experiments with combined NBI and O-X-B ECH heating (at $B = 0.9\text{--}1.1$ T) and cases with OH-current drive used to modify the rotational transform.

An attempt was made to compare the boundaries of the high- β operational regime with those of tokamaks. The basic concept is to adopt an equivalent toroidal current that produces the same rotational transform at the plasma edge as the transform produced by the stellarator coils. In particular, we equate the safety factor by $q_\psi(95\%) = 1/t(a)$ and use toroidally averaged flux surfaces, which can be well described by elongation and triangularity parameters of $\kappa \approx 2$ and $\delta \approx 0.3$, respectively. The shape parameters enter the relation between $q(95\%)$ and the tokamak current. The equivalent tokamak current can then be represented by [Uckan \(1990\)](#), [ITER Physics Expert Groups](#) (chapter 1) ([1999](#)):

$$I_{eq} = f(\varepsilon)t(a)(5a_{eff}^2 B/R)[1 + \kappa^2(1 + 2\delta^2 - 1.2\delta^3)]/2\kappa,$$

where $f(\varepsilon) = (1.17 - 0.65\varepsilon)/(1 - \varepsilon^2)^2$ with $\varepsilon = a/R$ inverse aspect ratio and $a \approx a_{eff}/\sqrt{\kappa}$ minor plasma radius. In this way, a comparison with the Greenwald limit and with the normalized β , β_N , can be made as in tokamaks. The operational diagram given in the right part of figure 105 (b) combines both the Greenwald density limit given by $n_{GWL} = I_{eq}/\pi a^2$ ([Greenwald 2002](#)) and the stability limit due to ideal ballooning modes, represented by the Troyon limit $\beta_N = \langle\beta\rangle/(I_{eq}/a \cdot B)$ ([Strait 1994](#)). The normalized data points of W7-AS are well outside the range of tokamaks. The strong correlation between β_N and the Greenwald factor n/n_{GW} is caused mainly by the application of I_{eq} for normalization in both directions.

The approach to formally translate parameters defined in tokamaks for use in currentless stellarators may not reflect the underlying stability physics correctly. Actually, the physics of high densities and high- β seem to be different. Whereas the Greenwald limit is an absolute density limit in tokamaks, the density limit in stellarators is determined by the power balance and hence depends on heating power. Also, the ideal MHD stability limit in tokamaks cannot be surpassed in experiment, whereas this is possible in stellarators (see section 9), presumably due to lower free energy.

Most of the W7-AS data are close to the W7-AS density limit represented by the scaling ([Giannone et al 2002a](#))

$$\bar{n}_{W7-DL} = 1.46 (P/V)^{0.48} \cdot B^{0.54} \quad [10^{20} \text{ m}^{-3}]$$

(absorbed power P in MW, volume V in m^3 , B in T), which is determined by the available power and radiation. Due to the absence of net toroidal currents in W7-AS, density excursions beyond the density limit are not accompanied by violent MHD activity. During phases of excessive density, the plasma suffers a slow thermal collapse and recovers if the particle source is switched off or additional heating is made available.

10.4. Equilibrium studies

The experimental verification of improved equilibrium properties by magnetic field optimization is an important issue in W7-AS. A quantitative equilibrium analysis requires full 3D equilibrium calculations by numerical tools such as VMEC or NEMEC ([Hirshman et al 1986a, 1990](#)) and STELLOPT ([Spong et al 2001, Strickler et al 2002](#)). The stellarator design-optimization code STELLOPT has been modified to reconstruct the W7AS equilibrium self-consistently ([Zarnstorff et al 2004](#)). STELLOPT uses VMEC to calculate

the 3D free-boundary plasma equilibrium given specified coil currents and plasma pressure and current profiles. Various constraints can be accounted for with respect to the measured plasma energy, the plasma size resulting from the contact to the plasma facing components, the shape of measured pressure profiles and various magnetic diagnostics. In addition, equilibrium recovery from a large pre-calculated equilibrium database could be achieved in W7-AS using function parametrization (FP) ([Callaghan et al 1997, 1999, 2000a](#)).

In order to identify the most important effects that cause the saturation of β in W7-AS, first the dependence of the maximum achievable β on the rotational transform has been investigated. The optimum cases were found in the vicinity of $\iota \approx 0.5$. The decrease of $\langle\beta\rangle$ towards low iota is attributed to pushing the plasma against the equilibrium limit causing increased energy transport as is inferred from the reduction of the confinement time, which is much larger than expected from the (weak) dependence of the confinement on iota in the ISS95 scaling law. Also, $\langle\beta\rangle$ shows saturation effects when the heating power is varied. On the other hand, the reduction at high iota appears to be caused by the increasing complexity of edge islands, which cannot be properly compensated by the control coils. The maximum β achieved at $\iota \approx 0.52$ almost coincides with maximum values expected from the power balance on the basis of the W795 confinement scaling and densities corresponding to the W7-AS density limit scaling (see previous section). The equilibrium limit was assessed from calculated flux surfaces using the VMEC code. Basically, the numerical results reflect the strong dependence of the simple analytical approximation of equilibrium β -limit on the rotational transform.

The large shift of the magnetic axis, nearing $a/2$, and the sensitivity of the achieved β to the magnetic configuration, suggests that the plasma confinement and β may be influenced by details of the equilibrium, including the formation of islands and stochastic edge regions. To assess this, the dependence of the plasma β on the control coil current has been studied using the PIES code ([Reiman and Greenside 1986, 1990](#)), which does not assume closed flux-surfaces. Free boundary three-dimensional equilibria have been numerically calculated for optimum configurations, scanning only the control coil current I_{CC} ([Zarnstorff et al 2004, 2005, Reiman et al 2006, 2007](#)). The calculations impose the pressure profiles from the equilibrium reconstructions with STELLOPT as discussed above.

It is found that the flux surfaces in the outer part become progressively stochastic as β is raised and that this effect can be mitigated by adjusting the field of the control coils. The basic results are summarized in figure 106. At first, PIES modelling was made for experimental cases with $I_{CC} = 0$, which achieved $\langle\beta\rangle = 1.8\%$, and with $I_{CC}/I_M = 0.15$, which achieved $\langle\beta\rangle = 2.7\%$ (I_M is the current in the modular field coils). In both cases, the calculations indicate that the flux surfaces in the outer $\sim 35\%$ of the minor radius are stochastic at their (different) $\langle\beta\rangle$ values (see insets). Radial transport in the stochastic region appears to be enhanced due to parallel transport associated with field line diffusion, limiting access to higher β . PIES equilibria were calculated as a function of $\langle\beta\rangle$, keeping the pressure profile shape fixed. The figure shows that the calculated fraction of good flux surfaces (where the field lines stay on nested surfaces) drops with increasing $\langle\beta\rangle$ for all cases, but the drop occurs at higher β for $I_{CC}/I_M = 0.15$ than for $I_{CC} = 0$.

The fraction of good flux surfaces continues to drop above the experimentally achieved $\langle\beta\rangle$. Thus, the PIES equilibria indicate that the experimental β -limit and its variation due to the control coil current may result from the deterioration of the flux surfaces and the effect of magnetic stochasticity on the plasma confinement. The plasmas with largest β were obtained with $I_{CC}/I_M = 0.24$ and a lower magnetic field (0.9 T), i.e. with a $\sim 60\%$ stronger perturbation by the control coils. However, for this case the computed fraction of good flux surfaces is not available. In the calculations it seems to be necessary to allow for a finite pressure

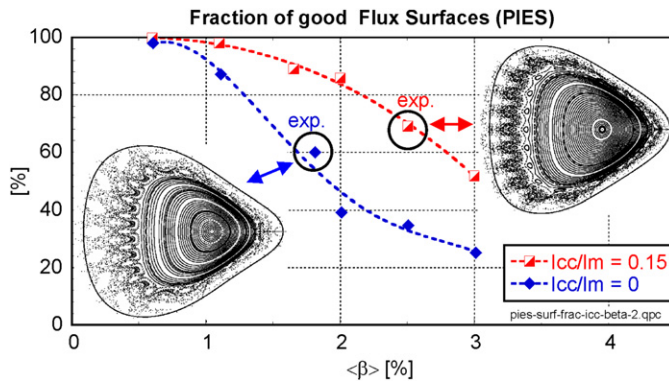


Figure 106. Pressure induced reduction of good flux surfaces predicted by the PIES code. The deterioration of the outer flux surfaces can be mitigated by adjusting the field of the control coils. Lower data points: without control coils, upper data points: $I_{cc}/I_m = 0.15$ (I_{cc} , I_m : currents of control coils and modular field coils). The insets show Poincaré plots of PIES runs for two experimental cases without and with optimized I_{cc} ($B = 1.25$ T, $t_{vac} = 0.52$, $P_{NBI} = 3.1$ MW). The outermost thick contours represent the plasma boundary defined by the scrape-off due to in-vessel components, as calculated by the VMEC code.

gradient in the edge region of stochastic field lines in order to obtain agreement with the experimental observations. In some cases the PIES calculations could be benchmarked by the HINT code (Geiger and Suzuki 2006). Similar observations regarding finite pressure gradients in β -induced stochastic field regions have been reported from LHD (Watanabe *et al* 2007, Suzuki *et al* 2006). A common qualitative explanation is that the parallel mean free path of this high collisional plasma is sufficiently short compared with the connection lengths in the peripheral stochastic region to the plasma facing components.

The β -induced effects on the plasma equilibrium flux surfaces have been investigated in various configurations (Weller *et al* 1990, 1997b), in particular by tomographic analysis of 2-D x-ray emissivity distributions near a toroidal plane with triangular surfaces (Görner *et al* 1997, Ertl *et al* 1996, Weller *et al* 2003, Jaenicke *et al* 1995). The constant x-ray emissivity contours were assumed to coincide with equilibrium flux surfaces. The x-ray measurements provide a measure for the shift of the hot plasma core, particularly the axis shift, which includes the free boundary shift of the plasma. The assessment of the Shafranov shift requires the axis position of a vacuum configuration with the last closed flux surface (LCFS) at the same position as in the finite- β case. Since this is inaccessible, the experimental data were compared with numerical free-boundary equilibrium results from the VMEC code. In low- β plasmas the shift could also be determined by ECE measurements (Fuchs *et al* 1999). Figure 107 summarizes typical results of the x-ray tomography analysis. The horizontal plasma shift along with changes of the flux surface geometry is clearly seen by comparing measured emissivity contours at different β . The basic features of the x-ray tomograms agree well with flux surfaces as obtained with VMEC by approximating the pressure profiles by standard parabolic ones. The current density profiles due to small net-currents are difficult to assess quantitatively. In the standard analysis parabolic profiles are used as an approximation of the total current density consisting of Ohmic, beam driven and bootstrap current density contributions. Frequently the x-ray contours exhibit a larger indentation at the inboard side than expected from the VMEC calculations on the basis of the standard analysis. However, more realistic current density profiles may be reconstructed

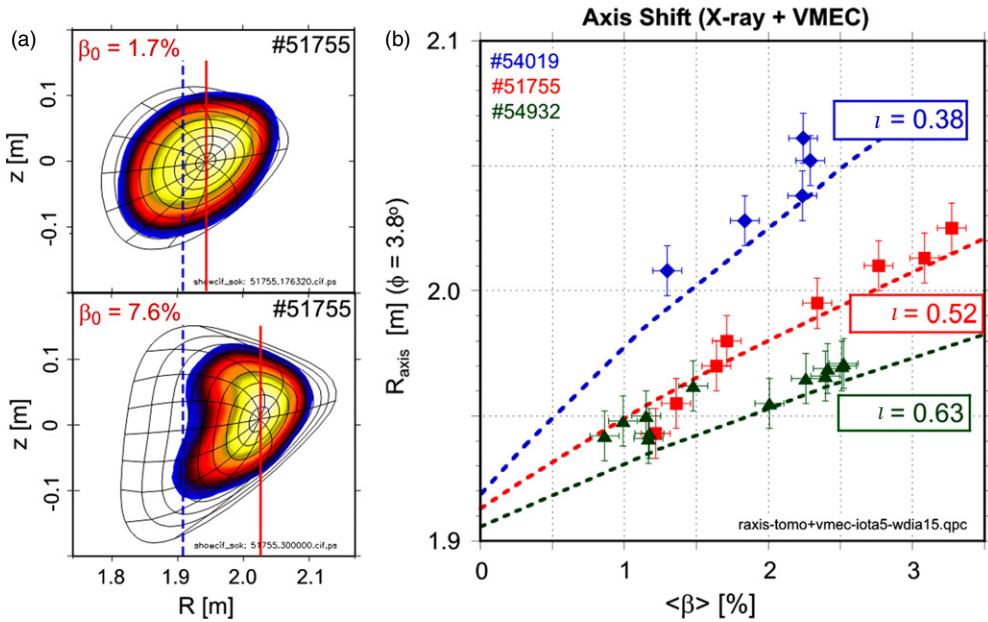


Figure 107. (a) Tomographic reconstructions of x-ray emissivity distributions referring to a configuration with $t_{ext} = 0.52$. At the maximum β of $\langle \beta \rangle \approx 3.25\%$ (bottom) the pressure induced horizontal shift is large compared with the low- β phase where $\langle \beta \rangle \approx 0.8\%$. For comparison corresponding flux surfaces according to free boundary VMEC calculations are included in the plots. The dashed and solid lines mark the locations of the magnetic axis of the vacuum and of the finite- β configurations, respectively. (b) The experimental data points represent the radial plasma axis positions as deduced from the peak position of the x-ray distributions for three configurations of different iota as a function of the volume averaged β . The dashed lines give the positions of the corresponding VMEC calculations.

by fitting VMEC calculations to tomographic and magnetic data (Zarnstorff *et al* 2005, 2004, Klose *et al* 2002, 2003, Geiger *et al* 2003).

The right part of figure 107(b) compiles the radial axis positions deduced from the peak positions in the x-ray emissivity as a function of the plasma β and on the rotational transform. The basic dependences are reflected in the experimental data as expected. The data are consistent with VMEC calculations, using standard parabolic pressure and current profiles as described above. This may give rise to errors in the calculated Shafranov shift, but within the experimental errors, the experimental pressure profiles are close to parabolic. The results concerning the horizontal plasma shift are also consistent with the magnitude of the Pfirsch–Schlüter currents as obtained from modelling the signals of the top and bottom saddle coils with the DIAGNO code which was previously also used for reconstruction of internal current densities (Anton *et al* 1999b).

Supplementary information about equilibrium properties in a wider range of the rotational transform were obtained using Ohmic current drive in co- and counter-directions changing the configuration via an increase and decrease of the total rotational transform, respectively. Additional effects are due to the current induced hoop force, which can be compensated by a vertical field. Actually, the direction of the $j \times B_z$ compensating force is opposite for co- and counter-current drive (Weller *et al* 2000).

Examples for dynamic configuration scans are given in figure 108. Here trajectories are shown representing the evolution of β as a function of the total edge transform within particular

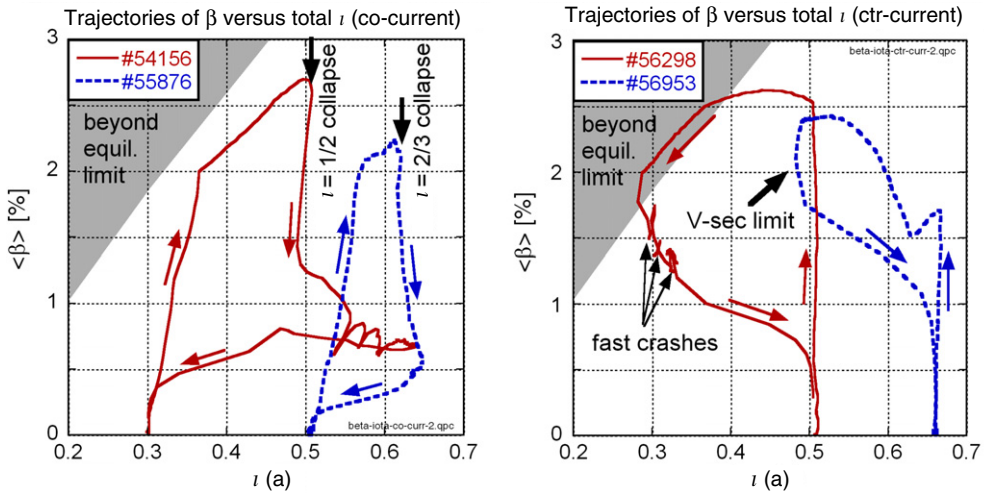


Figure 108. Evolution of β as a function of the total edge transform in discharges with significant toroidal (OH) current. Current ramps in co-direction (*a*) provoke collapses of the plasma energy induced by tearing modes at $\iota = 1/2$ and $\iota = 2/3$. The counter-current cases (*b*) appear tearing stable, but fast MHD crashes, presumably caused by resistive ballooning modes, can take place at the equilibrium boundary.

discharges, where the plasma β was ramped up followed by current ramps in both directions (co- and counter-currents leading to an increase or decrease of the total rotational transform, respectively). In each case the discharges were started with two different values of the external rotational transform. It should be noted that the profile of the rotational transform during the current ramp differs slightly from the case of a static current. However, the resistive current diffusion time is much less than the current ramp time.

During the co-current ramp, a steady increase of the plasma β is observed in the low-iota case and this is attributed to the increase of the equilibrium β -limit. The latter is inferred from the constant and close distance of the trajectory along the equilibrium limit. When the $\iota = 1/2$ surface has moved into the current gradient region, the plasma energy collapses due to the $(m, n) = (2, 1)$ tearing modes. These have been identified by x-ray tomography and magnetic probes. The current experiences only transient dips during its ramp through iota-resonances but the plasma does not recover when $\iota = 1/2$ is eventually shifted out of the plasma. In the case of higher external iota, a similar collapse is provoked presumably by the onset of the $(m, n) = (3, 2)$ tearing modes at $\iota = 2/3$.

Two examples of counter current ramp experiments are shown in the right part of the figure. The discharge starting with an external iota of $\iota_{\text{ext}} = 0.66$ is MHD quiescent up to the maximum current and is limited by the flux of the OH transformer. In the case of $\iota_{\text{ext}} = 0.52$, the trajectory is shifted close to the equilibrium limit by the decrease of the rotational transform during the current ramp. Again the energy transport adapts in such a way as to keep the trajectory at the equilibrium limit. Very frequently fast ELM-like MHD bursts are observed at the equilibrium limit, in particular at decreased temperatures and this leads to partial collapses of the plasma energy (Weller *et al.* 2005).

The discharges with counter current ramps appear to be tearing-stable even in case of crossing $\iota = 1/2$ and $\iota = 1/3$. The enhanced stability against tearing modes in these configurations with reduced normal shear or reversed shear may be partially due to neoclassical stabilization.

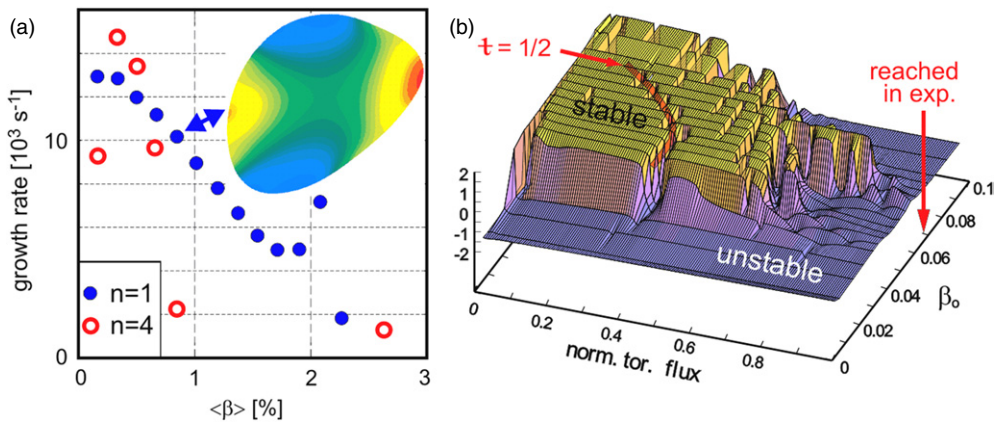


Figure 109. Stability analysis of equilibrium sequence in optimum high- β configuration (#51755, $B = 0.9 \text{ T}$, $t_{\text{ext}} = 0.52$, $\langle\beta\rangle \leq 3.3\%$). The growth rates of unstable ideal free boundary MHD perturbations, as calculated by the CAS3D global stability code, decrease with increasing β (*a*). The mode spectrum is dominated by $(m, n) = (2, 1)$, as indicated by the inset showing perturbed pressure contours. No unstable modes were found for $\langle\beta\rangle > 2.5\%$. The peak in the $n = 1$ growth rate at $\langle\beta\rangle \approx 2\%$ is due to the appearance of the rational surface $t = 5/11$ at the boundary. The local stability parameter according to the Mercier criterion (*b*) is shown as a function of β_0 (central value of parabolic β -profile) and normalized toroidal flux (radial coordinate). At low- β the configurations are Mercier unstable throughout the plasma radius. With increasing β the resonant surface $t = 1/2$ is generated and moves in radius. The stable region first expands and shrinks again beyond $\beta(0) \approx 7\%$ reached in experiment.

The achieved results are considered to verify the equilibrium properties of the magnetic configurations and hence also the effectiveness of the partial optimization in W7-AS. Although for reactor configurations a further reduction of the Shafranov shift is required, its beneficial effect of deepening the magnetic well strongly impacts the MHD stability.

10.5. MHD stability—low mode number

The general stability behaviour (in net current-free discharges) can be described by very weak MHD-activity in the high- β regime with $\langle\beta\rangle \geq 2.5\%$. Low-frequency MHD activity with poloidal mode number $m \leq 5$ is often observed for $1.5\% < \langle\beta\rangle < 2.5\%$, during the increase in β after the increase in beam power. These modes saturate without impeding access to higher- β values and do not degrade confinement in most cases.

This stability behaviour may be expected, since the relatively large vertical field required to control the plasma position in the high- β phase leads to a significant reduction of the magnetic well at low β . The increased stability in the high- β regime has to be attributed to the pressure induced deepening of the magnetic well and the increase of shear. These qualitative statements are substantiated by MHD stability code calculations that include the analysis of the local stability according to the Mercier- and resistive-interchange criteria and of the stability against pressure driven global ideal modes.

Linear ideal-MHD free-boundary stability calculations using CAS3D (Nührenberg 1999b) for a plasma with external iota of $t_{\text{ext}} = 0.52$, assuming a parabolic pressure profile, indicate that the $(m/n) = (2, 1)$ mode should be unstable for $\langle\beta\rangle < 2.5\%$ (Weller *et al.* 1998, 2003, Geiger *et al.* 2004b). Figure 109 shows the stability analysis for this case. Actually, the high- β discharges typically start in configurations, which are Mercier-unstable throughout the plasma cross-section. As β is raised, the plasma interior becomes stable but the plasma

edge remains unstable. The evaluation of the Mercier criterion was extended beyond the experimentally accessible range of $\beta(0) > 7\%$, where the stable region shrinks again. The observed MHD activity is consistent with CAS3D stability calculations. It should be noted here that the results of the numerical MHD analysis can depend on details of the pressure profiles via the equilibrium t -profiles and the local pressure gradients at rational surfaces (see figure 12 in Weller *et al* (2003)). In previous studies of high- β discharges, parabolic pressure profiles were found to be present and therefore used as model profiles (Jaenicke *et al* 1995, Kick *et al* 1996, Callaghan *et al* 1997, Geiger *et al* 2003). However, an exact reconstruction of the equilibrium with the available experimental data was not possible in most cases. Further calculations using the TERPSICHORE linear-stability code (Anderson *et al* 1990) and pressure profiles reconstructed from a STELLOPT fit have confirmed the CAS3D results. The $(m, n) = (2, 1)$ stability is affected by a steepening of the t -profile with increasing β . The calculated stability for $\langle \beta \rangle > 2.5\%$ is correlated with t moving away from $t = 1/2$ in the calculated equilibrium. Since the observed instabilities saturate and do not limit access to higher $\langle \beta \rangle$ values, the low- n ideal-MHD linear stability limit significantly underestimates the achievable β .

The dependence of the MHD stability on iota was investigated during the heating flat-top of high- β discharges. Significant MHD instabilities are observed only in very narrow regions of t_{ext} (Zarnstorff *et al* 2004). No disruptions were observed, in all cases the MHD activity saturated and the plasma continued. The two regions of stronger MHD activity correspond to $t_a = 1/2$ and $t_a = 3/5$. Under these conditions $m = 2$ and $m = 5$ modes, respectively, are found by x-ray tomography and analysis of magnetic data in consistency with the expected $(m, n) = (2, 1)$ and $(5, 3)$ mode structures (see figure 95). The flattop $\langle \beta \rangle$ varies smoothly with t_{ext} , except in the plasmas with large-amplitude MHD activity, which could be easily controlled by small changes in the external coil currents. Particularly large $(2, 1)$ modes were correlated with intermediate β and relatively flat t -profiles close to $t_a = 0.5$ (Weller *et al* 2003). In this case large island formation was indicated by mode locking, presumably due to the $(2, 1)$ error field of W7-AS (Jaenicke *et al* 1993).

10.6. MHD stability—high mode number

The high- β plasmas discussed so far are calculated to be stable to high- n ballooning instabilities using the COBRA code (Sanchez R *et al* 2000). For the bulk of the plasma profile, no nearby stability thresholds were found, thus ballooning modes are not expected to limit the plasma β . Direct experimental evidence of high mode-number instabilities could not be found. However, in cases of comparably low electron temperature effects due to resistive interchange/ballooning instabilities are indicated.

Actually, fast MHD bursts causing a rapid decay of the plasma energy (within $\approx 100 \mu s$) are occasionally observed, which are likely due to resistive interchange or ballooning modes. However, they typically do not occur in configurations optimized for high β . Such instabilities can almost precisely be provoked in discharges during reversed current ramp experiments. Under these conditions the discharges can be started with relatively high plasma β . These β -values may be in excess of values compatible with the equilibrium limit as the rotational transform is reduced in the ramp. The instability is not considered to be driven by the toroidal current itself but via the decrease of iota, which causes a local steepening of the pressure gradient at the outboard side due to the higher Shafranov shift. Similar crashes are also seen in currentless plasmas, preferentially in configurations with low rotational transform. The crashes occur typically in phases of decaying temperatures, reaching central values of ≈ 0.2 keV. The observations are consistent with a scaling of the linear growth rates for resistive ballooning

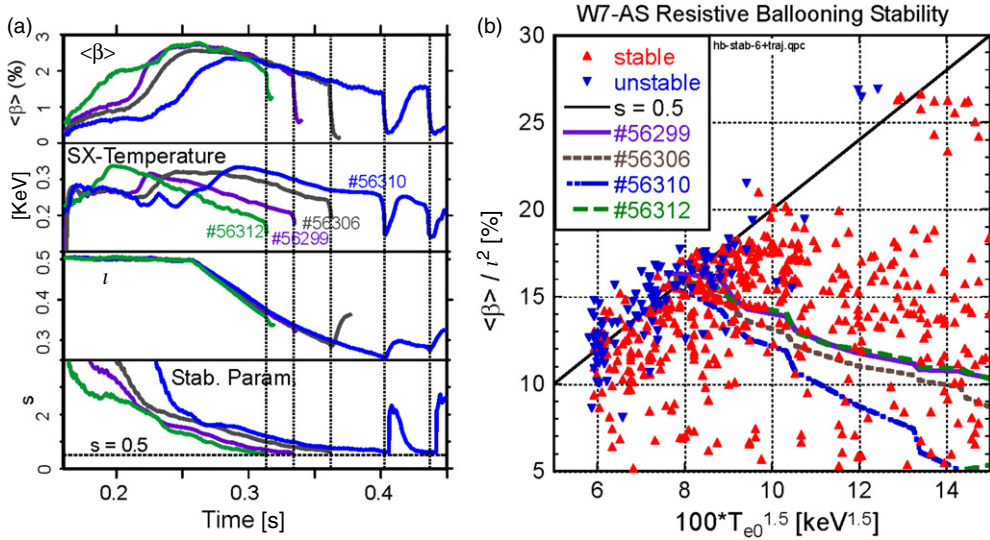


Figure 110. Partial thermal crashes induced by fast (50–200 μ s) MHD events. The left part (a) shows discharges of a magnetic field scan (1.05–1.65 T), in which a reverse ramp of the edge rotational transform was generated by inductive current drive during the density plateau. The crashes occur, when the parameter $s \equiv 100(t^2/\langle\beta\rangle) \cdot T_e^{3/2}$ (bottom) has decreased to $s \approx 0.5$ ($\langle\beta\rangle$ in %, T_e in keV). In the right part (b) volume averaged β -values normalized to t^2 from a database of 57 shots are plotted versus a conductivity parameter ($\sim T_e^{3/2}$). The parameters just prior to MHD crashes (solid triangles) are close to the value $s = 0.5$ represented by the dotted line. The solid lines are the trajectories of the discharges shown on the left.

(Miyamoto 1980, Zehrfeld and Geiger 1997) or interchange modes

$$\gamma \approx (\langle\beta\rangle/\langle\beta\rangle_c)\eta k^2/\mu_0 \propto (\langle\beta\rangle/t^2)T_e^{-3/2},$$

where $\langle\beta\rangle_c \propto t^2$ is the ideal ballooning limit which roughly coincides with the equilibrium β -limit. The linear dependence of γ on η results from the so-called resistive pressure convection limit model with the additional conditions of low growth rates and sufficiently low resistivity (Bateman and Nelson 1978, Kaiser 1993, Sanchez *et al* 1997). The database analysis is presented in figure 110(b). By using $\langle\beta\rangle$ from diamagnetic energy, $t \approx t_{\text{ext}}$ and $T_e = T_e(0)$ from x-ray analysis (example of time traces are shown in figure 110(a)), a critical stability parameter $s \approx 0.5$ was found (Weller *et al* 2005, 2006), where s is defined by $s \equiv 100(t^2/\langle\beta\rangle) \cdot T_e^{3/2}$ ($\langle\beta\rangle$ in %, T_e in keV). The characteristics of the instability are very similar to large edge localized modes (ELMs).

The explanation of the fast crashes in terms of ballooning modes is further supported by experimental results obtained in configurations of different modular magnetic field ripple, adjusted by I_5/I_m . The ballooning stability in these configurations is different due to the change of the curvature, local shear and connection lengths between good and bad curvature regions. Figure 111 shows pronounced bifurcations of the plasma β (left), which are controlled by the presence of strong ELM-like bursts and depend on the magnitude of the field ripple. This behaviour is qualitatively consistent with the stability diagram shown on the right. Here, stability boundaries of ideal ballooning modes are calculated by the COBRA code as a function of the coil current ratio I_5/I_m . The calculations were based on free-boundary VMEC equilibria assuming parabolic pressure profiles. The field line integration was truncated after 7 periods, which emphasizes medium- n modes. In the two stable regions corresponding to 1st and 2nd

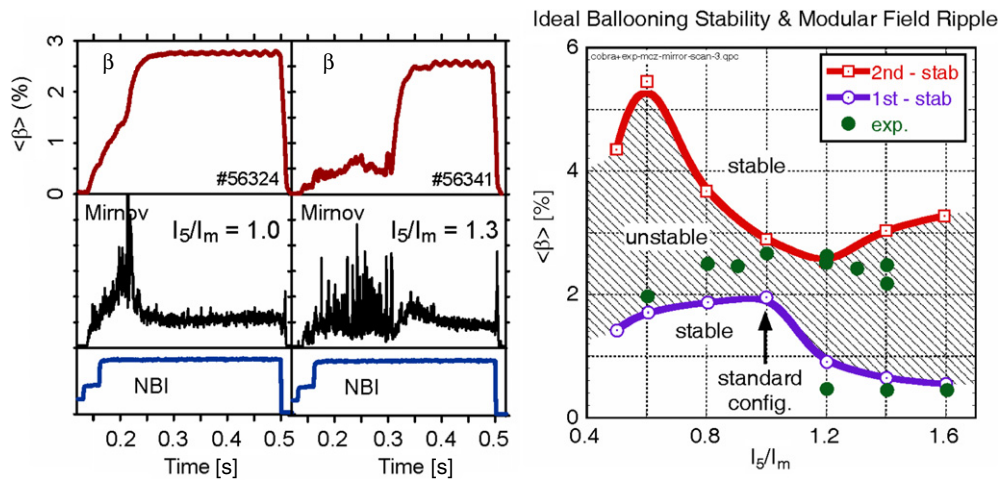


Figure 111. Characteristics of high- β discharges in configurations with different mirror ratio corresponding to $I_5/I_m = 1.0$ (standard case) and 1.3. The plasma β shows a bifurcation depending on the modular field ripple in correlation with strong MHD activity consisting of fast ELM-like bursts (left). The bifurcations appear to be correlated with the widening of the unstable gap between the 1st and 2nd stability boundaries as predicted by the ideal ballooning stability code COBRA for configurations with different modular field ripple adjusted by I_5/I_m (right).

stability all surfaces have been found to be stable. In particular, the bifurcated β -values at $I_5/I_m > 1$ are close to the 1st and 2nd stability boundaries. The standard case with $I_5/I_m = 1$ appears to be most stable, as indicated by the small gap between the 1st and 2nd stability regions.

The linear stability calculations of the ideal localized ballooning mode by COBRA indicate that the high β -phase appears to be in the second-stability regime. In order to understand how the second-stable regime was accessed, the analysis technique of Hudson and Hegna (2003) was used to evaluate local stability diagrams for a sequence of free-boundary equilibria with increasing β . It appears that the plasma can access this region along a stable trajectory, due to an increase of shear with plasma pressure and a deformation of the stability boundary. Figure 112 shows stability diagrams for two β values and for different surfaces.

10.7. Discussion

The volume averaged plasma β could significantly be raised to values in excess of 3% in configurations with edge islands being suppressed by using the divertor control coils. Another important achievement is quasi-stationary plasma operation compatible with the maximum β and good confinement properties up to the maximum β -values. The energy confinement remains clearly above the ISS95 scaling. The particle confinement in the high- β , high-density regime is only about twice the energy confinement time and therefore discharges with density control and low impurity radiation losses can be established. Even though less pronounced, the confinement properties exhibit all the features of the HDH mode found first in island bounded divertor configurations.

The limitation of the plasma β in W7-AS depends on the equilibrium properties of the configurations. In the optimum case with the external rotational transform in the vicinity of $t = 1/2$, the achievable β is solely limited by the available heating power. Towards low-iota

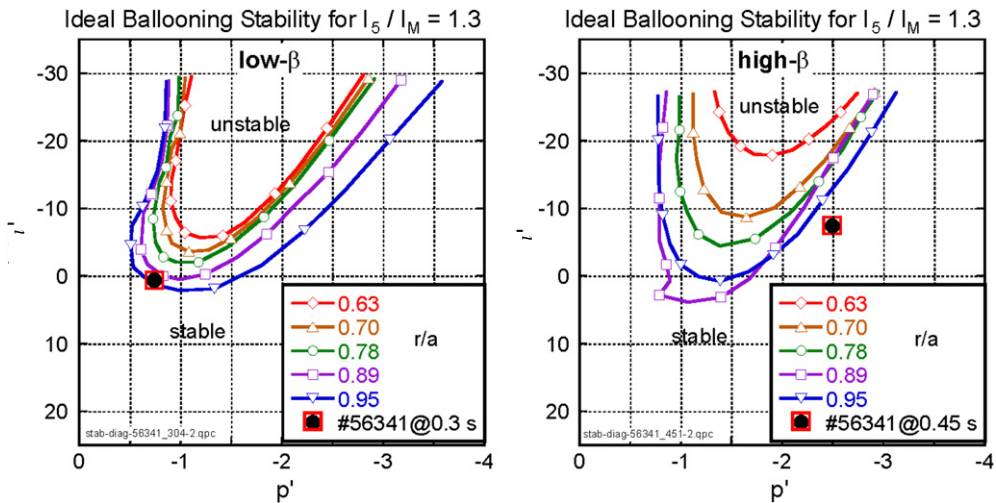


Figure 112. Marginal stability diagrams of high- n ballooning modes obtained by a 3D equilibrium perturbation method (Hegna, Hudson). The different contours represent stability boundaries for different surfaces in the range $r/a = 0.63, 0.95$. The two diagrams refer to the case of bifurcated equilibria (enhanced ripple configuration with $I_5/I_m = 1.3$) shown in figure 111. The large symbol marks the gradients of the initial equilibrium profiles. The low- β equilibrium (left) is kept close to the 1st stability boundary at the edge, whereas second stability is reached in the high- β phase (right).

configurations the maximum β is progressively reduced to an equilibrium β -limit, which is determined by a critical value of the Shafranov shift and strongly depends on iota. The adjustment of β at the equilibrium limit is taking place by a loss of flux surfaces at the edge and enhanced transport, involving neither MHD instabilities nor disruptive processes in most cases.

An important result of the high- β experiments is that the magnitude of the observed Shafranov shift as well as its dependence on the rotational transform is consistent with predictions for W7-AS. Hence, the partial optimization of the equilibrium in W7-AS by reducing the Pfirsch–Schlüter currents could be corroborated by experimental data.

Concerning the MHD stability, the most important result is that pressure driven MHD instabilities neither play a role in the range of highest- β nor cause any limitation of the plasma pressure.

The experience with toroidal currents in W7-AS shows that, in fact, rotational transform due to the plasma current can be used to establish configurations with different rotational transform. However, additional operational limits are introduced by current driven MHD modes causing thermal collapses, in particular at $t = 1/2$.

11. Summary and conclusions

The Wendelstein stellarator line has been developed as a low-shear concept, employing helical windings for the initial devices. W7-AS for the first time used modular coils which are necessary to ultimately overcome the technical limitations of helical coil systems in large stellarators. The successful operation of W7-AS proved that 3D magnetic field configurations with flux surfaces of high quality can be produced by modular field coils. Thus this concept provides the technical flexibility for building optimized stellarators.

Wendelstein 7-AS was the first step to test some of the basic elements of stellarator optimization and it showed that essential optimization criteria can be met simultaneously:

- An improved equilibrium with reduced Shafranov shift and improved stability properties resulted in β -values up to 3.4% (at 0.9 T). The magnitude of the observed Shafranov shift as well as its dependence on the rotational transform is consistent with predictions.
- The reduction of neoclassical transport in the plateau regime could be verified in good agreement with calculations confirming the reliability of neoclassical predictions and the concept of drift optimization.
- The bootstrap current was still ‘tokamak-like’ in W7-AS. No design effort has been made to reduce it by further optimization, but the results agree well with the expectations giving confidence in the desired minimization of the bootstrap current in W7-X.

11.1. Main results

The maximal parameters which have been achieved with W7-AS (in different discharges) are given below. They exceeded, in several cases even substantially, the predictions which were obtained on the basis of preceding classical stellarator devices:

$T_e(0) = 6.8 \text{ keV}$	$B_0 = 2.5 \text{ T}; t_a = 0.34; \bar{n}_e = 2 \times 10^{19} \text{ m}^{-3}; P_{\text{ECRH}} = 2 \text{ MW}$ electron-root (see section 5.3.1)
$T_i(0) = 1.7 \text{ keV}$	$B_0 = 2.5 \text{ T}; t_a = 0.52; \bar{n}_e = 5 \times 10^{19} \text{ m}^{-3}; P_{\text{ECRH}} = 0.5 \text{ MW}; P_{\text{NBI}} = 1.3 \text{ MW}$ ion-root; OC-regime, (see section 5.3.2)
$\bar{n}_e = 4 \times 10^{20} \text{ m}^{-3}$	$B_0 = 2.5 \text{ T}; t_a = 0.55; P_{\text{NBI}} = 2.8 \text{ MW}; T_e = 0.35 \text{ keV}$ HDH-mode (see section 7.6)
$\langle \beta \rangle = 3.4\%$	$B_0 = 0.9 \text{ T}; t_a = 0.5; \bar{n}_e = 2 \times 10^{20} \text{ m}^{-3}; P_{\text{NBI}} = 2.8 \text{ MW}$ HDH-mode (see section 10.3)
$\tau_E = 0.06 \text{ s}$	$B_0 = 2.5 \text{ T}; t_a = 0.345; \bar{n}_e = 1.1 \times 10^{20} \text{ m}^{-3}; P_{\text{NBI}} = 0.33 \text{ MW}$ OC-regime (see section 5.3.2)
$\bar{n} \cdot \tau_E \cdot T_i = 5 \times 10^{21} \text{ eV s m}^{-3}$	$B_0 = 2.5 \text{ T}; t_a = 0.345; \bar{n}_e = 1.1 \times 10^{20} \text{ m}^{-3}; P_{\text{NBI}} = 0.33 \text{ MW}$ OC-regime (see section 5.3.2)

The Ohmic transformer and the electron cyclotron current drive (ECCD) system allowed compensation of pressure driven currents as well as configuration control by driving positive and negative currents for realizing configurations with different rotational transform, and different magnetic shear.

A pronounced dependence of confinement on the rotational transform t exists, as generally observed in low-shear devices. At the maxima, confinement time is generally found to be above the international stellarator confinement scaling (ISS95) by about a factor of 1.5 to 2. With positive or negative shear, as induced by internal currents, the energy content loses its t -dependence and the confinement levels off at the t -maxima. Similar to the other helical devices the energy confinement time exhibits a positive density and negative power scaling close to ion-plateau transport (Lackner–Gottardi scaling) over a wide range of operational parameters up to high-density-H-mode (HDH) scenarios. At sufficiently high temperatures the plasma core is dominated by stellarator specific neoclassical transport both for ions and electrons; edge transport is generally governed by anomalous fluxes. The radial electric field plays a key role in setting the actual flux levels both in the core and at the edge. To a good approximation it is in agreement with the ambipolarity condition of the neoclassical fluxes.

For a wide range of P/n , neoclassical transport occurs at the level of the ion-root of the ambipolarity condition. The electron-root developed in the plasma core at low to medium densities with high T_e/T_i giving rise to peaked T_e -profiles with steep inner gradients.

The scaling of the particle diffusion (positive with heating power, negative with magnetic field and density) points to identical particle transport mechanisms in the density gradient region and in the SOL. Density control at low and medium density is achieved by ECRH (at a power level exceeding that of simultaneous NBI) resulting in peaked temperature profiles that give rise to degradation of particle confinement by thermodiffusion. At high densities and pure NBI heating density control is achieved in the HDH regime. No hard density limit is observed, instead the maximum attainable density is determined by impurity radiation and the available heating power only.

With separatrix, the H-mode could be realized with and without ELMs. The power threshold for a quiescent H-mode was found to be distinctively lower than predicted from tokamak scaling. ELMy H-modes exist with the capabilities of ELM mitigation by the choice of the edge configuration. Optimum Confinement conditions (with superior values of T_i , τ_E and $n_e \cdot \tau_E \cdot T_i$) are reached in a regime which develops on a transport timescale without a distinct transition, with narrow density and broad T_i -profiles and with a layer of strongly negative E_r at the edge. As in tokamaks, enhanced impurity confinement and low separatrix densities which are not favourable for divertor operation rule out both the optimum confinement (OC) regime and the quiescent H-mode as base-line scenarios towards high-confinement, steady-state operation. Thus, the discovery of the high density H-mode (HDH) on W7-AS was vitally important, as it combines superior energy- and low impurity confinement with high edge densities necessary for successful divertor operation. As a high-density regime not accessible in most tokamak devices (except C-MOD at twice the B -field), it has demonstrated that quasi-steady-state, high-density, high-confinement and robust high-power operation under ELM-free conditions is feasible over a wide range of divertor-compatible scenarios. The physics understanding of the HDH regime is at a phenomenological level only. The dominant attribute of impurity flushing at the transition to HDH may be modelled by postulating enhanced impurity diffusion in the gradient region where E_r is negative, but there is no doubtless understanding as to what this mechanism might be. In HDH a quasi-coherent mode activity with a density dependent frequency can occur at the plasma edge. Its presence is correlated with a reduction of impurity radiation; however, a causal relation between mode activity and enhanced impurity diffusion is not yet clear. Consequently, it is not possible at present to extrapolate the HDH regime to other devices.

Quasi-stationary discharges with β -values in excess of 3% were possible with good confinement properties. In the optimum case with the external rotational transform in the vicinity of $\iota = 1/2$, the achievable β is solely limited by the available heating power. Plasma performance and confinement quality do not noticeably degrade close to this (power determined) β -limitation although some degree of stochasticization of the outer flux surfaces increasing with β is indicated by equilibrium modelling. Towards configurations with lower ι the maximum attainable β is progressively reduced according to the equilibrium β -limit, which is determined by a critical value of the Shafranov shift and strongly depends on ι . The energy confinement remains clearly above the ISS95 scaling up to the maximum β values. The particle confinement is only about twice the energy confinement time and therefore discharges with density control and low impurity radiation losses could be established with characteristics attributed to HDH plasmas.

Stability studies do not show fast disruptive instabilities even close to operational limits but rather slow transitions to increased transport. Pressure driven MHD neither plays a role in the range of highest- β nor causes any limitation on the pressure gradient. The

local ideal MHD stability tends to underestimate the stability found in W7-AS (similarly as in the large helical device, LHD). Nevertheless, the linearized ideal MHD analysis still provides a useful reference: the observed pressure driven mode activity is mostly correlated with the predicted unstable regions whereas relevant MHD modes are absent if Mercier stability is ensured. Not surprisingly, additional operational limits arise if sufficiently high current gradients are introduced by the OH-transformer, by ECCD or by NBCD resulting in current-driven MHD that causes thermal collapses, in particular at $t = 1/2$. However, in the standard scenario with low shear at the plasma edge current-driven MHD can be prevented. Alfvén modes excited by fast resonant particles represent the most prominent instabilities observed in a wide parameter range. Stellarator field harmonics (helical or mirror components) cause a new variety of continuum gaps, global modes (HAE, MAE) and particle-wave resonances.

For the first time in a helical system, a modular island divertor was tested, with applicability to W7-X, conceptionally even to a stellarator reactor. The outstanding result of the divertor experiments was that the chain of natural boundary magnetic islands intersected by targets provides favourable operational conditions: there is strong radiation from the edge; a finite density range exists with stable partial detachment and adequately reduced power load on the targets and a considerable neutral compression is achieved in the sub-divertor region. Divertor operation leads to exceedingly high densities ($4 \times 10^{20} \text{ m}^{-3}$) well above the Greenwald limit of an equivalent tokamak. The observed tendencies including the major features of the detachment phenomenology are qualitatively described by the 3D edge code EMC3-EIRENE. Most of the specific features of the island divertor are consequences of a considerable contribution of cross-field transport within the SOL due to the small field line pitch inside the islands. Under high-density, low-temperature (HDH) conditions, a strong retention effect on the target-released carbon impurities results from the dominant outward-directed friction force which reflects the reduction of the parallel ion heat conductive transport in favour of the cross-field transport. The observed ‘partial’ character of stable detachment is attributed to the stabilizing effect of a hotter region at the upstream low-field sides of the elliptic cross-section planes where enhanced cross-field energy transport occurs due to radially more compressed flux surfaces and islands. EMC3-EIRENE is now used as a standard 3D code for helical systems and 3D problems in tokamaks (ITER, TEXTOR-DED).

11.2. W7-AS relevance for W7-X

The W7-X device presently under construction in Greifswald, Mecklenburg-Vorpommern, Germany, is expected to demonstrate that the low-shear, low-current concept of the Wendelstein line is able to confine a reactor grade plasma under stationary conditions. This demands superconducting coils. The lack of impurity accumulation up to $t_{\text{flatop}}/\tau_E \approx 100$ and a ratio τ_p/τ_E as low as 2—both shown in the HDH mode at W7-AS—give excellent prospects for this goal.

W7-X is a fully optimized stellarator founded on the theoretical progress achieved during the period of W7-AS operation. It was discovered that acceptable drift-orbit confinement, allowing low neoclassical transport losses and adequate fast-ion confinement, does not necessarily rely on axis-symmetry as in an ideal tokamak. In magnetic Boozer coordinates particle drifts depend on the *magnitude* of the magnetic field strength $|B|$ only (Boozer 1980). Good drift orbit confinement and adequate fast ion confinement can thus also be achieved in configurations with symmetry only pertaining to $|B|$ on the flux surfaces (Nührenberg and Zille 1988). In a torus quasi-symmetry cannot be exact (Garren and Boozer 1991) but can be realized to such an extent that the orbits of the

trapped particles drift continuously in the low- B minima such that neoclassical transport in the $1/\nu$ -regime becomes negligible (Nührenberg *et al* 1994). For an overview see Nührenberg (2006), Wobig (1999). Three lines emerged:

In quasi-helical symmetry (Nührenberg and Zille 1988, Lotz *et al* 1992) the reflected particles drift helically and the pitch of $|B| = \text{const.}$ is *larger* than the pitch of the field lines such that a considerable bootstrap current occurs in the direction which *reduces* the rotational transform. To compensate the reduction of t the poloidal field supplied by the external field coils must be increased, e.g., by a stronger shaping of the modular coils. The basic properties of this concept are currently tested in the Helical Symmetric Experiment (HSX) at the University of Wisconsin (Canik *et al* 2007).

In quasi-axisymmetry (Nührenberg *et al* 1994) the reflected particles drift toroidally and the pitch of $|B| = \text{const.}$ is *smaller* than the field line pitch driving a bootstrap current which *increases* the rotational transform as in a tokamak. The decisive question is to what extent associated current driven instabilities are stabilized by the external stellarator field components. A first realization, the quasi-axisymmetric National Compact Stellarator Experiment (NCSX), is under construction at Princeton (Zarnstorff *et al* 2001).

Continuous symmetry provides large bootstrap currents and thus large amounts of free energy. In contrast the concept of the Wendelstein stellarators aims at minimizing the free energy by minimizing parallel currents. This can be realized using quasi-isodynamicity (Gori *et al* 1996) which relies on the poloidal closure of contours of the second adiabatic invariant J by minimizing the *poloidal* variation of $|B|$. This reduces the radial component of the ∇B -drift and minimizes the Pfirsch–Schlüter and bootstrap currents (Wobig 1999). For poloidally closed contours of $|B|$ an ideal MHD equilibrium without net toroidal current and J a function of flux only for all reflected particles has *vanishing bootstrap current* in the $lmfp$ -regime (Subbotin *et al* 2006). Thus the free energy can be minimized and the optimized field structure becomes largely independent of β , thus opening it up for satisfying further criteria.

The W7-X device (Beidler *et al* 1990, Griege *et al* 1992) is the realization of such an integrated optimization concept, the HELIAS (HELIcally Advanced Stellarator) (Nührenberg and Zille 1986). Like its predecessor W7-AS it has a 5-fold rotational symmetry. The magnetic field is increased at the corners of the pentagon to localize reflected particles to the straight sectors where their orbits drift poloidally at finite β . As this review has shown, the results of W7-AS allow a high degree of confidence in the validity of this design, in particular

- that high-quality vacuum-field magnetic surfaces (regular boundary, avoidance of low-order resonances, adjustment of shear, sufficiently small internal islands) can be achieved with modular coils.
- that the Pfirsch–Schlüter currents $\langle j_{||}^2/j_{\perp}^2 \rangle$ can be reduced yielding improved equilibrium and stability. For W7-X this gives confidence to meet the expected good finite- β equilibrium properties with small Shafranov shift and good MHD stability with respect to local resistive interchange and ideal ballooning modes for β -values up to 5%.
- that neoclassical transport of the core plasma is well understood with predictable results including special features such as the development of the electron root. As core transport in the $lmfp$ -regime is limited by neoclassical losses, W7-X should outperform W7-AS in core transport owing to its more advanced neoclassical optimization, $\varepsilon_{\text{eff}} < 0.02$, resulting in diffusion coefficients a factor 3 to 6 below W7-AS. Moreover, an improved collisionless α -containment with lost energy fraction of a few percent only is expected due to the quasi-isodynamicity at operational values of β .
- that the bootstrap current can well be described by neoclassic theory, giving confidence in its minimization in W7-X.

Beyond its contribution to this optimization concept, W7-AS addressed topics necessary for W7-X to be operated as a high-performance steady-state experiment:

W7-X will be equipped with a steady-state capable island divertor based on the 4/5, 5/5 or 6/5 edge island chains and comprising 10 modules in the 5 field periods. W7-AS has demonstrated its rather promising potential. As in the low-shear device large boundary islands can be introduced by relatively small superimposed resonant fields, their structure is very sensitive to perturbations by plasma currents and/or error fields. W7-AS showed that the SOL scenarios, and hence divertor performance, are considerably influenced by details of the edge magnetic field configuration. W7-X in its standard configuration with $\tau = 5/5$ has to cope with these critical elements of the low-shear concept under conditions where the 5 diverting islands are separated such that field asymmetries cannot be balanced due to interlinked island structures and the danger of asymmetric heat-load exists. Therefore the exact knowledge and control of the actual equilibrium edge configuration are essential.

For this purpose W7-AS developed heating and EC-based current drive scenarios with promising results. If necessary this will be applied to W7-X for configuration control, e.g. to compensate excess bootstrap currents during dynamic phases (start-up) and for stable divertor operation. A particularly important contribution from W7-AS was the successful exploration of mode-conversion electron cyclotron heating and current drive schemes which allow operation at divertor relevant densities in excess of the ECRH X2 cut-off ($n_{e,\text{crit}} = 1.2 \times 10^{20} \text{ m}^{-3}$ for 140 GHz).

Increased losses of resonant particles may be caused by the excitation of Alfvén Eigenmodes. The analysis of the different classes of fast particle driven Alfvén modes in W7-AS and their effect on the fast particle confinement provide a good basis to assess the role of Alfvén instabilities in W7-X and beyond in a Helias type reactor. The high-density, low-temperature path to fusion as provided by HDH confinement would lead to comparably low fast ion populations and reduced drive. The relatively large non-axisymmetric field components in W7-X may help to stabilize certain Alfvén modes by increased continuum damping but also cause very wide gaps in the continuous Alfvén spectrum with a variety of weakly damped global modes.

With respect to turbulent transport a fundamental issue is the effect of drift-optimization on anomalous fluxes: most of the discussed mechanisms for exciting anomalous transport (stochasticity in vacuum and finite- β fields, trapped orbits, instabilities such as ballooning, tearing and trapped-particle drift modes) are reduced substantially. Moreover, a stellarator can operate at comparably high densities, where the anomalous electron heat transport is found to be reduced. W7-X will explore these turbulent transport properties which promise to yield optimum core conditions for fusion-based power stations.

The reduction of the geodesic curvature as a design quantity for isodynamicity is also expected to provide favourably low damping for zonal flows and a strong coupling between edge turbulence and zonal flows which could ease access to the H-mode (provided this mechanism is causing it). A satisfying explanation for the narrow H-mode windows in W7-AS is still missing, however, neoclassical plateau viscosity, which at low radial electric field exhibits a strong dependence on the rotational transform, may be a key element. If neoclassical viscosity is the reason for the H-mode windows, this effect should also occur in the neighbourhood of $\tau = 1$, where W7-X will operate.

Critical for high-density steady-state operation are the impurity transport properties with the danger of impurity accumulation. One of the most exciting questions will be whether for W7-X purification of the core is possible, e.g. by reaching the HDH mode. Not much is known about the scaling of the operational boundary of this regime but it could be that it can be accessed only after an upgrade of the heating power (with Stage II heating).

The experience gained with W7-AS is restricted to $t < 0.6$. W7-X will operate at $t = 1$. The increase in t has advantages; the operation close to $t = 1$ also bears risks. To identify the optimum operational point needs guidance by the experiment.

11.3. Prospects for the Helias reactor

The Helias reactor is the straightforward extrapolation of the Wendelstein 7-X device into the fusion regime (Wobig 1993, Beidler *et al* 2001, Wobig *et al* 2003). Although the step from Wendelstein 7-AS to a stellarator reactor is rather large, some conclusions concerning reactor prospects can be drawn.

The fusion power output of a Helias reactor with 3–3.5 GW, at a given magnetic field of about 5 T, leads to a plasma β of 4–5%. This implies an optimization of the MHD-equilibrium towards a reduced Shafranov shift. The latter also prevents a strong peaking of the neutron wall load at the low-field side and thus extends the lifetime of the first wall. As W7-AS equilibrium and equilibrium theory agree rather well and, since β is the only equilibrium scaling parameter, an extrapolation towards the reactor regime with $\beta = 4\text{--}5\%$ is justified. The same argument also applies to MHD-stability. In view of quiescent and reliable reactor operation, the most important result of W7-AS is the attainment of maximum β without violent MHD or disruptions.

Since a magnetic field of 5 T appears sufficient the conservative approach to use the well developed NbTi technology is also envisaged for the Helias reactor rather than the Nb₃Sn-based technology with their demanding processing of the superconductor. Manufacturing of large NbTi based superconducting modular coils under industrial series production has been demonstrated by W7-X. A non-planar test coil operating at 11 T resulting in about 5 T inside the plasma has been built and successfully tested at the FZK (Heller *et al* 2000). If the Nb₃Sn technology became feasible in the future it could be used with additional advantage by stellarators also.

From $\beta = 4\text{--}5\%$ and moderate $T_e \leqslant 15$ keV to minimize radiation losses and EC emission the average density in a Helias reactor will be about $2 \times 10^{20} \text{ m}^{-3}$, which has been clearly surpassed in W7-AS. Thus safe high density operation seems to be feasible. The high densities increase energy confinement and ensure ion-root operation with $T_e \approx T_i$ at minimum β_e . However, the radiative high density limit depends on the impurity species, and in a fusion reactor metal impurities must be expected, while in present experiments carbon and oxygen are the dominating species. Assessing the criticality of impurities, one should be aware that the heating power in a reactor grows with density, in contrast to present experimental devices, where the heating power is limited.

With divertor at HDH mode conditions a transition to partly detached plasmas became possible, resulting in a strong reduction of the heat load onto the divertor target plates. If in a fusion reactor only 50% of the alpha-heating power (about 300 MW) is deposited onto the target plates, this requires about 30–60 m² wetted area. Therefore, the short lifetime of the target plates presents a critical issue for the availability and the economic efficiency of a reactor. Detached operation would remove this burden from the target plates and distribute the power more evenly on the first wall via radiation. In a Helias reactor the first wall area is as large as about 2000 m². Thus the power load to the first wall is less demanding than in more compact devices.

Extrapolation of W7-AS scaling laws satisfies the ignition criteria in a Helias reactor. High density, high magnetic field and high rotational transform favour ignition. The increase of confinement with rotational transform has been confirmed by W7-AS and TJ-II; the rotational transform in a Helias reactor is larger by a factor two than in W7-AS, however. Therefore, the

extrapolation is uncertain. W7-X will operate at reactor iota and thus close this gap. As the H-mode confinement has not been considered the extrapolation is conservative.

11.4. Concluding remarks

W7-AS has contributed to further establish the Wendelstein stellarator line as an independent route to a fusion reactor by the following results: (1) steady-state operation has been demonstrated with long pulses ($t_{\text{flattop}}/\tau_E \approx 110$) under demanding conditions ($\beta = 3.4\%$, $\beta_N = 9.3$, $H_{\text{ISS95}} = 1.4$, $n_e/n_{GW} \approx 2.5$, $\tau_p/\tau_E = 2$) and (2) no current-driven instabilities were observed close to operational boundaries. Of high operational value are the slow timescales of the plasma decay at the density- and β -limits.

Both the equilibrium- and the stability β values were strongly improved over those of classical stellarators and it has been shown that stellarator optimization allows these deficiencies of the basic concept to be removed. The neoclassical part of energy transport in W7-AS was found to be reduced by the elongation of the flux surfaces and beyond this by the neoclassical impact of the radial electric field. The anomalous edge transport was reduced by the H-mode, observed for the first time in a ‘non-tokamak’. The impurity accumulation was found to be overcome in the HDH-mode.

The work with W7-AS has contributed to the understanding of toroidal confinement in stellarators and its complementary characteristics have helped to better understand also the tokamak. This applies to the differences in field structure, e.g. low global shear or strong toroidal viscosity, to features of the H-mode, e.g. the existence of iota-windows or the role of the neoclassical electric field at the plasma edge, to the spectrum of Alfvén-waves under strong shaping, to the bootstrap current, which can be much more easily measured without an inductive background, to the boundary-layer and divertor physics with 3D effects, e.g. with local limiters or ergodic boundary layers at the tokamak edge, to the physics of operational limits—those subject to MHD and those to power balance. This list could be extended.

W7-AS has stopped operation mid-2002. The continuation of the experimental stellarator work of IPP is expected by 2014. This gap reflects the step from a laboratory-based experiment, W7-AS, to the superconducting steady-state system W7-X, with fabrication and assembly complexity and the challenge of high-performance operation demanding for completely actively cooled first wall, divertor and in-vessel components. Fusion power plants have to operate steady-state, which is demanded by material aspects, by their large power to the grid and possibly by competitive considerations with regard to the next generation of fission reactors (Generation IV). The choices in fusion are either 3D systems with increased mechanical complexity but benign operational characteristics or 2D systems with higher operational complexity. The performance of W7-AS has shown that optimized stellarators are an option with high potential in the integrated development of fusion power.

Acknowledgments

Many scientists have contributed to the scientific and technological work done with and at W7-AS. A large number of guests from other laboratories and universities as well as PhD and graduate students stimulated discussions and thus the progress of research. The authors wish to acknowledge the outstanding contributions from H Renner, the first project head of W7-AS, and from other colleagues meanwhile in retirement. The complexity of W7-AS necessitated excellent technical teams for the operation of the basic device, for control and data acquisition, and for plasma heating. As representative of many others we wish to acknowledge D Dorst, the head of the technical staff, J Böhmerl, F Hoffmann, J Sapper and G Zangl representing the

operation team, H Kroiss, and J Saffert, representing the data acquisition team. The W7-AS Team also gratefully acknowledges excellent support from the workshops and the central technical services as well as from the administrative staff and secretaries.

References

- Akiyama T *et al* 2005 *32nd EPS Conf. on Controlled Fusion and Plasma Physics (Tarragona, Spain)* (ECA) P-2.070
- Alejaldre C *et al* 2002 *Proc. 19th IAEA Conf. on Fusion Energy (Lyon, France)* OV/4-4
- Alikaev V V *et al* 1984 *Proc. 10th Int. Conf. on Plasma Physics and Controlled Nuclear Fusion Research (London, UK)* p 419
- Anderson D V *et al* 1990 *Int. J. Supercomput. Appl.* **4** 34–47
- Anton M *et al* 1997 *24th EPS Conf. on Controlled Fusion and Plasma Physics (Berchtesgaden, Germany)* pp 1645–8
- Anton M *et al* 1998 *J. Plasma Fusion Res. Ser.* **1** 259–62
- Anton M *et al* 1999a *12th Int. Stellarator Workshop (Madison, WI)* <http://www-fusion.ciemat.es/cgi-bin/sw05/dir.cgi?conferences/madison99/Papers/>
- Anton M *et al* 1999b *Proc. 26th EPS Conf. on Controlled Fusion and Plasma Physics (Maastricht, The Netherlands)* pp 1461–4
- Bakhareva O A *et al* 2005 *Plasma Phys. Rep.* **31** 282–91
- Balbín R *et al* 1992 *EPS Proc. Int. Conf. on Plasma Physics (Innsbruck, Austria)* pp 783–6
- Baldzuhn J and Sandmann W 1993 *Plasma Phys. Control. Fusion* **35** 1413–31
- Baldzuhn J *et al* 1995 *Stellarator Workshop (Madrid, Spain)*
- Baldzuhn J *et al* 1997a *Proc. 24th EPS Conf. (Berchtesgaden, Germany)* pp 1585–8
- Baldzuhn J *et al* 1997b *Rev. Sci. Instrum.* **68** 1020–3
- Baldzuhn J 1998 *Proc. 25th EPS Conf. (Praha, Czech Republic)* pp 403–6
- Baldzuhn J *et al* 1998a *J. Plasma Fusion Res.* **1** 226–9
- Baldzuhn J *et al* 1998b *Plasma Phys. Control. Fusion* **40** 967–86
- Baldzuhn J *et al* 2000 *Plasma Phys. Control. Fusion* **42** 463–87
- Baldzuhn J *et al* 2002 *Proc. 13th Int. Stellarator Workshop (Canberra, Australia)*
- Baldzuhn J *et al* 2003a *Proc. 14th Int. Stellarator Workshop (Greifswald, Germany)*
- Baldzuhn J *et al* 2003b *Plasma Phys. Control. Fusion* **45** 891–910
- Baldzuhn J *et al* 2003c *Proc. 30th EPS Conf. on Controlled Fusion and Plasma Physics (St Petersburg, Russia)* P-4.166pd
- Baldzuhn J *et al* 2004 *Fusion Sci. Technol.* **46** 348–54
- Ballico M *et al* 1991 *AIP Conf. Proc. (Charleston, SC, USA)*
- Barkley H J *et al* 1988 *Int. J. Electron.* **64** 21–8
- Basse N *et al* 2001 *Proc. 28th EPS Conf. on Controlled Fusion and Plasma Physics (Madeira, Portugal)* pp 1941–4
- Basse N *et al* 2004 *31st EPS Conf. on Plasma Physics (London, UK)* P-2.161
- Basse N *et al* 2005 *Phys. Plasmas* **12** 012507
- Basse N P *et al* 2002a *Plasma Sources Sci. Technol.* **11** A138–42
- Basse N P *et al* 2002b *Proc. 13th Int. Stellarator Workshop (Canberra, Australia)*
- Basse N P *et al* 2002c *Phys. Plasmas* **9** 3035–49
- Basse N P *et al* 2003 *Plasma Phys. Control. Fusion* **45** 439–53
- Bateman G and Nelson D B 1978 *Phys. Rev. Lett.* **41** 1804–7
- Bauer F *et al* 1978 *A Computational Method in Plasma Physics* (New York: Springer)
- Bäumel S *et al* 1999 *26th Conf. on Controlled Fusion and Plasma Physics (Maastricht, The Netherlands)*
- Bäumel S *et al* 2003a *Proc. 14th Int. Stellarator Workshop (Greifswald, Germany)* P.Mo13
- Bäumel S *et al* 2003b *Rev. Sci. Instrum.* **74** 1441–4
- Behringer K 1987 Description of the impurity transport code STRAHL *JET report JET-R(87)08*
- Behrisch R and Eckstein W 1986 *Physics of Plasma-Wall Interactions in Controlled Fusion (NATO ASI Series B* vol 131) ed e b D E P a R Behrisch (New York: Plenum) p 413
- Beidler C *et al* 1990 *Fusion Technol.* **17** 148–68
- Beidler C D and Hitchon W N G 1994 *Plasma Phys. Control. Fusion* **36** 317
- Beidler C D *et al* 1987 *J. Comput. Phys.* **72** 220
- Beidler C D *et al* 1994 *Proc. 21st EPS Conf. on Controlled Fusion and Plasma Physics (Montpellier, France)* p 568
- Beidler C D *et al* 2001 *Nucl. Fusion* **41** 1759–66
- Beidler C D *et al* 2003a *Proc. 14th Int. Stellarator Workshop (Greifswald, Germany)*
- Beidler C D *et al* 2003b *30th EPS Conference on Controlled Fusion and Plasma Physics (St Petersburg, Russia)* P-3.2

- Belonohy E *et al* 2007a *Proc. 34th EPS Conf. (Warsaw, Poland)* P2.046
- Belonohy E *et al* 2007b *Proc. Plasma 2007 (Greifswald, Germany)*
- Bencze A and Zoleznik S 2005 *Phys. Plasmas* **12** 052323
- Berkl E *et al* 1966 *Phys. Rev. Lett.* **17** 906
- Berkl E 1968 *Proc. 3rd (IAEA) Int. Conf. on Plasma Physics and Controlled Nuclear Fusion Research (Novosibirsk)* **1** 513
- Biglari H *et al* 1990 *Phys. Fluids B* **2** 1
- Bindemann T *et al* 2002a Robust line density measurements at W7-AS using a Cotton–Mouton polarimeter *Advanced Diagnostics for Magnetic and Intertial Fusion* ed P E Scott and A Wootton (New York: Kluwer) pp 323–6
- Bindemann T *et al* 2002b *Proc. German–Polish Conf. on Plasma Diagnostics for Fusion and Applications (Garching, Germany)*
- Blaumoser M *et al* 1976 *IAEA (Berchtesgaden, Germany)* **2** 81–92
- Bleuel J 1998 Elektrostatische Turbulenz am Plasmaraud des Stellarators Wendelstein 7-AS *PhD Thesis Physikalisches Institut, München Technische Universität*
- Bleuel J *et al* 1996 *Proc. 23rd EPS Conf. on Controlled Fusion and Plasma Physics (Kiev, Ukraine)* pp 727–30
- Bleuel J *et al* 1997 *Proc. 24th EPS Conf. on Controlled Fusion and Plasma Physics (Berchtesgaden, Germany)* pp 1613–6
- Bleuel J *et al* 1998 *Proc. ICPP & 25th EPS Conf. on Controlled Fusion and Plasma Physics (Prague, Czech Republic)* pp 2330–3
- Bleuel J *et al* 1999 *26th EPS Conf. on Controlled Fusion and Plasma Physics (Maastricht, The Netherlands)* pp 61–4
- Bleuel J *et al* 2002 *New J. Phys.* **4** 38.1–38.38
- Boozer A H 1980 *Phys. Fluids* **23** 904
- Boozer A H and Kuo-Petravic G 1981 *Phys. Fluids* **24** 851
- Bornatici M *et al* 1983 *Nucl. Fusion* **23** 1153
- Boozer A H and Gardner H J 1990 *Phys. Fluids B* **2** 2408
- Brakel R and W7-AS Team 2002 *Nucl. Fusion* **42** 903–12
- Brakel R *et al* 1992 *J. Nucl. Mater.* **196–198** 431–5
- Brakel R *et al* 1993 *Proc. 20th EPS Conf. on Controlled Fusion and Plasma Physics (Lisbon, Portugal)* pp 361–4
- Brakel R *et al* 1997 *Plasma Phys. Control. Fusion* **39** B273–86
- Brakel R *et al* 1998 *Proc. ICPP & 25th EPS Conf. on Controlled Fusion and Plasma Physics (Prague, Czech Republic)* P1.030
- Brakel R *et al* 2002 *Proc. 19th (IAEA) Fusion Energy Conf. (Lyon, France)* EX/C5-4
- Branas B *et al* 1995 *Proc. Stellarator Workshop (Madrid, Spain)*
- Brañas B *et al* 1995 *22nd EPS Conf. on Controlled Fusion and Plasma Physics (Bournemouth, UK)* p 161
- Brañas B *et al* 1999 *Rev. Sci. Instrum.* **70** 1025–9
- Brandenburg R *et al* 1997 *24th Conf. on Controlled Fusion and Plasma Physics (Berchtesgaden, Germany)* pp 477–80
- Brossmann U *et al* 1982 *Proc. 9th (IAEA) Int. Conf. on Plasma Physics and Controlled Nuclear Fusion Research (Baltimore, MD)* pp 141–56, IAEA-CN-41/Q-5
- Bruchhausen M 2002 *PhD Thesis University of Düsseldorf, Germany and report of Forschungszentrum Jülich, Germany, July 2003*
- Bruchhausen M *et al* 2002 *Proc. 29th EPS Conf. on Plasma Physics and Controlled Fusion (Montreux, Switzerland)* P-3.214
- Bruchhausen M *et al* 2004 *Plasma Phys. Control. Fusion* **46** 489–505
- Büchse R *et al* 1993 *Proc. 20th EPS Conf. on Controlled Fusion and Plasma Physics (Lisbon, Portugal)* pp 365–8
- Burhenn R *et al* 1995 *Proc. 22nd EPS Conf. on Controlled Fusion and Plasma Physics (Bournemouth, UK)* pp 145–8
- Burhenn R *et al* 1997 *Proc. 24th EPS Conf. on Controlled Fusion and Plasma Physics (Berchtesgaden, Germany)* pp 1609–12
- Burhenn R *et al* 1998 *J. Plasma Fusion Res. Ser.* **1** 255–8
- Burhenn R *et al* 1999 *Rev. Sci. Instrum.* **1** 603–7
- Burhenn R *et al* 2000 *Proc. 27th EPS Conf. on Controlled Fusion and Plasma Physics (Budapest, Hungary)* pp 1000–3
- Burhenn R *et al* 2002 *Proc. 29th EPS Conf. on Plasma Physics and Controlled Fusion (Montreux, Switzerland)* P4.043
- Burhenn R *et al* 2003 *Proc. 30th EPS Conf. on Controlled Fusion and Plasma Physics (St Petersburg, Russia)* P-1.2
- Burhenn R *et al* 2004 *Fusion Sci. Technol.* **46** 115–28
- Burhenn R *et al* 2005 *Proc. 3rd German–Polish Conf. on Plasma Diagnostics for Fusion and Applications (Opole, Poland)* pp 19–26
- Burrell K H *et al* 2002 *Plasma Phys. Control. Fusion* **44** A253–63
- Callaghan H *et al* 1997 *Proc. 24th EPS Conf. on Controlled Fusion and Plasma Physics (Berchtesgaden, Germany)* pp 1617–20

- Callaghan H *et al* 1998 *25th EPS Conf. on Controlled Fusion and Plasma Physics (Prague, Czech Republic)* pp 1470–3
- Callaghan H *et al* 1999 *Nucl. Fusion* **39** 509–23
- Callaghan H *et al* 2000a *Plasma Phys. Control. Fusion* **42** 1013–22
- Callaghan H *et al* 2000b *27th EPS Conf. on Controlled Fusion and Plasma Physics (Budapest, Hungary)* pp 436–9
- Candy J *et al* 2004 *Phys. Plasmas* **11** 1879
- Canik J M *et al* 2007 *Phys. Plasmas* **14** 056107
- Cannici B *et al* 1978a *Proc. 7th Int. (IAEA) Conf. on Plasma Physics and Controlled Nuclear Fusion Research (Innsbruck, Austria)* p 265
- Cannici B *et al* 1978b *Proc. 7th Int. (IAEA) Conf. on Plasma Physics and Controlled Nuclear Fusion Research (Innsbruck, Austria)* p 272
- Cappa A and Castejon F 2004 *Nucl. Fusion* **44** 406–13
- Carreras B A *et al* 1988 *Nucl. Fusion* **28** 1613–94
- Carreras B A *et al* 1998 *Phys. Plasmas* **5** 3632–43
- Carreras B A *et al* 1999 *Phys. Plasmas* **6** 1885–92
- Carreras B A *et al* 2006 *Phys. Plasmas* **13** 122509
- Carter M D *et al* 1987 *Nucl. Fusion* **27** 985
- Cattanei G *et al* 1982 *Proc. 9th Int. Conf. on Controlled Nuclear Fusion Research (Baltimore, MD)* (Vienna: IAEA) IAEA-CN41L5
- Cattanei G *et al* 1992 *EPS Top. Conf. on Radio Frequency Heating and Current Drive (Brussels, Belgium)*
- Cattanei G *et al* 1996 *Proc. 23rd EPS Conf. on Controlled Fusion and Plasma Physics (Kiev, Ukraine)* p 499
- Chen L 1994 *Phys. Plasmas* **1** 1519–22
- Chernyshev 2003 *Proc. 30th EPS Conf. on Controlled Fusion and Plasma Physics (St Petersburg, Russia)*
- Chodura R *et al* 1981 *IEEE Trans. Plasma Sci.* **PS-9** 221
- Chodura R and Schlüter A 1981 *J. Comput. Phys.* **41** 68–88
- Connor J W and Taylor J B 1977 *Nucl. Fusion* **17** 1047–55
- Connor J W 1998 *Plasma Phys. Control. Fusion* **40** 191–213
- Cooper A W 1995 private communication
- Cox M *et al* 1993 *Nucl. Fusion* **33** 1657–76
- DeAngelo N *et al* 1963 *Proc. 6th Int. Conf. On Ionized Phenomena in Gases (Paris, France)* p 9
- Diamond P H *et al* 2000 *Phys. Rev. Lett.* **84** 4843–5
- Dinklage A *et al* 2007a *Fusion Sci. Technol.* **51** 1–7
- Dinklage A *et al* 2007b *Nucl. Fusion* **47** 1265–73
- Dommasch W 1981 *Z. Naturf.* **36a** 251
- Dommasch W 1978 *IPP Report*
- Dose V *et al* 1998a *Nucl. Fusion* **38** 571–83
- Dose V *et al* 1998b *Phys. Rev. Lett.* **81** 3407–10
- Eckhart D *et al* 1965 *Proc. 2nd Int. Conf. on Plasma Physics and Controlled Fusion (Culham, UK)* p 719
- Ehmler H 2001 *Proc. 28th EPS Conf. on Controlled Fusion and Plasma Physics (Madeira, Portugal)*
- Ehmler H *et al* 2002a *Proc. 29th EPS Conf. on Plasma Physics and Controlled Fusion (Montreux, Switzerland)* P-4.044
- Ehmler H *et al* 2002b *Plasma Phys. Control. Fusion* **44** 1411–22
- Ehmler H *et al* 2003a *Plasma Phys. Control. Fusion* **45** 53–62
- Ehmler H *et al* 2003b *Nucl. Fusion* **43** L11–13
- Ejima S *et al* 1974 *Phys. Rev. Lett.* **32** 872
- Endler M 1994 Experimentelle Untersuchung und Modellierung elektrostatischer Fluktuationen in den Abschälsschichten des Tokamak ASDEX und des Stellarators Wendelstein 7-AS *PhD Thesis Max-Planck-Institut für Plasmaphysik, Technische Universität München*
- Endler M 1999 *J. Nucl. Mater.* **266–269** 84–90
- Endler M *et al* 1995a *Nucl. Fusion* **35** 1307–39
- Endler M *et al* 1995b *Phys. Scr.* **51** 610–6
- Endler M *et al* 2002 *29th EPS Conf. on Plasma Physics and Controlled Fusion (ECA, Montreux, Switzerland)* O-3.24
- Erckmann V and Gasparino U 1994 *Plasma Phys. Control. Fusion* **36** 1869–962
- Erckmann V *et al* 1983 *5th Topical Conf. on Radio Frequency Plasma Heating (Madison, WI)* p 209
- Erckmann V *et al* 1984a *4th Int. Symp. on Heating in Toroidal Plasmas (Roma, Italy)* ed H Knoepfel and E Sidoni p 846
- Erckmann V *et al* 1984b *Proc. 10th Int. (IAEA) Conf. on Fusion Energy (London, UK)* (Vienna: IAEA) **2** 419
- Erckmann V *et al* 1985 *Fusion Technol.* **7** 275–82

- Erckmann V *et al* 1986a *Plasma Phys. Control. Fusion* **28** 1277
 Erckmann V *et al* 1986b *13th EPS Conf. on Controlled Fusion and Plasma Heating* (Schliersee, Germany) p 211
 Erckmann V *et al* 1987 *1st Eur. Quasi-Optical Conf. (3rd Workshop of the MTT-Chapter of the West Germany Sect. of IEEE)* (Bonn, Germany) p 102
 Erckmann V *et al* 1990 *Fusion Technol.* **17** 76
 Erckmann V *et al* 1991a *Int. School of Plasma Physics (ISPP-10) High Power Microwave Generation and Application* (Varenna, Italy) p 511
 Erckmann V *et al* 1991b *13th Int. Conf. on Plasma Physics and Controlled Nuclear Fusion Research* (Washington, DC) p 555
 Erckmann V *et al* 1992a *Proc. 14th (IAEA) Int. Conf. on Plasma Physics and Controlled Nuclear Fusion Research* (Würzburg, Germany) pp 469–81
 Erckmann V *et al* 1992b *Proc. 1992 ICPP & 19th EPS Conf. on Controlled Fusion and Plasma Physics* (Innsbruck, Austria) vol 16C pp 497–500
 Erckmann V *et al* 1992c *RF Heating and Current Drive of Fusion Devices* (Brussels, Belgium) (Europhysics Conference Abstracts) p 297
 Erckmann V *et al* 1992d *Plasma Phys. Control. Fusion* **34** 1917–23
 Erckmann V *et al* 1993a *Proc. 10th Topical Conf. on Radio Frequency Power in Plasmas* (Boston, MA) AIP Conf. Proc. 137–48
 Erckmann V *et al* 1993b *Proc. 20th EPS Conf. on Controlled Fusion and Plasma Physics* (Lisbon, Portugal) pp 345–8
 Erckmann V *et al* 1993c *20th EPS Conf. on Controlled Fusion and Plasma Physics* (Lisbon, Portugal) pp 1021–4
 Erckmann V *et al* 1993d *Phys. Rev. Lett.* **70** 2086
 Erckmann V *et al* 1994 *15th Int. Conf. Plasma Physics and Controlled Nuclear Fusion Research* (Seville, Spain) p 771
 Erckmann V *et al* 1995a *Fusion Eng. Des.* **26** 141–152
 Erckmann V *et al* 1995b *Proc. 22nd EPS Conf. on Controlled Fusion and Plasma Physics* (Bournemouth, UK) pp 389–92
 Erckmann V *et al* 1996 *Proc. 16th (IAEA) Int. Conf. on Fusion Energy* (Montreal, Canada) pp 119–26 IAEA-CN-64/CP-1
 Erckmann V *et al* 2001 *Fusion Eng. Des.* **53** 365–75
 Erckmann V *et al* 2002 *Proc. 19th (IAEA) Fusion Energy Conf.* (Lyon, France) IAEA-CN-94, EX/W-3
 Erckmann V *et al* 2003 *Nucl. Fusion* **43** 1313–23
 Erckmann V *et al* 2007 *Fusion Sci. Technol.* **52** 291–312
 Ertl K *et al* 1996 *Nucl. Fusion* **36** 1477–88
 Estrada T 1992 *EPS Proc. Int. Conf. on Plasma Physics* (Innsbruck, Austria)
 Estrada T *et al* 1993a *IAEA Technical Committee Meeting on Stellarators and other Helical Confinement Systems* (Garching, Germany) p 292
 Estrada T *et al* 1993b *20th EPS Conf. on Controlled Fusion and Plasma Physics* (Lisbon, Portugal) (ECA) I-369
 Estrada T *et al* 1994 *Proc. 21st EPS Conf. on Controlled Fusion and Plasma Physics* (Montpellier, France) pp 404–7
 Estrada T *et al* 2005 *Plasma Phys. Control. Fusion* **47** L57–63
 Estrada T *et al* 2007 *Nucl. Fusion* **47** 305–12
 Evans T E *et al* 2004 *Phys. Rev. Lett.* **92** 235003
 Feist J H *et al* 1984 *Proc. 4th Int. Symp. on Heating in Toroidal Plasmas* (Roma, Italy) p 1051
 Feng Y and Kisslinger J 2000 *Contrib. Plasma Phys.* **40** 271
 Feng Y *et al* 1997 *J. Nucl. Mater.* **241–243** 930–4
 Feng Y *et al* 1998 *Plasma Phys. Control. Fusion* **40** 371
 Feng Y *et al* 1999a *26th EPS Conf. on Controlled Fusion and Plasma Physics* (Maastricht, The Netherlands) p 1465
 Feng Y *et al* 1999b *12th Int. Stellarator Workshop* (Madison, WI, USA)
 Feng Y *et al* 1999c *J. Nucl. Mater.* **266–269** 812
 Feng Y *et al* 2000 *27th EPS Conf. on Controlled Fusion and Plasma Physics* (Budapest, Hungary) 3.098
 Feng Y *et al* 2001 *28th EPS Conf. on Controlled Fusion and Plasma Physics* (Madeira, Portugal) 5.046
 Feng Y *et al* 2002 *Contrib. Plasma Phys.* **42** 187
 Feng Y *et al* 2003a *J. Nucl. Mater.* **313–316** 857–862
 Feng Y *et al* 2003b *Proc. 30th EPS Conf. on Controlled Fusion and Plasma Physics* (St Petersburg, Russia) O-4.4C
 Feng Y *et al* 2004a *Plasma Phys. Control. Fusion* **44** 611
 Feng Y *et al* 2004b *Contrib. Plasma Phys.* **44** 57
 Feng Y *et al* 2005a *32th EPS Conf. on Controlled Fusion and Plasma Physics* (Tarragona, Spain) 1.012
 Feng Y *et al* 2005b *Phys. Plasmas* **12** 052505
 Feng Y *et al* 2005c *Nucl. Fusion* **45** 89
 Feng Y *et al* 2006a *Nucl. Fusion* **46** 807

- Feng Y *et al* 2006b *Contrib. Plasma Phys.* **46** 33
- Feng Y *et al* 2007 *J. Nucl. Mater.* **363–365** 353–8
- Fiedler S *et al* 1996 *Proc. 23rd EPS Conf. on Controlled Fusion Plasma Physics (Kiev, Ukraine)* p 1007
- Fiedler S 1999 *J. Nucl. Mater.* **266–269** 1279–84
- Fischer R *et al* 2002 *Plasma Phys. Control. Fusion* **44** 1501–19
- Fischer R *et al* 2003 *Plasma Phys. Control. Fusion* **45** 1095–111
- Fowler R H *et al* 1991 *Fusion Technol.* **20** 200
- Fuchs C and Hartfuß H J 1998 *Phys. Rev. Lett.* **81** 1626
- Fuchs C and Hartfuß H J 1999 *Rev. Sci. Instrum.* **70** 722
- Fuchs C and Hartfuß H J 2001a *Fusion Eng. Des.* **53** 451–6
- Fuchs C and Hartfuß H J 2001b *Rev. Sci. Instrum.* **72** 383–6
- Fuchs C *et al* 1999 *Proc. 26th EPS Conf. on Contr. Fusion and Plasma Physics (Maastricht, The Netherlands)* pp 1469–72
- Fuchs C *et al* 2001 *Fusion Eng. Des.* **53** 309–14
- Furth H P *et al* 1973 *Phys. Fluids* **16** 1054–63
- Fussmann G 1986 *Nucl. Fusion* **26** 983–1002
- Fussmann G *et al* 1990 *Nucl. Fusion* **30** 2319
- Gadelmeier F *et al* 2004 *Plasma Phys. Control. Fusion* **46** 711–21
- Galeev A A *et al* 1979 *Rev. Plasma Phys.* **7** 257
- Gandini F *et al* 2001a *Fusion Eng. Des.* **56–57** 975–9
- Gandini F *et al* 2001b *14th Topical Conf. on RF Power in Plasmas (Oxnard, CA) AIP Conf. Proc.* **595** 358
- Garbet X *et al* 1991 *Nucl. Fusion* **31** 967–72
- Garbet X *et al* 2001 *Phys. Plasmas* **8** 2793
- Garcia-Cortes I *et al* 2000 *Nucl. Fusion* **40** 1867
- Gardner H J 1990 *Nucl. Fusion* **30** 1417–24
- Garren D A and Boozer A H 1991 *Phys. Fluids B* **3** 2822
- Gasparino U 1990 *Int. Workshop on Theory of Fusion Plasmas (Varenna, Italy)* p 195
- Gasparino U *et al* 1990 *Proc. 17th EPS Conf. on Controlled Fusion Plasma Physics (Amsterdam, The Netherlands)* p 1275
- Gasparino U *et al* 1998a *Plasma Phys. Control. Fusion* **40** 233–44
- Gasparino U *et al* 1998b *Nucl. Fusion* **38** 223
- Geiger J and Hayashi T 2002 *Proc. 29th EPS Conf. on Plasma Physics and Controlled Fusion (Montreux, Switzerland)* P-5.035
- Geiger J and Suzuki Y 2006 *Proc. 33rd European Physical Society Conf. on Plasma Physics (Rome, Italy) (EPS)* P-2.115
- Geiger J and W7-AS Team 1993 *9th Int. Workshop on Stellarators (Garching, Germany)* (Vienna: IAEA) pp 222–6
- Geiger J *et al* 1994 *Proc. 21st EPS Conf. on Controlled Fusion and Plasma Physics (Montpellier, France)* pp 372–5
- Geiger J *et al* 1995 *10th Int. Conf. on Stellarators IEZ Techn. comm. Meeting (Madrid, Spain) EUR-CIEMAT 30* (Madrid: CIEMAT) pp 57–60
- Geiger J *et al* 1996 *Proc. 23rd EPS Conf. on Controlled Fusion and Plasma Physics (Kiev, Ukraine)* pp 491–4
- Geiger J *et al* 2003 *Proc. 30th EPS Conf. on Controlled Fusion and Plasma Physics (St Petersburg, Russia)* P-1.3
- Geiger J *et al* 2004a *31st EPS Conf. on Plasma Physics (London, UK)* P-1.207
- Geiger J *et al* 2004b *Fusion Sci. Technol.* **46** 13–23
- Geist T *et al* 1997 *Rev. Sci. Instrum.* **68** 1162
- Gentle K W 1988 *Phys. Fluids* **31** 1105
- Gentle K W *et al* 2006 *Phys. Plasmas* **13** 012311
- Giannone L *et al* 1992 *Nucl. Fusion* **32** 1985–99
- Giannone L *et al* 1994 *Phys. Plasmas* **1** 3614–21
- Giannone L *et al* 1996 *Plasma Phys. Control. Fusion* **38** 477
- Giannone L *et al* 1997 *Rev. Sci. Instrum.* **68** 762–5
- Giannone L *et al* 1999 *J. Nucl. Mater.* **266–269** 507–12
- Giannone L *et al* 2000a *J. Plasma Fusion Res. Ser.* **3** 129
- Giannone L *et al* 2000b *Plasma Phys. Control. Fusion* **42** 603–27
- Giannone L *et al* 2002a *Plasma Phys. Control. Fusion* **44** 2149–65
- Giannone L *et al* 2002b *Rev. Sci. Instrum.* **73** 3205–14
- Giannone L *et al* 2003 *Plasma Phys. Control. Fusion* **45** 1713–31
- Gibson G *et al* 1958 *Proc. 2nd UN Conf. on Peaceful Uses of Atomic Energy (Geneva, Switzerland)* **32** 275
- Gilgenbach R M *et al* 1980 *Phys. Rev. Lett.* **44** 647

- Gori S *et al* 1996 *Proc. Workshop Theory of Fusion Plasmas (Varenna, Italy)* p 335
- Görner C *et al* 1997 *Proc. 24th EPS Conf. on Controlled Fusion and Plasma Physics (Berchtesgaden, Germany)* pp 1625–8
- Görner C *et al* 1998a *Proc. 1998 ICPP & 25th EPS Conf. on Controlled Fusion and Plasma Physics (Prague, Czech Republic)* P1.029
- Görner C 1998b Tomographische Untersuchung von globalen Alfvén-Eigenmoden am Stellarator Wendelstein 7-AS
Report IPP III/230 PhD Thesis (in german)
- Gourdon C *et al* 1968 *Proc. 3rd Int. (IAEA) Conf. on Plasma Physics and Controlled Nuclear Fusion Research (Novosibirsk)* **1** 847
- Greenwald M *et al* 1999 *Phys. Plasmas* **6** 1943–9
- Greenwald M 2002 *Plasma Phys. Control. Fusion* **44** R27–80
- Grieger G and W7-X Team 1998 *J. Plasma Fusion Res. Ser.* **1** 53–6
- Grieger G *et al* 1971 *4th IAEA Conf. on Plasma Physics and Controlled Nuclear Fusion (Madison, WI)* **3** 27
- Grieger G *et al* 1985 *Nucl. Fusion* **25** 1231–42
- Grieger G *et al* 1986 *Plasma Phys. Control. Fusion* **28** 43–53
- Grieger G *et al* 1992 *Phys. Fluids B* **4** 2081–91
- Grigull P *et al* 1990 *J. Nucl. Mater.* **176–177** 975–82
- Grigull P *et al* 1992 *J. Nucl. Mater.* **196–198** 101–12
- Grigull P *et al* 1995 *Proc. 10th Int. Conf. on Stellarators (IAEA Technical Committee Meeting) (Madrid, Spain)*
- Grigull P *et al* 1996 *Proc. 16th Int. Conf. On Fusion Energy (Montreal, Canada)* IAEA-CN-64/CP-25
- Grigull P *et al* 1997 *J. Nucl. Mater.* **241–243** 935–40
- Grigull P *et al* 1998 *J. Plasma Fusion Res. Ser.* **1** 291–4
- Grigull P *et al* 1999a *26th EPS Conf. on Controlled Fusion and Plasma Physics (Maastricht, The Netherlands)*
23J 1473–6
- Grigull P *et al* 1999b *Proc. 12th Int. Stellarator Workshop (Madison, WI, USA)*
- Grigull P *et al* 2001a *J. Nucl. Mater.* **290–293** 1009–12
- Grigull P *et al* 2001b *Plasma Phys. Control. Fusion* **43** A175–93
- Grigull P *et al* 2002 *J. Plasma Fusion Res. Ser.* **5** 118–23
- Grigull P *et al* 2003a *J. Nucl. Mater.* **313–316** 1287–91
- Grigull P *et al* 2003b *Fusion Eng. Des.* **66–68** 49–58
- Grove D J *et al* 1961 *Proc. 1st (IAEA) Conf. on Plasma Physics and Controlled Nuclear Fusion Research (Salzburg, Austria)* *Nucl. Fusion* 1962 **1** 203
- Grulke O *et al* 2001 *Phys. Plasmas* **8** 5171–80
- Hacker H *et al* 1975 *5th Int. Conf. on Plasma Physics and Controlled Fusion (Tokyo, Japan)* p 3
- Haese M *et al* 1998 *J. Plasma Fusion Res. Ser.* **1** 99
- Hanatani K and Penningsfeld F P 1992 *Nucl. Fusion* **32** 1769
- Harmeyer E *et al* 1985 *Proc. 10th IAEA Conf. (Vienna, Austria)*
- Hartfuß H J 1987 *Proc. 12th IEEE Int. Conf. on Infrared and MM-Waves (Orlando, FL)* (IEEE) Cat No. Ch 2990–1, 360
- Hartfuß H J 1998 *Plasma Phys. Control. Fusion* **40** A231–50
- Hartfuß H J and Häse M 1997 *10th Joint Workshop on Electron Cyclotron Emission and Electron Cyclotron Heating EC-10 (Ameland, The Netherlands)* (Singapore: World Scientific) p 119
- Hartfuß H J and Tutter M 1985 *Rev. Sci. Instrum.* **56** 1703–5
- Hartfuß H J *et al* 1993 *Local Transport Studies in Fusion Plasmas (Varenna, Italy)* Bologna (1994) p 119
- Hartfuß H J *et al* 1998 *25th EPS Conf. on Controlled Fusion and Plasma Physics (Prague, Czech Republic)* p 399
- Hartfuß H J *et al* 1986 *Nucl. Fusion* **26** 678
- Hartfuß H J *et al* 1994a *Plasma Phys. Control. Fusion* **36** B17–37
- Hartfuß H J *et al* 1994b *Rev. Sci. Instrum.* **65** 2284–90
- Hartfuß H J *et al* 1996 *Plasma Phys. Control. Fusion* **38** A227–36
- Hartfuß H J *et al* 1997a *Plasma Phys. Control. Fusion* **39** 1693–769
- Hartfuß H J *et al* 1997b *Fusion Eng. Des.* **34–35** 81–7
- Hartfuß H J *et al* 2003 *30th EPS Conf. on Controlled Fusion and Plasma Physics (St Petersburg, Russia)* O-3.2C
- Hartmann D A *et al* 1998 *Proc. 17th Int. Conf. on Fusion Energy 1998 (Yokohama, Japan)* CD-ROM file CD1/5
- Häse M *et al* 1997a *10th Joint Workshop on Electron Cyclotron Emission and Electron Cyclotron Heating EC-10 (Ameland, The Netherlands)* (Singapore: World Scientific) p 139
- Häse M *et al* 1997b *10th Joint Workshop on Electron Cyclotron Emission and Electron Cyclotron Heating, EC-10 (Ameland, The Netherlands)* (Singapore: World Scientific) p 131
- Häse M *et al* 1999 *Rev. Sci. Instrum.* **70** 1014–7
- Hastings D E 1985 *Phys. Fluids* **28** 334

- Hastings D E *et al* 1985 *Nucl. Fusion* **23** 445
- Hegna C C 1998 *Phys. Plasmas* **5** 1767–74
- Heifetz D B *et al* 1982 *J. Comput. Phys.* **46** 309
- Heinrich O *et al* 1997 *Proc. 24th EPS Conf. on Controlled Fusion Plasma Physics (Berchtesgaden, Germany)* 15931596
- Heller R *et al* 2000 *Cryogenics* **40** 561–7
- Henle W *et al* 1990 *Fusion Technol.* **2** 1142–6
- Hennequin P *et al* 2005 *Proc. 7th Int. Reflectometry Workshop for Fusion Plasma Diagnostics (IRW7) (Garching, Germany)* (Garching, Germany: Max-Planck-Institut für Plasmaphysik) IPP 2/9
- Herre G 1999 Untersuchung der Plasmaraumschicht am Stellarator Wendelstein 7-AS *PhD Thesis* Garching, Munich, Germany
- Herre G *et al* 1997 *J. Nucl. Mater.* **241–243** 941–5
- Herre G *et al* 1999 *J. Nucl. Mater.* **266** 1015–101
- Hidalgo C *et al* 2005 *Nucl. Fusion* **45** 266
- Hildebrandt D *et al* 1992 *J. Nucl. Mater.* **196–198** 436–42
- Hildebrandt D *et al* 1995 *J. Nucl. Mater.* **220** 703–7
- Hildebrandt D *et al* 1997 *J. Nucl. Mater.* **241–243** 950–5
- Hildebrandt D *et al* 2003a *J. Nucl. Mater.* **313–316** 738–42
- Hildebrandt D *et al* 2003b *Proc. Inframotion (Las Vegas, NV, USA)* pp 91–8
- Hinton F L and Hazeltine R D 1976 *Rev. Mod. Phys.* **48** 239
- Hirsch M and Holzhauer E 2004 *Plasma Phys. Control. Fusion* **46** 593–609
- Hirsch M *et al* 1995a *22nd EPS Conf. on Controlled Fusion and Plasma Physics (Bournemouth, UK)* p 141
- Hirsch M *et al* 1995b *Rev. Sci. Instrum.* **66** 412
- Hirsch M *et al* 1996a *Rev. Sci. Instrum.* **67** 1807–13
- Hirsch M *et al* 1996b *Proc. 16th (IAEA) Fusion Energy Conf. (Montreal, Canada)* pp 315–21 IAEA-CN-64/CP-26
- Hirsch M *et al* 1997 *Proc. 24th EPS Conf. on Controlled Fusion and Plasma Physics (Berchtesgaden)* pp 1601–4
- Hirsch M *et al* 1998a *Plasma Phys. Control. Fusion* **40** 631–4
- Hirsch M *et al* 1998b *Proc. 25th EPS Conf. on Controlled Fusion and Plasma Physics (Praha, Czech Republic)* pp 2322–5
- Hirsch M *et al* 2000 *Plasma Phys. Control. Fusion* **42** A231–6
- Hirsch M *et al* 2001a *Rev. Sci. Instrum.* **72** 324–7
- Hirsch M *et al* 2001b *Plasma Phys. Control. Fusion* **43** 1641–60
- Hirsch M *et al* 2006 *Plasma Phys. Control. Fusion* **48** S155–67
- Hirshman S *et al* 1986 *Comput. Phys. Commun.* **43** 143–55
- Hirshman S P 1980 *Phys. Fluids* **23** 1238
- Hirshman S P *et al* 1986a *Comput. Phys. Commun.* **43** 143–55
- Hirshman S P *et al* 1986b *Phys. Fluids* **29** 2951–9
- Hirshman S P *et al* 1990 *J. Comput. Phys.* **87** 396–407
- Hofmann J 1991 Max-Planck Institut für Plasmaphysik IPP, III/174
- Hofmann J V *et al* 1994 *21st EPS Conf. on Controlled Fusion and Plasma Physics (Montpellier, France)* 18B pp 392–5
- Hofmann J V *et al* 1996 *Plasma Phys. Control. Fusion* **38** A193–211
- Hogeweij G M D *et al* 1998 *Nucl. Fusion* **38** 1881
- Holzhauer E and W7-AS Team 1996 *Plasma Phys. Control. Fusion* **38** 1267–71
- Holzhauer E *et al* 1996 *Proc. 23rd EPS Conf. on Controlled Fusion and Plasma Physics (Kiev, Ukraine)* 20C pp 467–70
- Holzhauer E *et al* 1998 *Plasma Phys. Control. Fusion* **40** 1869–86
- Hudson S R and Hegna C C 2003 *Phys. Plasmas* **10** 4716–27
- Ida K *et al* 1996 *Phys. Rev. Lett.* **76** 1268–71
- Ida K *et al* 1999 *Nucl. Fusion* **39** 1649
- Ida K *et al* 2002 *Phys. Rev. Lett.* **88** 015002
- Ida K *et al* 2003 *Plasma Phys. Control. Fusion* **45** 1931–8
- Igitkhanov Y 1988 *Contrib. Plasma Phys.* **28** 47
- Igitkhanov Y *et al* 2002 *Proc. 29th EPS Conf. (Montreux, Switzerland)* P-1.106
- Igitkhanov Y *et al* 2006 *Fusion Sci. Technol.* **50** 268–75
- Igitkhanov Y L *et al* 2004 *Fusion Sci. Technol.* **46** 101–5
- Isaev M *et al* 2006 *Fusion Sci. Technol.* **50** 440–6
- ITER Physics Expert Groups 1999 ITER Physics Basis (Chapter 1) *Nucl. Fusion* **39** 2137–74
- ITER Physics Expert Groups 1999 ITER Physics Basis (Chapter 2) *Nucl. Fusion* **39** 2175–249
- ITER Physics Expert Groups 1999 ITER Physics Basis *Nucl. Fusion* **39** 2137–638

- ITER Physics Expert Groups 2007 Progress in the ITER Physics Basis *Nucl. Fusion* **47** S1–403
- Itoh K and Itoh S I 1988 *J. Phys. Soc. Japan* **57** 1269
- Jaenicker R and WVII-A Team 1980 *Nucl. Fusion* **20** 1093–100
- Jaenicker R et al 1992 *Proc. 14th (IAEA) Int. Conf. on Plasma Physics and Controlled Nuclear Fusion Research (Würzburg, Germany)* pp 483–91
- Jaenicker R et al 1993 *Nucl. Fusion* **33** 687–704
- Jaenicker R et al 1994 *Proc. 21th EPS Conf. on Controlled Fusion and Plasma Physics (Montpellier, France)* pp 396–8
- Jaenicker R et al 1995 *Plasma Phys. Control. Fusion* **37** A163–76
- Jaenicker R et al 2000 *18th IAEA Fusion Energy Conf. (Sorrento, Italy)* IAEA-CN-77 OV4/3
- Jaenicker R et al 2002a *Proc. 13th Int. Stellarator Workshop (Canberra, Australia)* OI:6
- Jaenicker R et al 2002b *Plasma Phys. Control. Fusion* **44** B193–205
- Jaenicker R 2003 *Proc. 14th Int. Stellarator Workshop (Greifswald, Germany)* IM01
- Jenko F and Kendl A 2002a *New J. Phys.* **4** 35.1–35.12
- Jenko F and Kendl A 2002b *Phys. Plasmas* **9** 4103
- Kadomtsev B 1975 *Sov. J. Plasma Phys. Control. Fusion* **1** 295
- Kaiser R 1993 *Nucl. Fusion* **33** 1281–91
- Karger F and Lackner K 1977 *Phys. Lett. A* **61** 385–7
- Kendl A et al 2000 *Plasma Phys. Control. Fusion* **42** L23–9
- Kendl A and Scott B D 2003 *Phys. Rev. Lett.* **90** 035006
- Kendl A et al 2003 *Phys. Plasmas* **10** 3694
- Kick M et al 1996 *Proc. 16th (IAEA) Int. Conf. on Fusion Energy (Montreal, Canada)* vol 34 pp 27–39 IAEA-CN-64/C1-4
- Kick M et al 1998 *J. Plasma Fusion Res. Ser.* **1** 19
- Kick M et al 1999 *Plasma Phys. Control. Fusion* **41** A549–59
- Kim J et al 1994 *Phys. Rev. Lett.* **72** 2199–2202
- Kisslinger J and Wobig H 1985 *13th EPS Conf. on Controlled Fusion and Plasma Physics (Budapest, Hungary)* p 453
- Kisslinger J et al 1993 *Proc. IAEA Technical Committee Meeting on Stellarators and other Helical Confinement Systems (Garching, Germany)* p 385
- Kisslinger J et al 1995 *Proc. 22nd EPS Conf. on Controlled Fusion Plasma Physics (Bournemouth, UK)* p 149
- Kleiber R and Scott B 2005 *Phys. Plasmas* **12** 102507
- Klose S et al 2002 *Proc. 29th EPS Conf. on Plasma Physics and Controlled Fusion (Montreux, Switzerland)* P5.032
- Klose S et al 2003 *Proc. 14th Int. Stellarator Workshop (Greifswald, Germany)* PMo4
- Knauer J P et al 1999 *Proc. 12th Int. Stellarator Workshop (Madison, WI, USA)*
- Knauer J P et al 2003 *Rev. Sci. Instrum.* **74** 1679–82
- Kobayashi M et al 2004a *Contrib. Plasma Phys.* **44** 25
- Kobayashi M et al 2004b *Nucl. Fusion* **44** 64
- Kobayashi M et al 2007a *Nucl. Fusion* **47** 61
- Kobayashi M et al 2007b *J. Nucl. Mater.* **363–365** 294–300
- Kocsis G et al 1995 *22nd EPS Conf. on Controlled Fusion and Plasma Physics (Bournemouth, UK)* p 269
- Kolesnichenko Y I et al 2002 *Nucl. Fusion* **42** 949–58
- Kolesnichenko Y I et al 2003 *Proc. 30th EPS Conf. on Controlled Fusion and Plasma Physics (St Petersburg, Russia)* P-3.5
- Kolesnichenko Y I et al 2004 *Fusion Sci. Technol.* **46** 54–63
- Kolesnichenko Y I et al 2007a *34th EPS Conf. (Warsaw, Poland)* 31F P-4.147
- Kolesnichenko Y I et al 2007b *Plasma Phys. Control. Fusion* **49** A159–66
- Kolesnichenko Y I et al 2000 Alfvén eigenmodes in helias configurations (Part I) *IPP Report III/261*
- Kolesnichenko Y I et al 2001 *Phys. Plasmas* **8** 491–509
- Kolesnichenko Y I et al 2002 *Phys. Plasmas* **9** 517–28
- Kolesnichenko Y I et al 2005a *Phys. Rev. Lett.* **94** 165004
- Kolesnichenko Y I et al 2005b *32nd EPS Conf. on Plasma Physics (Tarragona, Spain)* P-2.125
- Kolesnichenko Y I et al 2006 *Nucl. Fusion* **46** 753–69
- Kolesnichenko Y I et al 2007 *34th EPS Conf. on Plasma Physics*
- Könies A 2000 *Phys. Plasmas* **7** 1139–47
- Könies A 2003 private communication
- Könies A 2005 *9th IAEA Technical Meeting on Energetic Particles in Magnetic Confinement Systems (Takayama, Japan)*
- König R et al 2001 *J. Nucl. Mater.* **290–293** 882–6
- König R et al 2002 *Plasma Phys. Control. Fusion* **44** 2365–422

- König R *et al* 2003 *Rev. Sci. Instrum.* **74** 2052–5
- König R *et al* 2004 *Fusion Sci. Technol.* **46** 152–66
- Konrad Ch 1995 *Annual Report IPP 2.5.5* Max-Planck-Institut für Plasmaphysik, Germany
- Koponen J P T and Dumbrais O 1997 *Rev. Sci. Instrum.* **68** 4038–42
- Koponen J P T *et al* 2000a *Nucl. Fusion* **40** 365
- Koponen J P T *et al* 2000b *Plasma Phys. Control. Fusion* **42** 1123–36
- Kovrizhnykh L M 1984 *Nucl. Fusion* **24** 851
- Kreter A *et al* 2002 *Proc. 29th EPS Conf. on Plasma Physics and Controlled Fusion (Montreux, Switzerland)* P-5.033
- Kreter A *et al* 2003 *Proc. 14th Int. Stellarator Workshop (Greifswald, Germany)*
- Krychowiak M *et al* 2003 *Verhandl. DPG(6)* P10.14
- Kuehner G *et al* 1990 *14th Conf. on Controlled Fusion and Plasma Physics (Amsterdam, The Netherlands)*
- Kühner G *et al* 1994 *Proc. 15th (IAEA) Int. Conf. on Plasma Physics and Controlled Nuclear Fusion Research (Seville, Spain)* p 145–154 IAEA-CN-60/A1-8
- Kuteev B V *et al* 2003 *Tech. Phys. Lett.* **29** 302–4
- Lackner L and Gottardi A O 1990 *Nucl. Fusion* **30** 767
- Laqua H 2007 *Plasma Phys. Control. Fusion* **49** R1–R42
- Laqua H and Schneider F 2000 *Fusion Eng. Des.* **48** 143–7
- Laqua H P *et al* 1997 *Phys. Rev. Lett.* **78** 3467–70
- Laqua H P *et al* 1998 *Phys. Rev. Lett.* **81** 2060–3
- Laqua H P *et al* 1999 *Plasma Phys. Control. Fusion* **41** A273–84
- Laqua H P *et al* 2001 *Proc. 28th EPS Conf. on Controlled Fusion and Plasma Physics (Madeira, Portugal)* pp 1277–80 P3.099
- Laqua H P *et al* 2003a *Phys. Rev. Lett.* **90** 75003.1–75003.4
- Laqua H P *et al* 2003b *Nucl. Fusion* **43** 1324–8
- Lazaros A and Weller A 1990 Equilibrium and stability studies by the X-ray diagnostics in the W7-AS stellarator *IPP Report III/159*
- Ledl L 1995 Untersuchungen zum Verunreinigungstransport von Aluminium und Eisen im Stellarator W7-AS mittels Laser-Ablationstechnik *Diploma Thesis* Munich Technical University
- Ledl L 1999a Verunreinigungspelletinjektion am Stellarator Wendelstein 7-AS *TU Munic PhD Thesis*
- Ledl L *et al* 1999b *Proc. 20th EPS Conf. on Controlled Fusion and Plasma Physics (Maastricht, The Netherlands)* 23J 1477–80
- Ledl L *et al* 2004 *Nucl. Fusion* **44** 600–8
- Lengyel L L *et al* 1999 *Nucl. Fusion* **39** 791–813
- Li Y M *et al* 1987 *Phys. Fluids* **30** 1466–84
- Liewer P C 1985 *Nucl. Fusion* **25** 543–621
- Lister G G *et al* 1983 *Proc. 11th Eur. Conf. on Controlled Fusion and Plasma Physics (Aachen, Germany)* VI.2 pp 323–6
- Lister G G 1985 FAFNER—a fully 3-D neutral beam injection code using Monte Carlo methods *IPP Report*
- Litvak A G *et al* 1994 *Phys. Lett. A* **188** 64
- Lopes-Cardozo N J 1995 *Plasma Phys. Control. Fusion* **37** 799–854
- Lopes-Cardozo N J *et al* 1997 *Plasma Phys. Control. Fusion* **39** B303
- Lotz W *et al* 1992 *Plasma Phys. Control. Fusion* **34** 1034
- Luce T C and Petty C C 1994 *Nucl. Fusion* **34** 121
- Luce T C *et al* 1992 *Phys. Rev. Lett.* **68** 52
- Lutsenko V V *et al* 2002 *Proc. 19th (IAEA) Fusion Energy Conf. (Lyon, France)* TH/P3-16
- Lyon J F *et al* 1997 *Proc. 24th EPS Conf. on Controlled Fusion and Plasma Physics (Berchtesgaden, Germany)* pp 1629–32
- Maaßberg H 2004 private communication
- Maaßberg H and Beidler C D 2004 *Proc. 31st EPS Conf. on Plasma Physics (London, UK)* P-1.100
- Maaßberg H and Dylabin K S 1993 *Proc. 20th EPS Conf. on Controlled Fusion Plasma Physics (Lisbon, Portugal)* p 409
- Maaßberg H *et al* 1993a *Plasma Phys. Control. Fusion* **35** B319–32
- Maaßberg H *et al* 1993b *Phys. Fluids B* **5** 3627
- Maaßberg H *et al* 1993c *Phys. Fluids B* **5** 3728
- Maaßberg H *et al* 1996 *Proc. 23rd EPS Conf. on Controlled Fusion Plasma Physics (Kiev, Ukraine)* p 487
- Maaßberg H *et al* 1999 *Plasma Phys. Control. Fusion* **41** 1135–53
- Maaßberg H *et al* 2000a *Strong Microwaves in Plasmas* (Nizhny Novgorod, Russia: Institute of Applied Physics) ed A G Litvak

- Maaßberg H *et al* 2000b *Phys. Plasmas* **7** 295
- Maaßberg H *et al* 2005 *Plasma Phys. Control. Fusion* **47** 1137–63
- Marushchenko N B *et al* 1997 *Comput. Phys. Commun.* **103** 145–56
- Marushchenko N B *et al* 2002 *Proc. 29th EPS Conf. on Plasma Physics and Controlled Fusion (Montreux, Switzerland)* D-5.003
- Marushchenko N B *et al* 2004 *31st EPS Conf. on Plasma Physics and Controlled Fusion (London, UK)* P-1.204
- Mathis R and Sapper J 1990 *Fusion Eng. Des.* **11** 399–422
- Mazurenko A *et al* 2002 *Phys. Rev. Lett.* **89** 22500
- McCormick K *et al* 1997 *Fusion Eng. Des.* **34–35** 125–34
- McCormick K *et al* 1999a *12th Int. Stellarator Workshop (Madison, WI, USA)*
- McCormick K *et al* 1999b *Plasma Phys. Control. Fusion* **41** B285–304
- McCormick K *et al* 2001 *J. Nucl. Mater.* **290–293** 920–4
- McCormick K *et al* 2002 *Phys. Rev. Lett.* **89** 15001
- McCormick K *et al* 2003a *Proc. 30th EPS Conf. on Controlled Fusion and Plasma Physics (St Petersburg, Russia)* P-1.1
- McCormick K *et al* 2003b *14th Int. Stellarator Workshop (Greifswald, Germany)*
- McCormick K *et al* 2003c *J. Nucl. Mater.* **313–316** 1131–40
- McCormick K *et al* 2005 *J. Nucl. Mater.* **337–339** 520–4
- McCormick K *et al* 2007 *J. Nucl. Mater.* **363–365** 389–94
- Merkel P 1987 *Nucl. Fusion* **27** 867
- Merkel P and Nührenberg C 1996 *Proc. Joint Varenna-Lausanne Int. Workshop on Theory of Fusion Plasmas (Varenna, Italy)* pp 233–40
- Miyamoto K 1980 *Plasma Physics for Nuclear Fusion* (Cambridge, MA: MIT Press)
- Michel G *et al* 2001 *14th Topical Conf. on Radio Frequency Power in Plasmas (Oxnard, CA)* ed T K Mau and J DeGrassie, pp 354–8
- Miyamoto K 1980 *Plasma Physics for Nuclear Fusion* (Cambridge, MA: MIT Press)
- Mjølhus E 1984 *J. Plasma Phys.* **31** 7
- Morisaki T *et al* 2005 *J. Nucl. Mater.* **337–339** 154–60
- Morita S and Baldzuhn J 1994 Zeff Measurements and Analysis of Reheat-Mode Discharges in W7-AS Max-Planck Institut Für Plasmaphysik IPP, III/199
- Mossessian D A *et al* 2002 *Plasma Phys. Control. Fusion* **44** 423
- Motojima O *et al* 2003 *Nucl. Fusion* **43** 1674–83
- Moyer R A *et al* 2001 *Phys. Rev. Lett.* **87** 135001
- Müller G A *et al* 1995 *Proc. 11th Topical Conf. on Radio Frequency Power in Plasmas (Palm Springs, CA)* pp 133–42
- Murakami M *et al* 1991 *Phys. Rev. Lett.* **66** 707–10
- Murakami S *et al* 1996 *17th IAEA Fusion Energy Conf. (Montreal, Canada)* IAEA-CN-69/TH2/1
- Murakami S *et al* 1998 *Proc. 17th IAEA Fusion Energy Conf. (Yokohama, Japan)* (Vienna: IAEA) p 1383
- Murakami S *et al* 2000 *Nucl. Fusion* **40** 693
- Mynick H E and Hitchon W N G 1983 *Nucl. Fusion* **23** 1053
- Mynick H E *et al* 1982 *Phys. Rev. Lett.* **48** 322
- Nagasaki K *et al* 2005 *Nucl. Fusion* **45** 13–21
- Nakajima N and Okamoto M 1990 *NIFS Report* 27
- Nakajima N and Okamoto M 1992 *J. Phys. Soc. Japan* **61** 833
- Nakajima N *et al* 1992 *Phys. Fluids B* **4** 1115–21
- Nakamura Y *et al* 2002 *28th Eur. Conf. on Controlled Fusion and Plasma Physics (Madiera, Portugal)* p 1481
- Naujoks D *et al* 1997 *J. Nucl. Mater.* **241–243** 925–9
- Navarro A 1989 *7th Int. Stellarator Workshop (Oak Ridge, TN, USA)*
- Navarro A *et al* 1991 *IEEE Trans. Plasma Sci.* **19** 569–79
- Nazikian R *et al* 1997 *Phys. Rev. Lett.* **78** 2976–9
- Nedospasov A V 1989 *Sov. J. Plasma Phys.* **15** 659–61
- Nührenberg C 1999a *Plasma Phys. Control. Fusion* **41** 1055–70
- Nührenberg C 1999b *Phys. Plasmas* **6** 137–47
- Nührenberg C 2001 private communication
- Nührenberg J and Zille R 1984 *Proc. IAEA Technical Committee Meeting on Plasma Confinement and Heating in Stellarators Schloss (Ringberg, Germany)* pp 339–56
- Nührenberg J and Zille R 1986 *Phys. Lett. A* **114** 129
- Nührenberg J and Zille R 1987 *Theory of Fusion Plasmas (Varenna, Italy)* (Bologna: Editrice Compositori) p 3–23
- Nührenberg J and Zille R 1988 *Phys. Lett. A* **129** 113

- Nührenberg J *et al* 1994 *Proc. Workshop Theory of Fusion Plasmas (Varenna, Italy)* p 3
- Nührenberg J 2006 *Fusion Sci. Technol.* **50** 146–57
- Ogawa Y *et al* 1992 *Nucl. Fusion* **32** 119
- Okamura S *et al* 1999 *Nucl. Fusion* **39** 1337
- Okubo K *et al* 1981 *Nucl. Fusion* **21** 1320
- Ott W and Speth E 2002 *Nucl. Fusion* **42** 796–804
- Ott W *et al* 1983 *Rev. Sci. Instrum.* **54** 50
- Ott W *et al* 1990 *17th EPS Conf. on Controlled Fusion and Plasma Heating (Amsterdam, The Netherlands)* p 483
- Ott W *et al* 1996 *Proc. 19th Symp. on Fusion Technology (Lisbon, Portugal)* pp 641–4
- Ott W *et al* 1998 *Proc. 25th EPS Conf. on Controlled Fusion and Plasma Physics (Prague, Czech Republic)* p 1202
- Ott W *et al* 1999 *Proc. 26th EPS Conf. Controlled Fusion and Plasma Physics (Maastricht, The Netherlands)* p 1565
- Otte M and Jaenike R 2007 *Stellarator News* (Fusion Energy Division, Oak Ridge National Laboratory) 1002–5
www.ornl.sci/fed/stelnews
- Palumbo D 1968 *IC Nuovo Cimento* **1** 847
- Palumbo D 1971 *Proc. Int. School of Plasma Physics on Instabilities and confinement in Toroidal Plasmas (Varenna, Italy)* p 91–107
- Papp C *et al* 2005 *32nd ERS Conf. on Plasma Physics (Tarragona, Spain)* p 5-021
- Pedersen T Sunn *et al* 2000 *Nucl. Fusion* **40** 1795
- Pedrosa M A *et al* 1999 *Phys. Rev. Lett.* **82** 3621–4
- Pedrosa M A *et al* 2005 *Plasma Phys. Control. Fusion* **47** 777–88
- Penningsfeld F P *et al* 1985 *Proc. 12th Eur. Conf. on Controlled Fusion und Plasma Physics (Budapest, Hungary)* p 397
- Penningsfeld F P *et al* 1991 *Proc. 18th Eur. Conf. on Controlled Fusion and Plasma Physics (Berlin, Germany)* vol 2 p 201
- Penningsfeld F P *et al* 1996 *Proc. 23rd EPS Conf. on Controlled Fusion and Plasma Physics (Kiev, Ukraine)* pp 483–6
- Pereverzev G V and Yushmanov P N 2002 *IPP Report IPP 5/98*
- Pernreiter W *et al* 1997 *10th Joint Workshop on Electron Cyclotron Emission and Electron Cyclotron Heating, EC-10 (Ameland, the Netherlands)* (Singapore: World Scientific) p 241
- Peters M 1995 *Electron Heat Transport in Current Carrying and Currentless Thermonuclear Plasmas PhD Thesis* Technische Universiteit Eindhoven
- Peters M *et al* 1994 *Proc. 21st EPS Conf. on Controlled Fusion and Plasma Physics (Montpellier, France)* pp 158–61
- Peters M *et al* 1995 *Proc. 22nd EPS Conf. on Controlled Fusion and Plasma Physics (Bournemouth, UK)* pp 37–40
- Peterson B *et al* 2001 *Phys. Plasmas* **8** 3861
- Peterson B *et al* 2004 *Annual Report 2004* National Institute for Fusion Science (NIFS), Japan p 6
- Pfeiffer U *et al* 1998 *Contrib. Plasma Phys.* **38** 134–44
- Pfirsch D and Schlüter A 1962 Der Einfluß der elektrischen Leitfähigkeit auf das Gleichgewichtsverhalten von Plasmen niedrigen Drucks in Stellaratoren *MPI-report*
- Pfirsch D and Wobig H 1965 *Proc. IAEA-Conf. (Culham, UK)* (Vienna) p 757
- Pietrzyk Z A *et al* 1993 *Nucl. Fusion* **33** 197
- Pinches S D *et al* 1998 *Comput. Phys. Commun.* **111** 133–49
- Pitcher C S and Stangeby P C 1997 *Plasma Phys. Control. Fusion* **39** 779–930
- Pokol G *et al* 2003 *Proc. 30th EPS Conf. on Controlled Fusion and Plasma Physics (St. Petersburg, Russia)* 27A P-307
- Pokol G *et al* 2004 *Proc. 20th (IAEA) Int. Conf. on Fusion Energy (Vilamoura, Portugal)* PS-EX/P6-22
- Pokol G *et al* 2005 *IAEA Conf. & Symp. Papers* vol 25 PS-EX/P6-22
- Pokol G *et al* 2007 *Plasma Phys. Control. Fusion* **49** 1391–1408
- Preinhäler J and Kopecky V 1973 *J. Plasma Phys.* **10** 1
- Preuss R *et al* 1999 *Nucl. Fusion* **39** 849–62
- Preuss R *et al* 2007 *Phys. Rev. Lett.* **99** 245001
- Pustovitov V D 1994 *J. Plasma Fusion Res. Ser.* **70** 943–91
- Ramasubramanian N *et al* 2004 *Nucl. Fusion* **44** 992–8
- Rau F *et al* 1982 Vacuum Magnetic Field and Modular Coil System of the Advanced Stellarator Wendelstein VII-AS *IPP-Report*
- Rau F *et al* 1994 *21st EPS Conf. on Controlled Fusion and Plasma Physics (Montpellier, France)* pp 400–3
- Rau F *et al* 1996 *Proc. 23rd EPS Conf. on Plasma Physics and Controlled Fusion (Kiev, Ukraine)* pp 400–3
- Reiman A and Greenside H 1986 *Comput. Phys. Commun.* **43** 157–67
- Reiman A H and Greenside H S 1990 *J. Comput. Phys.* **87** 349–65
- Reiman A *et al* 2006 *Proc. 21st IAEA Fusion Energy Conf. (Chengdu, China)* TH/P7-3

- Reiman A *et al* 2007 *Nucl. Fusion* **47** 572–8
- Reiter D 1992 The EIRENE code (Users Manual) p 2599
- Reiter D *et al* 2005 *Fusion Sci. Technol.* **47** 172–86
- Renner H *et al* 1989 *Plasma Phys. Control. Fusion* **31** 1579
- Renner H *et al* 1990 *Proc. 13th (IAEA) Int. Conf. on Plasma Physics and Controlled Nuclear Fusion Research (Washington, DC)* pp 439–54
- Renner H *et al* 1992 *Proc. 19th EPS Conf. on Controlled Fusion and Plasma Heating (Innsbruck, Austria)* p 501
- Renner H *et al* 2002 *Plasma Phys. Control. Fusion* **44** 1005–19
- Renner T *et al* 2000 *Nucl. Fusion* **40** 1083
- Ringler E *et al* 1990 *Plasma Phys. Control. Fusion* **32** 933–48
- Ringler H *et al* 1987 *Proc. 11th Int. Conf. on Plasma Physics and Controlled Nuclear Fusion Research (Kyoto, Japan)* p 603
- Romé M *et al* 1997 *Plasma Phys. Control. Fusion* **39** 117–158
- Romé M *et al* 1998 *Plasma Phys. Control. Fusion* **40** 511–30
- Romé M *et al* 2003 *Plasma Phys. Control. Fusion* **45** 783–92
- Romé M *et al* 2006 *Plasma Phys. Control. Fusion* **48** 353
- Rust N *et al* 1995 *Proc. 22nd EPS Conf. on Controlled Fusion and Plasma Physics (Bournemouth, UK)* p 137
- Rust N *et al* 1997 *Proc. 24th EPS Conf. on Controlled Fusion and Plasma Physics (Berchtesgaden, Germany)* pp 1621–4
- Rust N *et al* 2000 *Proc. 27th EPS Conf. on Controlled Fusion and Plasma Physics (Budapest, Hungary)* pp 1621–4
- Rust N *et al* 2001 *Proc. 28th EPS Conf. on Controlled Fusion and Plasma Physics (Madeira, Portugal)* P3.060
- Rust N *et al* 2002 *Proc. 29th EPS Conf. on Plasma Physics and Controlled Fusion (Montreux, Switzerland)* P-4.045
- Rust N *et al* 2003 *Proc. 14th Int. Stellarator Workshop (Greifswald, Germany)*
- Rutherford P H 1973 *Phys. Fluids* **16** 1903–8
- Ryter F *et al* 2001 *Phys. Rev. Lett.* **86** 2325–8
- Ryter F *et al* 2006 *Plasma Phys. Control. Fusion* **48** B453–63
- Saffman M *et al* 2001 *Rev. Sci. Instrum.* **72** 2579–92
- Sallander E *et al* 2000 *Nucl. Fusion* **40** 1499–509
- Sanchez E *et al* 2000 *Phys. Plasmas* **7** 1408–16
- Sanchez J *et al* 1989 *16th Eur. Conf. on Controlled Fusion and Plasma Physics (Venice, Italy)* p 1565
- Sanchez J *et al* 1990 *Nucl. Fusion* **30** 2383
- Sanchez J *et al* 2005 *Proc. 32nd EPS Conf. (Tarragona, Spain) Plasma Phys. Control. Fusion* **47** B349
- Sanchez R *et al* 1997 *Nucl. Fusion* **37** 1363–73
- Sanchez R *et al* 2000 *J. Comput. Phys.* **161** 576–88
- Sano F *et al* 2004 *20th IAEA Fusion Energy Conf. (Vilamoura, Portugal)* EX/9-2
- Sano F *et al* 2005 *Nucl. Fusion* **45** 1557–70
- Sapper J and Renner H 1990 *Fusion Technol.* **17** 61–75
- Sardei F *et al* 1990 *Proc. 17th Eur. Conf. on Controlled Fusion and Plasma Heating (Amsterdam, The Netherlands)* (EPS) p 471
- Sardei F *et al* 1991 *Proc. 18th EPS Conf. on Controlled Fusion and Plasma Physics (Berlin, Germany)* p 193
- Sardei F *et al* 1992 *J. Nucl. Mater.* **196–198** 443–7
- Sardei F *et al* 1995 *J. Nucl. Mater.* **220** 736–40
- Sardei F *et al* 1997 *J. Nucl. Mater.* **241** 135–48
- Sardei F *et al* 2007 *J. Nucl. Mater.* **363–365** 511–16
- Sattler S and Hartfuß H 1993 *Plasma Phys. Control. Fusion* **35** 1285
- Sattler S *et al* 1994a *21st EPS Conf. on Controlled Fusion and Plasma Physics (Montpellier, France)* p 1220
- Sattler S *et al* 1994b *Phys. Rev. Lett.* **72** 653
- Schilham A M R *et al* 2000 *Proc. 27th EPS Conf. on Controlled Fusion and Plasma Physics (Budapest, Hungary)* p 1132
- Schirmer J *et al* 2006 *Nucl. Fusion* **46** S780–91
- Schmidt M 2002 *Proc. 29th EPS Conf. on Plasma Physics and Controlled Fusion (Montreux, Switzerland)* P-4.112
- Schmidt M and Werner A 2003 *Proc. 30th EPS Conf. on Controlled Fusion and Plasma Physics (St Petersburg, Russia)* P-1.15
- Schmidt M *et al* 2004 *Proc. 31st EPS Conf. on Plasma Physics (London, UK)* P-1.200
- Schneider R *et al* 2006 *Contrib. Plasma Phys.* **46** 3–191
- Schubert M *et al* 2002 *Proc. 29th EPS Conf. on Plasma Physics and Controlled Fusion (Montreux, Switzerland)* P-3.218

- Schubert M 2005 Fluctuations of temperature and turbulent radial energy transport in the edge plasma of the Wendelstein 7-AS stellarator *PhD Thesis* Physikalisches Institut, Greifswald Ernst-Moritz-Arndt-Universität Greifswald
- Schüller F C *et al* 2000 *Proc. 27th EPS Conf. on Controlled Fusion and Plasma Physics (Budapest, Hungary)* p 1697
- Schwab C 1993 *Phys. Fluids* **B** **5** 3195–206
- Scott S *et al* 1996 *16th IAEA Fusion Energy Conf. (Montreal, Canada)* p 573
- Sergeev V Yu *et al* 2006 *Tech. Phys. Lett.* **51** 1462
- Shaing K C 1984 *Phys. Fluids* **27** 1567
- Shaing K C 1993 *Phys. Fluids* **B** **5** 3841–3
- Shaing K C and Hokin S A 1983 *Phys. Fluids* **26** 2136
- Shaing K C *et al* 1984 *Plasma. Phys. Control. Nucl. Fusion* **2** 189
- Shalashov A G *et al* 2003 *Plasma Phys. Control. Fusion* **45** 395–412
- Sharma D *et al* 2005 *Nucl. Fusion* **45** 825
- Sharma D *et al* 2006 *Nucl. Fusion* **46** 127
- Shats M G *et al* 1994 *Nucl. Fusion* **34** 1653
- Snipes J A *et al* 2001 *Plasma Phys. Control. Fusion* **44** L23
- Solano E R *et al* 1998 *Proc. 25th EPS Conf. on Controlled Fusion and Plasma Physics (Prague, Czech Republic)* p 1714
- Speth E 1989 *Rep. Prog. Phys.* **52** 57
- Spitzer L 1958 *Phys. Fluids* **1** 253
- Spong D A *et al* 1992 *Phys. Fluids* **B** **4** 3316–28
- Spong D A *et al* 1994a *Phys. Plasmas* **1** 1503–10
- Spong D A *et al* 1994b *Proc. 15th Int. Conf. on Plasma Physics and Controlled Nuclear Fusion Research (Seville, Spain)* (Vienna: IAEA) D-P-17 pp 567–74
- Spong D A *et al* 2001 *Nucl. Fusion* **41** 711–6
- Spong D A *et al* 2003 *Phys. Plasmas* **10** 3217–24
- Stangeby P C 1995 *Plasma Phys. Control. Fusion* **37** 1031
- Stangeby P C 2000 *The Plasma Boundary of Magnetic Fusion Devices* (Bristol: Institute of Physics Publishing)
- Stober J *et al* 2001 *Nucl. Fusion* **41** 1123–33
- Straut E J 1994 *Phys. Plasmas* **1** 1415–31
- Strickler D J *et al* 2002 *Proc. 19th IAEA Fusion Energy Conf. (Lyon, France)* FT/P2-06
- Stroth U 1998 *Plasma Phys. Control. Fusion* **40** 9
- Stroth U *et al* 1993a *Proc. 20th Eur. Conf. on Controlled Fusion and Plasma Heating (Lisbon, Portugal)* p 349
- Stroth U *et al* 1993b *Proc. Varenna Meeting on Local Transport (Varenna, Italy)* p 161
- Stroth U *et al* 1993c *Phys. Rev. Lett.* **70** 936–9
- Stroth U *et al* 1995a *Proc. 6th Int. Conf. on Plasma Physics and Controlled Nuclear Fusion (Toki City, Japan)* p 169
- Stroth U *et al* 1995b *Phys. Scr.* **51** 655–64
- Stroth U *et al* 1996a *Proc. 16th Conf. on Fusion Energy (Montreal, Canada)* pp 127–33
- Stroth U *et al* 1996b *Plasma Phys. Control. Fusion* **38** 1087
- Stroth U *et al* 1996c *Nucl. Fusion* **36** 1063–77
- Stroth U *et al* 1998 *Plasma Phys. Control. Fusion* **40** 1551–65
- Stroth U *et al* 1999 *Phys. Rev. Lett.* **82** 928
- Stroth U *et al* 2001 *Phys. Rev. Lett.* **86** 5910–3
- Subbotin A *et al* 2006 *Nucl. Fusion* **46** 921–7
- Sudo S *et al* 1990 *Nucl. Fusion* **30** 11–21
- Sugama H and Nishimura S 2002 *Phys. Plasmas* **9** 4637
- Sugama H and Watanabe T H 2006 *Phys. Plasmas* **13** 012501
- Sünder D and Wobig H 2006 *Plasma Phys. Control. Fusion* **48** 1201–32
- Suttrop W *et al* 2005 *Nucl. Fusion* **45** 721–30
- Suvorov E V *et al* 1995a *Proc. 22nd EPS Conf. on Controlled Fusion and Plasma Physics (Bournemouth, UK)* pp 429–32
- Suvorov E V *et al* 1995b *Plasma Phys. Control. Fusion* **37** 1207–13
- Suvorov E V *et al* 1997 *Plasma Phys. Control. Fusion* **39** B337–51
- Suvorov E V *et al* 1998 *Nucl. Fusion* **38** 661–71
- Suzuki Y *et al* 2006 *Nucl. Fusion* **46** L19–24
- Svensson J *et al* 2004 *Rev. Sci. Instrum.* **75** 4219–21
- Taguchi M 1989 *Plasma Phys. Control. Fusion* **31** 241–54
- Takeiri Y *et al* 1999 *26th Eur. Conf. on Controlled Fusion and Plasma Physics (Maastricht, The Netherlands)* p 1365

- Team W7-A and NI Group 1980 *8th Int. (IAEA) Conf. on Plasma Physics and Controlled Nuclear Fusion Research (Vienna, Austria)* p 185
- Teo C Y *et al* 1998 *Nucl. Fusion* **38** 409–17
- Teubel A and Penningsfeld F P 1992 *Proc. 19th Eur. Conf. on Controlled Fusion and Plasma Physics (Innsbruck, Austria)* p 537
- Teubel A and Penningsfeld F P 1994 *Plasma Phys. Control. Fusion* **36** 143–52
- Theimer G *et al* 1995 *22nd EPS Conf. on Controlled Fusion and Plasma Physics (Bournemouth, UK)* pp 301–4
- Thomsen H *et al* 2001 *Czech. J. Phys.* **51** 1079
- Thomsen H 2002a A dynamics investigation into edge plasma turbulence *PhD Thesis* Max-Planck-Institut für Plasmaphysik, TI Greifswald, Greifswald Ernst-Moritz-Arndt Universität
- Thomsen H 2002b A dynamics investigation into edge plasma turbulence *IPP 15/I*
- Thomsen H *et al* 2002a *Phys. Plasmas* **9** 1233–40
- Thomsen H *et al* 2002b *Proc. 29th EPS Conf. on Plasma Physics and Controlled Fusion (Montreux, Switzerland)* P-4.079
- Thomsen H *et al* 2003a *Proc. 14th Int. Stellarator Workshop (Greifswald, Germany)* PMo8
- Thomsen H *et al* 2003b *Proc. 30th EPS Conf. on Controlled Fusion and Plasma Physics (St Petersburg, Russia)* P-3.191
- Thomsen H *et al* 2004 *Nucl. Fusion* **44** 820–6
- Thomsen H *et al* 2005 *Plasma Phys. Control. Fusion* **47** 1401–14
- Timokhin V M *et al* 2004 *Tech. Phys. Lett.* **30** 298–300
- Toi K *et al* 1996 *Plasma Phys. Control. Fusion* **38** 1289–93
- Toi K *et al* 2004 *Nucl. Fusion* **44** 217–25
- Tribaldos V 2001 *Phys. Plasmas* **8** 1229
- Tutter M *et al* 1991 *Proc. 18th Eur. Conf. on Controlled Fusion and Plasma Physics (Berlin, Germany)* pp 205–8
- Uckan N A 1990 *ITER Physics Design Guidelines: 1989 (ITER Documentation Series)* 10
- Unger E 1992 *Report IPP-III/187*, Max-Planck Institute für Plasmaphysik, Germany
- Unger E 1995 Spektroskopische transportstudien am stellarator Wendelstein 7-AS *PhD Thesis* Munich Technical University
- Uo K *et al* 1971 *Proc. 4th Int. IAEA Conf. on Plasma Physics and Controlled Nuclear Fusion Research (Madison)* **3** 109
- Uo K *et al* 1985 *Plasma Physics and Controlled Nuclear Fusion Research (London, UK)* (Vienna: IAEA) p 383
- Ushakov *et al* 1999 *Proc. 26th Conf. on Controlled Fusion and Plasma Physics (Maastricht, The Netherlands)* (ECA) 23J 1481-4
- van Rij W I and Hirshman S P 1989 *Phys. Fluids B* **1** 563–9
- Volpe F *et al* 2002 Electron Bernstein emission diagnostic of electron temperature profiles at W7-AS stellarator *Advanced Diagnostics for Magnetic and Inertial Fusion* ed P E W Stott *et al* (New York: Kluwer) pp 347–54
- Volpe F *et al* 2003a *12th Joint Workshop on Electron Cyclotron Emission and Electron Cyclotron Heating (Aix-en-Provence, France)* (Singapore: World Scientific) pp 221–2
- Volpe F *et al* 2003b *Rev. Sci. Instrum.* **74** 1409–13
- W7A-Team 1980 *Nucl. Fusion* **20** 1093–1100
- W7A-Team and NI Group 1982 *Proc. 9th Int. (IAEA) Conf. on Plasma Physics and Controlled Nuclear Fusion Research (Baltimore, MD)* **2** p 241
- W7A-Team and NBI-Group 1985 *Nucl. Fusion* **25** 1593
- W7AS-Team 1981 Application for preferential support, Phase I for Wendelstein 7-AS Report, Max-Planck Institut für Plasmaphysik, Garching, Germany
- Wagner F 2007 *Plasma Phys. Control. Fusion* **49** B1–33
- Wagner F and Stroth U 1993 *Plasma Phys. Control. Fusion* **35** 1321–71
- Wagner F *et al* 1994a *Trans. Fusion Technol.* **27** 32
- Wagner F *et al* 1994b *Plasma Phys. Control. Fusion* **36** A61–74
- Wagner F *et al* 2002 *Proc. 19th (IAEA) Fusion Energy Conf. (Lyon, France)* OV/2-4
- Wagner F *et al* 2005 *Phys. Plasmas* **12** 072509
- Wagner F *et al* 2006 *Plasma Phys. Control. Fusion* **48** A217–39
- Wakatani M and Sudo S 1996 *Plasma Phys. Control Fusion* **38** 937–88
- Walter H *et al* 1998a *25th EPS Conf. on Controlled Fusion and Plasma Physics (Prague, Czech Republic)* p 411
- Walter H *et al* 1998b *Plasma Phys. Control. Fusion* **40** 1661–72
- Walter H 2005 Streuexperimente (????) zur Untersuchung des Energietransports im Stellarator Wendelstein 7-AS *PhD Thesis* Max-Planck-Institut für Plasmaphysik, Garching

- Watanabe K 2005 *Nucl. Fusion* **45** 1247–54
- Watanabe K Y *et al* 2003 *Proc. 14th Int. Stellarator Workshop (Greifswald, Germany)* I.Fr5
- Watanabe K Y *et al* 2004a *J. Plasma Fusion Rev. Ser.* **6** 523–6
- Watanabe K Y *et al* 2004b *Proc. 20th IAEA Fusion Energy Conf. (Vilamoura, Portugal)* EX/3-3
- Watanabe K Y *et al* 2004c *Fusion Sci. Technol.* **46** 24–33
- Watanabe K Y *et al* 2007 *Plasma Phys. Control. Fusion* **49** 605–18
- Watts C *et al* 1997 *10th Joint Workshop on Electron Cyclotron Emission and Electron Cyclotron Heating, EC-10 (Ameland, the Netherlands)* (Singapore: World Scientific) p 147
- Watts C *et al* 2004 *Rev. Sci. Instrum.* **75** 3177
- Weller A 1985 *IPP Report*
- Weller A 1986 *JET Report*
- Weller A 2003 *45th Annual Meeting of the Division of Plasma Physics (DPP03) (Albuquerque, NM)* invited talk LI1
- Weller A and Spong D A 1993 *Proc. 9th Int. Workshop on Stellarators (Garching, Germany)* pp 554–60
- Weller A *et al* 1989 *Proc. 7th Int. Workshop on Stellarators (Oak Ridge, TN)* pp 583–8
- Weller A *et al* 1990 *Proc. 17th EPS Conf. on Controlled Fusion and Plasma Heating (Amsterdam, The Netherlands)* pp 479–82
- Weller A *et al* 1991 *Plasma Phys. Control. Fusion* **33** 1559–78
- Weller A *et al* 1992 *Proc. 1992 ICPP & 19th EPS Conf. on Controlled Fusion and Plasma Physics (Innsbruck, Austria)* pp 549–52
- Weller A *et al* 1993 *Proc. 20th EPS Conf. on Controlled Fusion and Plasma Physics (Lisbon, Portugal)* pp 337–40
- Weller A *et al* 1994a *Proc. 15th (IAEA) Int. Conf. on Plasma Physics and Controlled Nuclear Fusion Research (Seville, Spain)* (Vienna: IAEA) A-6-I-5 pp 791–6
- Weller A *et al* 1994b *Proc. 21st EPS Conf. on Controlled Fusion and Plasma Physics (Montpellier, France)* pp 408–11
- Weller A *et al* 1994c *Phys. Rev. Lett.* **72** 1220–3
- Weller A *et al* 1995 *Proc. 10th Int. Conf. on Stellarators (Madrid, Spain)* pp 61–4
- Weller A *et al* 1996 *Fusion Eng. Des.* **34/35** 17
- Weller A *et al* 1997a *Proc. 24th EPS Conf. on Controlled Fusion and Plasma Physics (Berchtesgaden, Germany)* pp 1649–52
- Weller A *et al* 1997b *Fusion Eng. Des.* **34–35** 17–24
- Weller A *et al* 1998 *Proc. 17th IAEA Fusion Energy Conf. (Yokohama, Japan)* EX2/1
- Weller A *et al* 1999a Survey of MHD Instabilities in W7-AS *Proc. 12th Int. Stellarator Workshop (Madison, WI, USA)*
- Weller A *et al* 1999b *Rev. Sci. Instrum.* **70** 484–8
- Weller A *et al* 2000 *Proc. 18th IAEA Fusion Energy Conf. (Sorrento, Italy)* IAEA-CN-69, EX7/4
- Weller A *et al* 2001 *Phys. Plasmas* **8** 931–56
- Weller A *et al* 2002a *Proc. 13th Int. Stellarator Workshop (Canberra, Australia)*
- Weller A *et al* 2002b *Proc. 19th (IAEA) Fusion Energy Conf. (Lyon, France)* EX/S3-1
- Weller A *et al* 2003 *Plasma Phys. Control. Fusion* **45** A285–308
- Weller A *et al* 2005 *32nd EPS Conf. on Plasma Physics (Tarragona, Spain)* P-4.056
- Weller A *et al* 2006 *Fusion Sci. Technol.* **50** 158–70
- Weller A *et al* 2007 *34th EPS Conf. on Plasma Physics (Warsaw, Poland)*
- Wendland C *et al* 1999 *Proc. 26th EPS Conf. on Plasma Physics and Controlled Fusion (Maastricht, The Netherlands)* p 1489
- Wenzel U *et al* 2002 *Plasma Phys. Control. Fusion* **44** L57–62
- Wenzel U *et al* 2003 *J. Nucl. Mater.* **313–316** 1098–102
- Wenzel U *et al* 2004 *Nucl. Fusion* **44** 1130–40
- Wenzel U *et al* 2005 *J. Nucl. Mater.* **337–339** 196–200
- Werner A 2005 private communication
- Werner A *et al* 2000 *Proc. 27th EPS Conf. on Controlled Fusion and Plasma Physics (Budapest, Hungary)* pp 988–91
- Werner A *et al* 2001 *Rev. Sci. Instrum.* **72** 780–3
- Wesner F *et al* 1988 *Proc. 5th Symp. on Fusion Technology (Utrecht, The Netherlands)* p 475
- Wilhelm R *et al* 1984a *Plasma Phys. Control. Fusion* **26** 1433–44
- Wilhelm R *et al* 1984b *Plasma Phys. Control. Fusion* **26** 259
- Wobig H 1993 *Plasma Phys. Control. Fusion* **35** 903–17
- Wobig H 1999 *Plasma Phys. Control. Fusion* **41** A159–73
- Wobig H 2000 *Plasma Phys. Control. Fusion* **42** 931–48
- Wobig H and Kisslinger J 1995 *Plasma Phys. Control. Fusion* **37** 893–922

- Wobig H and Kisslinger J 1997 *Proc. 24th EPS Conf. on Controlled Fusion and Plasma Physics (Brechtsgaden, Germany)* pp 1669–72
- Wobig H and Kisslinger J 2000 *Plasma Phys. Control. Fusion* **42** 823–41
- Wobig H and Rehker S 1972 *Proc. 7th Symp. on Fusion Technology (Grenoble, France)* pp 333–43
- Wobig H *et al* 1987 *11th Int. Conf. on Plasma Physics and Controlled Fusion Research (Kyoto, Japan)* p 367
- Wobig H *et al* 2003 *Nucl. Fusion* **43** 889–98
- Wolle B *et al* 1999 *Rev. Sci. Instrum.* **70** 1197–200
- Wong K-L 1999 *Plasma Phys. Control. Fusion* **41** R1–56
- Yakovenko Yu V *et al* 2007 *Plasma Phys. Control. Fusion* **49** 535–58
- Yamada H *et al* 1994 Remarks on Application of VMEC and PROCTR to the W7-AS Experiments *Report IPP/194*, Max-Planck Institut für Plasmaphysik, Germany
- Yamada H *et al* 2001 *Plasma Phys. Control. Fusion* **43** A55–71
- Yamada H *et al* 2004 *Fusion Sci. Technol.* **46** 82–90
- Yamada H *et al* 2005 *Nucl. Fusion* **45** 1684–93
- Yamazaki *et al* 2003 *30th EPS Conf. on Controlled Fusion and Plasma Physics (St Petersburg, Russia)* 27A P-3.16
- Yao L and Baldzuhn J 2003 *Plasma Sci. Technol.* **5** 1933–8
- Yokoyama *et al* 2006 *Fusion Sci. Technol.* **50** 327
- Yokoyama M *et al* 2007 *Nucl. Fusion* **47** 1213–9
- Yoshinuma M *et al* 2004 *Rev. Sci. Instrum.* **75** 4136
- Zarnstorff M *et al* 2004 *20th IAEA Fusion Energy Conf. (Vilamoura, Portugal)* EX/3-4
- Zarnstorff M C *et al* 2001 *Plasma Phys. Control. Fusion* **43** A237–49
- Zarnstorff M C *et al* 2005 *32nd EPS Conf. on Plasma Physics (Tarragona, Spain)* P-1.062
- Zebisch P *et al* 1997 *J. Nucl. Mater.* **241** 919–24
- Zegenhagen S 2005 *Proc. German-Polish Conf. on Plasma Diagnostics for Fusion and Applications (Krakow, Poland)*
- Zegenhagen S 2006 Destabilization of Alfvén Eigenmodes by Fast Particles in W7-AS *Doctor Rerum Naturalium*: 157 Mathematisch-Naturwissenschaftliche Fakultät, Greifswald, Germany Ernst-Moritz-Arndt-University
- Zegenhagen S *et al* 2006a *Plasma Phys. Control. Fusion* **48** 1333–46
- Zegenhagen S *et al* 2006b *33rd EPS Conf. on Plasma Physics (Rome, Italy)* P-2.117
- Zehrfeld H P and Geiger J 1997 *Proc. 24th Conf. on Controlled Fusion and Plasma Physics (Brechtsgaden, Germany)* pp 1561–4
- Zhuravlev V *et al* 1997 *Fusion Eng. Des.* **34–35** 421–4
- Zohm H 1996 *Plasma Phys. Control. Fusion* **38** 105
- Zohm H *et al* 1997 *Plasma Phys. Control. Fusion* **39** B237–46
- Zoletnik S 1998 *Plasma Phys. Control. Fusion* **40** 1399
- Zoletnik S *et al* 1999 *Phys. Plasmas* **6** 4239–47
- Zoletnik S *et al* 2002 *Plasma Phys. Control. Fusion* **44** 1581–607
- Zoletnik S *et al* 2005a *32nd EPS Conf. on Plasma Physics (Tarragona, Spain)* P-5.023
- Zoletnik S *et al* 2005b *Rev. Sci. Instrum.* **76** 073504
- Zonca F and Chen L 1996 *Phys. Plasmas* **3** 323–43
- Zurro B *et al* 2003 *Proc. 30th EPS Conf. on Controlled Fusion and Plasma Physics (St Petersburg, Russia)* P-2.79
- Zurro B *et al* 2004 *Rev. Sci. Instrum.* **75** 4231–3